Modelling and Numerical Simulation of Species Transfer in Bubbly Flows using OpenFOAM®

Zur Erlangung des akademischen Grades Doktor-Ingenieur (Dr.-Ing.)
genehmigte Dissertation von Daniel Deising aus Koblenz
Tag der Einreichung: 05.11.2018
Tag der Prüfung: 06.02.2019
Darmstadt — D 17

1. Gutachten: Prof. Dr. Dieter Bothe
2. Gutachten: Prof. Dr. Cameron Tropea

TECHNISCHE UNIVERSITÄT DARMSTADT

Center of Smart Interfaces

Modelling and Numerical Simulation of Species Transfer in Bubbly Flows using OpenFOAM®

Genehmigte Dissertation von Daniel Deising aus Koblenz

1. Gutachten: Prof. Dr. Dieter Bothe
2. Gutachten: Prof. Dr. Cameron Tropea

Tag der Einreichung: 05.11.2018
Tag der Prüfung: 06.02.2019

Darmstadt — D 17

Bitte zitieren Sie dieses Dokument als:
URN: urn:nbn:de:tuda-tuprints-85227
URI: http://tuprints.ulb.tu-darmstadt.de/id/eprint/8522

Jahr der Veröffentlichung der Dissertation auf TUprints: 2019

Acknowledgements

My biggest thanks goes to my family, my wife Yangmei, my parents and grand parents as well as my brother, for their everlasting support and understanding.

Secondly, I would like to thank my supervisors Prof. Dr. Dieter Bothe and Dr. Holger Marschall for a multitude of great scientific discussions and ideas. The same goes to all the colleagues at Mathematical Modelling and Analysis institute at TU Darmstadt. Personally, I wish to thank here foremost Matthias Niethammer, Dr. Xingyuan Chen and Dr. Tomislav Maric for their support and close cooperation.

Also, I would like to thank Daniel Rettenmaier (Institute for Fluid Mechanics and Aerodynamics, Prof. Dr. Cameron Tropea, TU Darmstadt) for his close cooperation regarding improvements to the underlying flow solver and enhancement of adaptive mesh and load balancing techniques. In this scope I would like to extend my thanks to the Institute of Technical Thermodynamics, Prof. Dr. Peter Stephan, TU Darmstadt (especially Dr. Stefan Batzdorf and Dr. Christian Kunkelmann) and the School of Aeronautics and Astronautics, Prof. Timothee Pourpoint, University of Purdue (namely Tyler G. Voskuilen) for their recent developments regarding load balancing.

Additionally, I would like to thank Simon Hill (Linde AG and Chair of Plant and Process Technology, Prof. Dr. Harald Klein, TU Munich) for his cooperation and continuing work regarding numerical discretization and further development of the CST method, as well as the Institute for Multiphase Flow, Prof. Dr. Michael Schlüter, Hamburg University of Technology (namely Dr. Marko Hoffmann and Daniel Bezecny) for their cooperation regarding the application of the CST method to the simulation of species transfer processes in bubbly flows.

Last but not least, I wish to thank my current employer Engys Ltd., especially Dr. Eugene de Villiers, for the free time to finish my publications and this thesis, the Lichtenberg High Performance Computer Center (HHLR) for their support during the vast amount of CPU hours consumed in this work as well as the German Federal Ministry of Education and Research (BMBF) for the funding in scope of the project "Multiscale Modelling for Multiphase Reactors" (FKZ:033RC1102H) and Evonik Industries AG, especially Dr. Georg Skillas, for the extended funding and cooperation in scope of this research project.

Zusammenfassung

Das Ziel dieser Arbeit ist die Herleitung eines verbesserten Schliessungsmodells zur Beschreibung von Stofftransportprozessen in Zwei-Phasen Gas-Flüssig-Strömungen, welches im weiteren unter anderem zur Simulation von Blasensäulenreaktoren mittels Zwei-Fluid Modell oder auch zur verbesserten Auslegung von Strömungsreaktoren genutzt werden kann. Um detailierte Einblicke in den Prozess zu gewinnen, fokussiert sich diese Forschungsarbeit auf die Direkte Numerische Simulation (DNS) von Stofftransportprozessen an aufsteigenden Einzelblasen (und Blasengruppen) von der Gas- in die Flüssigphase. Aufgrund der besonderen Eignung für das vorliegende Problem, wird hierzu ein algebraisches *Volume-of-Fluid (VoF)* Verfahren basierend auf dem OpenFOAM® interFoam Löser verwendet. Der Stofftransport wird mittels eines neuen Ein-Gleichungs-Modells Namens *Continuous Species Transfer (CST)* Modell abgebildet, welches eine genaue Beschreibung des Stoffübergangs im Kontext der algebraischen Volume-of-Fluid Methode erlaubt.

Eine weitere Neuheit der vorliegenden Arbeit ist, dass im Gegensatz zur gängigen Fachliteratur der Einfluss der Blasenform auf den Stoffübergang als weitere Einflussgrösse berücksichtigt wird. Es wird gezeigt, dass eine detailierte Beschreibung des Stofftransportprozesses nur durch die Betrachtung zweier getrennter Mechanismen möglich ist: der Generierung neuer Grenzfläche durch Verformung der Grenzschicht und der Änderung der Konzentrationsgradienten an der Blasengrenzfläche.

Der Großteil dieser Arbeit befasst sich mit der umfassenden Herleitung, Verifizierung und Validierung des numerischen Modells. Änderungen an dem verwendeten Strömungslöser werden ebenfalls vorgestellt und die Verbesserungen quantifiziert.

Abstract

The aim of this work is the derivation of an improved closure model for the description of species transfer processes in two-phase gas-liquid flows which in the following, among others, can be used for the numerical simulation of bubble column reactors using a two-fluid model or also to obtain an improved design of fluid reactors. To gain detailed insight into the process, this research is focussed on the Direct Numerical Simulation (DNS) of species transport processes at single rising bubbles (and bubble groups) from the gas into the liquid phase. Due to the special suitability an algebraic Volume-of-Fluid (VoF) method based on the OpenFOAM® interFoam solver is utilized. The species transfer is herein modelled employing a new single-field model named Continuous Species Transfer (CST) model which enables a detailed decription of the species transfer process in context of algebraic Volume-of-Fluid methods.

A further novelty of the present work is that in contrast to common literature the influence of the bubble shape on the species transfer is considered as an additional influence variable. It is shown that the overall species transfer rate is effectively influenced by two separate mechanisms, leading to a more detailed description of species transfer processes: the generation of new interfacial area due to bubble deformation and the change of the concentration gradient at the bubble interface.

The majority of this work is concerned with the comprehensive derivation, verification and validation of the presented numerical model. Modifications to the utilized flow solver are additionally presented and the improvements are quantified.

Contents

Nomenclature

Abbreviations

AMR Adaptive Mesh Refinement

CD Central differencing (scheme)

COM Centre-of-Moment Reference Frame

CVA Conditional volume averaging

CST Continuous Species Transfer (model)

CSF Continuous Surface Force

CV Control volume

DNS Direct Numerical Simulation

DNS Direct Numerical Simulation

DD Downwind discretization (scheme)

FVM Finite Volume Method

FCT Flux Corrected Transport

HPC High Performance Computing

IRF Inertial Reference Frame

MRF Moving Reference Frame

NVF normalised variable formulation

TFM Two-Fluid Model

UD Upwind discretization (scheme)

VA Volume averaging

VOF Volume-of-Fluid

Dimensionless numbers

Eo Eötvös number

Gr Grashof number

Mo Morton number

Pe	Peclet number	
Ra	Rayleigh number	
Re	Reynolds number	
Sc	Schmidt number	
Sh	Sherwood number	

Discretization

F_ρ	(mass) face flux	kg/s
F	(volumetric) face flux	m^3/s
f	cell face (centre position)	-
$\mathbf{S}_f$	cell face normal vector times face area	m^2
γ	cell face/interface orientation / interpolation blending factor	-
$\mathbf{d}$	distance vector between neighbouring cell centres	m
C_f	face Courant number	-
$\phi_{f(S)}$	face interpolation of quantity ϕ using scheme $'S'$	$[\phi]$
β	face interpolation weights	-
S_u, S_p	general source terms	$[\mathbf{\Phi}]\cdot$kg/s, kg/s
$[\![\ldots[\phi]]\!]$	implicit FV discretization with respect to ϕ	-
Δ, $\mathbf{k}$	mesh non-orthogonality vectors	m^2
$\mathbf{m}$	mesh skewness vector	m
N	neighbour cell centre	-
P	parent cell centre	-
$\mathbf{x}$	position vector	m
$\nabla_f^\perp$	surface normal gradient	$[\mathbf{\Phi}]\cdot m^{-1}$
U	upwind cell centre	-

Other symbols/Notation

e, E	error measures	$[e]$, $[E]$
$[\![\ldots]\!]$	Jump bracket notation	-
ϕ_F	quantity ϕ in reference frame	$[\phi]$

Hydrodynamic variables

ϕ	arbitrary scalar-valued quantity	$[\phi]$
$\mathbf{\Phi}$	arbitrary vector-valued quantity	$[\mathbf{\Phi}]$
d_b	bubble diameter	m
V	cell volume	m^3
$\mathbf{j}$	diffusive flux	$\mathrm{kg/m\,s^2}$
ρ	fluid density	$\mathrm{kg/m^3}$
μ	fluid dynamic viscosity	$\mathrm{kg/m\,s}$
S_Σ	fluid interface in control volume	-
Σ	fluid interface	-
ν	fluid kinematic viscosity	$\mathrm{m^2/s}$
$\Gamma_{\mathbf{\Phi},d}$	general diffusion coefficient of arbitrary quantity $\mathbf{\Phi}$	$\mathrm{kg/m\,s}$
$\mathbf{g}$	gravitational acceleration vector	$\mathrm{m/s^2}$
κ	interface curvature	$\mathrm{m^{-1}}$
δ_Σ	interface delta function	-
$\mathbf{n}_\Sigma$	interface normal vector	-
$\mathbf{u}^\Sigma$	interface velocity vector	$\mathrm{m/s}$
a_Σ	interfacial area density	$\mathrm{m^{-1}}$
$\mathbf{n}$	normal vector	-
p	pressure	$\mathrm{kg/m\,s^2}$
σ	surface tension coefficient	$\mathrm{kg/m\,s^2}$
$\mathbf{f}_\sigma$	surface tension force	$\mathrm{kg/m^2\,s^2}$
$\mathbf{u}$	velocity vector	$\mathrm{m/s}$

Volume averaging

$\langle\phi\rangle_\mathrm{a}$	arithmetic mean quantity	$[\phi]$
$\overline{\mathbf{u}_m}$	barycentric velocity	$\mathrm{m/s}$
$\langle\phi\rangle_\mathrm{h}$	harmonic mean quantity	$[\phi]$
$\langle\phi\rangle$	mean quantity	$[\phi]$
χ_1	phase indicator of phase 1	-
$\overline{\phi}^{1,2}$	phasic averaged quantity of phase 1, 2	$[\phi]$

$\mathbf{u}_r$	relative velocity between phases 1 and 2	m/s
$\overset{\frown}{\phi}$	surface averaged quantity	$[\phi]$
$\overline{\phi}$	volume averaged (mixture) quantity	$[\phi]$
α_1	volumetric phase fraction of phase 1	-

Mass transfer variables

$k_l A$	$k_l A$ coefficient (k_l times area)	m^3/s
H	Henry coefficient	-
k_l	mass transfer coefficient	m/s
R	reaction rate	$mol/m^3\,s$
c_Σ	species concentration at the interface	mol/m^3
c_∞	species concentration in the bulk	mol/m^3
c	species concentration	mol/m^3
D	species diffusion coefficient	m^2/s

List of Figures

List of Tables

1 Introduction

This work is dedicated to the study of two-phase gas-liquid systems in which the gas phase is dispersed in the liquid into a multitude of bubbles. Focus of this contribution lies on the numerical investigation of species transfer of a dilute species over the liquid-gas interface of single rising bubbles in quiescent liquids. For this purpose, a new species transfer model named *Continuous Species Transfer (CST)* model is introduced which enables the Direct Numerical Simulation (DNS) of species transfer processes across fluid interfaces based on algebraic Volume-of-Fluid methods. In order to enable the accurate simulation of interfacial mass transfer from single rising bubbles, improvements to the utilized numerical method for the hydrodynamics are additionally needed. They are described in this work only when essential for the understanding of the utilized method. The larger part of this development can be found in the Appendix of this work as supplement.

The scientific aim of this research is to obtain a better understanding of the underlying process and to use this knowledge for the enhancement of existing correlations to quantify mass transfer processes at single rising bubbles.

1.1 Relevance

In many industrial processes – especially in the chemical and bio-technological industry – two-phase gas-liquid systems are employed. Examples are aerated bioreactors, which usually do not have any moving parts and aerated stirred tank reactors (Deckwer, 1985), which are stirred by one or multiple impellers and play a major role e.g. in waste water treatment, where often continuous-flow stirred tank reactors are employed. One other two-phase system of major industrial interest is the dispersed gas-liquid flow in bubble column reactors. This reactor type is widely employed in the chemical and biochemical industry, whenever mass transfer is needed and the underlying chemistry is comparably slow. Bubble column reactors are often utilized in production processes of base chemicals as oxidation, hydrogenation, phosgenation, alkylation and hydroformylation with a total annual production volume of more than $10^8\,t$ (Dudukovic, 2007).

In order to design such reactors, a detailed understanding of the interaction between the hydrodynamics and interfacial mass transfer processes is of major importance. A common approach to quantify mass transfer in industrial-scale bubble column reactors predictively is to conduct a series of experiments and obtain integral measurements or measurements at specified fixed positions for a fixed material system and varying superficial velocity and/or sparger geometry. The collected data is then used to obtain correlations for the overall mass transfer. This approach is usually very expensive and may not be feasible for many processes as desired measurement locations or measurement quantities may not be accessible. Further, the obtained *knowledge* in form of a mass transfer correlation can most probably not be extrapolated to operation conditions outside the conducted experimental study, i.e. may only be applicable to the studied material system, utilized tank and sparger geometries, and employed superficial gas velocities.

This is the starting-point for the development of numerical methods, which allow for a more detailed description of the mass transfer processes and even enable the predictive simulation of such processes. Major benefit of the usage of numerical methods to investigate species transfer over fluid interfaces is that a large range of material systems and model parameters can be investigated in a relatively short amount of time. Also, the costs to conduct numerical simulations are typically significantly lower compared to the conduction of experiments.

1.2 Research Motivation

While bubble column reactor design in many cases is still based on simple correlations derived from experimental results, considerable efforts are made to construct a multitude of numerical models, which vary significantly in complexity. On one side are shortcut models as e.g. dispersion and compartment models which enable the modelling of complete industrial-scale processes with very small computational efforts. This naturally comes at a price, here, in terms of accuracy. These shortcut models, commonly also referred to as detail-reduced models, are derived by application of averaging procedures and/or simplifications of the set of governing equations, where information about flow phenomena below averaging-scale is inherently lost and closure modelling becomes necessary. Thus, in order to utilize such methods, correlations to describe the underlying mass transfer processes are still needed. A good characterization and description of different modelling approaches applied in the chemical industry is given in Nauman (2002). The interested reader in detail-reduced mathematical models is referred to Jakobsen (2008).

To describe mass transfer problems phenomenologically, many simplified theories for the transport of a fluid phase through the interface have been developed. Most prominent among them are the (two-)film theory (Nernst, 1904; Whitman, 1923), the penetration theory (Higbie,1935), the surface renewal theory (Danckwerts, 1951) and the film penetration theory (Toor, 1958), which can be found e.g. in (Cussler, 2009). All these theories share a common description of the mass transfer over a fluid interface. The mass transfer of a component i from the disperse gas phase into the liquid phase is herein modeled as

$$\dot{m}_i = \tilde{k}_{l,i}\left(\rho_{i,\text{gas}} - \rho_{i,\text{liq}}\right)A_\Sigma = k_{l,i}\left(c_{i,\text{gas}} - c_{i,\text{liq}}\right)a_\Sigma V\,, \tag{1.1}$$

based on the mass transfer coefficient $k_{l,i}$, the interfacial area A_Σ and the driving force of mass transfer, the difference of the species concentrations in the respective bulk phases. If the diffusion coefficient ratio is very large, the resistance to mass transfer in the phase with higher diffusion coefficient can be completely neglected as is the case in gas-liquid systems, leading to

$$\dot{m}_i = k_{l,i}\left(c_{i,\text{liq},\Sigma} - c_{i,\text{liq},\infty}\right)a_\Sigma V\,. \tag{1.2}$$

A schematic drawing of the two-film theory is shown in Figure 1.1, where in typical gas-liquid systems $c_{\text{gas},\Sigma} = c_{\text{gas},\infty}$ can be assumed, leading to above Equation (1.2). Based on this analysis,

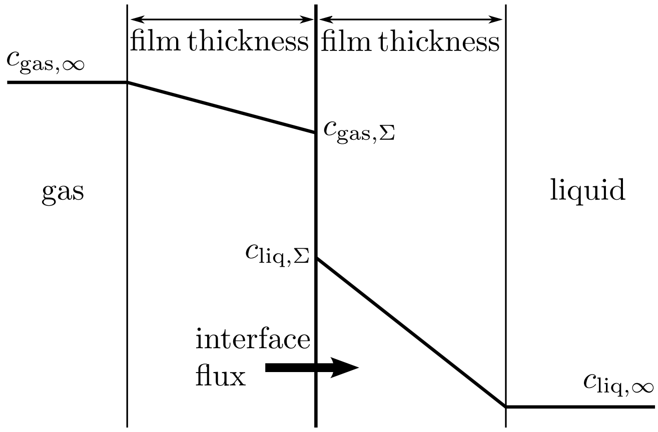

Figure 1.1.: Engineering approach to mass transfer – Two-film model

the mass transfer can be described by introducing the dimensionless Sherwood number

$$\text{Sh} := \frac{k_l d_b}{D}, \tag{1.3}$$

depending on the bubble diameter d_b and the diffusion coefficient in the liquid D. Sherwood number correlations are mainly based on experimental or theoretical investigation of mass transfer processses. A multitude of different correlations for the mass transfer coefficient or Sherwood number are available in the literature. A comprehensive list of relevant correlations is given in (Green and Perry, 2007, pp. 5-71 to 5-73) or in Colombet et al. (2014). Further relevant correlations can be found in Lochiel and Calderbank (1964), Oellrich et al. (1973), Clift et al. (1978), Takemura and Yabe (1998). Relevant correlations for mass transfer from rising bubbles are summarized in Table 1.1.

Simplified theories as the two-film model are not able to correctly capture the influence of physical properties like diffusion coefficient and local varying velocities onto the mass transfer. Also, experimental studies are limited in their investigated parameter range and relevant quantities as local concentration gradients and interfacial area are mostly inaccessible. Therefore, in the last decade, sophisticated methods for the Direct Numerical Simulation (DNS) of species transfer at fluid bubble interfaces have evolved. Due to the high computational costs involved, these methods are limited to the study of a few bubbles (commonly around 10) and their direct environment. However, in return, they enable the predictive simulation of mass transfer at fluid interfaces, yielding detailed information about the underlying process. It should further be noted that the modelling of mass transfer based on Equation (1.2) necessitates the formulation of two separate closure relations – for the mass transfer coefficient but also for the interfacial area. Thus, one main benefit of numerical simulations in comparison to experimental studies is that the change in transferred mass due to increased mass transfer coefficient and due to increase in bubble area can be quantified separately, leading to a better understanding of mass transfer processes and thus, in principle, to more reliable correlations.

Table 1.1.: Sherwood correlations for mass transfer from single rising bubbles

Correlation	Comments (E = Empirical, S = Semiempirical, T = Theoretical)	References
$\mathrm{Sh} = 1.0(\mathrm{Re\,Sc})^{1/3}$	[T] solid sphere, contaminated spherical bubble	McCabe et al. (2005); Sherwood et al. (1975); Green and Perry (2007)
$\mathrm{Sh} = 1.13(\mathrm{Re\,Sc})^{1/2}$	[T] small (spherical) bubbles	Sherwood et al. (1975); Green and Perry (2007)
$\mathrm{Sh} = 1.13(\mathrm{Re\,Sc})^{1/2}\left(\frac{d_b}{0.45\,\mathrm{cm} + 0.2 d_b}\right)$	[S] medium to large bubble, carbon dioxide & butene in water, $0.6\,\mathrm{cm} \leq d_b \leq 4\,\mathrm{cm}$	Johnson et al. (1969); Sherwood et al. (1975); Green and Perry (2007)
$\mathrm{Sh} = 2 + 0.31\,\mathrm{Gr}^{1/3}\,\mathrm{Sc}^{1/3}$ with $\mathrm{Ra} = \mathrm{Gr\,Sc} = \frac{d_b^3 \lvert\rho_G - \rho_L\rvert g}{\mu_L D_L}$	[S] Calderbank and Moo-Young correlation, carbon dioxide in water/glycerol, $d_b <$ 2.5 mm	Calderbank and Moo-Young (1961); Geankoplis (1993) Kirwan (1987); Treybal (1980); Shah et al. (1982); Green and Perry (2007)
$\mathrm{Sh} = 0.42\,\mathrm{Gr}^{1/3}\,\mathrm{Sc}^{1/2}$	[S] Calderbank and Moo-Young correlation, carbon dioxide in water/glycerol, $d_b >$ 2.5 mm	Calderbank and Moo-Young (1961); Geankoplis (1993); Green and Perry (2007); Kirwan (1987); Lee (1992); Shah et al. (1982)
$\mathrm{Sh} = 2 + 0.061\,\mathrm{Sc}^{0.546}\,\mathrm{Re}_s^{0.779}\left(\frac{d_b g^{1/3}}{D_L^{2/3}}\right)^{0.116}$	[E] Hughmark correlation, Re_s with slip velocity, air/water-glycerol system	Hughmark (1967); Treybal (1980); Green and Perry (2007)
$\mathrm{Sh} = 2 + 0.651\frac{(\mathrm{Re\,Sc})^{1.72}}{1 + (\mathrm{Re\,Sc})^{1.22}}$	[T] Oellrich correlation, small bubbles, $\mathrm{Re} \to 0$, $\mathrm{Sc} \to \infty$	Oellrich et al. (1973); Clift et al. (1978); Fleckenstein and Bothe (2015)
$\mathrm{Sh} = 2 + \frac{0.232(\mathrm{Re\,Sc})^{1.72}}{1 + 0.205(\mathrm{Re\,Sc})^{1.22}}$	[T] Oellrich correlation, large bubbles, $\mathrm{Re} \to \infty$, $\mathrm{Sc} \to 0$	Oellrich et al. (1973); Clift et al. (1978); Fleckenstein and Bothe (2015)
$\mathrm{Sh} = 1.13(\mathrm{Re\,Sc})^{1/2} f(\chi)$ with $f(\chi) = \left[\frac{2}{3}(1+k)\right]^{1/2} \frac{2\chi^{1/3}(\chi^2-1)^{1/2}}{\chi(\chi^2-1)^{1/2} + \ln(\chi + (\chi^2-1)^{1/2})}$, $k = -\frac{e\chi^2 - \chi \sin^{-1} e}{e - \chi \sin^{-1} e}$, $e = (1 - \chi^{-1})^{1/2}$	[T] aspect ratio χ, for oblate spheroids	Lochiel and Calderbank (1964); Colombet et al. (2014)
$\mathrm{Sh} = 1.13(\mathrm{Re\,Sc})^{1/2} f(\chi)$ with $f(\chi) = 0.524 + 0.88\chi - 0.49\chi^2 + 0.086\chi^3$	[S] aspect ratio $\chi \in [1, 3]$, $500 \leq (\frac{\chi}{8})^{1/3}\,\mathrm{Re} \leq 1000$, $\mathrm{Sc} > 100$	Figueroa-Espinoza and Legendre (2010); Colombet et al. (2014)
$\mathrm{Sh} = 1.13\left[1 - \frac{2}{3}\frac{1}{(1 + 0.09\,\mathrm{Re}^{2/3})^{3/4}}\right]^{1/2}(2.5 + \mathrm{Pe}^{1/2})$	[E] nearly spherical bubbles, $0 < \mathrm{Re} \leq 100$, $\mathrm{Sc} \gg 1$	Takemura and Yabe (1998); Colombet et al. (2014)

In scope of numerical methods, the term *species transfer* is introduced, meaning the simplification of mass transfer processes to the transport of an inert scalar representing the species concentration, neglecting volume effects and mass transfer processes due to relative velocities (phase change). Thus, most numerical models for the investigation of mass transfer are limited to the study of dilute species without phase change and are therefore referred to as species transfer models. In this work, a strict distinction between *mass transfer* and *species transfer* is made, where the latter implies the numerical transport of an inert scalar. Thus, in the following, the wording *species transfer* is utilized, whenever referring to the presented method. An analysis of the validity of the necessary simplifications and the range of applicability is given in Bothe and Fleckenstein (2013).

Developed methods for the simulation of species transfer cover the physisorption of a dilute species (Davidson and Rudman, 2002, Darmana et al., 2006, Figueroa-Espinoza and Legendre, 2010, Haroun et al., 2010, Aboulhasanzadeh et al., 2012, Marschall et al., 2012, Bothe and Fleckenstein, 2013, Deising et al., 2016) and the chemisorption of a dilute species (Khinast, 2001, Khinast et al., 2003, Koynov et al., 2005, Deshpande and Zimmerman, 2006, Darmana et al., 2007, Radl et al., 2008, Alke and Bothe, 2008, Onea et al., 2009, Bothe et al., 2010), in both cases neglecting mass transfer effects on the phase continuity and momentum balance equations. Volume effects of the species transfer are accounted for e.g. by Fleckenstein and Bothe (2015) and Hayashi and Tomiyama (2011). The conceptual approaches to simulate species transfer in two-phase flow systems cover Front Tracking (Khinast, 2001, Khinast et al., 2003, Koynov et al., 2005, Darmana et al., 2007, Radl et al., 2008, Aboulhasanzadeh et al., 2012) Level-Set (Yang and Mao, 2005, Deshpande and Zimmerman, 2006), Volume-of-Fluid (VOF) methods (Bothe et al., 2003, 2004, Haroun et al., 2010, Marschall et al., 2012, Bothe and Fleckenstein, 2013, Deising et al., 2016), ALE Interface Tracking methods (Weber et al., 2017, Tukovic and Jasak, 2008), and Finite Element-based methods (Lehrenfeld, 2015, Bäumler, 2014). An overview of relevant numerical models for the direct numerical simulation of species transfer in two-phase flows is given in Table 1.3.

Despite the large number of available numerical methods, there are some general difficulties that have not been solved yet. Numerical methods for species transfer in two-phase flow systems mainly suffer from numerical difficulties due to the concentration jump at the interface, resulting from different species solubility at both sides of the interface, and from a very thin concentration boundary layer at the interface which need to be resolved. Also, the range of applicability for many existing methods is very limited. As such, most existing method can only be applied to Cartesian meshes, enabling the study of two-phase flows in only very simple geometries. Furthermore, none of the existing methods have yet been applied to dynamically changing meshes, allowing at best for static refinement of the interfacial area. Due to the steep concentration gradients near the interface, this requires an extremely large number of cells in the computational domain to sufficiently resolve the concentration boundary layer.

Table 1.3.: Different numerical methods for DNS of interfacial species transfer sorted by employed codes

Authors & publication year	numerical method species transfer*	subject	remark/restrictions
Darmana et al. (2007), Roghair (2012), Roghair et al. (2016)	Front-tracking; single-field/immersed boundary	3D rising single bubbles and bubble groups w/o reaction	not inherently mass conservative; Concentration jump $\mathrm{He} = 1.2$; Peclet up to $\mathrm{Pe} \approx 1000$ (under-resolved)
Koynov et al. (2005), Radl et al. (2008), Aboulhasanzadeh et al. (2012)	Front-tracking; single-field approach subgrid-scale model	2D rising bubbles and bubble groups w/o reaction	resolved simulations with Peclet up to $\mathrm{Pe} = 900$; simulations with subgrid-scale model up to $\mathrm{Pe} = 6 \cdot 10^4$ (no reaction); not inherently mass conservative
Hayashi and Tomiyama (2011), Hayashi et al. (2014)	Geometrical VOF; single-field approach	2D rising single bubbles (rotational symmetry)	also consider volume-loss due to species transfer; loss of inherent mass conservativeness of VOF due to model reformulation; only 2D simulations; very high Peclet numbers up to $\mathrm{Pe} > 10^6$ (under-resolved)
Weber et al. (2017)	Interface Tracking (ALE); two-field approach	3D rising single bubbles	Concentration jump $\mathrm{He} = 30$, Peclet numbers up to $\mathrm{Pe} = 77000$, $D_{\mathrm{gas}}/D_{\mathrm{gas}} > 1000$
Bothe and Fleckenstein (2013), Gründing et al. (2016), Weiner and Bothe (2017)	Geometrical VOF; two-field approach subgrid-scale model	3D rising single bubbles	no artificial species transfer; applied to rising single bubbles at very high Peclet numbers (SGS, $\mathrm{Pe} = 4 \cdot 10^6$); restricted to simple geometries (structured Cartesian grids)
Haroun et al. (2010)	Algebraic VOF; single-field equation	2D thin liquid wavy films	concentration jumps up to $\mathrm{He} = 10$; very high Peclet numbers up to $\mathrm{Pe} = 3 \cdot 10^6$ (steady-state laminar film)

* **General remarks**:
- None of the listed methods use dynamic mesh adaptivity.
- For the listed methods, which are not inherently mass conservative, conservation errors are not discussed.

1.3 Utilized Numerical Framework

In this work, a Finite Volume-based algebraic VOF approach on arbitrary unstructured meshes, implemented in the OpenFOAM®solver *interFoam* is utilized, which however was considerably modified and extended for the simulation of species transfer at rising single bubbles and bubble groups. OpenFOAM®is an open source C++-library for the numerical solution of partial differential equations whose development is mainly community-driven and thus very flexible. Due to its object-oriented implementation, the library allows for equation mimicking in the implementation of partial differential equations (OFuserGuide, 2013). Further, the domain discretization, equation implementation and numerical equation discretization are strictly separated, allowing for fast testing of different discretizations and algorithms on different mesh types. One powerful asset regarding the simulation of species transfer is the availability of High Performance Computing-relevant tools such as dynamic adaptive mesh refinement (AMR) and dynamic load balancing (LB) within the OpenFOAM-library. This enables to locally increase the mesh resolution at the interface and in the concentration wake and thus capture the species concentration boundary layer and species transport accurately in a computationally highly efficient way by significantly reducing the overall number of control volumes compared to structured meshes.

1.4 Goals & Achievements

In the scope of this thesis, direct numerical simulations of mass transfer from rising bubbles are performed in order to deduce an improved mass transfer correlation for single rising bubbles. To this end, a single-field model formulation (also called one-field model) for interfacial species transfer across fluid interfaces for VOF interface capturing methods based on the work of Marschall et al. (2012) is derived, implemented and validated. Their work is herein connected to the one of Haroun et al. (2010) and both methods are combined within one unified formulation. Both authors already provide a single-field model, however, the presented derivation guided by the conditional volume averaging technique reveals problems which are discussed and corrected. The resulting method for interfacial species transfer presented in this thesis is entitled *Continuous Species Transfer (CST)* Model (Deising et al., 2016, 2018). The model's name is adopted from Marschall et al. (2012), since the derived model can be seen as an enhancement and generalization of their work.

The model's core idea lies within the intuitive statement that for a consistent numerical treatment of continuum problems with discontinuities of transport properties and/or quantities, one cannot simply stay with a local instantaneous continuum model formulation, since any numerical solution method will inherently rely on a discrete domain representation, i.e. it will use a computational mesh with finite resolution, which is incapable of resolving local jumps. Exceptions are XFEM and interface tracking methods which allow for direct incorporation of the interfacial jump conditions. Significant problems with stability and/or accuracy and the loss of conservativeness and boundedness properties are most often in the literature attributed to the

’numerics’. The CST model can be seen as one example, where a consistent mathematical and numerical model development based on the conditional volume averaging technique virtually removes critical numerical issues. As a single-field equation, the CST model is valid throughout the computational domain and only boundary conditions for a single set of mixture concentration transport equations are to be prescribed, while the interfacial jump conditions – the purely numerical treatment of which is utmost demanding – are taken care of automatically by additional closure terms. These terms stem from a mathematically rigorous derivation applying the concept of conditional volume averaging (Dopazo, 1977, Whitaker, 1999) and can be interpreted as diffusive solutal species fluxes across the interface. In effect, the species transfer at the fluid interface is casted into interfacial species flux terms appearing in the presented single-field equation.

Using the Finite Volume Method for discretization, this results in an inherently mass conservative approach. Conceptually, the close relationship between the volume averaging technique and the Finite Volume Method is exploited: the analysis of the physical nature of these interfacial species flux terms *guides* their consistent discretization within the Finite Volume framework, which becomes intuitive. The resulting CST method can be discretized in a fully time implicit manner, thus removing diffusive time step restrictions of an explicit discretization. To enforce a consistent advection of volumetric phase fraction and species concentration fields, specialized Interface Capturing Schemes for the discretization of the advection terms are employed. This is shown to significantly reduce artificial species transfer due to inconsistent advection of species concentration and phase fraction – a challenge in common to all interface capturing approaches. Moreover, the CST method is applicable to any algebraic VOF method, on structured and unstructured grids and is capable of handling a realistic range of Henry coefficients and diffusivity ratios. Thus, many numerical issues of existing methods have been resolved in this work, yielding a very robust and accurate method, with a wide range of applicability. The range of applicability covers different numerical methods for the hydrodynamics on one side and a large variety of physical problems and geometries on the other. The presented CST model is utilized within this work to simulate species transfer from rising single bubbles, based on specialized solvers developed in scope of this work.

Utilizing the introduced CST model, an extensive parameter study for species transfer from single rising bubbles is conducted and the obtained numerical results are compared to relevant correlations reported in the literature. Based on the results of the numerical investigation, existing correlations for interfacial species transfer can be improved (see also Deising et al. (2018)). Furthermore, the influence of bubble shape on mass transfer is investigated and – although mostly disregarded throughout literature – identified as an important parameter regarding optimization of industrial scale mass transfer processes.

Additional research material, which is essential for the success of this work but not directly related to mass transfer, is provided as supplementary material in the appendix to this work. For the successful application of the presented model to complex geometries, a new method for the correction of mesh-skewness to ensure a bounded scalar transport is introduced in scope of this work (Hill et al., 2018). Additionally, available high performance computing techniques within the OpenFOAM® framework are improved to ensure efficient numerical computation and a multi-criterion refinement similar to Fuster et al. (2009) is introduced, allowing for a user-friendly customization of the refinement levels and further efficiency increase due to a reduction of the number of cells in the computational mesh. A main focus in scope of the presented work is also the improvement of available algebraic VOF methods as well as an extensive review and enhancement of the theory of algebraic advection methods.

1.5 List of Scientific Publications

D. Deising, H. Marschall, and D. Bothe. A unified single-field model framework for Volume-Of-Fluid simulations of interfacial species transfer applied to bubbly flows. *Chem. Eng. Sci.*, 139: 173 – 195, 2016.

D. Deising, H. Marschall, and D. Bothe. Direct numerical simulation of mass transfer in bubbly flows. *Computers & Fluids*, 2018.

S. Hill, D. Deising, T. Acher, H. Klein, D. Bothe, and H. Marschall. Boundedness-preserving implicit correction of mesh-induced errors for VoF based heat and mass transfer. *J. Comput. Phys.*, 352:285–300, 2018.

H. Marschall, D. Deising, K. Dieter-Kissling, T. Marić, P. Weber, and D. Bothe. On numerical methods for the Direct Numerical Simulation of bubbly flow and interfacial mass transfer using OpenFOAM. In *2nd International Symposium on Multiscale Multiphase Process Engineering (MMPE2)*, Hamburg, Germany, September 24-27 2014.

2 Continuum and Numerical Modelling

For the numerical modelling of two-phase flows, a multitude of different approaches has been developed. This work is mainly concerned with the micro-scale of disperse two-phase flows, at which interfacial phenomena and transfer processes can be observed in detail. Such are e.g. the transport of heat/mass over the interface and the dynamic behaviour/deformation of the interface under external forces. A detailed numerical study of such phenomena requires a suitable simulation technique in terms of accuracy and computational feasibility. While those phenomena could – in principle – be studied at the nanoscale, where the interaction of molecules is directly modelled (Molecular Dynamics), the computational effort involved is way out of scope for nowadays computers.

Usually, the details of the flow at the molecular level are not required. For most purposes, a continuum description is sufficient. Fluctuations or details in the flow thus must only be resolved to the extent that they effect the mean flow (Drew, 1983). In the remainder of this Chapter, continuum mechanical models are introduced, where the material properties of the system are assumed to be constant over the spatially resolved scales. The most detailed numerical methods in the class of continuum mechanical models, which resolve all relevant scales of the fluid system are commonly referred to as *Direct Numerical Simulation* methods.

This work is constrained to the study of Newtonian, incompressible, immiscible fluid phases with constant surface tension coefficient under isothermal conditions. Further, the focus lies on a sub-class of continuum models, the so-called sharp interface models, where the phase-separating interface is treated as a mathematical surface (of zero thickness) at which the fluid properties change discontinuously. Here, the interface is also assumed to be massless so that transport on the interface does not take place, which corresponds to pure or clean fluids.

2.1 Two-Phase Flow Modelling

Based on the concept of continuum mechanics, a set of local instantaneous balance equations for single-and two-phase flows can be derived. For single-phase flows, this leads to the well-known Navier-Stokes equation, a closed set of balance equations for mass and momentum. In single-phase flows, the phase does not necessarily have to be composed of only one chemical component (or species) but rather can be composed of many chemical species which are then commonly assumed to be ideally mixed on the micro-scale level (ideal mixture) and hence as *interpenetrating continua* (e.g. gas mixtures). If the chemical species are not ideally mixed, additional balance equations e.g. for the mass of each species must be added for a complete description of the system.

Modelling a fluid system containing two or more immiscible fluid phases, however, adds complexity to the mathematical modelling effort and numerical methods, due to tracking of the phase-separating interface(s) and handling of the abrupt change of material parameters over the interface. Commonly, the interface has a thickness of only a few molecule lengths, a length-scale far below the typical spatial resolution applied in DNS methods.

2.1.1 Concept of Sharp Interface

Different mathematical approaches for the modelling of fluid-fluid interfaces have been developed which can be separated into two groups, *sharp interface models* (Stokes, 1848, Casey, 2011) and *diffuse interface models* (Cahn and Hilliard, 1958, Allen and Cahn, 1972). The aim these methods share is to provide an accurate evolution description of the interface. In the so-called sharp interface models, the interface is viewed to be a mathematical surface of zero thickness, also called a hypersurface. This modelling is justified by the very thin interfacial transition zone in real two-phase fluid systems which is many orders of magnitude below the resolved macroscopic flow length scale of interest and hence cannot be directly included in/or resolved by a mathematical model. In the sharp interface models, the two-phase system is characterized by continuous physical quantities inside the bulk phases and jump discontinuities at the phase boundaries. To capture the sharp interface, a phase indicator function $\chi : \Omega \to \{0, 1\}$ is introduced. Mathematically, this leads to a so-called *free boundary problem*, a partial differential equation to be solved for both an unknown function ϕ and an unknown domain Ω which is temporally changing due to the interface movement. In diffuse interface models as e.g.

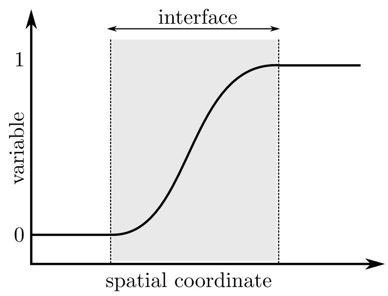

(a) diffuse interface.

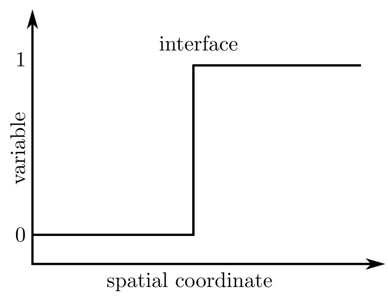

(b) sharp interface.

Figure 2.1.: Sharp interface and diffuse interface models – schematic

the phase field model, the entire microstructure is represented continuously by a single order parameter ψ. The range over which the parameter changes between its maximum and minimum value ($\psi : \Omega \to [0, 1]$ or $\psi : \Omega \to [-1, 1]$, respectively) relates to the width of the interface. The exact form of the interface is motivated from thermodynamics, selecting an equation of state for the free energy of the system. Depending on the definition of the problem, either the entropy (isolated system; non-isothermal problem), Gibbs free energy (isothermal system at constant pressure) or Helmholtz free energy (temperature and volume kept constant) is utilized to this purpose.

Compared to the sharp interface models, diffuse interface models introduce terms depending on the interface thickness which is then modelled to be of the order of the provided mesh resolution and thus many orders of magnitude thicker than the actual interface. Moreover, the diffuse interface models may not converge to the correct sharp interface model when decreasing the interface thickness. Due to these challenges and for reasons of the numerical modelling and treatment, sharp interface models are the focus in the remainder of this thesis. To be more specific, the Volume-of-Fluid interface capturing method based on continuum sharp interface modelling is utilized in this work.

2.1.2 Local Instantaneous Balance Equations

Based on continuum modelling, conserved quantities such as mass, momentum and energy are assumed to change continuously in each phase. Within the sharp interface concept, these quantities may be discontinuous over the fluid-fluid interface. The fluid behaviour can thus be fully described by a set of balance equations which describe the transport of the conserved quantities in the respective bulk phases and their interfacial jump and transmission conditions.

To formulate the balance equations describing the fluid motion, the flow can be specified in two different ways, moving through a spatially fixed control volume V (Eulerian specification) or moving with a time-dependent material volume $V(t)$ (Lagrangian specification). A material volume is defined in such a way that a zero net flux of the respective transported quantity over the volume boundaries is observed. To simplify the derivation of the local instantaneous governing equations, the Eulerian specification is chosen here.

Single-Phase Flow

Consider a spatially fixed control volume V of general shape as shown in Figure 2.2. Let $\mathbf{\Phi}(\mathbf{x}, t)$ denote an arbitrary intensive transport quantity (scalar or tensor of any rank). The rate of change of this transport quantity $\mathbf{\Phi}$ within V constitutes of different contributions. In single-phase flows, these contributions are the advective and diffusive transport of the quantity over the control volume surface and source/sink terms acting on the volume, leading to

$$\frac{d}{dt}\int_V \rho\mathbf{\Phi}\, dV = -\oint_S \mathbf{n}\cdot(\rho\mathbf{\Phi}\mathbf{u})\, dS - \oint_S \mathbf{n}\cdot(-\mathbf{j})\, dS + \int_V S_{\mathbf{\Phi}}(\mathbf{\Phi})\, dV\,. \tag{2.1}$$

In above equation, ρ, $\mathbf{u}$ and $\mathbf{j}$ denote the phase density, velocity and diffusive flux respectively. The diffusive flux is defined with opposite sign compared to standard literature to obtain a positive diffusion coefficient in the closure. Employing the Reynolds transport theorem (Reynolds, 1903) to Equation (2.1) enables the switching of integral and derivative, yielding

$$\int_V \partial_t(\rho\mathbf{\Phi})\, dV = -\oint_S \mathbf{n}\cdot[\rho\mathbf{\Phi}(\mathbf{u}-\mathbf{u}_S)]\, dS - \oint_S \mathbf{n}\cdot(-\mathbf{j})\, dS + \int_V S_{\mathbf{\Phi}}(\mathbf{\Phi})\, dV\,. \tag{2.2}$$

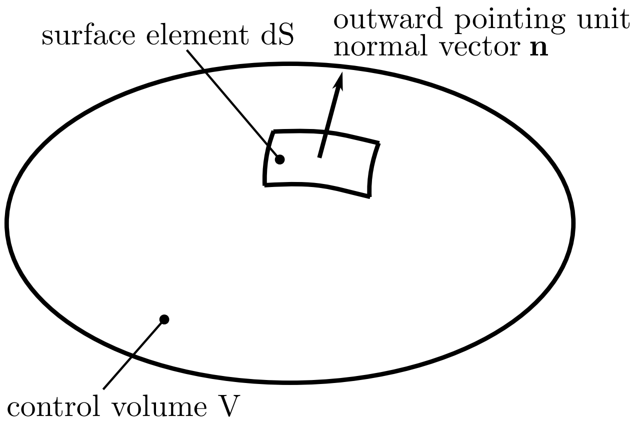

Figure 2.2.: Control volume for single-phase flow

Due to the considered control volume being fixed in time and space, the displacement velocity of the control volume surface is zero ($\mathbf{u}_S \equiv 0$). Applying Gauss' theorem, the appearing surface integrals can be formulated in terms of volume integrals. Then, Equation (2.2) can be formulated as

$$\int_V \partial_t(\rho\mathbf{\Phi})\,dV + \int_V \nabla\cdot(\rho\mathbf{\Phi}\mathbf{u})\,dV = -\int_V \nabla\cdot(-\mathbf{j})\,dV + \int_V S_{\mathbf{\Phi}}(\mathbf{\Phi})\,dV\,. \tag{2.3}$$

Using a localization argument, (2.3) is transformed into a partial differential equation

$$\partial_t(\rho\mathbf{\Phi}) + \nabla\cdot(\rho\mathbf{\Phi}\mathbf{u}) = -\nabla\cdot(-\mathbf{j}) + S_{\mathbf{\Phi}}(\mathbf{\Phi})\,. \tag{2.4}$$

From this, the set of local instantaneous governing equations in single-phase flows, also known as the Navier-Stokes equations, can be obtained by inserting the respective transport quantities and closure terms, leading to

$$\partial_t\rho + \nabla\cdot(\rho\mathbf{u}) = 0 \tag{2.5}$$

$$\partial_t(\rho\mathbf{u}) + \nabla\cdot(\rho\mathbf{u}\mathbf{u}) = -\nabla p + \rho\mathbf{g} + \nabla\cdot\boldsymbol{\tau}, \tag{2.6}$$

where the first equation describes the conservation of mass and the second the conservation of momentum.

Two-Phase Flow

When dealing with two-phase flows, the control volume changes somewhat from above definition due to the presence of the fluid-fluid interface (see Figure 2.3). The control volume V is again general in shape and fixed in space and time but is now comprised of two separate time-dependent volumes for the two immiscible phases ($V = V_1(t) \cup V_2(t)$) due to the interface motion. This entails the presence of more mechanisms (compared to single-phase flows) which contribute to a change of the arbitrary quantity $\mathbf{\Phi}$ in V, as now also the transport of $\mathbf{\Phi}$ on and

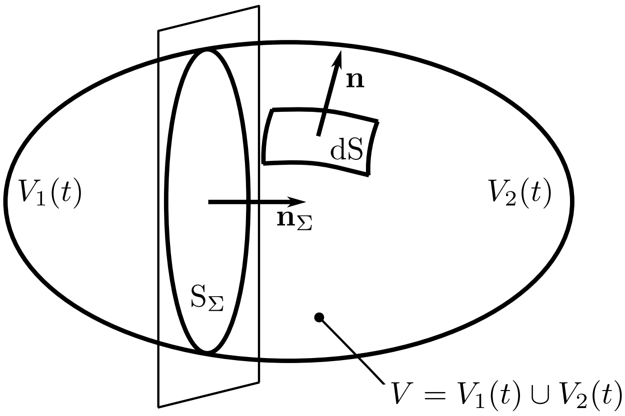

Figure 2.3.: Control volume for two-phase flow

over the interface has to be considered. In this work however, the interface is considered to be massless, hence cannot contain any chemical species and thus species transport processes on the interface do not occur. Then, the balance equation for $\mathbf{\Phi}$ within the fixed control volume V containing the interface segment $S_\Sigma(t) := \Sigma \cap V$ (see Figure 2.3) reads

$$\begin{aligned} \frac{d}{dt}\int_V \rho\mathbf{\Phi}\, dV &= -\int_{\partial V} \mathbf{n}\cdot(\rho\mathbf{\Phi}\mathbf{u})\, dS - \int_{\partial V} \mathbf{n}\cdot(-\mathbf{j})\, dS + \int_{V\setminus S_\Sigma(t)} S_{\mathbf{\Phi}}(\mathbf{\Phi})\, dV + \int_{S_\Sigma(t)} S^\Sigma_{\mathbf{\Phi}}(\mathbf{\Phi})\, dS \\ \Leftrightarrow \int_{V\setminus S_\Sigma(t)} \partial_t(\rho\mathbf{\Phi})\, dV - \int_{S_\Sigma(t)} [\![\rho\mathbf{\Phi}]\!]\, \mathbf{u}^\Sigma\cdot\mathbf{n}_\Sigma\, dS &= -\int_{V\setminus S_\Sigma(t)} \nabla\cdot(\rho\mathbf{\Phi}\mathbf{u})\, dV - \int_{S_\Sigma(t)} [\![\rho\mathbf{\Phi}\mathbf{u}]\!]\cdot\mathbf{n}_\Sigma\, dS \\ &- \int_{V\setminus S_\Sigma(t)} \nabla\cdot(-\mathbf{j})\, dV - \int_{S_\Sigma(t)} [\![-\mathbf{j}]\!]\cdot\mathbf{n}_\Sigma\, dS + \int_{V\setminus S_\Sigma(t)} S_{\mathbf{\Phi}}(\mathbf{\Phi})\, dV + \int_{S_\Sigma(t)} S^\Sigma_{\mathbf{\Phi}}(\mathbf{\Phi})\, dS\,, \end{aligned} \tag{2.7}$$

where the two-phase divergence theorem

$$\int_{\partial V} \mathbf{\Phi}\cdot\mathbf{n}\, dS = \int_{V\setminus S_\Sigma(t)} \nabla\cdot\mathbf{\Phi}\, dV + \int_{S_\Sigma(t)} [\![\mathbf{\Phi}]\!]\cdot\mathbf{n}_\Sigma\, dS \tag{2.8}$$

and the two-phase transport theorem

$$\frac{d}{dt}\int_V \rho\mathbf{\Phi}\, dV = \int_{V\setminus S_\Sigma(t)} \partial_t(\rho\mathbf{\Phi})\, dV - \int_{S_\Sigma(t)} [\![\rho\mathbf{\Phi}]\!]\, \mathbf{u}^\Sigma\cdot\mathbf{n}_\Sigma\, dS \tag{2.9}$$

have been used. The jump bracket $[\![\cdots]\!]$ employed above is a shortcut notation defined as

$$[\![\mathbf{\Phi}]\!](\mathbf{x}) := \lim_{\delta\to 0+} \left(\mathbf{\Phi}(\mathbf{x}+\delta\mathbf{n}_\Sigma) - \mathbf{\Phi}(\mathbf{x}-\delta\mathbf{n}_\Sigma)\right) \quad \text{for } \mathbf{x}\in S_\Sigma(t)\,. \tag{2.10}$$

Ordering of the volume and surface integrals in Eq. (2.7) and localization yields the following set of local instantaneous transport equation in the bulk phases and local instantaneous jump condition:

$$\partial_t(\rho\mathbf{\Phi}) + \nabla\cdot(\rho\mathbf{\Phi}\mathbf{u}) = \nabla\cdot\mathbf{j} + S_{\mathbf{\Phi}}(\mathbf{\Phi}) \tag{2.11}$$

$$[\![\rho\mathbf{\Phi}\left(\mathbf{u}-\mathbf{u}^\Sigma\right) - \mathbf{j}]\!]\cdot\mathbf{n}_\Sigma = S^\Sigma_{\mathbf{\Phi}}(\mathbf{\Phi})\,. \tag{2.12}$$

Substituting the respective transport quantities into Equations (2.11) and (2.12), inserting the diffusion and source terms derived from exploiting the second law of thermodynamics and assuming incompressible flow ($\nabla\cdot\mathbf{u} \equiv 0$), the set of local instantaneous two-phase flow equations reads

Mass balance:

$$\partial_t \rho + \nabla\cdot(\rho\mathbf{u}) = 0 \tag{2.13}$$

$$[\![\rho\left(\mathbf{u}-\mathbf{u}^{\Sigma}\right)]\!]\cdot\mathbf{n}_{\Sigma} = 0 \tag{2.14}$$

Momentum balance:

$$\partial_t(\rho\mathbf{u}) + \nabla\cdot(\rho\mathbf{u}\mathbf{u}) = -\nabla p + \nabla\cdot\boldsymbol{\tau} + \rho\mathbf{g} \tag{2.15}$$

$$[\![\rho\mathbf{u}\left(\mathbf{u}-\mathbf{u}^{\Sigma}\right)-\boldsymbol{\tau}]\!]\cdot\mathbf{n}_{\Sigma} = \sigma\kappa\mathbf{n}_{\Sigma} + \nabla_{\Sigma}\sigma - [\![p\mathbf{I}]\!]\cdot\mathbf{n}_{\Sigma}\,. \tag{2.16}$$

Above set of equations in this form is not suitable for numerical computation. The only exception being interface tracking methodologies (Tukovic and Jasak, 2012), where two different mesh regions for the two bulk phases are used. In the following, the transformation of Equations (2.13) to (2.16) into a set of single-field equations is shown – a set of equations more suitable for numerical computation. This set of equations can then be utilized for the Direct Numerical Simulation of two-phase flow systems, employing different methods as, e.g., Volume-of-Fluid methods, Level-Set methods or diffuse interface phase field methods.

Constitutive Closure and Assumptions

To arrive at a closed mathematical description of the single- or two-phase fluid flow system, closure models need to be included for the remaining unclosed terms. Further, different assumptions are made in order to simplify the mathematical problem but still retain a valid model to describe the relevant physics in two-phase bubbly flow systems. The diffusive fluxes are herein modelled by employing Fick'ean diffusion. In this work only Newtonian fluids are considered, leading to a Fick'ean-like diffusion term which reads

$$\nabla\cdot\boldsymbol{\tau} = \nabla\cdot\left[\mu\left(\nabla\mathbf{u} + (\nabla\mathbf{u})^{\mathrm{T}}\right)\right] \tag{2.17}$$

with constant viscosities in the respective phases. The momentum diffusion term (viscous stress) in above equation is obtained by splitting $\nabla\mathbf{u}$ into an objective (Euclidean invariant) and non-objective tensor according to

$$\nabla\mathbf{u} = \mathbf{D} + \mathbf{S}\,,\ \text{with}\ \mathbf{D} := \frac{1}{2}\left(\nabla\mathbf{u} + (\nabla\mathbf{u})^{\mathrm{T}}\right)\ \text{and}\ \mathbf{S} := \frac{1}{2}\left(\nabla\mathbf{u} - (\nabla\mathbf{u})^{\mathrm{T}}\right),$$

with the objective deformation tensor $\mathbf{D}$ and the non-objective vorticity tensor $\mathbf{S}$. This allows for the total stress tensor $\boldsymbol{\sigma}$ to be written as

$$\boldsymbol{\sigma} \equiv -p\mathbf{I} + \boldsymbol{\tau},\ \text{with}\ \boldsymbol{\tau} := 2\mu\mathbf{D}\,. \tag{2.18}$$

The modelling of the stress tensor by means of Fick'ean-like diffusion is a consequence of its constitutive equation derived from the entropy equation for pure substance phases in combination with the second law of thermodynamics, see e.g. Slattery (1999), Ishii and Hibiki (2011). If the considered phase constitutes of a mixture of several components i, cross-diffusion would also occur, resulting in the Maxwell-Stefan diffusion tensor. However, as this work focuses only on the transfer of dilute species in bubbly flows, the Fick'ean diffusion model remains a valid approximation. In this case, the viscosity and fluid velocity are to be seen as mixture quantities. Closure modelling of these quantities will be discussed in the following Sections in context of conditional volume-averaged single-field models.

For the study of two-phase flow systems, several assumptions are made in scope of this work as already mentioned above. The phases are considered to be incompressible with constant fluid properties. Regarding interfacial species transfer, only transfer processes of dilute species (e.g. without volume effects due to phase-change) are considered in this work. Further, the interface is considered to not adsorb (or store) mass such that transport processes on the interface do not take place and the interface jump condition of the species concentration is significantly simplified (Bothe and Fleckenstein, 2013).

2.2 Conditional Volume Averaging Technique

To obtain equations which do not contain all details of the considered fluid system, a customary approach is to apply some sort of averaging (or spatial filtering) procedure. Drew (1983) stresses that it is not essential to do so and that a valid set of macroscopic equations can also be postulated without reference to any microscopic equations. However, Drew (1983) also points out the advantage in averaging techniques, that the resulting equations are directly related to the microscopic variables which ensures the completeness of the equations and simplifies and/or guides interpretation and closure modelling for the respective terms.

In general, many different averaging procedures can be applied. The most frequently used amongst them are the volume, time and ensemble averaging techniques (Whitaker, 1999, Jakobsen, 2008). In this work, the Finite Volume Method (FVM) (Patankar and Spalding, 1972, Patankar, 1980, Eymard et al., 2000, LeVeque, 2002, Hirsch, 2007) is employed which is inherently related to the concept of volume averaging (VA) since the method is based on the integral formulation of partial differential equations, i.e. the discretized version of the equations is obtained by volume integration of the conserved quantity over the control volumes. Due to this relation of FVM and VA, the concept of volume averaging – and its counterpart in multiphase flows (conditional volume averaging, CVA) – is a known technique in the derivation of consistent numerical methods in the Finite Volume framework (Dopazo, 1977, Whitaker, 1999). The concept of CVA has been successfully applied in the past e.g. to derive two-fluid models or to derive single-field formulations to be used in Volume-of-Fluid methods (Ubbink, 1997, Wörner, 2003, Weller, 2005b, Marschall, 2011, Deising et al., 2016). Another frequently employed averaging technique is the ensemble averaging, which – compared to the volume averaging technique – is not dependent on the separation of spatial scales (Prosperetti, 1998). In the framework of

Direct Numerical Simulation where the relevant temporal and spatial scales are well-resolved, this averaging technique holds no advantage over volume averaging. Regarding the derivation of Two-Fluid Models however, ensemble-averaging or consecutive averaging in space and time is usually preferable to volume averaging techniques (Prosperetti, 1998).

To model a two-phase flow consisting of two immiscible fluids, the interface between them can be considered to be immersed or embedded into the computational domain. To this end, Peskin (1977) developed the immersed boundary method which is mainly based upon the use of discrete approximations to delta distributions to deal with forces acting only at the internal boundaries. The main concept of this approach is adopted in the present work in form of the immersed interface concept. As a result, the set of governing equations derived by this method is valid throughout the whole computational domain including the interface and boundary conditions only need to be prescribed at the domain boundaries. The starting point to obtain such set of equations are the local instantaneous balance equations and the corresponding interfacial jump and transmission conditions. In the following, the technique of conditional volume averaging is introduced (for further, more detailed descriptions see, e.g., Hassanizadeh and Gray (1979), Drew (1983), Hill (1998), Jakobsen (2008), Marschall (2011), Marschall et al. (2012)).

2.2.1 Averaging Models/Strategies

It should be noted that there are two different levels of modelling to be distinguished in this work. On one hand is the local instantaneous *continuum* model for the transport quantities, which is valid in the respective bulk phases, while on the other, (volume-) averaged *numerical* models are considered. These numerical models appear in the present work in form of conditional volume-averaged single-field equations for Direct Numerical Simulation of incompressible two-phase flows. Single-field equations are valid throughout the whole computational domain and readily suitable for numerical discretization using the Finite Volume Method. Such single-field equations describe the transport of mixture quantities.

Now, let $\overline{\phi\left(\mathbf{x},t\right)}$ denote the averaged field corresponding to a local instantaneous quantity $\phi\left(\mathbf{x},t\right)$. The different averaging techniques are then defined as

$$\overline{\phi\left(\mathbf{x},t\right)}^{t} := \frac{1}{T}\int_{t-T}^{t} \phi\left(\mathbf{x},t'\right)dt' \quad \text{(time averaging)}, \tag{2.19}$$

$$\overline{\phi\left(\mathbf{x},t\right)}^{v} := \frac{1}{|V|}\int_{V} \phi\left(\mathbf{x}',t\right)dx' \quad \text{(volume averaging)}, \tag{2.20}$$

$$\overline{\phi\left(\mathbf{x},t\right)}^{e} := \frac{1}{|\Omega|}\int_{\Omega} \phi\left(\mathbf{x},t;\omega\right)d\mu(\omega) \quad \text{(ensemble averaging)}. \tag{2.21}$$

In the respective averaging techniques, the integration is performed over the time interval T, the volume interval V or the set of realizations of an experiment Ω with identical initial conditions. The focus in the following lies in the volume averaging technique and thus the index

"v" is omitted in the remainder whenever denoting volume averaging. Instead, the index in the overbar-notation is used to indicate over which phase an average is performed. Due to the importance of distinguishing between local-instantaneous mathematical continuum models and averaged models, this work makes strict use of the overbar-notation for averaged quantities.

Additionally, in the present work a distinction between *mixture* and *mean* quantities is made. Only transport quantities appearing in the conditional volume-averaged single-field equations are denoted as *mixture quantities*, whereas the fluid properties are denoted as *mean values* whose definition mainly depends on closure modelling as will be discussed later. To indicate mean values, an angle bracket notation $\langle \cdots \rangle$ is introduced. Central mean quantities appearing in this thesis are the mean viscosity $\langle \mu \rangle$ and the mean diffusion coefficient $\langle D \rangle$.

2.2.2 Phase Indicator and Averaging Rules

Consider a two-phase system with the phases 1 and 2. To distinguish the two phases separated by a fluid interface $\Sigma(t)$, a phase-indicator function for phase 1 is defined as

$$\chi_1(\mathbf{x}, t) \equiv \begin{cases} 1 & \text{if } \mathbf{x} \in \Omega_1(t) \text{ at time } t \\ 0 & \text{otherwise.} \end{cases} \tag{2.22}$$

As it is common practice, e.g. Drew (1983), the phase indicator function $\chi_1(\mathbf{x}, t)$ is dealt with as generalized function. As such, its spatial derivative can be expressed as a set of test functions, which are sufficiently smooth and exhibit a compact support. Hence, if the "jump set" of $\chi_1(\mathbf{x}, t)$ is sufficiently regular, then in a mathematically weak sense

$$\mathbf{n}_\Sigma = -\frac{\nabla \chi_1(\mathbf{x}, t)}{|\nabla \chi_1(\mathbf{x}, t)|}\,. \tag{2.23}$$

The generalization to functions of bounded variation (i.e., functions with a distributional derivative being a vector-valued Radon measure) is found in Evans and Gariepy (1992). The spatial derivative of the indicator function is thus well-defined and can be expressed in terms of the interface normal vector $\mathbf{n}_\Sigma$ pointing from phase 1 into phase 2 and the interface delta function δ_Σ as $\nabla \chi_1 = -\mathbf{n}_\Sigma \delta_\Sigma$.

Throughout this work it will further be assumed that phase change does not occur, employing $\chi_1(t, \mathbf{x}(t)) \equiv const$ along the trajectories $\mathbf{x}(\cdot)$ of $\dot{\mathbf{x}}(t) = \mathbf{u}(t, \mathbf{x}(t))$, where $\mathbf{u}$ denotes the velocity field ($\chi_1 \mathbf{u} =: \mathbf{u}_1$ in $\Omega_1(t)$, resp. $\chi_2 \mathbf{u} =: \mathbf{u}_2$ in $\Omega_2(t)$). Hence, the Lagrangian derivative of χ reads

$$\frac{D\chi_1}{Dt} = 0.$$

Formally, this yields the well-known interface transport equation

$$\partial_t \chi_1 + \mathbf{u} \cdot \nabla \chi_1 = 0 \tag{2.24}$$

for the phase indicator χ_1, sometimes also referred to as topological equation. However, as stressed before, the individual terms in (2.24) are only defined in a weak, say distributional, sense due to the jump of χ_1 at $\Sigma(t)$.

Consider the local instantaneous generic transport equation for a quantity $\mathbf{\Phi}$ in the bulk of phase 1, i.e.

$$\partial_t(\rho\mathbf{\Phi}) + \nabla\cdot(\rho\mathbf{\Phi}\mathbf{u}) + \nabla\cdot\left(-\Gamma_{\mathbf{\Phi},d}\nabla\mathbf{\Phi}\right) - S_{\mathbf{\Phi}}(\mathbf{\Phi}) = 0 \qquad \text{in } \Omega_1(t)\cup\Omega_2(t)\setminus\Sigma(t). \tag{2.25}$$

The application of the conditional volume averaging technique consists of two steps. The equation is first 'conditioned' for phase discrimination by multiplication with the phase-indicator function χ_1, which renders the equation valid throughout the entire computational domain. In a second step, volume averaging is applied to this conditioned equation. For a generic transport quantity $\mathbf{\Phi}$ this reads

$$\overline{\chi_1\mathbf{\Phi}} \equiv \frac{1}{|V|}\int\limits_V \chi_1(\mathbf{x}+\boldsymbol{\eta},t)\,\mathbf{\Phi}(\mathbf{x}+\boldsymbol{\eta},t)\,d\boldsymbol{\eta} \tag{2.26}$$

$$= \frac{|V_1|}{|V|}\frac{1}{|V_1|}\int\limits_{V_1}\mathbf{\Phi}(\mathbf{x}+\boldsymbol{\eta},t)\,d\boldsymbol{\eta} =: \alpha_1\overline{\mathbf{\Phi}}^1. \tag{2.27}$$

In (2.26), the averaging is performed over a fixed control volume $V\subset\Omega$ with the centre $\mathbf{x}$, where the phase indicator is used for phase discrimination. The overbar notation

$$\overline{\mathbf{\Phi}} := \frac{1}{|V|}\int\limits_V \mathbf{\Phi}(\mathbf{x}+\boldsymbol{\eta},t)\,d\boldsymbol{\eta} \tag{2.28}$$

is used to indicate volume averaging. In (2.27), $\overline{\mathbf{\Phi}}^1$ denotes the so-called phasic average, which indicates that the considered averaging volume is the actual phase volume $V_1 := V\cap\Omega_1$. Moreover, within the context of CVA, the volume-averaged indicator function $\overline{\chi_1}$ can be intuitively identified as the volumetric phase-fraction α_1 (cp. (2.27)),

$$\overline{\chi_1} \equiv \frac{1}{|V|}\int\limits_V \chi_1(\mathbf{x}+\boldsymbol{\eta},t)\,d\boldsymbol{\eta} = \frac{1}{|V|}\int\limits_{V_1} 1\,d\boldsymbol{\eta} = \frac{|V_1|}{|V|} =: \alpha_1. \tag{2.29}$$

In the context of sharp interface models, as outlined in Section 2.1.1, the interface is seen to be a mathematical surface separating the phases 1 and 2. By application of conditional volume averaging, i.e. by spatial filtering, the interfacial surface becomes an interfacial transition zone of well-defined finite width within the computational domain. The volumetric phase-fraction α_1 takes the values

$$\overline{\chi_1(\mathbf{x},t)} \equiv \alpha_1 \begin{cases} = 1 & \text{within phase 1} \\ = 0 & \text{within phase 2} \\ \in (0,1) & \text{in cells containing interface.} \end{cases} \tag{2.30}$$

In the interfacial region, material and transport properties vary smoothly but rapidly towards the values in the respective bulk phases.

Conditioning of (2.25) with phase indicator χ_1 and volume averaging of the generic transport equation (2.25) then reads

$$\overline{\chi_1 \partial_t (\rho \boldsymbol{\Phi})} + \overline{\chi_1 \nabla \cdot (\rho \boldsymbol{\Phi} \mathbf{u})} - \overline{\chi_1 \nabla \cdot \left(\Gamma_{\boldsymbol{\Phi},d} \nabla \boldsymbol{\Phi} \right)} - \overline{\chi_1 S_{\boldsymbol{\Phi}}(\boldsymbol{\Phi})} = 0 \qquad \text{in } \Omega. \tag{2.31}$$

As can be seen in Eq. (2.25), the local instantaneous balance equations contain spatial and temporal derivatives of their dependent variables. When applying the conditional volume averaging technique, the Gauss and Leibniz rules (Drew and Passman, 1999, Jakobsen, 2008) are used,

$$\overline{\chi_1 \nabla \boldsymbol{\Phi}} = \overline{\nabla (\chi_1 \boldsymbol{\Phi})} - \overline{\boldsymbol{\Phi} \nabla \chi_1} = \nabla \left(\overline{\chi_1 \boldsymbol{\Phi}} \right) - \overline{\boldsymbol{\Phi} \nabla \chi_1} = \nabla \left(\alpha_1 \overline{\boldsymbol{\Phi}}^1 \right) - \overline{\boldsymbol{\Phi} \nabla \chi_1}, \tag{2.32}$$

$$\overline{\chi_1 \nabla \cdot \boldsymbol{\Phi}} = \overline{\nabla \cdot (\chi_1 \boldsymbol{\Phi})} - \overline{\boldsymbol{\Phi} \cdot \nabla \chi_1} = \nabla \cdot \left(\overline{\chi_1 \boldsymbol{\Phi}} \right) - \overline{\boldsymbol{\Phi} \cdot \nabla \chi_1} = \nabla \cdot \left(\alpha_1 \overline{\boldsymbol{\Phi}}^1 \right) - \overline{\boldsymbol{\Phi} \cdot \nabla \chi_1}, \tag{2.33}$$

$$\overline{\chi_1 \partial_t \boldsymbol{\Phi}} = \overline{\partial_t (\chi_1 \boldsymbol{\Phi})} - \overline{\boldsymbol{\Phi} \partial_t \chi_1} = \partial_t \left(\overline{\chi_1 \boldsymbol{\Phi}} \right) - \overline{\boldsymbol{\Phi} \partial_t \chi_1} = \partial_t \left(\alpha_1 \overline{\boldsymbol{\Phi}}^1 \right) - \overline{\boldsymbol{\Phi} \partial_t \chi_1} \tag{2.34}$$

and the volume-averaged form of (2.24) is exploited,

$$\overline{\partial_t \chi_1} + \overline{\mathbf{u}^\Sigma \cdot \nabla \chi_1} = 0. \tag{2.35}$$

For (2.32)–(2.34), also $\overline{\nabla \boldsymbol{\Phi}}^1 = \nabla \overline{\boldsymbol{\Phi}}^1$ (Jakobsen, 2008) was used – disregarding commutation errors (i.e. a homogeneous spatial filter is presumed). With this, Eq. (2.31) becomes

$$\begin{aligned} &\partial_t \left(\alpha_1 \overline{\rho \boldsymbol{\Phi}}^1 \right) + \nabla \cdot \left(\alpha_1 \overline{\rho \boldsymbol{\Phi} \mathbf{u}}^1 \right) - \nabla \cdot \left(\alpha_1 \overline{\Gamma_{\boldsymbol{\Phi},d} \nabla \boldsymbol{\Phi}}^1 \right) - \alpha_1 \overline{S_{\boldsymbol{\Phi}}(\boldsymbol{\Phi})}^1 \\ &= \overline{\rho \boldsymbol{\Phi} (\mathbf{u} - \mathbf{u}^\Sigma) \cdot \nabla \chi_1} - \overline{\Gamma_{\boldsymbol{\Phi},d} \nabla \boldsymbol{\Phi} \cdot \nabla \chi_1}. \end{aligned} \tag{2.36}$$

In order to further simplify the notation and in analogy to the overbar notation for volume-averaged quantities, an overbrace notation is introduced to denote surface averaged quantities as

$$\begin{aligned} \overbrace{\boldsymbol{\Phi}} &:= \frac{1}{|S_\Sigma|} \int_{S_\Sigma} \boldsymbol{\Phi}(\mathbf{x}, t) \, dS \\ &= \frac{1}{a_\Sigma} \lim_{\delta \to 0} \overline{\frac{1}{\delta V} \int_{\mathbb{U}_\delta(S_\Sigma)} \boldsymbol{\Phi}(\mathbf{x}, t) \; dV}, \end{aligned} \tag{2.37}$$

where $\mathbb{U}_\delta (S_\Sigma) = \{ \mathbf{x} + h \mathbf{n}_\Sigma (\mathbf{x}) : \mathbf{x} \in S_\Sigma, h \in [-\delta, \delta] \}$ denotes the vicinity of the interface depicted in Figure 2.4 and a_Σ the surface area per unit volume (also referred to as interfacial area density) which is defined as

$$a_\Sigma := \frac{|S_\Sigma|}{|V|} = \lim_{\delta \to 0} \overline{\frac{1}{\delta V} \int_{\mathbb{U}_\delta(S_\Sigma)} 1 \; dV}. \tag{2.38}$$

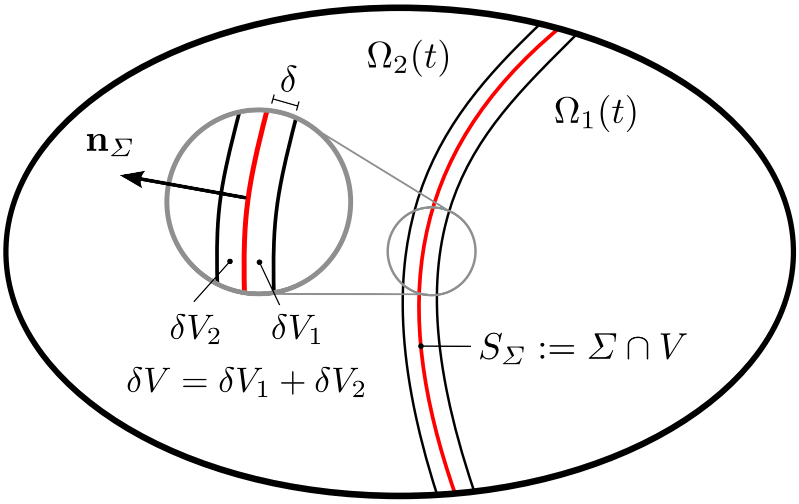

Figure 2.4.: Averaging control volume

A different interpretation of the interfacial are density a_Σ is through the magnitude $\overline{|\nabla \chi_1(\mathbf{x},t)|}$ of the volume-averaged indicator function derivative (Drew, 1983)

$$\overline{|\nabla \chi_1(\mathbf{x},t)|} := \frac{1}{|V|}\int_V |-\mathbf{n}_\Sigma \delta_\Sigma|\, dV = \frac{1}{|V|}\int_V \delta_\Sigma\, dV = \frac{|S_\Sigma|}{|V|} \equiv a_\Sigma\,. \tag{2.39}$$

From above definition of a_Σ the connection to the volumetric phase fraction can be made, leading to a numerically well-suited form for the calculation of the interfacial area density

$$a_\Sigma \equiv \overline{|\nabla \chi_1(\mathbf{x},t)|} \approx |\nabla \overline{\chi_1(\mathbf{x},t)}| = |\nabla \alpha_1|\,. \tag{2.40}$$

Whenever $\mathbf{\Phi}$ exhibits a jump across the interface, its two one-sided limits to the phase boundary are to be considered. Following Hill (1998) and Marschall (2011), the phasic surface average $\widetilde{\mathbf{\Phi}}^1$ of a generic transport quantity $\mathbf{\Phi}$ is introduced as the phase 1-sided surface integral per unit volume divided by the surface area per unit volume (cp. Fig. 2.4):

$$\widetilde{\mathbf{\Phi}}^1 := \frac{1}{a_\Sigma}\lim_{\delta\to 0+} \overline{\frac{1}{\delta V_1}\int_{\mathbb{U}^1_\delta(S_\Sigma)} \mathbf{\Phi}(\mathbf{x},t)\; dV}\,, \tag{2.41}$$

with $\mathbb{U}^1_\delta(S_\Sigma) = \{\mathbf{x} + h\mathbf{n}_\Sigma(\mathbf{x}) : \mathbf{x} \in S_\Sigma, h \in [-\delta, 0]\}$. The phase 1-sided surface integral is to be understood as the surface integral over the phase 1-sided limit of the integrand or the volume integral over the 1-sided interface vicinity $\mathbb{U}^1_\delta(S_\Sigma)$. Recalling the definition of the indicator function spatial derivative and assuming constant density in phase 1, the conditional volume-averaged transport equation for a generic transport quantity $\mathbf{\Phi}$ yields

$$\begin{aligned}&\partial_t\left(\alpha_1 \overline{\rho}^1 \overline{\mathbf{\Phi}}^1\right) + \nabla\cdot\left(\alpha_1 \overline{\rho}^1 \overline{\mathbf{\Phi u}}^1\right) - \nabla\cdot\left(\alpha_1 \overline{\Gamma_{\mathbf{\Phi},d}\nabla\mathbf{\Phi}}^1\right) - \alpha_1 \overline{S_{\mathbf{\Phi}}(\mathbf{\Phi})}^1 \\ &= -\widetilde{\rho\mathbf{\Phi}\left(\mathbf{u}-\mathbf{u}^\Sigma\right)\cdot\mathbf{n}_\Sigma}^1 a_\Sigma + \widetilde{\Gamma_{\mathbf{\Phi},d}\nabla\mathbf{\Phi}\cdot\mathbf{n}_\Sigma}^1 a_\Sigma\,.\end{aligned} \tag{2.42}$$

As stated before, the main interest is the derivation of a single-field model. Therefore, the conditional volume averaging technique is first applied to the bulk conservation equations for all phases, resulting in additional interface-averaged terms (as shown in Eq. (2.42)). In a second step, all conditional volume-averaged equations are summed up, yielding a single-field transport equation for a new 'mixture' transport variable $\overline{\mathbf{\Phi}}$ consisting of the sum of the conditional volume-averaged transport quantity $\alpha_k \overline{\mathbf{\Phi}}^k$ in both phases

$$\overline{\mathbf{\Phi}} := \sum_{k=1,2} \alpha_k \overline{\mathbf{\Phi}}^k . \tag{2.43}$$

In a last step, to arrive at an exploitable single-field equation for the new mixture quantity $\overline{\mathbf{\Phi}}$, surface-averaged jump conditions are used, which results in the additional interfacial terms either simplifying or canceling out. Still this equation might require closure, i.e. values of the phasic averaged quantities $\overline{\mathbf{\Phi}}^1$, $\overline{\mathbf{\Phi}}^2$ must be related to the mixture quantity $\overline{\mathbf{\Phi}}$.

2.3 Volume-of-Fluid Method

In order to study the free-surface and two-phase flow of two incompressible, immiscible fluids, an algebraic VOF approach based on the OpenFOAM® interFoam solver is applied, which was considerably modified and extended for the simulation of interfacial species transfer. The Volume-of-Fluid methods are based upon a set of single-field equations to describe the fluid dynamics of two-phase flows, which are obtained by means of conditional volume averaging of the local instantaneous conservation equations of mass and momentum. Here, the term *single-field* refers to the transport of a mixture quantity rather than solving for two separate bulk equations including coupling at the interface. Some DNS methods, however, such as the interface tracking or cut-cell methods do not rely on a single-field model and instead solve for sets of balance equations in two separate domains where the interfacial jump conditions are applied as boundary conditions of the respective domains. The starting point for the derivation of the Volume-of-Fluid governing equations is the conditional volume-averaged transport equation for a generic transport quantity $\mathbf{\Phi}$ (Eq. (2.42)). A concise and consistent derivation of the single-field VOF equations is also found in Wörner et al. (2001), who introduce the so-called volume-averaged Volume-of-Fluid (VA-VOF) equations.

2.3.1 Volume-of-Fluid Governing Equations

To arrive at a set of single-field equations for the simulation of multiphase flow, the conditional volume averaging technique is applied to the local instantaneous balance equations of mass and momentum (cf. Equations (2.13) to (2.16)). In a two-phase system, this leads to the following set of governing equations:

$$\nabla \cdot \overline{\mathbf{u}_m} = \nabla \cdot \left(\alpha_1 \alpha_2 \frac{\overline{\rho}^2 - \overline{\rho}^1}{\overline{\rho}} \mathbf{u}_r \right) \tag{2.44}$$

$$\partial_t \alpha_1 + \nabla\cdot (\alpha_1 \overline{\mathbf{u}_m}) = \nabla\cdot \left(\alpha_1 \alpha_2 \left(1 + \alpha_1 \frac{\overline{\rho}^2 - \overline{\rho}^1}{\overline{\rho}} \right) \mathbf{u}_r \right) \tag{2.45}$$

$$\partial_t (\overline{\rho}\, \overline{\mathbf{u}_m}) + \nabla\cdot (\overline{\rho}\, \overline{\mathbf{u}_m}\, \overline{\mathbf{u}_m}) + \nabla\cdot \mathbf{D}_\Sigma = -\nabla p + \nabla\cdot \left[\langle \mu \rangle \left(\nabla \overline{\mathbf{u}_m} + \nabla \overline{\mathbf{u}_m}^{\mathrm{T}} \right) \right] + \nabla\cdot \boldsymbol{\tau}_\Sigma + \overline{\rho}\, \mathbf{g} + \mathbf{f}_\sigma \tag{2.46}$$

with the barycentric mixture velocity $\overline{\mathbf{u}_m}$ defined as

$$\overline{\mathbf{u}_m} := \frac{\alpha_1 \overline{\rho}^1 \overline{\mathbf{u}}^1 + \alpha_2 \overline{\rho}^2 \overline{\mathbf{u}}^2}{\overline{\rho}} \tag{2.47}$$

and the momentum drift-flux term $\mathbf{D}_\Sigma$ and the interfacial friction tensor $\boldsymbol{\tau}_\Sigma$ (Wörner, 2003, Marschall, 2011), defined as

$$\mathbf{D}_\Sigma := \alpha_1 \alpha_2 \frac{\overline{\rho}^1 \overline{\rho}^2}{\overline{\rho}} \mathbf{u}_r \mathbf{u}_r \tag{2.48}$$

$$\begin{aligned} \boldsymbol{\tau}_\Sigma := & \alpha_1 \overline{\mu}^1 \left[\nabla \left(\alpha_2 \frac{\overline{\rho}^2}{\overline{\rho}} \mathbf{u}_r \right) + \nabla \left(\alpha_2 \frac{\overline{\rho}^2}{\overline{\rho}} \mathbf{u}_r \right)^{\mathrm{T}} \right] \\ & - \alpha_2 \overline{\mu}^2 \left[\nabla \left(\alpha_1 \frac{\overline{\rho}^1}{\overline{\rho}} \mathbf{u}_r \right) + \nabla \left(\alpha_1 \frac{\overline{\rho}^1}{\overline{\rho}} \mathbf{u}_r \right)^{\mathrm{T}} \right] . \end{aligned} \tag{2.49}$$

Eq. (2.44) results from the conservation of mass and (2.45) from the topological equation, where $\mathbf{u}_r$ denotes the relative velocity between the two adjacent phases ($\mathbf{u}_r := \overline{\mathbf{u}}^2 - \overline{\mathbf{u}}^1$). From the mixture assumption (cf. Section 2.3.2) it follows that $\mathbf{u}_r \equiv 0$ which leads to the well-known set of VOF governing equations:

$$\nabla\cdot \overline{\mathbf{u}} = 0 \tag{2.50}$$

$$\partial_t \alpha_1 + \nabla\cdot (\alpha_1 \overline{\mathbf{u}}) = 0 \tag{2.51}$$

$$\partial_t (\overline{\rho}\, \overline{\mathbf{u}}) + \nabla\cdot (\overline{\rho}\, \overline{\mathbf{u}}\, \overline{\mathbf{u}}) = -\nabla p + \nabla\cdot \langle \tau \rangle + \overline{\rho}\, \mathbf{g} + \mathbf{f}_\sigma . \tag{2.52}$$

It should be noted here that while the above set of equations might resemble the local instantaneous balance equations in the respective bulk phases (see Section 2.1.2), in fact, these are the conditional volume-averaged transport equations for the mixture quantities α_1, $\overline{\mathbf{u}}$ and the mean pressure p, obtained by the procedure as outlined in the previous subsections.

Since in (2.52) the mixture density varies across the interface, utmost care is necessary to assemble a consistent mass flux for the momentum equation after the solution of the phase fraction advection equation, such that the convection term can be treated momentum conservative (Weymouth and Yue, 2010). Otherwise, spurious acceleration would occur at the interface even at a moderate density ratio.

2.3.2 Assumptions and Numerical Closure

To arrive at a set of closed single-field equations, the well-established so-called mixture assumption is adopted in which each phase moves with the mixture velocity $\overline{\mathbf{u}}$:

$$\overline{\mathbf{u}} = \overline{\mathbf{u}}^k = \widetilde{\mathbf{u}}^k = \widetilde{\mathbf{u}} . \tag{2.53}$$

Further, it is assumed that all phases share a mean pressure field p

$$p = \overline{p}^k = \widetilde{p}^k . \tag{2.54}$$

It should also be noted that the mixture assumption and mean pressure assumption pose a limitation of the applicability of the VOF methods. Validity of the assumptions depends on the local resolution of the interface curvature, as well as the hydrodynamic boundary layer at the interface. This is a standard requirement for all DNS methods. The mixture assumption (2.53) is also valid in the utilized fluid system with interfacial species transfer, since only transfer processes of dilute species are considered and the interface is further assumed to not adsorb (or store) mass (cf. Chapter 2.1.2). Additionally, the surface tension coefficient σ is assumed to be constant, thus the influence of Marangoni effects is neglected within the simulations presented in this thesis.

Applying conditional volume averaging to a conservation equation causes terms that are unknown (due to averaging) and need modelling. The terms that require appropriate modelling are the mean quantities: (sum of the phasic averaged) viscous stress tensor $\langle \boldsymbol{\tau} \rangle$ and the surface tension force $\mathbf{f}_\sigma$. The Newtonian stress model in combination with the mixture assumption ($\mathbf{u}_r \equiv 0$) suggests the following closure modelling approach for the conditional volume-averaged viscous stress tensor

$$\langle \boldsymbol{\tau} \rangle = \langle \mu \rangle \left(\nabla \overline{\mathbf{u}} + \nabla \overline{\mathbf{u}}^{\mathrm{T}} \right) , \tag{2.55}$$

where the mean viscosity $\langle \mu \rangle$ is still unclosed and needs modelling. A detailed derivation of the volume-averaged viscous stress tensor can be found in Marschall (2011). As for its discretization, the viscous stress term in (2.52) is treated in a semi-implicit manner and has been decomposed for this purpose as

$$\nabla \cdot \left(\langle \mu \rangle \left(\nabla \overline{\mathbf{u}} + \nabla \overline{\mathbf{u}}^{\mathrm{T}} \right) \right) = \nabla \cdot \left(\langle \mu \rangle \nabla \overline{\mathbf{u}} \right) + \left(\nabla \overline{\mathbf{u}} \right) \cdot \nabla \langle \mu \rangle + \langle \mu \rangle \nabla \left(\nabla \cdot \overline{\mathbf{u}} \right) \tag{2.56}$$

$$= \nabla \cdot \left(\langle \mu \rangle \nabla \overline{\mathbf{u}} \right) + \left(\nabla \overline{\mathbf{u}} \right) \cdot \nabla \langle \mu \rangle , \tag{2.57}$$

where $\nabla \cdot \overline{\mathbf{u}} = 0$ has been exploited. While the first term can be treated fully implicit, the latter is discretized explicitly.

The conditional volume-averaged form of the momentum equation suggests a modelling of the mean viscosity as serial (arithmetic) mean

$$\langle \mu \rangle = \langle \mu \rangle_{\mathrm{a}} = \sum_{k=1,2} \alpha_k \overline{\mu}^k . \tag{2.58}$$

The correct mean value formulation for the viscosity is very important in order to correctly capture the influence of the viscous term at the interface. As the viscosity usually experiences a jump at the interfaces over several orders of magnitude, the choice of mean value formulation is found to influence the interface dynamics in numerical simulations. Additionally, the viscosity has to be evaluated where it is needed: at the face centres, while in the utilized collocated grid arrangement it is stored in the cell centres (Kothe, 1999). Consequently, this identifies the interpolation procedure central for an accurate formulation of the numerical model. The averaging procedure for the mean viscosity adopted in this work was introduced by Kothe (1999) and reads

$$\langle \mu_f \rangle = \gamma_f \langle \mu_f \rangle_\mathrm{h} + (1-\gamma_f)\langle \mu_f \rangle_\mathrm{a} \,, \tag{2.59}$$

where the quantities $\langle \mu_f \rangle_\mathrm{h}$ and $\langle \mu_f \rangle_\mathrm{a}$ in above equation are the harmonic (or parallel) and arithmetic (or serial) mean viscosities at the face centres, respectively. An explanation of this choice is presented in Section 3.1.2.

The surface tension force at the interface is modelled by the Continuous Surface Force (CSF) method of Brackbill et al. (1992). In the sharp interface model, the surface tension force acts only at the interface which is a mathematical surface. The CSF model converts this force density into a volumetric force density present in the interfacial area by multiplying the force with the interfacial area density ($\widetilde{\mathbf{n}_\Sigma} a_\Sigma = -\overline{\nabla \chi_1} \approx -\nabla \overline{\chi_1} = -\nabla \alpha_1$). Then,

$$\begin{aligned}\mathbf{f}_\sigma &:= \frac{1}{|V|}\int\limits_{S_\Sigma} \sigma \kappa_\Sigma \mathbf{n}_\Sigma \, dS \approx \sigma \, \widetilde{\kappa_\Sigma} \, \widetilde{\mathbf{n}_\Sigma} a_\Sigma \approx -\sigma \, \widetilde{\kappa_\Sigma} \nabla \alpha_1 \\ &\text{with} \quad \widetilde{\kappa_\Sigma} = \widetilde{\nabla\cdot(-\mathbf{n}_\Sigma)} = -\nabla\cdot\left(\widetilde{\mathbf{n}_\Sigma}\right) \approx \nabla\cdot\left(\frac{\nabla\alpha_1}{|\nabla\alpha_1|}\right) .\end{aligned} \tag{2.60}$$

In above equation, the assumption of constant surface tension coefficient – as previously mentioned – is utilized and thus the Marangoni term does not appear.

2.4 Continuous Species Transfer Method - Governing Equation

The main focus of this thesis, outlined in the introduction, is the numerical study of interfacial mass transfer in two-phase flows on the highest level of detail. In this Section, the development of a predictive simulation method in the framework of algebraic Volume-of-Fluid methods for Direct Numerical Simulation of interfacial species transfer is presented. Here, the model's restriction so far lies on *species transfer*, meaning that its derivation is based on the transport equation for a dilute species and effects of *mass transfer* are not considered. Thus, the species transport is modelled by an additional passive scalar transport equation.

2.4.1 Single-Field vs. Two-Field Approach

To simulate species transfer processes in two-phase systems employing the Volume-of-Fluid method, two conceptually different approaches can be used, namely the single-field and two-field approaches. Despite their capabilities to incorporate interfacial species transfer in a realistic range of Henry coefficients and diffusivity ratios into the framework of the Volume-of-Fluid methodology, both the single-field and the two-field approach exhibit method-specific advantages and disadvantages. The two different methodologies are assessed here and compared regarding model characteristics and numerical properties:

- Conservation
  Both formulations allow for a conservative discretization. However, when relying on a reformulation to alleviate the interfacial concentration jump (e.g. Francois and Carlson (2010)), resulting single-field formulations are not conservative. On the other hand, two-field models inherently suffer from the *small cell problem* (Berger et al., 2003, Hartmann et al., 2011), which can introduce conservation problems with the transported species concentration.
- Consistency
  Model consistency is a prerequisite but not sufficient to prevent artificial mass transfer. This has two main (numerical) causes: advection errors which locally change the concentration field and non-consistent advection of volumetric phase fraction (or indicator function in context of VOF methods with geometrical reconstruction) and the species concentration field.
  Consistency is also the main criterion as to whether the single-field or two-field approach should be used. If a geometrical VOF method is employed, the two-field model is the native choice as it allows for consistent advection. In algebraic VOF methods, two-field models are not beneficial as they require the exact interface position for computation of the species transfer term. Thus, for algebraic VOF methods, a single-field model should be utilized. Influence of artificial mass transfer onto the proposed single-field CST method is studied in more detail in Sections 3.2.4 and 5.2.1.
- Subgrid-scale modelling
  Subgrid-scale modelling requires the one-sided concentrations and concentration gradients at the interface as well as analytical reconstruction of the face fluxes in interface cells ((Weiner and Bothe, 2017)). Thus, this information is only readily available in two-field models. For single-field models, no subgrid-scale models are currently available. Such a model would require to be based on volume averaging rather than fitting of local concentration profiles as can straight-forward be included in two-field models.
- Computation of local quantities
  Computation of local quantities as the local Sherwood number requires the one-sided concentrations and/or gradients, which are only readily available in two-field models. In single-field models, new concepts to assess local quantities have to be envisioned. Possible approaches for single-field methods are outlined in Section 2.4.7.
- Accuracy
  Given a fixed resolution, the two-field model with geometric interface reconstruction will produce more accurate results due to the additional information about the exact interface position and the local concentrations and concentration gradient values. However, single-field methods in general are also shown to be sufficiently accurate. Disregarding advection errors, the single-field and two-field models are comparable in accuracy if no subgrid-scale model is used. Without sub-grid scale modelling, the required mesh resolution for both methods is at least four cells in the concentration boundary layer.

- Complex geometries
  Complex geometries entail usage of unstructured meshes of general topology. In principle, single-field and two-field models are both suited for discretization on such meshes. However, only the single-field approach has – to the author's best knowledge – been put forth thus far to unstructured meshes (e.g. Hill et al. (2018)).
- Implicit discretization
  Time-implicit discretization enhances numerical stability and is needed to overcome time-step restrictions due to high diffusion coefficients. Straight-forward implicit discretization is only feasible for single-field models and two-field models would require – at the very least – implicit coupling algorithms between the two concentration fields.
- Computational costs
  With a given mesh, the single-field model is significantly faster: The single-field approach takes about 10% of the computational time per time step for each simulated species concentration field, while the two-field approach takes about 30% (data stem from comparison for heat transfer in FS3D). Considering, however, the time-to-solution for a given problem with very thin concentration boundary layer, then the two-field model is considerably faster when utilizing a subgrid-scale model, since a much coarser computational mesh can be used to achieve the same overall accuracy. Therefore, in this work adaptive mesh refinement is used, significantly reducing the time-to-solution for the single-field model.

Conclusively, the two-field approach in combination with a geometrical VOF method is more accurate than the single-field approach on a given mesh resolution. Main reasons are the error introduced by the advection of the mixture concentration and the straight-forward use of subgrid-scale models. However, benefit of single-field models is the numerical robustness and straight-forward application to unstructured meshes of general topology, which – as of today – makes it the more versatile approach for industrial usage. Clearly, there is scope for even further improvements for both methods and thus they are subject to ongoing research.

2.4.2 Model Derivation

The derivation of the single-field formulation for interfacial species transfer presented here is based on the conditional volume averaging technique, applied to the local instantaneous governing equation for the species concentration including interface jump conditions. Assuming a dilute species, the local instantaneous species transport equation valid in the bulk of phases 1 and 2 reads

$$\partial_t c + \nabla\cdot(c\mathbf{u}) - \nabla\cdot(D\nabla c) = R, \qquad \text{in } \Omega_1(t) \cup \Omega_2(t) \setminus \Sigma(t) \tag{2.61}$$

with the interfacial jump conditions

$$[\![(-D\nabla c)\cdot\mathbf{n}_\Sigma]\!] = 0 \qquad \text{on } \Sigma(t) \tag{2.62}$$

$$c_{\Sigma,1} = \mathrm{H} c_{\Sigma,2} \qquad \text{on } \Sigma(t). \tag{2.63}$$

Here, the one-sided interface values, denoted by $c_{\Sigma,1}$ and $c_{\Sigma,2}$ are defined as

$$c_{\Sigma,1} := \lim_{\delta_\Sigma \to 0+} c(\mathbf{x}_\Sigma - \delta_\Sigma \mathbf{n}_\Sigma) \quad \text{and} \quad c_{\Sigma,2} := \lim_{\delta_\Sigma \to 0+} c(\mathbf{x}_\Sigma + \delta_\Sigma \mathbf{n}_\Sigma)\,, \tag{2.64}$$

where $\mathbf{n}_\Sigma$ is the outward-pointing normal vector of region Ω_1 and $[\![\cdots]\!]$ denotes the jump bracket defined in Eq. (2.10). The first jump condition is the interface transmission condition and expresses the conservation of molar mass at the interface under the assumption that the interface cannot store mass. In that case, interfacial chemical reactions and adsorption processes to the interface are not considered. Moreover, for Eq. (2.62) to be valid, the species needs to be dilute. The second jump condition is Henry's law which is valid if local thermodynamic equilibrium can be assumed at the interface. For a detailed discussion about the range of validity of above mathematical model, it is referred to Bothe and Fleckenstein (2013).

Applying conditional volume averaging to Eq. (2.61) with respect to phase 1 yields

$$\begin{aligned} &\overline{\chi_1 \partial_t c} + \overline{\chi_1 \nabla\cdot(c\mathbf{u})} = \overline{\chi_1 \nabla\cdot(D\nabla c)} + \overline{\chi_1 R} \\ \Leftrightarrow\ &\partial_t(\alpha_1 \overline{c}^1) + \nabla\cdot\left(\alpha_1 \overline{c}^1 \overline{\mathbf{u}}^1\right) = \nabla\cdot\left(\alpha_1 \overline{D}^1 \nabla \overline{c}^1\right) + \alpha_1 \overline{R}^1 + \widetilde{D\nabla c\cdot\mathbf{n}_\Sigma}^1 a_\Sigma\,. \end{aligned} \tag{2.65}$$

Employing the immersed interface concept, above equation is summed up for both phases 1 and 2 in order to obtain a single-field formulation for interfacial species transfer. In the present work chemical reactions are only allowed to take place in the liquid phase such that $\overline{R}^1 = 0$. Then, Eq. (2.65) leads to

$$\partial_t \overline{c} + \nabla\cdot(\overline{c}\,\overline{\mathbf{u}}) = \nabla\cdot\left(\alpha_1 \overline{D}^1 \nabla\overline{c}^1 + \alpha_2 \overline{D}^2 \nabla\overline{c}^2\right) + \alpha_2 \overline{R}^2\,. \tag{2.66}$$

Since the interfacial transmission condition (2.62) equates to zero locally at the interface, then its surface-averaged counterpart does as well

$$\sum_{k=1,2} \widetilde{D\nabla c\cdot\mathbf{n}_\Sigma}^k a_\Sigma \equiv 0\,.$$

This condition has been employed to simplify the one-sided interfacial flux terms in Eq. (2.65) to arrive at (2.66). As stated in Chapter 2.3.2, the assumption of equal velocities ($\mathbf{u}_r \equiv 0$) at the interface is employed. In the context of species transfer, this assumption is valid for physical transfer processes of dilute species without phase change. The mixture concentration $\overline{c}$ in Eq. (2.66) is defined as $\overline{c} := \alpha_1 \overline{c}^1 + \alpha_2 \overline{c}^2$. In its current form, Equation (2.66) cannot be solved since a closure for the r.h.s. term needs to be formulated which relates the phasic averages $\overline{c}^1$ and $\overline{c}^2$ to the mixture concentration $\overline{c}$ within the interfacial region.

To arrive at a closed single-field formulation for interfacial species transfer, which is readily usable for Finite Volume discretization, the phasic averaged concentrations at the interface are related employing Henry's law which is the most simple approach and alternative approaches are subject to ongoing research. The *local* instantaneous concentration jump at the interface is given in (2.63), connecting the one-sided concentrations on both sides of the interface. To employ this law with phasic averaged concentrations, it is referred to the work of Haroun et al. (2010) and Marschall et al. (2012) who relate them directly to the one-sided interface concentrations as

$$H = \frac{c_{\Sigma,1}}{c_{\Sigma,2}} = \frac{\overset{\frown}{c}^{1}}{\overset{\frown}{c}^{2}} \approx \frac{\overline{c}^{1}}{\overline{c}^{2}} \,. \tag{2.67}$$

The closure relation derived in Eq. (2.67) consists of two steps. The first step is obviously fulfilled exactly and states that if a constant concentration jump exists locally at each point of the interface, the same jump (assuming a constant Henry coefficient) will also exist for interface-averaged concentrations. In the second step, it is assumed that the ratio of the interface-averaged concentrations is equal to the ratio of the phasic-averaged concentrations in each computational cell containing the interface. This assumption clearly implies a constraint on the model in terms of spatial resolution as the high concentration gradients at the interface need to be sufficiently resolved. By inserting (2.67) into the definition of the mixture concentration $\overline{c}$, it is now possible to reformulate the phasic averaged concentrations in terms of the mixture concentration and volumetric phase fraction as

$$\begin{aligned} &\overline{c} := \alpha_1 \overline{c}^1 + \alpha_2 \overline{c}^2 \approx \overline{c}^1 \left(\alpha_1 + \frac{1-\alpha_1}{H} \right) \\ &\Rightarrow \overline{c}^1 \approx \frac{\overline{c}}{\alpha_1 + \frac{1-\alpha_1}{H}}, \quad \overline{c}^2 \approx \frac{1}{H} \frac{\overline{c}}{\alpha_1 + \frac{1-\alpha_1}{H}} \,. \end{aligned} \tag{2.68}$$

This now enables the formulation of a closed set of single-field governing equations for interfacial species transfer. However, for the full single-field model based on Eq. (2.66) the definition of a mean diffusion coefficient is still required, which is discussed in the following.

2.4.3 Choice of Mean Diffusion Coefficient

The r.h.s of Eq. (2.66) can be rewritten in different ways, depending on the definition of the mean diffusion coefficient. The mean value calculations typically applied are the arithmetic or harmonic mean. It will be shown that it is possible to obtain different single-field equations for interfacial species transfer, depending solely on the definition of the mean diffusion coefficient. Indeed, depending on this choice, it will be shown that the resulting single-field model resembles the different forms postulated by Haroun et al. (2010) (harmonic mean diffusion coefficient) and Marschall et al. (2012) (arithmetic mean diffusion coefficient) independently. This said, the CST method developed in this work is to be seen as a generic and unified framework for single-field species transfer models.

Starting from Eq. (2.66), the r.h.s. can be split into two terms, one bulk and one interface contribution, as

$$\nabla\cdot\left(\alpha_1\overline{D}^1\nabla\overline{c}^1+\alpha_2\overline{D}^2\nabla\overline{c}^2\right)=\nabla\cdot\nabla\left(\alpha_1\overline{D}^1\overline{c}^1+\alpha_2\overline{D}^2\overline{c}^2\right)-\nabla\cdot\left(\left(\overline{D}^1\overline{c}^1-\overline{D}^2\overline{c}^2\right)\nabla\alpha_1\right)\;. \tag{2.69}$$

Here, constant diffusion coefficients in both phases are assumed, which is a valid assumption for isothermal two-phase systems with dilute species. As previously shown for the single-field momentum equation, one needs to introduce mean coefficients to arrive at a closed formulation. One standard mean value calculation is the arithmetic mean. Defining an arithmetic mean diffusion coefficient as

$$\langle D\rangle_{\mathrm{a}}\equiv\alpha_1\overline{D}^1+\alpha_2\overline{D}^2\;, \tag{2.70}$$

Eq. (2.69) can be rewritten using

$$\alpha_1\overline{D}^1\overline{c}^1+\alpha_2\overline{D}^2\overline{c}^2=\langle D\rangle_{\mathrm{a}}\,\overline{c}+\alpha_1(1-\alpha_1)\left(\overline{D}^1-\overline{D}^2\right)\left(\overline{c}^1-\overline{c}^2\right)\;. \tag{2.71}$$

Using Equations (2.68), (2.69) and (2.71) and inserting into Eq. (2.66), one finally arrives at a closed single-field formulation which reads

$$\begin{aligned}\partial_t\overline{c}+\nabla\cdot(\overline{c}\,\overline{\mathbf{u}})=\nabla\cdot(\langle D\rangle_{\mathrm{a}}\nabla\overline{c})+\nabla\cdot(\overline{c}\nabla\langle D\rangle_{\mathrm{a}})-\nabla\cdot\left(\frac{\overline{D}^1-\frac{\overline{D}^2}{\mathrm{H}}}{\alpha_1+\frac{1-\alpha_1}{\mathrm{H}}}\overline{c}\nabla\alpha_1\right)\\+\Delta\left(\alpha_1(1-\alpha_1)\left(\overline{D}^1-\overline{D}^2\right)\overline{c}\frac{1-\frac{1}{\mathrm{H}}}{\alpha_1+\frac{1-\alpha_1}{\mathrm{H}}}\right)\;.\end{aligned} \tag{2.72}$$

With regard to the implicit numerical solution of above equation which will be discussed later, it is helpful to split the last term of Eq. (2.72) into terms of the divergence and Laplacian of the mixture concentration $\overline{c}$ as

$$\begin{aligned}&\Delta\left(\alpha_1(1-\alpha_1)\left(\overline{D}^1-\overline{D}^2\right)\frac{1-\frac{1}{\mathrm{H}}}{\alpha_1+\frac{1-\alpha_1}{\mathrm{H}}}\overline{c}\right)\\&=\nabla\cdot\left(\left(\overline{D}^1-\overline{D}^2\right)\alpha_1\left(\frac{1}{\alpha_1+\frac{1-\alpha_1}{\mathrm{H}}}-1\right)\nabla\overline{c}\right)\\&+\nabla\cdot\left(\left(\overline{D}^1-\overline{D}^2\right)\overline{c}\left(\frac{1}{\mathrm{H}}\frac{1}{\left(\alpha_1+\frac{1-\alpha_1}{\mathrm{H}}\right)^2}-1\right)\nabla\alpha_1\right)\;.\end{aligned} \tag{2.73}$$

Finally, the term $\nabla\cdot\left(\bar{c}\nabla\langle D\rangle_{\mathrm{a}}\right)=\nabla\cdot\left(\bar{c}\left(\overline{D}^{1}-\overline{D}^{2}\right)\nabla\alpha_1\right)$ in Eq. (2.72) can be eliminated to arrive at the single-field equation for interfacial species transfer using an arithmetic mean mixture diffusion coefficient:

$$\boxed{\begin{aligned}\partial_t\bar{c}+\nabla\cdot\left(\bar{c}\,\bar{\mathbf{u}}\right)&=\nabla\cdot\left(\langle D\rangle_{\mathrm{a}}\nabla\bar{c}\right)+\nabla\cdot\left(\left(\overline{D}^{1}-\overline{D}^{2}\right)\alpha_1\left(\frac{1}{\alpha_1+\frac{1-\alpha_1}{\mathrm{H}}}-1\right)\nabla\bar{c}\right)\\&+\nabla\cdot\left[\frac{\bar{c}}{\alpha_1+\frac{1-\alpha_1}{\mathrm{H}}}\left(\frac{1}{\mathrm{H}}\frac{\overline{D}^{1}-\overline{D}^{2}}{\alpha_1+\frac{1-\alpha_1}{\mathrm{H}}}-\left(\overline{D}^{1}-\frac{\overline{D}^{2}}{\mathrm{H}}\right)\right)\nabla\alpha_1\right]+\alpha_2\overline{R}^{2}\,.\end{aligned}}\tag{2.74}$$

This model, written in the form of (2.72), has the same form as the one obtained by Marschall et al. (2012), except the last term on the r.h.s. which accounts for curvature effects and was missing in the original work.

Harmonic mean Mixture Diffusion Coefficient

Another frequently used mean value definition is the harmonic mean. To examine the resulting (different) single-field formulation, let us start from Eq. (2.66) and define a harmonic mean mixture diffusion coefficient as

$$\langle D\rangle_{\mathrm{h}}\equiv\frac{\overline{D}^{1}\,\overline{D}^{2}}{\alpha_1\overline{D}^{2}+\alpha_2\overline{D}^{1}}\,.\tag{2.75}$$

The right hand side of Eq. (2.66) can then be rewritten as

$$\begin{aligned}\nabla\cdot\left(\alpha_1\overline{D}^{1}\nabla\bar{c}^{1}+\alpha_2\overline{D}^{2}\nabla\bar{c}^{2}\right)&=\nabla\cdot\left(\left(\alpha_1\overline{D}^{1}\nabla\bar{c}^{1}+\alpha_2\overline{D}^{2}\nabla\bar{c}^{2}\right)\frac{\alpha_1\overline{D}^{2}+\alpha_2\overline{D}^{1}}{\alpha_1\overline{D}^{2}+\alpha_2\overline{D}^{1}}\right)\\&=\nabla\cdot\left(\langle D\rangle_{\mathrm{h}}\left(\nabla\bar{c}-\left(\bar{c}^{1}-\bar{c}^{2}\right)\nabla\alpha_1\right)\right)+\nabla\cdot\left(\langle D\rangle_{\mathrm{h}}\,\alpha_1\alpha_2\left(\left(\frac{\overline{D}^{1}}{\overline{D}^{2}}-1\right)\nabla\bar{c}^{1}+\left(\frac{\overline{D}^{2}}{\overline{D}^{1}}-1\right)\nabla\bar{c}^{2}\right)\right)\,.\end{aligned}\tag{2.76}$$

Here, the identity

$$\nabla\bar{c}\equiv\nabla\left(\alpha_1\bar{c}^{1}+\alpha_2\bar{c}^{2}\right)=\alpha_1\nabla\bar{c}^{1}+\alpha_2\nabla\bar{c}^{2}+\left(\bar{c}^{1}-\bar{c}^{2}\right)\nabla\alpha_1\tag{2.77}$$

was used. Now, to arrive at a closed single-field formulation, consider again the interface transmission condition for the species concentration

$$[\![(-D\nabla c)\cdot\mathbf{n}_\Sigma]\!]=0\quad\Rightarrow\quad\sum_{k=1,2}\overbrace{D\nabla c\cdot\mathbf{n}_\Sigma}^{k}\,a_\Sigma=0\,.\tag{2.78}$$

Analogous to the procedure in Reynolds averaging, each quantity $\mathbf{\Phi}$ can be split into an average value and its deviation as $\mathbf{\Phi}=\widetilde{\mathbf{\Phi}}+\mathbf{\Phi}^{\#}$. If the averaging volume is sufficiently small, deviations from the average value can be neglected which leads to

$$\left(\widetilde{D}^{1}\nabla\widetilde{c}^{1}-\widetilde{D}^{2}\nabla\widetilde{c}^{2}\right)\cdot\widetilde{\mathbf{n}_\Sigma}=0\,.\tag{2.79}$$

This equation now relates the normal gradients of the surface-averaged species concentrations for each phase at the interface. Now let us have a closer look at the concentration gradients in tangential direction to the interface $\left({\overbrace{D}}^{1} \nabla_\Sigma {\overbrace{c}}^{1} - {\overbrace{D}}^{2} \nabla_\Sigma {\overbrace{c}}^{2} \right)$ with the surface gradient ∇_Σ. If the concentration at one side of the interface is approximately constant along the interface, it follows from the Henry jump condition (Eq. (2.63)) that the other concentration is constant as well. Regarding the species transfer of a dilute gas from a rising bubble into a surrounding liquid, the concentration in the bubble is approximately uniform due to the recirculation of fluid in the bubble. Therefore, the concentration gradients tangential to the interface can be neglected

$$
{\overbrace{D}}^{1} \nabla_\Sigma {\overbrace{c}}^{1} - {\overbrace{D}}^{2} \nabla_\Sigma {\overbrace{c}}^{2} = \nabla_\Sigma \overbrace{\left({\overbrace{D}}^{1} {\overbrace{c}}^{1} - {\overbrace{D}}^{2} {\overbrace{c}}^{2} \right)}^{\approx \text{const}} \approx 0 \,, \tag{2.80}
$$

which allows us to reformulate Eq. (2.79) into

$$
{\overbrace{D}}^{1} \nabla {\overbrace{c}}^{1} - {\overbrace{D}}^{2} \nabla {\overbrace{c}}^{2} = 0 \,. \tag{2.81}
$$

To further simplify this equation, let us reconsider the closure assumption (2.67) that allowed us to relate the phasic averaged concentrations to the mixture concentration. Here, the ratio of the surface averaged concentrations is assumed to be equal to the ratio of the phasic averaged concentrations. Now, a further assumption is added that not only the ratio is equal but that the surface averaged and phasic averaged concentrations are equal as well

$$
{\overbrace{c}}^{1} = \overline{c}^{1} \quad \text{and} \quad {\overbrace{c}}^{2} = \overline{c}^{2} \,. \tag{2.82}
$$

With the assumption of negligible concentration gradients tangential to the interface (2.80) and assumption (2.82) the interface transmission condition (Eq. 2.78) can be simplified into

$$
\overline{D}^{1} \nabla \overline{c}^{1} = \overline{D}^{2} \nabla \overline{c}^{2} \,. \tag{2.83}
$$

To summarize, the assumptions which lead to (2.83) are a sufficient resolution of the concentration boundary layer (2.82) and a vanishing or, compared to the normal component, negligible tangential concentration gradient to the interface, which is fulfilled for most two fluid systems of technical relevance. Given that the assumptions (2.82) and (2.83) hold true, the last term in Eq. (2.76) reduces to

$$
\left(\frac{\overline{D}^{1}}{\overline{D}^{2}} - 1 \right) \nabla \overline{c}^{1} + \left(\frac{\overline{D}^{2}}{\overline{D}^{1}} - 1 \right) \nabla \overline{c}^{2} = 0 \,. \tag{2.84}
$$

Substituting the first r.h.s. term of Eq. (2.66) with Eq. (2.76) and inserting Eq. (2.84) then yields:

$$
\partial_t \, \overline{c} + \nabla \cdot \left(\overline{c} \, \overline{\mathbf{u}} \right) = \nabla \cdot \left[\langle D \rangle_{\mathrm{h}} \left(\nabla \overline{c} - \left(\overline{c}^{1} - \overline{c}^{2} \right) \nabla \alpha_1 \right) \right] + \alpha_2 \overline{R}^{2} \,. \tag{2.85}
$$

Using the closure assumption for the one-sided concentrations at the interface (Eq. (2.67)), one arrives at the single-field equation for interfacial species transfer using a harmonic mean mixture diffusion coefficient

$$\boxed{\partial_t \overline{c} + \nabla\cdot(\overline{c}\,\overline{\mathbf{u}}) = \nabla\cdot(\langle D\rangle_{\mathrm{h}} \nabla\overline{c}) - \nabla\cdot\left(\langle D\rangle_{\mathrm{h}} \frac{1-\frac{1}{\mathrm{H}}}{\alpha_1 + \frac{1-\alpha_1}{\mathrm{H}}} \overline{c}\nabla\alpha_1\right) + \alpha_2 \overline{R}^2 .} \tag{2.86}$$

This equation has the same form as the single-field formulation obtained by Haroun et al. (2010). However, it should be noted that the derivation presented here states that above model is only valid when using a harmonic mean mixture diffusion coefficient, while the derivation of Haroun suggests that above equation could be used with any definition of the mixture diffusion coefficient. Only through validation of their numerical model with suitable test cases did they find that a harmonic mean diffusion coefficient is the only appropriate choice for above single-field equation. Moreover, the derivation procedure as presented above reveals that this formulation requires an additional closure compared to the presented single-field formulation with arithmetic mean diffusion coefficient (Eq. (2.74)) and is strictly valid only for negligible concentration gradients tangential to the interface which is fulfilled in the case of gas-liquid flows studied here, where the concentration within the bubble is approximately uniform. The two main assumptions in the present thesis, (2.67) and (2.82), both pose restrictions to the applicability of the derived single-field models, but up to this point it is not clear which of the two introduced assumptions poses the stronger limitation in terms of mesh resolution. Hence, one pivotal question is: which of the two single-field models, Eq. (2.74) or (2.86) is more suited for the simulation of interfacial species transfer in two-phase flow systems. This question is answered by validation test cases presented in Chapter 5.

2.4.4 Final Form of the Model

There is a close conceptual relationship between the volume averaging technique and the Finite Volume Method. Discretization of spatial transport terms within the present Finite Volume framework is accomplished by applying Gauss' theorem, yielding a flux-based transport formulation which is inherently conservative. This conversion of volume integrals into surface integrals, however, necessitates the knowledge of the values at the face centres which are obtained by appropriate interpolation of the cell-centred values. To arrive at a numerical model consistent to the Finite Volume Method, flux-related terms need to be computed correctly where they are needed: at the face centres. Therefore, the interface / cell-face orientation needs to be taken into account as suggested e.g. by Patankar (1980) and Kothe (1999) for heat and momentum flux, respectively (see Chapter 2.3.2) . As the validation in Chapter 5.2 does not show significant differences with respect to accuracy between the two presented single-field formulations for the relevant case of large Henry coefficients (i.e. $\mathrm{H} \approx 30$), one shall stay on the safe side and follow the work of Kothe (1999), evaluating the mean diffusivity within the CST model based on the cell-face/interface orientation which then reads

$$\left\langle D_f \right\rangle \equiv \gamma_f \left\langle D_f \right\rangle_{\mathrm{h}} + \left(1-\gamma_f\right)\left\langle D_f \right\rangle_{\mathrm{a}} = \gamma_f \left(\frac{\overline{D}^1 \, \overline{D}^2}{\alpha_1 \overline{D}^2 + \alpha_2 \overline{D}^1} \right)_f + \left(1-\gamma_f\right)\left(\alpha_1 \overline{D}^1 + \alpha_2 \overline{D}^2\right)_f , \tag{2.87}$$

where $\gamma_f = |\widehat{\mathbf{n}_f} \cdot \widehat{\mathbf{n}_\Sigma}|$. In the following the above evaluation procedure of the mixture diffusion coefficient based on interface/cell-face orientation will be motivated and it will be shown that it is indeed a good choice. Therefore, recall that the derivation of Equation (2.86) is based on the assumption of a negligible concentration gradient parallel to the interface. A standard discretization procedure based on the FVM would transform the divergence terms applying Gauss' theorem into flux-based terms in face-normal direction. Starting again at Eq. (2.76) and introducing Gauss' theorem will introduce terms of the following form

$$\sum_f (K)_{f(S,\gamma)} \left[\left(\frac{\overline{D}^1}{\overline{D}^2} - 1 \right) \nabla \overline{c}^1 + \left(\frac{\overline{D}^2}{\overline{D}^1} - 1 \right) \nabla \overline{c}^2 \right]_{f(S,\gamma)} \cdot \mathbf{S}_f = 0 , \tag{2.88}$$

where K is a scalar field and S denotes an arbitrary scheme used for discretization. If such a discretization technique is employed, it is observed that Eq. (2.86) is strictly valid only when the cell-face is aligned with the interface or tangential concentration gradients at the interface can be neglected. Comparing the performance of both derived single-field formulations for a one-dimensional diffusion case over a planar interface, it was found that Eq. (2.74) requires a smaller averaging volume (higher mesh resolution) as Eq. (2.86), to obtain comparable results (cf. Chapter 5 for details). Therefore it seems an appropriate choice to base the evaluation of the mean mixture diffusion coefficient on the cell-face / interface orientation, using the advantage of Eq. (2.86) in terms of mesh resolution when the cell-faces are aligned with the interface and otherwise to blend with Eq. (2.74). Thus, the new single-field equation model for interfacial species transfer, termed Continuous Species Transfer (CST) method reads, in the spirit of Kothe and Patankar

$$\boxed{\begin{aligned} \partial_t \overline{c} + \nabla\cdot(\overline{c}\,\overline{\mathbf{u}}) &= \nabla\cdot(\langle D\rangle \nabla \overline{c}) - \nabla\cdot\left(\gamma_f \langle D\rangle_{\mathrm{h}} \frac{1-\frac{1}{\mathrm{H}}}{\alpha_1 + \frac{1-\alpha_1}{\mathrm{H}}} \overline{c} \nabla \alpha_1 \right) \\ &+ \nabla\cdot\left[\left(1-\gamma_f\right)\left(\overline{D}^1 - \overline{D}^2\right)\alpha_1 \left(\frac{1}{\alpha_1 + \frac{1-\alpha_1}{\mathrm{H}}} - 1 \right) \nabla \overline{c} \right] \\ &+ \nabla\cdot\left[\left(1-\gamma_f\right) \frac{\overline{c}}{\alpha_1 + \frac{1-\alpha_1}{\mathrm{H}}} \left(\frac{1}{\mathrm{H}} \frac{\overline{D}^1 - \overline{D}^2}{\alpha_1 + \frac{1-\alpha_1}{\mathrm{H}}} - \left(\overline{D}^1 - \frac{\overline{D}^2}{\mathrm{H}} \right) \right) \nabla \alpha_1 \right] . \end{aligned}} \tag{2.89}$$

It should be noted that the resulting CST method is a unification of the work of Marschall et al. (2012) and Haroun et al. (2010) into one single-field formulation which is consistent to the FVM framework and applicable to any algebraic VOF method on structured and unstructured mesh topologies. The presented single-field equation does not only unify both work but also removes the shortcomings of their respective models. In the work of Marschall et al. (2012), an assumption was made regarding Equation (2.71) that lead to a missing curvature-related term which is set out here, and the range of validity of the single-field model derived by Haroun et al. (2010), which was not discussed in their work, is finally shown. As will be shown later, the final model, Equation (2.89), can be discretized fully time-implicit, thus removing time step limitations present for explicit solutions. Furthermore, the model can be discretized in a mass conservative manner.

2.4.5 Influence of Mesh Resolution

As mentioned before, the central aspect for the successful application of the derived model is the constraint which the closure assumptions (2.67) and (2.82) pose to the mesh resolution for the derived single-field equations (2.74), (2.86) and (2.89) to be sufficiently accurate. For the relevant case of rising bubbles at a moderate or large particle Reynolds number, i.e. $\mathrm{Re}_p \ll 1$, a thin liquid-sided boundary layer with steep normal gradient of the concentration appears at the interface. Additionally, in scope of gas-liquid systems, concentration gradients tangential to the interface can indeed be neglected.

To simulate species transfer from rising bubbles, a major difficulty therefore is to resolve the thin concentration boundary layer at the interface. To successfully apply the derived CST model to the case of species transfer from rising bubbles, sufficient resolution has to be provided in order to resolve the concentration boundary layer. For the presented model, the required resolution is determined by the closure assumptions (2.67) and (2.82). However, numerical results presented hereafter suggest that assumption (2.67) is the limiting condition since the CST model with harmonic mean diffusion coefficient, Eq. (2.86), shows slight benefits compared to Eq. (2.74) in terms of accuracy for a given mesh resolution.

Further, it was observed that the concentration boundary layer needs to be resolved with at least 4-5 computational cells in order to obtain sufficiently accurate results for the diffusive mass transfer over the interface. However, as will be discussed in Sections 3.2.4 and 5.2.1, the necessary mesh resolution is strongly influenced by the discretization of the species advection term due to numerical diffusion or anti-diffusion. Moreover, if the concentration boundary layer is under-resolved and $\mathrm{H} > 1$, the diffusion terms in the CST model will always lead to an over-prediction of the species transfer. From the closure assumption (2.67), it is obvious that the limiting term for species transfer, $(\bar{c}^1 - \bar{c}^2)$, will be always under-predicted if the concentration boundary layer is under-resolved, which leads to an increased species transfer over the interface.

2.4.6 Zero-Solubility Limit

In special cases it might be important that a species should stay solely within one phase, e.g. in case of chemical reaction simulations. Thus, setting the diffusion coefficient within one phase to zero or the Henry coefficient to a very high number should lead to no interfacial mass transfer within the numerical model. In scope of algebraic VOF methods, this imposes two conditions on the numerical model: First, the diffusive terms in the transport equation need to vanish at the interface and second, the employed advection algorithm must ensure that no mass is transferred over the interface. This is indeed a challenge for algebraic methods and requires consistent advection between volumetric phase fraction and species concentration fields (cf. Chapter 5.2.1). To assess the capabilities of the CST model for modelling zero solubility, hence, four different limiting cases must be studied:

1. $\mathrm{H} \to \infty$, 2. $\mathrm{H} \to 0$, 3. $\overline{D}^1 \to 0$, 4. $\overline{D}^2 \to 0$.

Consider first the interfacial flux for the CST model with harmonic mean diffusion coefficient, here repeated for convenience of the reader

$$\langle D \rangle_{\mathrm{h}} \left[\nabla \overline{c} - \frac{1 - \frac{1}{\mathrm{H}}}{\alpha_1 + \frac{1-\alpha_1}{\mathrm{H}}} \overline{c} \nabla \alpha_1 \right] .$$

Here, the limiting values of a *discrete function* at face centres is considered, so partial knowledge of the discretization procedure introduced in Chapter 3.2.3 is presumed. As face centre values only depend on face-neighbour cell values and the flux-based discretization only considers face-normal gradients, the four limiting cases need only be studied in the interfacial region, i.e. in computational cells with $\alpha_1 \in (0, 1)$. Before continuing the investigation of limiting values for the flux terms, the limits of concentration and concentration gradient need to be investigated. Considering the definition of the mixture concentration, one obtains

$$\lim_{\mathrm{H}\to 0} \overline{c} = \begin{cases} (1-\alpha_1)\,\overline{c}^2 & \text{if } \alpha_1 \mathrm{H} \ll 1-\alpha_1 \\ \overline{c}^1 \equiv 0 & \text{if } \alpha_1 \equiv 1 \end{cases}, \qquad \lim_{\mathrm{H}\to \infty} \overline{c} = \begin{cases} \alpha_1 \overline{c}^1 & \text{if } \alpha_1 \mathrm{H} \gg 1-\alpha_1 \\ \overline{c}^2 \equiv 0 & \text{if } \alpha_1 \equiv 0 \end{cases}, \tag{2.90}$$

$$\lim_{\mathrm{H}\to 0} \nabla\overline{c} = \begin{cases} \nabla\big((1-\alpha_1)\,\overline{c}^2\big) & \text{if } \alpha_1 \mathrm{H} \ll 1-\alpha_1 \\ \nabla\overline{c}^1 \equiv 0 & \text{if } \alpha_1 \equiv 1 \end{cases}, \qquad \lim_{\mathrm{H}\to \infty} \nabla\overline{c} = \begin{cases} \nabla\big(\alpha_1 \overline{c}^1\big) & \text{if } \alpha_1 \mathrm{H} \gg 1-\alpha_1 \\ \nabla\overline{c}^2 \equiv 0 & \text{if } \alpha_1 \equiv 0 \end{cases}. \tag{2.91}$$

With above limits of the mixture concentration and its gradient, the limiting values of the harmonic CST model can be calculated to prove that the proposed formulation is capable of modelling the limiting cases of zero solubility.

1. case $\mathrm{H} \to \infty$:

$$\lim_{\mathrm{H}\to\infty} \nabla\overline{c} - \frac{1 - \frac{1}{\mathrm{H}}}{\alpha_1 + \frac{1-\alpha_1}{\mathrm{H}}} \overline{c} \nabla \alpha_1 = \begin{cases} \nabla\overline{c} - \frac{\overline{c}}{\alpha_1}\nabla\alpha_1 = \alpha_1 \nabla\overline{c}^1 \,, & \text{if } \alpha_1 \mathrm{H} \gg 1-\alpha_1 \\ \nabla\overline{c} - \mathrm{H}\,\overline{c}\nabla\alpha_1 \equiv 0 \,, & \text{if } \alpha_1 \equiv 0 \\ \in \big(0,\, \alpha_1 \nabla\overline{c}^1\big) & \text{else}\,. \end{cases} \tag{2.92}$$

2. case $\mathrm{H} \to 0$:

$$\lim_{\mathrm{H}\to 0} \nabla\overline{c} - \frac{1 - \frac{1}{\mathrm{H}}}{\alpha_1 + \frac{1-\alpha_1}{\mathrm{H}}} \overline{c} \nabla \alpha_1 = \begin{cases} \nabla\overline{c} + \frac{\overline{c}}{1-\alpha_1}\nabla\alpha_1 = (1-\alpha_1)\nabla\overline{c}^2 \,, & \text{if } \alpha_1 \mathrm{H} \ll 1-\alpha_1 \\ \nabla\overline{c} - \frac{\overline{c}}{\alpha_1}\nabla\alpha_1 \equiv 0 \,, & \text{if } \alpha_1 \equiv 1 \\ \in \big(0,\, (1-\alpha_1)\,\nabla\overline{c}^2\big) & \text{else}\,. \end{cases} \tag{2.93}$$

3. case $\overline{D}^1 \to 0$:

$$\lim_{\overline{D}^1 \to 0} \langle D \rangle_\mathrm{h} = \begin{cases} \overline{D}^2 & \text{if } \alpha_1 \equiv 0 \\ 0 & \text{if } \alpha_1 \overline{D}^2 \gg 0 \\ \in \left(0, \overline{D}^2\right) & \text{else}\,. \end{cases} \tag{2.94}$$

4. case $\overline{D}^2 \to 0$:

$$\lim_{\overline{D}^2 \to 0} \langle D \rangle_\mathrm{h} = \begin{cases} \overline{D}^1 & \text{if } \alpha_1 \equiv 1 \\ 0 & \text{if } (1-\alpha_1)\,\overline{D}^1 \gg 0 \\ \in \left(0, \overline{D}^1\right) & \text{else}\,. \end{cases} \tag{2.95}$$

Hence, the harmonic CST model is expected to be capable of successfully modelling each of the four limiting cases without producing artificial mass transfer, which is confirmed in test cases presented in Chapter 5.2.5. The same analysis can be performed for the arithmetic CST model.

2.4.7 Sherwood Number Calculation

To quantitatively assess the interfacial mass transfer, the global and local Sherwood numbers need to be computed from numerical results. For computation of the global Sherwood number, different possible formulations can be utilized. The simplest and in case of algebraic VOF methods most accurate way is to compute the global Sherwood number from depletion of the average concentration within the bubble over time

$$\mathrm{Sh} := \widetilde{\mathrm{Sh}_\mathrm{loc}} = \frac{1}{|S_\Sigma|} \int\limits_{S_\Sigma} \nabla c \cdot \mathbf{n}_\Sigma \frac{d_b}{c_\Sigma - c_\infty}\, dS\,, \tag{2.96}$$

$$\int\limits_{S_\Sigma} D \nabla c \cdot \mathbf{n}_\Sigma \, dS = \int\limits_{V_\mathrm{b}} \partial_t c \, dV = \partial_t \int\limits_{V_\mathrm{b}} c \, dV$$

$$\Rightarrow \mathrm{Sh} \approx \frac{1}{|S_\Sigma|} \frac{d_b}{D_\mathrm{liq}\left(c_{\mathrm{liq},\Sigma} - c_{\mathrm{liq},\infty}\right)} \partial_t \int\limits_{V_\mathrm{b}} c \, dV\,. \tag{2.97}$$

For reasons of comparability with experimental results it is important to note that experimentalists usually use the interface area of a volume-equivalent spherical bubble instead of the actual bubble area to compute the global Sherwood number or mass transfer coefficient. This is due to the fact that the real interface area can be assessed only with great difficulty in experimental results. Instead, the area of a volume-equivalent spherical bubble is used, where only the equivalent diameter needs to be estimated. Hence, when comparing to experimental results, it is important to first check, how the Sherwood numbers are computed in the experimental setup.

The calculation of local Sherwood numbers in context of algebraic VOF methods remains a difficult problem. Since no actual interface in sense of a mathematical surface per interface cell exists, the calculation of normal gradients is not suitable to compute local Sherwood numbers. The approach suggested here, which however is very noise-sensitive, is to compute all diffusive fluxes at face centres in the vicinity of the interface. These fluxes are then reconstructed on a per-cell basis to obtain cell-centred flux vector fields which are then simply weighted with the local interfacial area density, which yields

$$\mathrm{Sh}_{\mathrm{loc}} = \left[F_{f,\,\mathrm{diff}} \frac{d_b}{c_{\Sigma,\mathrm{liq}} D_{\mathrm{liq}}} \right]_{\mathrm{recon}} \cdot \mathbf{n}_\Sigma a_\Sigma \,, \tag{2.98}$$

where the face flux field $F_{f,\,\mathrm{diff}}$ is directly taken from the discretized CST model equation. In above Equation, $[\ldots]_{\mathrm{recon}}$ denotes the reconstruction algorithm as utilized in the interFoam solver

$$\left[F_f \right]_{\mathrm{recon}} = \left(\sum_f \frac{\mathbf{S}_f}{|\mathbf{S}_f|} \otimes \mathbf{S}_f \right)^{-1} \cdot \sum_f \frac{\mathbf{S}_f}{|\mathbf{S}_f|} F_f \,. \tag{2.99}$$

However, local disturbances in the concentration field introduced mainly by the advection term lead to strongly temporal and spatial varying local Sherwood profiles. To evade this problem, an algebraic advection method would have to be found which allows for the consistent advection of volumetric phase fraction and species concentration without locally changing the profiles (cf. Section 5.2.1).

For the setup of numerical simulations, it is important to get an a-priori estimate of the species concentration boundary layer thickness. Based on the definition of the local Sherwood number, it is possible to derive such an estimate:

$$\mathrm{Sh} := \overbrace{\nabla c \cdot \mathbf{n}_\Sigma \, \frac{d_b}{c_\Sigma - c_\infty}} \approx \overbrace{\frac{c_\Sigma - c_\infty}{\delta x} \, \frac{d_b}{c_\Sigma - c_\infty}} \quad \Rightarrow \quad \widetilde{\delta x} \approx \frac{d_b}{\mathrm{Sh}} \,. \tag{2.100}$$

Hence, existing correlations for the global Sherwood number can be used to a-priori estimate the boundary layer thickness using above Equation.

3 Numerical Method

This chapter is concerned with the numerical solution to partial differential equations in the context of the Finite Volume Method. The set of mathematical single-field governing equations derived in the previous chapter is transferred into algebraic equations ready for numerical solution. Aim of this work is to find a suitable discretization for the CST equation for interfacial species transfer, especially regarding the non-standard interfacial terms. A further challenge discussed in this chapter is the discretization of the advection terms regarding consistent transport of volumetric phase fraction and species concentration fields. Having derived a mathematical model in form of a set of balance equations describing the flow problem, a suitable discretization of the equation set needs to be found for the numerical calculation. The discretization transforms the partial differential equations (PDE's) into a set of (discrete) algebraic equations at specified locations (or nodes) within the continuous domain. For the numerical discretization of PDE's, many different techniques are available, each possessing certain advantages and disadvantages. In this work, the Finite Volume Method (FVM) is utilized due to its various advantages in the field of two-phase flow modelling, mainly the inherent conservation property and method robustness as well as the suitability in complex geometries by utilizing unstructured meshes of general topology.

3.1 Finite Volume Method

The FVM is based on the integral formulation of the set of balance equations. Discretizing the computational domain into *finite volumes*, different variable arrangements can be chosen where the values are stored either in the cell or face centres (Hirsch, 2007). The different choices are also known as *staggered* or *collocated* grid arrangement. On a staggered grid arrangement, scalar-valued quantities are stored in the control volume centres whereas vector- and tensor-valued quantities are typically located at the face centres. In collocated grid arrangements, all physical quantities are stored in the cell centres. The latter can introduce numerical difficulties due to an odd-even decoupling between pressure and velocity fields (Rhie and Chow, 1983). In this work, a pseudo-staggered grid arrangement is utilized, where all transported quantities are stored in the cell centres, the numerical algorithm however is based on velocity fluxes which are stored in the face centres. This arrangement allows for a momentum conservative discretization and inherently contains the interpolation correction of Rhie and Chow (1983).

Before discussing the method details, a closer look needs to be taken at the different possible definitions of finite control volumes (CV). The resulting spatial decomposition of the computational domain Ω into finite control volumes V can be structured or unstructured. In structured arrangements, every cell has two well-defined neighbours in d independent local directions in

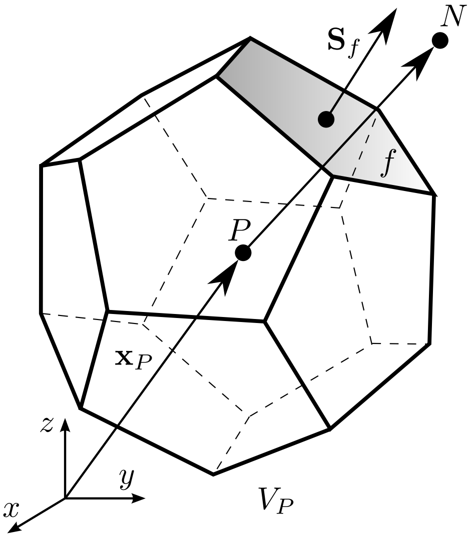

Figure 3.1.: General polyhedral control volume in unstructured meshes

$\mathbb{R}^d$ and cell addressing is achieved by incrementing a counter in every dimension. As a result, control volumes in structured meshes are limited regarding their shape to be hexahedral. Unstructured meshes allow for control volumes of more general shape. A CV can be a general polyhedron as depicted in Figure 3.1 which however must be convex. This generally complicates indexing of the cells and makes indexing based on spatial dimensions impossible. Commonly, only information about direct face-neighbouring cells is stored in unstructured meshes (as is the case in this work), which leads to the notation P for parent and N for neighbour cells. A consequence is that the discretization is usually realized using only information of face-neighbouring cells as otherwise costly search algorithms would have to be employed.

To introduce the Finite Volume Method, the starting point is the local instantaneous partial differential equation for an arbitrary transport quantity $\mathbf{\Phi}$ in single-phase flow (Equation 2.4)

$$\partial_t(\rho\mathbf{\Phi}) + \nabla\cdot(\rho\mathbf{\Phi}\mathbf{u}) = -\nabla\cdot\left(-\Gamma_{\mathbf{\Phi},d}\nabla\mathbf{\Phi}\right) + S_{\mathbf{\Phi}}(\mathbf{\Phi}) \,,$$

repeated here for convenience. The Finite Volume Method is characterized through the application of Gauss' and Leibniz' rule to the integral formulation of the balance equations. Integration over the spatially and temporally fixed control volume V and application of Gauss' and Leibniz' rules as well as the Reynolds transport theorem leads to (see Section 2.1.2)

$$\int\limits_V \underbrace{\partial_t(\rho\mathbf{\Phi})}_{\text{time derivative}}\, dV = -\oint\limits_S \underbrace{\mathbf{n}\cdot(\rho\mathbf{\Phi}\mathbf{u})}_{\text{advection term}}\, dS - \oint\limits_S \underbrace{\mathbf{n}\cdot\left(-\Gamma_{\mathbf{\Phi},d}\nabla\mathbf{\Phi}\right)}_{\text{diffusion term}} dS + \int\limits_V \underbrace{S_{\mathbf{\Phi}}(\mathbf{\Phi})}_{\text{source term}}\, dV \,. \tag{3.1}$$

The numerical treatment of the different terms in above equation within the Finite Volume framework is shown in the following. The general principle is to approximate the surface integrals in terms by the values of the transported quantity at the face centre positions and to approximate volume integrals by the cell centre values. Thus, the Finite Volume Method is at best second-order in terms of accuracy. To prove this, consider a second-order Taylor series expansion of a scalar-valued arbitrary quantity ϕ around the control volume centre position P and the face centre position f. Integration then yields for

- surface integrals:

$$\oint_S \phi \mathbf{n}\, dS = \sum_f \int_{S_f} \phi \mathbf{n}\, dS \overset{\text{sec. order}}{\approx} \sum_f \int_{S_f} \left[\phi(\mathbf{x}_f) + \left(\mathbf{x} - \mathbf{x}_f\right) \cdot \nabla\phi(\mathbf{x}_f) \right] \mathbf{n}\, dS$$
$$= \sum_f \int_{S_f} \left[\phi_f + \left(\mathbf{x} - \mathbf{x}_f\right) \cdot (\nabla\phi)_f \right] \mathbf{n}\, dS$$
$$= \sum_f \left[\int_{S_f} \phi_f \mathbf{n}\, dS + \mathbf{n} \left((\nabla\phi)_f \cdot \underbrace{\int_{S_f} \left(\mathbf{x} - \mathbf{x}_f\right) dS}_{\equiv 0} \right) \right] = \sum_f \mathbf{S}_f \phi_f \,. \tag{3.2}$$

- volume integrals:

$$\int_V \phi\, dV \overset{\text{sec. order}}{\approx} \int_V \left[\phi(\mathbf{x}_P) + (\mathbf{x} - \mathbf{x}_P) \cdot \nabla\phi(\mathbf{x}_P) \right] dV$$
$$= \int_V \phi(\mathbf{x}_P)\, dV + \nabla\phi(\mathbf{x}_P) \cdot \underbrace{\int_V (\mathbf{x} - \mathbf{x}_P)\, dV}_{\equiv 0} = \phi_P V_P \,. \tag{3.3}$$

To achieve the optimal second-order convergence, the face-interpolated quantities have to be evaluated with at least second order accuracy. On unstructured meshes of general topology this requires corrections to standard interpolation schemes as discussed later.

Depending on the employed Finite Volume Method – staggered or collocated grid arrangement – the values of different quantities are either known on the face or at cell centres. From above approximations (Equations 3.2 and 3.3) it becomes evident that quantities whose values are unknown in the specified locations have to be estimated by means of interpolation. In the Finite Volume approach employed in this work, all relevant quantities are stored in the cell centres except for the volumetric flux $F \equiv \mathbf{S}_f \cdot \mathbf{u}_f$ which is stored in the face centres. As a result, the calculation of surface integrals of the transported quantities requires the interpolation of these quantities from the cell centres to the face centres.

Due to the nature of the Finite Volume Method, the specification of maximum error bounds as frequently used e.g. in Finite Element Methods, is not possible. Instead, truncation errors of the FVM depending on the employed interpolation schemes can be studied. An analysis of truncation errors for some specific Finite Volume discretizations on unstructured meshes can be found in Jasak (1996), Juretic (2004), Juretic and Gosman (2010) and more general investigations on truncation errors are given in Turkel (1985), Roe (1987).

3.1.1 Advection Term

The advection term has a special significance in this work due to its importance to algebraic VOF methods as discussed later. It should be noted that the term *advection* is used in this thesis to describe the passive transport of a quantity by a given velocity field. This stands in contrast to the term *convection*, which is herein used to describe the transport of the momentum equation, i.e. a non-linear transport term. The advection term in Equation (3.1) can be formulated as a sum over the control volume faces as

$$\oint_S \mathbf{n}\cdot(\rho\phi\mathbf{u})\,dS \overset{\text{sec. order}}{\approx} \sum_f \mathbf{S}_f\cdot(\rho\phi\mathbf{u})_f \approx \sum_f \mathbf{S}_f\cdot(\rho\mathbf{u})_f\,\phi_f = \sum_f \rho_f F_f \phi_f\,, \tag{3.4}$$

where $\rho_f F_f \equiv \mathbf{S}_f\cdot(\rho\mathbf{u})_f$ denotes the face mass flux. Here, two approximations are made subsequently. The first approximation is the mid-point approximation introduced in Eq. (3.2). The second approximation stems from interpolation errors of the transported quantity. Only when all necessary face interpolations are at least second-order accurate, the approximation of the surface integral remains second-order. The face volumetric flux F_f is provided from the applied algorithm for pressure-velocity coupling and needs to ensure for incompressible flows in each CV

$$\int_V \nabla\cdot\mathbf{u}\,dV \overset{\text{sec. order}}{\approx} \sum_f \mathbf{S}_f\cdot(\mathbf{u})_f = \sum_f F_f \overset{!}{=} 0\,. \tag{3.5}$$

The choice of appropriate face interpolation or differencing schemes to obtain the face centre values $\mathbf{\Phi}_f$ for the advection term (also referred to as *advection schemes*) is a topic in its own and due to its importance to this work is discussed in detail in Appendix A. Advection schemes need to fulfil a series of requirements. This class of interpolation schemes needs to be accurate, bounded and numerically stable. In context of the transport of strong gradients and discontinuities, a suitable interpolation scheme is further required to be compressive, meaning that the face interpolation must minimize or counteract numerical diffusion. The accuracy of a scheme is dependent on the order of Taylor series approximation (cf. Equations 3.6 and 3.7). Achieving a certain convergence order or even a certain overall accuracy may still not be sufficient in many cases, as the transported physical quantity might have natural bounds which need to be enforced. An interpolation scheme which ensures the solution to be within the specified bounds is called a *boundedness-preserving* or simply a *bounded* scheme. In case of algebraic Volume-of-Fluid methods, the volumetric phase fraction α_1 is such an example, as it can only take values in the interval $[0, 1]$. How boundedness and a sharp field can be preserved by advection schemes is part of Appendix A.

Interpolation schemes

On unstructured meshes of general topology, interpolation schemes commonly are based on information within a small computational stencil as depicted in Figures 3.2a and 3.2b. Based on a Taylor series expansion around nodes P and N, as well as U, a multitude of different face-interpolation schemes, each with different numerical properties, can be derived. One of the most frequently used interpolation schemes, which is of second-order accuracy, is the central differences scheme. It is widely utilized in Finite Difference and Finite Volume methods but, for reasons explained in Section A, is not necessarily suited for

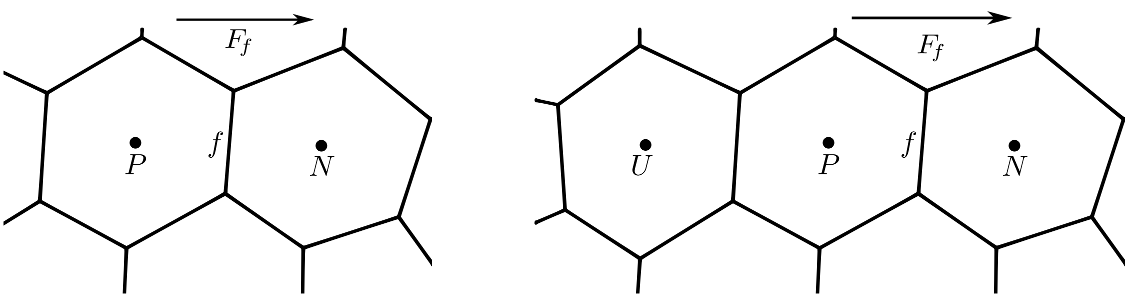

(a) Two-node stencil. **(b)** Three-node stencil.

Figure 3.2.: Interpolation stencils of face-neighbouring cells

the discretization of the advection term. The scheme utilizes a stencil only of the two face-neighbouring nodes, P and N (see Figure 3.2a). A second-order Taylor series expansion around the face centre to approximate the values at P and N reads

$$\phi_P = \phi_f - (1 - f_x) \nabla \phi_f \cdot \mathbf{d} + \mathcal{O}\left(\mathbf{d}^2\right) \tag{3.6}$$
$$\phi_N = \phi_f + f_x \nabla \phi_f \cdot \mathbf{d} + \mathcal{O}\left(\mathbf{d}^2\right) . \tag{3.7}$$

Multiplication of (3.6) with f_x and (3.7) with $(1 - f_x)$ and summation yields the central differencing interpolation scheme

$$\phi_{f\,(\mathrm{CD})} = \phi_P f_x + \phi_N (1 - f_x) , \tag{3.8}$$

with the linear interpolation factor f_x defined as

$$f_x \equiv \frac{|\mathbf{x}_f - \mathbf{x}_N|}{|\mathbf{d}|} = \frac{\overline{fN}}{\overline{PN}} . \tag{3.9}$$

The central differences scheme, due to its nature, is also frequently termed *linear interpolation*.

To implement three-point stencil interpolation schemes on unstructured meshes, the so-called *downwind weighting factor* formulation (Moukalled et al., 2015) is utilized, which explicitly lumps the upwind bias of the interpolation scheme into the interpolation weigths for nodes P and N, resulting in any three-stencil interpolation scheme to be written as

$$\phi_f = \gamma_P \phi_P + (1 - \gamma_P) \phi_N . \tag{3.10}$$

The advection schemes utilized in this Thesis, namely the CICSAM scheme (Ubbink, 1997) and the MULES advection algorithm with counter-gradient diffusion (Weller, 2006), as well as the theory behind these discretization practices is given in Appendix A.

Employing the same surface integral approximation as for the advection term, the diffusion term can be transformed into

$$\oint_S \mathbf{n}\cdot\left(\Gamma_{\phi,d}\nabla\phi\right) dS \overset{\text{sec. order}}{\approx} \sum_f \mathbf{S}_f\cdot\left(\Gamma_{\phi,d}\nabla\phi\right)_f \approx \sum_f \left(\Gamma_{\phi,d}\right)_f \mathbf{S}_f\cdot\left(\nabla\phi\right)_f \,. \tag{3.11}$$

The two face-interpolated quantities $\left(\Gamma_{\phi,d}\right)_f$ and $\mathbf{S}_f\cdot(\nabla\phi)_f$ in the above equation need further consideration. It should be noted that any stable numerical discretization requires $\left(\Gamma_{\mathbf{\Phi},d}\right)_f > 0$ (Hirsch, 2007, LeVeque, 2002). Focusing now only on a suitable discretization in context of the VOF equations, where the diffusion coefficient is a mean quantity (see Section 2.3), face interpolation in the bulk phases can be achieved by any higher-order scheme. Most commonly, diffusion coefficients in the respective bulk phases are assumed to be constant or only slightly changing anyway. The difficulty in face interpolation of $\left\langle\Gamma_{\mathbf{\Phi},d}\right\rangle$ arises at the fluid-fluid interface, where the diffusion coefficient commonly experiences a discontinuous jump over several orders of magnitude. Thus, the face interpolation of $\left\langle\Gamma_{\mathbf{\Phi},d}\right\rangle$ is bound to influence the accuracy of the numerical method. In general, it can be said that no specific best interpolation practice exists but rather that a suitable interpolation method depends on the employed numerical method. In the following, some literature examples for suitable choices of interpolation for diffusion coefficients are recalled.

Based on a one-dimensional steady heat conduction problem, Patankar (1980) showed that the correct interpolation technique for the interface conductivity (evaluated at the faces) is a parallel (or harmonic) mean. This procedure can be transferred to the viscosity interpolation in the momentum equation as shown e.g. by Kothe (1999) which leads to

$$\left\langle\mu_f\right\rangle_{\mathrm{h}} = \left(\sum_{k=1,2} \frac{(\alpha_k)_{f,CD}}{\overline{\mu}^k}\right)^{-1} , \tag{3.12}$$

where the volumetric phase fraction α is interpolated from the cell centres to the faces by central differences (CD). Kothe (1999) pointed out that a serial mean of the viscosity in some cases causes an artificial acceleration of the lighter phase, resulting in too high velocities due to an unphysical viscous term. He extended the idea of Patankar (1980) to three dimensions and based on an analysis of the stress tensor, suggests an averaging procedure taking into account the cell-face / interface orientation. In the unstructured Volume-of-Fluid method, the equations are discretized on control volumes of general polyhedral shape whose faces are denoted with f and the cell-face/interface orientation is taken into account by $\gamma_f := |\widehat{\mathbf{n}_f}\cdot\widehat{\mathbf{n}_\Sigma}|$. The averaging procedure for the mean viscosity introduced by Kothe (1999) reads

$$\left\langle\mu_f\right\rangle = \gamma_f\left\langle\mu_f\right\rangle_{\mathrm{h}} + \left(1-\gamma_f\right)\left\langle\mu_f\right\rangle_{\mathrm{a}} , \tag{3.13}$$

where the quantities $\langle \mu_f \rangle_\mathrm{h}$ and $\langle \mu_f \rangle_\mathrm{a}$ in above equation are the harmonic (or parallel) and arithmetic (or serial) mean viscosities, respectively. This approach is adopted in the present work for the estimation of face-centred viscosities and can be employed also in context of the Continuous Species Transfer Model as shown in Section 2.4.

Now consider the second term in Equation (3.11). The term $\mathbf{S}_f \cdot (\nabla\phi)_f$ represents the projection of the gradient of the transported quantity onto the face normal direction. On structured meshes, different treatments of this term are possible. In unstructured meshes as employed in the present work, the general approach is to calculate the *surface normal gradient* only from information at face neighbour points which yields

$$\mathbf{S}_f \cdot (\nabla\phi)_f = |\mathbf{S}_f| \nabla_f^\perp \phi \approx |\mathbf{S}_f| \frac{\phi_N - \phi_P}{|\mathbf{d}|}\,, \tag{3.14}$$

where $\nabla_f^\perp \phi$ denotes the *surface normal gradient*, the gradient of the transported quantity in face-normal direction.

3.1.3 Time Derivative

The treatment of the temporal term is presented last, as it requires the numerical treatment of all previous steps and completes the Finite Volume Method. Consider a time integration over an interval Δt of Equation (3.1) according to

$$\int_t^{t+\Delta t} \left[\int_V \partial_t(\rho\mathbf{\Phi})\, dV \right] dt = - \int_t^{t+\Delta t} \left[\oint_S \mathbf{n}\cdot(\rho\mathbf{\Phi}\mathbf{u})\, dS \right] dt \\ - \int_t^{t+\Delta t} \left[\oint_S \mathbf{n}\cdot\left(-\Gamma_{\mathbf{\Phi},d}\nabla\mathbf{\Phi}\right) dS \right] dt + \int_t^{t+\Delta t} \left[\int_V S_{\mathbf{\Phi}}(\mathbf{\Phi})\, dV \right] dt$$

which after spatial discretization becomes

$$\int_t^{t+\Delta t} V_P \partial_t(\rho_P \mathbf{\Phi}_P)\, dt = \int_t^{t+\Delta t} \left[-\sum_f F\mathbf{\Phi}_f + \sum_f \left(\Gamma_{\mathbf{\Phi},d}\right)_f \mathbf{S}_f \cdot \nabla\mathbf{\Phi}_f + \left(S_u V_P + S_p \mathbf{\Phi}_P V_P\right) \right] dt\,. \tag{3.15}$$

Above equation is known as the “semi-discretized form” of the generic transport equation (Hirsch, 2007). For the discretization of the temporal term (l.h.s. of Eq. (3.15)), different numerical schemes can be applied. The most common time discretization schemes which are applied in Finite Volume and Finite Difference Methods are the *explicit/implicit Euler* and the *Crank-Nicholson* scheme.

- **Explicit Euler** is a first-order accurate time discretization, where the values of $\mathbf{\Phi}$ and $\nabla\mathbf{\Phi}$ are taken from the old time step, denoted with '*o*'. The value of the transported quantity in the new time level '*n*' is then calculated from

$$\frac{\rho_P^n \mathbf{\Phi}_P^n - \rho_P^o \mathbf{\Phi}_P^o}{\Delta t} V_P = -\sum_f F^o \mathbf{\Phi}_f^o \sum_f \left(\Gamma_{\mathbf{\Phi},d}\right)_f^o \mathbf{S}_f \cdot \nabla \mathbf{\Phi}_f^o + \left(S_u V_P + S_p \mathbf{\Phi}_P^o V_P\right)$$
$$\Leftrightarrow \frac{\rho_P^n \mathbf{\Phi}_P^n - \rho_P^o \mathbf{\Phi}_P^o}{\Delta t} V_P = \mathscr{S}(t^o) \,. \qquad (3.16)$$

As can be seen, the explicit Euler discretization leads to a system of algebraic equations for $\mathbf{\Phi}_P$ which can be solved explicitly, thus the name of the scheme. From an error analysis of the time discretization it can be shown (e.g. Jasak (1996)) that the explicit Euler scheme introduces numerical anti-diffusion of the same magnitude as the first-order upwind discretization. Due to the anti-diffusion this time discretization scheme is not unconditionally stable, which results in time step limitations. For the first-order explicit Euler discretization of the advection equation, the limiting time step criterion is the well-known Courant number limit or CFL (Courant-Friedrichs-Lewis) condition

$$\mathrm{C}_f = \frac{\mathbf{u}_f \cdot \mathbf{d}}{\Delta t} \leq 1. \qquad (3.17)$$

Other explicit time step restrictions can be derived from the stability analysis of different flow problems, as e.g. the diffusion equation. In this work, the Courant number criterion poses the limiting time step restriction as discussed later.

- **Implicit Euler** is the implicit counter-part to above scheme and reads

$$\frac{\rho_P^n \mathbf{\Phi}_P^n - \rho_P^o \mathbf{\Phi}_P^o}{\Delta t} V_P = \mathscr{S}(t^n) \,, \qquad (3.18)$$

leading to a system of algebraic equations which has to be solved for the implicitly given $\mathbf{\Phi}_P$. Implicit treatment of all terms increases stability, since it adds numerical diffusion (Jasak, 1996, Juretic, 2004). The numerical diffusion of the implicit Euler scheme is of the same magnitude as the explicit Euler scheme but with positive sign (Jasak, 1996). As the explicit Euler scheme, it is of first-order accuracy. A fully implicit discretization as in Equation (3.18) leads to an unconditionally stable numerical method (Hirsch, 2007) in terms of time step restrictions.

- **Crank-Nicholson** is a second-order accurate time discretization utilizing only the current and new time levels. It can be thought of as central differences in time which reads

$$\frac{\rho_P^n \mathbf{\Phi}_P^n - \rho_P^o \mathbf{\Phi}_P^o}{\Delta t} V_P = \frac{1}{2}\left(\mathscr{S}(t^o) + \mathscr{S}(t^n)\right) . \qquad (3.19)$$

Due to the second-order accuracy, the Crank-Nicholson scheme is preferable to the Euler time discretization schemes. However, while the scheme is unconditionally stable (Hirsch, 2007), numerical issues with boundedness and solver convergence might arise (Jasak, 1996), depending on the regarded flow problem. These can be remedied by blending the Crank-Nicholson scheme with the implicit Euler scheme, which in effect adds numerical diffusion to the discretization. The blended Crank-Nicholson scheme depending on the blending factor $\gamma_{\mathrm{CN}} \in [0, 1]$

$$\begin{aligned} \frac{\rho_P^n \boldsymbol{\Phi}_P^n - \rho_P^o \boldsymbol{\Phi}_P^o}{\Delta t} V_P &= \frac{1}{2}\gamma_{\mathrm{CN}} \left[\mathscr{S}(t^o) + \mathscr{S}(t^n) \right] + (1 - \gamma_{\mathrm{CN}}) \mathscr{S}(t^n) \\ &= \frac{1}{2}\gamma_{\mathrm{CN}} \mathscr{S}(t^o) + \left(1 - \frac{1}{2}\gamma_{\mathrm{CN}}\right) \mathscr{S}(t^n) \end{aligned} \tag{3.20}$$

recovers the original scheme for $\gamma_{\mathrm{CN}} = 1$ and reduces to the Euler implicit scheme for $\gamma_{\mathrm{CN}} = 0$. The Crank-Nicholson scheme is implemented in its blended version (Eq. (3.20)) in the open source C++-library OpenFOAM®. However, for the implementation of time discretization schemes to be completely independent of spatial discretizations, the Crank-Nicholson scheme is implemented in a special way, storing time derivatives of old time steps. It was found in this study that this special implementation of the Crank Nicholson scheme in OpenFOAM® performs considerably worse in terms of boundedness compared to its original definition (Eq. (3.19) or (3.20)). Therefore, the standard Crank-Nicolson scheme is utilized in the present work.

As shown in Moukalled and Darwish (2012), the discretization of the temporal term can also be used to increase the compression of the numerical model for the transport of sharp fields by exploiting the anti-diffusion-like truncation errors of the explicit Euler scheme. Enforcing boundedness criteria analogous to the *Convection Boundedness Criterion* (see Appendix A) leads to a new class of compressible time discretization schemes. Moukalled and Darwish (2012) have shown that this new class of time discretization scheme is especially beneficial to the transport of the volumetric phase fraction in algebraic Volume-of-Fluid methods.

3.1.4 Source Term

The handling of source terms in context of the Finite Volume Method is closely related to the approximation of volume integrals as shown in Equation (3.3). Source terms are considered to be all terms which cannot be formulated as advection, diffusion or temporal terms in the respective transport equation. The source (or sink, depending on its sign) $S_{\boldsymbol{\Phi}}(\boldsymbol{\Phi})$, independent from its exact form, is therein linearized

$$S_{\boldsymbol{\Phi}}(\boldsymbol{\Phi}) \approx S_u + S_p \boldsymbol{\Phi} \quad \text{, where} \quad S_p \equiv \frac{\partial}{\partial \boldsymbol{\Phi}} \left(S_{\boldsymbol{\Phi}}(\boldsymbol{\Phi}) \right) . \tag{3.21}$$

The Finite Volume Discretization of source terms then reads

$$\int_{V_P} S_{\boldsymbol{\Phi}}(\boldsymbol{\Phi}) \, dV \overset{\text{sec. order}}{\approx} \int_{V_P} \left(S_u + S_p \boldsymbol{\Phi} \right) dV \overset{\text{sec. order}}{\approx} S_u V_P + S_p \boldsymbol{\Phi}_P V_P \, , \tag{3.22}$$

where Equation (3.3) was used to approximate the volume integrals. Generally, it is preferable to discretize the source term as implicit as possible to enhance the method's stability. As can be seen in Equation (3.22), a standard treatment would thus mean that S_u would be treated explicitly while S_p would go into the matrix to solve for $\mathbf{\Phi}_P$. However, for the matrix solvers to obtain a solution, the diagonal dominance of the matrix is very important. Therefore, it is usually advisable to treat S_p explicitly if $S_p > 0$ and implicitly if $S_p < 0$.

3.1.5 Mesh-Skewness Correction

The vast majority of available literature regarding discretization methods is considered with Cartesian meshes, where the above methods can readily be applied. On the other hand, the vast majority of industrial applications considers complex geometries, where unstructured meshes of general topology are required. Such meshes typically suffer from two types of skewness-induced errors: non-orthogonality and non-conjunctionality errors (cf. Figures 3.3 and 3.4). Discretization errors due to mesh skewness can severely deteriorate the numerical fidelity of the method resulting in loss of boundedness, accuracy and order of convergence. Consequently, the discretization practices introduced above are no longer applicable and mesh skewness correction becomes necessary.

Many skewness correction approaches have been devised for FV discretisation and are nowadays well established practice. Classical approaches are explicit and correct for non-orthogonality during discretisation of diffusion terms and non-conjunctionaly during FV discretisation of advection terms, respectively. For an overview of state-of-the-art classical approaches to skewness correction the interested reader is referred to Jasak (1996), Ferziger and Peric (2002), Moukalled et al. (2015). A non-classical explicit approach is the ghost-point method set out in Ferziger and Peric (2002), correcting for both non-conjunctionality and non-orthogonality simultaneously. However, applying classical (explicit) skewness correction approaches to the VoF advection equation on distorted meshes results directly in severe unboundedness of the volume fraction and as a consequence in substantial problems with stability and/or accuracy. The reason for this resides in the fact that due to the typically high density ratios even small errors in the volume fraction cause large errors in mass fraction and consequently in the momentum. It has been found that in such cases implicit correction approaches are needed, see Croft (1998), Zhang and Zhao (2006), Zhang and Jain (2007) and more recently Denner and van Wachem (2014, 2015). Taking interfacial species transfer into consideration renders the situation even more challenging, since there are now both the discretised advection and diffusion terms to be skewness corrected.

To overcome these problems, a suitable discretization procedure for the skewness correction of scalar-valued transport quantities has been devised in the scope of this work (Hill et al., 2018) and is briefly introduced below. For a full description of the introduced approach as well as the validation study, proving that the approach is indeed capable of retaining the convergence order from Cartesian meshes, the interested reader is referred to Hill et al. (2018).

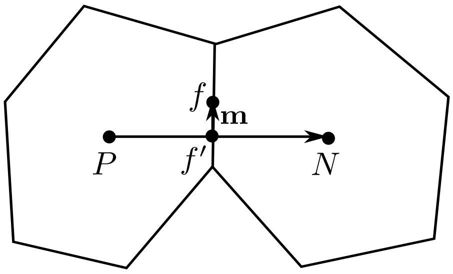

Figure 3.3.: Non-conjunctionality error at face interpolation

Advection Term

As mentioned above, the mesh quality plays a major role in the accurate discretization of advection terms. Standard interpolation procedures utilize information from interpolation stencils as shown in Figures 3.2a and 3.2b. Given the central differences scheme as example, second-order accuracy requires the face centre to be located on a line connecting both cell centre positions. If $\mathbf{d} \equiv \overline{PN} \nparallel \overline{Pf}$, mesh-induced *non-conjunctionality errors* occur (see Figure 3.3), which in effect reduce the accuracy of face integrals to first-order and introduce additional numerical diffusion (Jasak, 1996). Interpolation schemes using information from P and N will give an approximation of the value at f' which is not necessarily the face centre position. Thus, the approximation of the face integral introduces a diffusion-like error which scales with $\mathbf{m}\cdot\nabla\phi_{f'}$ (Jasak, 1996).

To account for mesh skewness, different corrections can be applied (Demirdzic and Muzaferija, 1995, Juretic and Gosman, 2010, Denner and van Wachem, 2014). The most common approach is an *explicit correction*, here shown for an arbitrary interpolation scheme with weight $\beta_{f'}$, which reads

$$\phi_f = \underbrace{\phi_P\beta_{f'} + \phi_N\left(1-\beta_{f'}\right)}_{\equiv\phi_{f'}} + \mathbf{m}\cdot\nabla\phi_{f'}\,. \tag{3.23}$$

A drawback of this approach is that boundedness of the transported variable cannot be ensured. To remedy this problem, an *implicit skewness correction* was proposed in Denner and van Wachem (2014) and Hill et al. (2018), which essentially looks like the explicit correction but lumps the correction into the weighting factors:

$$\begin{aligned}
&\phi_f = \phi_{f'} + \mathbf{m}\cdot\nabla\phi_{f'} \\
&\Leftrightarrow \phi_P\beta_f^s + \phi_N\left(1-\beta_f^s\right) = \phi_P\beta_{f'} + \phi_N\left(1-\beta_{f'}\right) + \mathbf{m}\cdot\nabla\phi_{f'} \\
&\Leftrightarrow \beta_f^s = \beta_{f'} + \frac{\mathbf{m}\cdot\nabla\phi_{f'}}{\phi_P-\phi_N}\,.
\end{aligned} \tag{3.24}$$

Boundedness is then enforced by limiting the interpolation weights using a positivity-based criterion like TVD or CBC. The corrected weighting factor β_f^s corrects the face interpolation implicitly if mesh skewness occurs ($|\mathbf{m}| > 0$), considering information from the face-neighbour cells as well as magnitude and direction of the gradient of the interpolated value. This approach is adopted in the present work.

Diffusion Term

The approximation of the surface normal gradient given in Equation (3.14) is only valid on orthogonal meshes, where the cell distance vector $\mathbf{d}$ and the face normal vector $\mathbf{S}_f$ are parallel. If $\mathbf{d} \nparallel \mathbf{S}_f$, i.e. on non-orthogonal meshes (cf. Fig. 3.4), numerical errors are introduced in Eq. (3.14). There are several possibilities to account for non-orthogonality errors which are

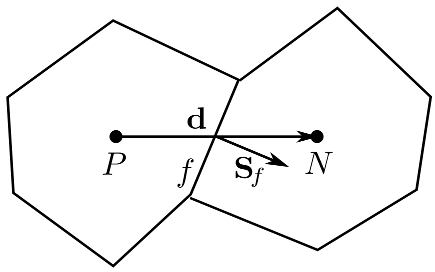

Figure 3.4.: Non-orthogonality error at face gradient computation

discussed in Jasak (1996). The basis is to split up the scalar product into two terms as

$$\mathbf{S}_f \cdot (\nabla\phi)_f = \Delta \cdot (\nabla\phi)_f + \mathbf{k} \cdot (\nabla\phi)_f \quad \text{with } \mathbf{S}_f = \Delta + \mathbf{k}, \tag{3.25}$$

where the vector Δ is chosen to be parallel to $\mathbf{d}$ and $\mathbf{k}$ can be chosen from several options, namely the minimum correction approach, orthogonal correction approach or over-relaxed approach (Jasak, 1996). The latter is the standard correction approach utilized within the OpenFOAM®-library and reads

$$\Delta = \frac{\mathbf{d}}{\mathbf{d} \cdot \mathbf{S}_f} |\mathbf{S}_f|^2 \quad \Rightarrow \quad \mathbf{k} = \mathbf{S}_f - \frac{\mathbf{d}}{\mathbf{d} \cdot \mathbf{S}_f} |\mathbf{S}_f|^2 . \tag{3.26}$$

It should be noted that the diffusion term in its discretized form of (3.25) only exhibits boundedness on orthogonal meshes. The non-orthogonal correction may therefore introduce unboundedness. If boundedness of the transported quantity is of major importance to the underlying algorithm, the non-orthogonal correction needs to be limited or completely omitted. A suitable limiting criterion must be based on the stability and boundedness criterion for diffusion equations, namely, that the diffusive transport needs to be always directed in the direction of the gradient. This requires a positive diffusion coefficient and that the numerical exact gradient and the approximated discretized gradient have the same direction. On strongly distorted meshes, this might depend on the choice of the applied non-orthogonal correction approach as well as the employed gradient scheme. If a suitable limiting criterion can be derived, the non-orthogonal correction could be implemented implicitly analogous to the skewness correction (see Hill et al. (2018)).

On general unstructured mesh topologies, both errors occur simultaneously and can both be accounted for. As can be seen in Equation (3.25), the non-orthogonality correction depends on the gradient at the face centre position. This gradient needs to be interpolated from the neighbouring cell centres, where again the mesh skewness error occurs. Unfortunately, to compute the cell-centred gradient of a quantity, e.g. using Gauss' theorem, one needs to know the face-centred values. Thus, when wanting to correct for both errors, a loop is produced. This is emphasized in Equation system (3.27)

$$\begin{aligned} \mathbf{S}_f \cdot (\nabla\phi)_f &= |\Delta| \nabla_f^{\perp} \phi + \mathbf{k} \cdot (\nabla\phi)_f \\ \nabla\phi &= \frac{1}{|V|} \sum_f \phi_f \mathbf{S}_f \\ \phi_f &= \phi_{f'} + \mathbf{m} \cdot (\nabla\phi)_f \ . \end{aligned} \tag{3.27}$$

There are several ways to overcome this problem. Croft (1998) and Zhang and Zhao (2006) introduced iterative methods, essentially solving above equations in a loop which is very costly. A much easier and nonetheless accurate approach is to use a different gradient scheme as the (implicit) least-squares scheme introduced in Zhang and Jain (2007). Their proposed gradient scheme is available as an explicit scheme within the OpenFOAM® library and is utilized for all mesh error corrections in scope of this work. Ferziger and Peric (2002) proposed ghost point-based schemes, a different class of interpolation schemes which can be seen as an alternative that also inherently corrects for non-orthogonality and skewness errors simultaneously.

An alternative approach to account for both mesh-induced errors simultaneously is devised in scope of this work (Hill et al., 2018). In a first step the non-conjunctional corrected gradient of the transported variable ϕ analogous to Equation (3.23) is obtained:

$$\mathbf{S}_f \cdot (\nabla\phi)_f = \mathbf{S}_f \cdot \left[(\nabla\phi)_{f'} + \nabla(\nabla\phi)_{f'} \cdot \mathbf{m} \right] .$$

Using Equation (3.25) to discretise $\mathbf{S}_f \cdot (\nabla\phi)_{f'}$ finally yields:

$$\begin{aligned} \mathbf{S}_f \cdot (\nabla\phi)_f &= \Delta \cdot (\nabla\phi)_{f'} + \mathbf{k} \cdot (\nabla\phi)_{f'} + \mathbf{S}_\mathbf{f} \cdot \left[\nabla (\nabla\phi)_{f'} \cdot \mathbf{m} \right] \\ &= |\Delta| \frac{\phi_N - \phi_P}{|\mathbf{d}|} + \mathbf{k} \cdot (\nabla\phi)_{f'} + \mathbf{S}_\mathbf{f} \cdot \left[\nabla (\nabla\phi)_{f'} \cdot \mathbf{m} \right] . \end{aligned} \tag{3.28}$$

Analogously to the approach previously introduced for advection terms, the above discretisation of the diffusive term can also be rearranged in a way that allows for implicit bounding. This is done by rearranging Equation (3.28) to formally correspond to the uncorrected discretisation of the diffusive term (cf. Equation 3.14):

$$\left(\Gamma_\phi\right)_f \mathbf{S}_f \cdot (\nabla\phi)_f \stackrel{!}{=} \left(\Gamma_\phi\right)_{f,m} |\mathbf{S}_f| \frac{\phi_N - \phi_P}{|\mathbf{d}|} . \tag{3.29}$$

Comparing Equation (3.29) with Equation (3.14) reveals that the diffusive coefficient $\left(\Gamma_\phi\right)_{f,m}$ has to be defined as

$$\left(\Gamma_\phi\right)_{f,m} = \frac{\left(\Gamma_\phi\right)_f |\mathbf{d}|}{|\mathbf{S}_f|} \left[\frac{|\Delta|}{|\mathbf{d}|} + \frac{\mathbf{k} \cdot (\nabla\phi)_{f'}}{\phi_N - \phi_P} + \frac{\mathbf{S}_f \cdot \left[\nabla (\nabla\phi)_{f'} \cdot \mathbf{m} \right]}{\phi_N - \phi_P} \right] . \tag{3.30}$$

This formulation now enables the implicit application of limiting criteria to the diffusive coefficient $\left(\Gamma_\phi\right)_{f,m}$, which in turn contains the explicit correction.

After the discussion of suitable discretization practices for the advection and diffusion terms as well as the time derivative, the concrete discretization applied in this work is outlined. As the major focus of this work is the numerical study of species transfer in two-phase flows, two important foci are the consistent advection and the handling of interfacial terms appearing in the CST model (Equations 2.74, 2.86 and 2.89).

3.2.1 Volume-of-Fluid Transport Equation

One major challenge for the direct numerical simulation of two phase flows employing the VOF method is the transport of the phase indicator or volumetric phase fraction field. While the first, i.e. the evolution of a discontinuous step function, has to be typically accomplished by means of geometrical transport algorithms, the latter i.e. a smooth yet sharp phase fraction field is commonly advected by algebraic methods. In both cases the VOF advection algorithm needs to be sufficiently accurate, maintain a bounded solution and ensure a sharp interface representation. In this work, an algebraic advection approach is employed, meaning that the volumetric phase fraction α is transported directly by discretizing and solving the underlying advection equation, which reads

$$\partial_t \alpha_1 + \mathbf{u} \cdot \nabla \alpha_1 = 0 \quad \text{in } \Omega \,. \tag{3.31}$$

To maintain a bounded solution, the form of Equation (3.31) is not very suited. Utilizing the solenoidal condition of a divergence-free velocity field ($\nabla \cdot \mathbf{u} \equiv 0$), the Equation can be re-written into a conservative form,

$$\partial_t \alpha_1 + \nabla \cdot (\alpha_1 \mathbf{u}) = 0 \quad \text{in } \Omega \,. \tag{3.32}$$

This form of the VOF advection equation has two major advantages over (3.31): it allows for a conservative discretization and is generally suited to preserve boundedness, since in the limit (cf. Weller (2006))

$$\nabla \cdot (\alpha_1 \mathbf{u}) \xrightarrow{\alpha_1 \to 1} 0 \qquad \text{since } \nabla \cdot \mathbf{u} \equiv 0 \tag{3.33}$$

$$\nabla \cdot (\alpha_1 \mathbf{u}) \xrightarrow{\alpha_1 \to 0} 0 \qquad \text{by definition/construction} \,. \tag{3.34}$$

Discretizing Equation (3.32) under the restrictions of accuracy, boundedness and sharpness of the transported field is the most challenging scenario for algebraic methods and necessitates the development of specialized interpolation schemes (Zalesak, 1979, Harten, 1983, Leonard, 1991, Ubbink, 1997, Muzaferija et al., 1999) and/or artificial compression or counter-gradient diffusion algorithms (Olsson and Kreiss, 2005, Weller, 2006, So et al., 2011). To obtain a bounded advective transport algorithm, two different approaches are possible: One can either enforce *universal a-priori* boundedness criteria as the *positivity*, *Total Variation Diminishing*

(TVD), *Convection Boundedness Criterion (CBC)* and *Local Extrema Diminishing* onto the employed face interpolation, or utilize a *Flux Corrected Transport (FCT)* algorithm to *locally* adjust computed fluxes. Detailed information about boundedness criteria, interpolation schemes and FCT algorithms is given in Appendix A.

The available interFoam solver utilizes an advection approach by Weller (2006), employing an artificial counter-gradient compression term in the phase fraction transport equation to maintain a sharp interface representation (cf. Appendix A.6). However, this approach introduces artificial deformation and surface wave structures (cf. Appendix D.3). The reason for this behaviour lies within the artificial term which requires the interface normal as direction for the compression. Thus, the accuracy of normal vector calculation will strongly influence the advection. However, even with improved normal calculations, artificial field deformations cannot be avoided.

Based on an extensive literature survey and the background of discretization boundedness criteria, the best choice of interpolation schemes for the problems studied here is the CICSAM scheme of Ubbink (1997), which is therefore employed in this work. Unlike algorithms employing an artificial compression term, the anti-diffusion produced by the CICSAM scheme (and other important Interface Capturing Schemes) scales anti-proportional to the local Courant number. In effect, sharpness of the transported field is only preserved for sufficiently small Courant numbers, typically, $C_f < 0.1$.

However, Interface Capturing Schemes exhibit another very important condition, which schemes relying on artificial compression lack: They enable the consistent transport for volumetric phase fraction and temperature field or species concentration (Darwish and Moukalled, 2003) which minimizes artificial mass transfer and therefore is highly relevant for the simulation of interfacial heat or mass transfer. Details about the employed advection algorithm for the species concentration fields are given in Chapter 3.2.3. Some discussion about artificial mass transfer is given in Chapter 3.2.4 and numerical results of consistent advection are presented in Chapter 5.2.1. To emphasize the importance of the advection algorithm, note that the introduced errors of (species) advection are the leading errors in the presented numerical study of interfacial mass transfer from rising bubbles.

The discretization discussed here is the method implemented in the interFoam solver. However, the transport equation for the volumetric phase-fraction is discretized using the CICSAM scheme rather than the original discretization practice introduced by Weller (2006), who introduces a counter-gradient diffusion term and the MULES FCT algorithm (cf. Appendix A.6). The discretized phase-fraction advection equation then reads:

$$[\![\partial_t[\alpha_1]]\!] + \left[\!\!\left[\nabla\cdot\left(\mathbf{u}[\alpha_1]_{f(\text{CICSAM},F_f,\gamma)}\right)\right]\!\!\right] = 0 \,, \tag{3.35}$$

where the double square brackets $[\![\cdot]\!]$ indicate a term being discretized implicitly with respect to the transport quantity denoted in single square brackets (Weller, 2005a). This notation is not to be confused with jump brackets in the continuum modelling part of this thesis. To verify the choice of using Interface Capturing Schemes within this work, different advection methods are compared regarding consistent advection in Chapter 5.2.1.

In this work, the PISO algorithm is utilized to handle the pressure-velocity coupling, where the full momentum equation is only used as a momentum predictor. The left-hand side and the diffusion term in Eq. (2.52) are discretized in a standard way whereas the additional force terms on the r.h.s. are reconstructed from a flux field:

$$\begin{aligned} &[\![\partial_t(\rho[\mathbf{u}])]\!] + \left[\!\!\left[\nabla\cdot\left(F_\rho[\mathbf{u}]\right)\right]\!\!\right] - [\![\nabla\cdot(\mu_{\text{eff}}\nabla[\mathbf{u}])]\!] - \nabla\mathbf{u} :\, \nabla\mu_{\text{eff}} = \\ &[\sigma\kappa\nabla\alpha_1 - (\mathbf{g}\cdot\mathbf{x})\nabla\rho - \nabla p]_{\text{recon}} \,, \end{aligned} \tag{3.36}$$

where the reconstructed r.h.s. of above Equation reads

$$\begin{aligned} &[\sigma\kappa\nabla\alpha_1 - (\mathbf{g}\cdot\mathbf{x})\nabla\rho - \nabla p]_{\text{recon}} = \\ &\left(\sum_f \frac{\mathbf{S}_f \otimes \mathbf{S}_f}{|\mathbf{S}_f|}\right)^{-1} \cdot \sum_f \frac{\mathbf{S}_f}{|\mathbf{S}_f|}\left[(\sigma\kappa)_f\,\nabla_f^{\perp}\alpha_1 - (\mathbf{g}\cdot\mathbf{x})_f\,\nabla_f^{\perp}\rho - \nabla_f^{\perp}p\right]|\mathbf{S}_f|\,. \end{aligned} \tag{3.37}$$

The mass flux F_ρ is herein consistently computed from the phase fraction transport flux

$$F_\rho = \alpha_{1f(\text{CICSAM})}\left(\overline{\rho}^1 - \overline{\rho}^2\right)F + \overline{\rho}^2 F\,. \tag{3.38}$$

The reconstruction algorithm is used to construct a cell-centred vector field from a given face flux field. This needs to be done since the interFoam solution algorithm is flux-based, meaning that it is solved for the face fluxes $F := \mathbf{u}_f \cdot \mathbf{S}_f$ rather than the cell-centred velocities $\mathbf{u}_P$ which are, as stated above, only used in the momentum predictor step. Details about the employed pressure-velocity coupling can be found, e.g., in Ubbink (1997) and Rusche (2002).

3.2.3 Continuous Species Transfer Method

Finite Volume discretization of the derived single-field CST model needs special attention due to the additional interfacial terms and the advection term. The discretization of the CST interfacial species flux terms is demanding and of crucial importance. It will be shown, however, that the correct discretization procedure is guided by the derivation of the CST model. To motivate and outline the utilized discretization procedure, let us consider the CST single-field formulation using a harmonic mean diffusion coefficient (Eq. (2.86)), which is repeated here for convenience

$$\partial_t\,\overline{c} + \nabla\cdot(\overline{c}\,\overline{\mathbf{u}}) = \nabla\cdot(\langle D\rangle_{\text{h}}\nabla\overline{c}) - \nabla\cdot\left(\langle D\rangle_{\text{h}}\frac{1-\frac{1}{\text{H}}}{\alpha_1 + \frac{1-\alpha_1}{\text{H}}}\nabla\alpha_1\,\overline{c}\right)\,.$$

On the r.h.s., it can be seen that the diffusion process over the interface is split into a Laplacian term and a divergence term for the mixture concentration $\overline{c}$. This poses a problem, since up to this point it is not clear how a divergence term needs to be discretized to appropriately mimic a diffusive process on the discrete level.

Let us first consider a standard FVM discretization procedure. The general FVM discretization practice for Laplacian terms reads (on orthogonal meshes)

$$\int_{V_p} \nabla\cdot\left(\Gamma_\phi \nabla\phi\right) dV \approx \sum_f \left(\Gamma_\phi\right)_f (\nabla\phi)_f \cdot \mathbf{S}_f = \sum_f \left(\Gamma_\phi\right)_f \frac{\phi_N - \phi_P}{|\mathbf{d}_{PN}|} |\mathbf{S}_f| \tag{3.39}$$

and for divergence terms

$$\int_{V_p} \nabla\cdot(\phi \mathbf{u})\, dV \approx \sum_f (\phi)_f\, \mathbf{S}_f \cdot (\mathbf{u})_f \ , \tag{3.40}$$

where P and N denote the centre of a polyhedral cell and its neighbour, respectively (cf. Fig. 3.1). With this, a fully implicit standard FV discretization for the CST single-field equation reads in FV notation (Weller, 2005a, Marschall et al., 2012)

$$\begin{aligned} [\![\partial_t([\,\overline{c}\,])]\!] + \left[\!\!\left[\nabla\cdot\left(F[\,\overline{c}\,]_{f(F,\mathrm{CICSAM},\gamma_f)}\right)\right]\!\!\right] = \left[\!\!\left[\nabla\cdot\left((\langle D\rangle_{\mathrm{h}})_f\, \nabla[\,\overline{c}\,]\right)\right]\!\!\right] \\ - \left[\!\!\left[\nabla\cdot\left(\left((\langle D\rangle_{\mathrm{h}})_f \left(\frac{1-\frac{1}{\mathrm{H}}}{\alpha_1 + \frac{1-\alpha_1}{\mathrm{H}}}\right)_{f(S,\gamma)} \nabla_f^{\perp}\alpha_1\right)[\,\overline{c}\,]_{f(S,\gamma)}\right)\right]\!\!\right] . \end{aligned} \tag{3.41}$$

In (3.41), $\nabla_f^{\perp}\alpha_1$ denotes the gradient of α_1 in the face normal direction, i.e. on orthogonal meshes

$$\nabla_f^{\perp}\alpha_1 \equiv \mathbf{S}_f \cdot \nabla_f \alpha_1 \approx \frac{\alpha_N - \alpha_P}{|\mathbf{d}_{PN}|} |\mathbf{S}_f| \, . \tag{3.42}$$

The face interpolation of the harmonic mean diffusion coefficient is done according to Eq. (3.12)

$$(\langle D\rangle_{\mathrm{h}})_f = \left(\sum_{k=1,2} \frac{(\alpha_k)_{f,CD}}{\overline{D}^k}\right)^{-1} . \tag{3.43}$$

To be able to implement and solve Equation (3.41), one needs to find a consistent interpolation scheme 'S' with parameter γ which would allow us to mimic the diffusion process over the interface via above divergence term. The key point here is to reconsider the unclosed harmonic CST Model, Eq. (2.85), and recall that the term in question results from the application of the closure assumption (2.68). This term must therefore be discretized in a way such that

$$\left(1 - \frac{1}{\mathrm{H}}\right) \frac{(\overline{c})_{f(S,\gamma)}}{\left(\alpha_1 + \frac{1-\alpha_1}{\mathrm{H}}\right)_{f(S,\gamma)}} \approx \left(\overline{c}^1 - \overline{c}^2\right)_{f(S,\gamma)} \tag{3.44}$$

also is valid in a discrete sense for face-interpolated values. The splitting of the face interpolation on the l.h.s. into numerator and denominator is done in order to achieve a form suitable for time-implicit discretization. To clarify, above equation is only shown to emphasize the discretization idea. Obviously, the r.h.s. term is unclosed and cannot be discretized. Assuming one would attempt to discretize the r.h.s. term, a proper choice in terms of accuracy would be a second-order central differencing scheme, which for non-uniform mesh size at the interface yields

$$\left(\bar{c}^1-\bar{c}^2\right)_{f(S,\gamma)}=\omega_{\mathrm{CD}}\left[\left(\bar{c}^1\right)_P-\left(\bar{c}^2\right)_P\right]+\left(1-\omega_{\mathrm{CD}}\right)\left[\left(\bar{c}^1\right)_N-\left(\bar{c}^2\right)_N\right]. \tag{3.45}$$

Consequently, a consistent discretization procedure (that allows for time-implicit discretization) for above term with a special (a priori unknown) discretization scheme S', which is employed in the present work, reads (on non-equidistant meshes)

$$\begin{aligned}\left(1-\frac{1}{\mathrm{H}}\right)\frac{(\bar{c})_{f(S',\gamma)}}{\left(\alpha_1+\frac{1-\alpha_1}{\mathrm{H}}\right)_{f(S',\gamma)}}=\left(1-\frac{1}{\mathrm{H}}\right)\Bigg[&\omega_{\mathrm{CD}}\frac{(\bar{c})_{f(F_l,\mathrm{UD})}}{\left(\alpha_1+\frac{1-\alpha_1}{\mathrm{H}}\right)_{f(F_l,\mathrm{UD})}}\\&+\left(1-\omega_{\mathrm{CD}}\right)\frac{(\bar{c})_{f(F_l,\mathrm{DD})}}{\left(\alpha_1+\frac{1-\alpha_1}{\mathrm{H}}\right)_{f(F_l,\mathrm{DD})}}\Bigg],\end{aligned} \tag{3.46}$$

where UD and DD denote the upwind and downwind discretization based on a flux F_l respectively. In above discretization, it was assumed that the upwind cell is the parent cell "P". Otherwise, the weighting factors would need to be switched. The flux F_l can be chosen arbitrarily as it is only needed to distinguish between a face parent and neighbour cell on unstructured meshes. Further, it was argued by Haroun et al. (2010) that a discretization of a single-field model for an advection-diffusion equation should fulfil one condition: in a steady-state case without convection, the interfacial flux term should exactly balance the diffusion term, which reads for Eq. (2.86):

$$\nabla\cdot\left(\langle D\rangle_{\mathrm{h}}\nabla\bar{c}\right)-\nabla\cdot\left(\langle D\rangle_{\mathrm{h}}\frac{1-\frac{1}{\mathrm{H}}}{\alpha_1+\frac{1-\alpha_1}{\mathrm{H}}}\bar{c}\nabla\alpha_1\right)\overset{!}{=}0. \tag{3.47}$$

It can be proven that this condition is fulfilled for the derived single-field CST Equations (2.74), (2.86) and (2.89) when using the presented discretization procedure.

For the harmonic CST model, the discretization of the r.h.s. terms (on a uniform mesh) reads

$$\begin{aligned}&\sum_f\left(\langle D\rangle_{\mathrm{h}}\right)_f|\mathbf{S}_f|\left[\nabla_f^{\perp}\bar{c}-\left(\frac{1-\frac{1}{\mathrm{H}}}{\alpha_1+\frac{1-\alpha_1}{\mathrm{H}}}\bar{c}\right)_{f(S',\gamma)}\nabla_f^{\perp}\alpha_1\right]\\&=\sum_f\left(\langle D\rangle_{\mathrm{h}}\right)_f|\mathbf{S}_f|\left[\frac{\bar{c}_N-\bar{c}_P}{|\mathbf{d}_{PN}|}-\frac{1}{2}\left(1-\frac{1}{\mathrm{H}}\right)\left(\frac{\bar{c}_N}{\alpha_{1,N}+\frac{1-\alpha_{1,N}}{\mathrm{H}}}-\frac{\bar{c}_P}{\alpha_{1,P}+\frac{1-\alpha_{1,P}}{\mathrm{H}}}\right)\frac{\alpha_{1,N}-\alpha_{1,P}}{|\mathbf{d}_{PN}|}\right].\end{aligned} \tag{3.48}$$

To show that this discretization practice is indeed suitable, the steady-state case in absence of advection is studied. Denoting the phase fraction-dependent terms with

$$\gamma_N \equiv \alpha_{1,N} + \frac{1-\alpha_{1,N}}{\mathrm{H}} \quad \text{, and} \quad \gamma_P \equiv \alpha_{1,P} + \frac{1-\alpha_{1,P}}{\mathrm{H}} \ ,$$

the discretization practice yields

$$\begin{aligned}
&\sum_f (\langle D\rangle_\mathrm{h})_f \frac{|\mathbf{S}_f|}{|\mathbf{d}_{PN}|}\left[(\bar{c}_N - \bar{c}_P) - \frac{1}{2}(\gamma_N - \gamma_P)\left(\frac{\bar{c}_N}{\gamma_N} + \frac{\bar{c}_P}{\gamma_P}\right)\right] \\
=&\sum_f (\langle D\rangle_\mathrm{h})_f \frac{|\mathbf{S}_f|}{|\mathbf{d}_{PN}|}\frac{1}{2}\frac{\gamma_N+\gamma_P}{\gamma_N\gamma_P}\left[\gamma_P\,\bar{c}_N - \gamma_N\,\bar{c}_P\right] \stackrel{!}{=} 0 \, .
\end{aligned} \tag{3.49}$$

In case of a one-dimensional steady-state diffusion, the analytical solution is a linear concentration profile in both phases with a concentration jump over the interface. Thus, the transported species concentration flux is a constant in the whole domain. From Eq. (3.49), it is easy to see that a linear concentration profile is the numerical exact solution in the bulk phases.

An alternative discretization method was suggested by Haroun (2008). The term in question can also be discretized, using central differences in the numerator and denominator separately

$$\left(\bar{c}^1 - \bar{c}^2\right)_f \approx \left(1 - \frac{1}{\mathrm{H}}\right)\left(\frac{\bar{c}}{\alpha_1 + \frac{1-\alpha_1}{\mathrm{H}}}\right)_f = \left(1-\frac{1}{\mathrm{H}}\right)\frac{\frac{\bar{c}_P+\bar{c}_N}{2}}{\frac{\alpha_{1,P}+\alpha_{1,N}}{2} + \frac{1-\frac{\alpha_{1,P}+\alpha_{1,N}}{2}}{\mathrm{H}}} \, . \tag{3.50}$$

This, however, is not a second-order approximation to the original unclosed equation. In the case of steady-state one-dimensional diffusion, this discretization yields

$$\begin{aligned}
&\sum_f (\langle D\rangle_\mathrm{h})_f \frac{|\mathbf{S}_f|}{|\mathbf{d}_{PN}|}\left[(\bar{c}_N - \bar{c}_P) - \frac{\left(1-\frac{1}{\mathrm{H}}\right)\frac{\bar{c}_P+\bar{c}_N}{2}}{\frac{\alpha_{1,P}+\alpha_{1,N}}{2}\left(1-\frac{1}{\mathrm{H}}\right)+\frac{1}{\mathrm{H}}}\left(\alpha_{1,N}-\alpha_{1,P}\right)\right] \\
=&\sum_f (\langle D\rangle_\mathrm{h})_f \frac{|\mathbf{S}_f|}{|\mathbf{d}_{PN}|}\frac{2}{\gamma_N+\gamma_P}\left(\gamma_P\,\bar{c}_N - \gamma_N\,\bar{c}_P\right) \, .
\end{aligned} \tag{3.51}$$

This discretization practice also obviously yields a linear concentration profile in the bulk phases for the one-dimensional steady-state diffusion problem.

When the concentration profiles in both phases are constant, the discretization practices Eq. (3.49) and Eq. (3.51) both ensure that the face fluxes are exactly zero, also in interface cells. Given the discretization stencil in Figure 3.5, the discretization can be simplified by using

$$\begin{aligned}
&\alpha_U = \gamma_U = 1\,, \quad \alpha_P = \alpha, \ \gamma_P = \alpha + \frac{1-\alpha}{\mathrm{H}}, \quad \alpha_N = 0, \ \gamma_N = \frac{1}{\mathrm{H}}, \\
&\overline{c_U} = \overline{c_U}^1 = c_\mathrm{gas}\,, \quad \overline{c_P}^1 = \frac{\overline{c_P}}{\gamma_P} = c_\mathrm{gas}\,, \quad \overline{c_P}^2 = \frac{\overline{c_P}}{\mathrm{H}\gamma_P} = c_\mathrm{liq} = \frac{c_\mathrm{gas}}{\mathrm{H}}\,, \quad \overline{c_N} = \overline{c_N}^2 = c_\mathrm{liq} = \frac{c_\mathrm{gas}}{\mathrm{H}}
\end{aligned}$$

which leads to

$$
\begin{aligned}
(\gamma_P\,\overline{c_U}-\gamma_U\,\overline{c_P}) &= \gamma_P\,\overline{c_U}^1-\gamma_P\,\overline{c_P}^1=\gamma_P\left(c_{\text{gas}}-\overline{c_P}^1\right)\equiv 0\\
(\gamma_N\,\overline{c_P}-\gamma_P\,\overline{c_N}) &= \frac{1}{\mathrm{H}}\,\overline{c_P}^2\mathrm{H}\,\gamma_P-\gamma_P\,\overline{c_N}^2=\gamma_P\left(\overline{c_P}^2-c_{\text{liq}}\right)\equiv 0\;.
\end{aligned}
\tag{3.52}
$$

This shows that the discretization practices introduced in Equation (3.46) and (3.50) are indeed suitable.

The discretization practice for the CST model using arithmetic mean diffusion coefficient (Marschall et al., 2012, Deising et al., 2016) is based on above discretization practice and can be derived accordingly, leading to the discretized form of the Continuous Species Transfer (CST) model, which then reads

$$
\begin{aligned}
&[\![\partial_t\,([\,\bar{c}\,])]\!]+\left[\!\!\left[\nabla\cdot\left(F[\,\bar{c}\,]_{f(F,\text{CICSAM},\gamma_f)}\right)\right]\!\!\right]=[\![\nabla\cdot\left((\langle D\rangle)_f\,\nabla[\,\bar{c}\,]\right)]\!]\\
&-\left[\!\!\left[\nabla\cdot\left(\gamma_f\,(\langle D\rangle_{\mathrm{h}})_f\,\frac{1-\frac{1}{\mathrm{H}}}{\left(\alpha_1+\frac{1-\alpha_1}{\mathrm{H}}\right)_{f(F_l,S')}}\,\nabla_f^{\perp}\alpha_1[\,\bar{c}\,]_{f(F_l,S')}\right)\right]\!\!\right]\\
&+\left[\!\!\left[\nabla\cdot\left(\left(1-\gamma_f\right)\left(\overline{D}^1-\overline{D}^2\right)(\alpha_1)_{f(CD)}\left(\frac{1}{\left(\alpha_1+\frac{1-\alpha_1}{\mathrm{H}}\right)_{f(CD)}}-1\right)\nabla[\,\bar{c}\,]\right)\right]\!\!\right]\\
&+\left[\!\!\left[\nabla\cdot\left(\left(1-\gamma_f\right)\frac{1}{\left(\alpha_1+\frac{1-\alpha_1}{\mathrm{H}}\right)_{f(F_l,S')}}\left(\frac{1}{\mathrm{H}}\frac{\overline{D}^1-\overline{D}^2}{\left(\alpha_1+\frac{1-\alpha_1}{\mathrm{H}}\right)_{f(CD)}}-\left(\overline{D}^1-\frac{\overline{D}^2}{\mathrm{H}}\right)\right)\nabla_f^{\perp}\alpha_1[\,\bar{c}\,]_{f(F_l,S')}\right)\right]\!\!\right],
\end{aligned}
\tag{3.53}
$$

with the scheme S' shown in Equation (3.46).

3.2.4 Addressing Artificial Mass Transfer

In two-phase flow systems with species transfer over a fluid-fluid interface, two different sources of artificial species transfer can arise when employing an algebraic VOF method. First, the employed advection algorithm might not be able to maintain a sharp interface, resulting in an artificial transfer of species over the interface as a result of numerical diffusion. Second, due to a difference in the advection of phase fraction and species concentration fields.

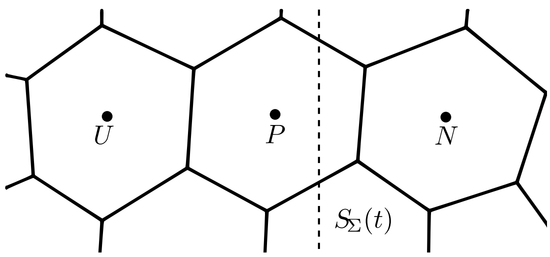

Figure 3.5.: Discretization in interface cell

The first source of artificial species transfer can be prevented by employing compressive interpolation schemes like the CICSAM scheme and sufficiently small time steps (i.e. moderate Courant numbers). As a result, standard TVD schemes are not very suitable due to the limited amount of downwinding compared to the transient CBC criterion and the resulting Interface Capturing Scheme CICSAM. Ubbink (1997) reported in his Taylor bubble simulations about smearing of the interface especially in the rear of bubbles where small parts of the phase fraction field can separate from the interface and be transported downstream due to the lack of local compression. In simulations which are concerned only with the hydrodynamics, this smearing of the interface might have only a negligible effect on the solution. When simulating additional species transfer at realistic Henry numbers (e.g. $\mathrm{H}_i \approx 30$ for oxygen dissolving in water), this smearing due to numerical diffusion can be of the same order or even higher than the species concentrations at the liquid side of the bubble interface, which results in an over-prediction of the transferred species.

Regarding the second source of artificial species transfer, Darwish and Moukalled (2003) present a class of advection schemes for interface capturing techniques called χ-Schemes, which are derived to allow for consistent advection. They show that a consistent advection is given when using the same interpolation weights for the advection terms of all transported quantities and that all linear schemes fulfil this criterion. Hence, a non-linear High Resolution Scheme is rewritten as a combination of the first-order upwind scheme with a higher-order (HO) scheme:

$$\widetilde{\phi}_{f,HR} = \widetilde{\phi}_C + \chi\left(\widetilde{\phi}_{f,HO} - \widetilde{\phi}_C\right) . \tag{3.54}$$

From (3.54) it is clear that forcing all related equations to share the same value of χ in each control volume ensures consistency. As boundedness needs to be preserved for all transported quantities ϕ_i, the limiter χ is chosen to be the minimum over all χ_i ($\chi = \min(\chi_i)$). While this method ensures consistency, it also introduces additional numerical diffusion compared to the original High Resolution Scheme and thus χ-schemes are not well-suited in the present case. However, Darwish and Moukalled (2003) also showed that the inconsistency due to advection using normalised variable formulation (NVF) schemes is still acceptable.

The major drawback of using a very compressive discretization scheme as CICSAM is that, while maintaining a consistent advection, the concentration gradient at the interface is steepened by the advection scheme, i.e. species is compressed back from the liquid-sided bulk into the interface. Thus, instead of creating numerical diffusion, one adds numerical anti-diffusion to the species transfer at the interface. Optimally, a discretization practice could be found which cancels numerical diffusion without creating anti-diffusion. However, a fully consistent advection is only possible within a two-field approach, which requires an ideally sharp (interface in one cell) volume fraction field, as well as the geometric reconstruction of an interface.

To maintain a consistent advection and minimize artificial anti-diffusion, the CICSAM scheme is used in a blended manner for the advection of phase fraction and species concentration fields. The introduced blending strategy allows using the full CICSAM scheme only in a narrow band around the interface and switching to the Ultimate-Quickest scheme (i.e. the base scheme of CICSAM) in the bulk phases. The narrow band around the interface in which the CICSAM scheme is utilized is herein found as all faces where

$$|\alpha_{1,P} - \alpha_{1,N}| \geq \delta_\alpha \,, \tag{3.55}$$

given a user-defined threshold δ_α (default: $\delta_\alpha = 0.03$).

4 Solution Algorithm and Implementation

The employed two-phase solver is based on the interFoam solver but contains a series of enhancements and additions which are discussed in this chapter. To briefly introduce the utilized interFoam solver, some comments are given here on the employed algorithm and available literature. Main focus in this introduction is on the flux-based formulation and the algebraic advection algorithm. For a detailed description and derivation of the employed algebraic advection algorithm in the standard interFoam solver, the interested reader is referred to Appendix A.6.

The interFoam solver is based on the Volume-of-Fluid Equations (2.50 to 2.52) and suitable for the numerical simulation of immiscible incompressible two-phase flows of Newtonian fluids. The implementation of the governing equations in the interFoam solver resembles – due to the utilized technique of equation mimicking – the set of balance equations given in (2.50) to (2.52). However, the solver utilizes a flux-based formulation for the set of equations, i.e. does not solve for the velocity $\mathbf{u}$ but for the face flux defined as $F_f := \mathbf{S}_f \cdot \mathbf{u}_f$. The surface tension force is added using the Continuous Surface Force (CSF) model by Brackbill et al. (1992). The discretization of the CSF model is flux-based as well, leading to a formally *balanced-force* algorithm (cf. Chapter D.2). Descriptions of the algorithm and the solver in general can be found, e.g., in Ubbink (1997), Rusche (2002), Deshpande et al. (2012).

The interFoam solver employs an algebraic VOF method, meaning that the transport of the volumetric phase fraction field α is handled by solving the respective transport equation numerically without reconstructing the interface. Algebraic VOF methods are widely employed also in commercial CFD codes as Ansys CFX and Fluent but usually exhibit difficulties with the transport of sharp fields. The algebraic advection in the solver-family interFoam utilizes the flux-corrected transport (FCT) method introduced in Weller (2006), called MULES (multidimensional universal limiter with explicit solution). This FCT is unique in the way the limiter is calculated at each cell face, using an iterative approach. The algorithm is implemented for an explicit solution (as the naming suggests) as well as for an implicit solution. However, the implicit solution strategy of the MULES algorithm is based on deferred correction, where only the upwind contribution goes into the matrix and the anti-diffusive flux into the explicit source term. The solution of the phase fraction equation is then repeated multiple times with varying flux limiters, until a bounded solution is obtained. Sharpness of the transported phase fraction field is ensured by addition of a counter-gradient diffusion term (Weller, 2006). However, unlike the standard interFoam solver, this work utilizes the Interface Capturing Scheme CICSAM (Ubbink, 1997) for advection of the phase fraction field.

One main contribution of this work is the addition of the CST model into the algebraic VOF solver framework interFoam. To incorporate the different derived CST model formulations (Equations (2.74), (2.86) and (2.89)) in a user-friendly way, a library of run time selective models is implemented. Discretization of the different CST models is accomplished inside the model library, which returns the respective interface terms as a matrix. The implementation also ensures that the advection of volumetric phase fraction and species concentration are discretized with the same schemes to ensure consistency in the advection and minimize artificial species transfer.

Additionally, the existing library for chemical reactions in OpenFOAM®was adapted to and coupled with the interFoam solver and returns the time-explicit reaction term. Both libraries for species transfer and chemical reaction are completely separated from each other. For the interested reader, the code structure of the libraries is outlined below. In terms of code structure, the species transfer library was designed to introduce the smallest possible amount of changes in the existing interFoam solver and to be easily handled in top level development.

```
// set-up species properties
species
(
    C0
    {
        cstModel   harmonic;
        He         He [ 0 0 0 0 0 ] 30;
        D1         D1 [ 0 2 -1 0 0 ] 3e-05;
        D2         D2 [ 0 2 -1 0 0 ] 2e-09;
    }
    C1
    {
        cstModel   arithmetic;
        He         He [ 0 0 0 0 0 ] 10;
        D1         D1 [ 0 2 -1 0 0 ] 1.5e-05;
        D2         D2 [ 0 2 -1 0 0 ] 5e-09;
    }
    ...
);
```

```
// set-up chemistry reader
chemistryReader foamChemistryReader;

// set-up chemistry solver
chemistry           on;
chemistrySolver     ode;
odeCoeffs { // solver settings }

// set-up reactions
species ( C0 C1 C2 C3 ... );
reactions
(
    irreversibleConstRateReaction
    C0 + C1 = C2
    (10 0)

    irreversibleConstRateReaction
    C0 + C2 = C3
    (30 0)
    ...
);
```

Listing 4.1.: User input to simulate reactive species transfer (consecutive competitive reaction)

For usage of the library, the user only needs to specify the material parameter and utilized CST model formulation for each species as shown in Listing 4.1 (left side) in a text file called *speciesProperties.H*. If no further user input is made, chemical reactions will be disabled automatically. As previously stated in Chapter 2.4.2, chemical reactions are considered to take place in the continuous phase only. The utilized library for modeling of chemical reactions is a customized and simplified version of the *thermophysicalModels* library readily available within OpenFOAM®. To add chemical reactions, the reader for chemical reactions (currently only *foamChemistryReader* available) has to be specified. Additionally, the solver settings for the reaction terms have to be specified. Finally, the chemical reactions are to be specified in terms of simple equations for a user-defined reaction rate model. In above example setting, a constant rate reaction model with user-specified forward and backward reaction rates is used.

```
PtrList<volScalarField> C(n);
  ...
// create instance of cst-model class
speciesTransfer specTrans(alpha1);

// set-up chemistry
chemistryModel* chemistry(NULL);
reactiveMixture* reaction(NULL);
if (useChemistry)
{
    // create reactiveMixture class
    reaction = new reactiveMixture(
            mixtureProperties,
            C,
            mesh
        );
    // Create chemical reactions
    chemistry = new chemistryModel(
            mesh,
            *reaction
        );
}
```

```
if (useChemistry) { chemistry->solve(); }

// solve for all species concentrations
for (label i=0; i <C.size(); i++)
{
    volScalarField& Ci = C[i];

    fvScalarMatrix CiEqn =
    (
        fvm::ddt(Ci)
      + fvm::div(phi, Ci, divCiScheme)
      - fvm::laplacian(specTrans.Dmean(Ci.name()))
      - specTrans.interfacialTerms(Ci.name())
    );

    if (useChemistry)
    {CiEqn -= chemistry->RR(i) * (1. - alpha1);}

    CiEqn.relax();
    CiEqn.solve(mesh.solver("Ci"));
}
```

Listing 4.2.: Top-level implementation

The top-level implementation is outlined in Listing 4.2, displaying the CST model initialization – which is executed only once during simulation start – on the left side and the discretization and matrix solving of the CST model – which is executed every time step – on the right. At simulation start-up, first all specified species fields are generated and then the *speciesTransfer*-class is initialized. During initialization, for each species the material parameter are read and a *cstModel*-class is initialized, fixing a specific discretization of the CST model (*harmonic*, *arithmetic* or *blended*). If chemical reactions are to be simulated, the *reactiveMixture* and *chemistryModel* are initialized. The *reactiveMixture*-class holds references to all species concentration fields, creates the chemistry reader and reads in all specified chemical reactions. This information is then given to the *chemistryModel* which holds the chemistry solver and computes the source terms due to chemical reaction.

The right-hand side of Listing 4.2 shows the top-level implementation of the CST model discretization, which is independent of the underlying mesh structure and uses *equation mimicking*. The respective interface transfer terms and mean diffusion coefficients of the different derived CST model formulations are returned from the respective *cstModel* via the *speciesTransfer*-class.

The structure of the implemented library is depicted in Listing 4.3. Main class is the *speciesTransfer*-class, which holds all information about the different species, their material parameter and respective CST model formulation. Its member functions allow top-level access to the res-

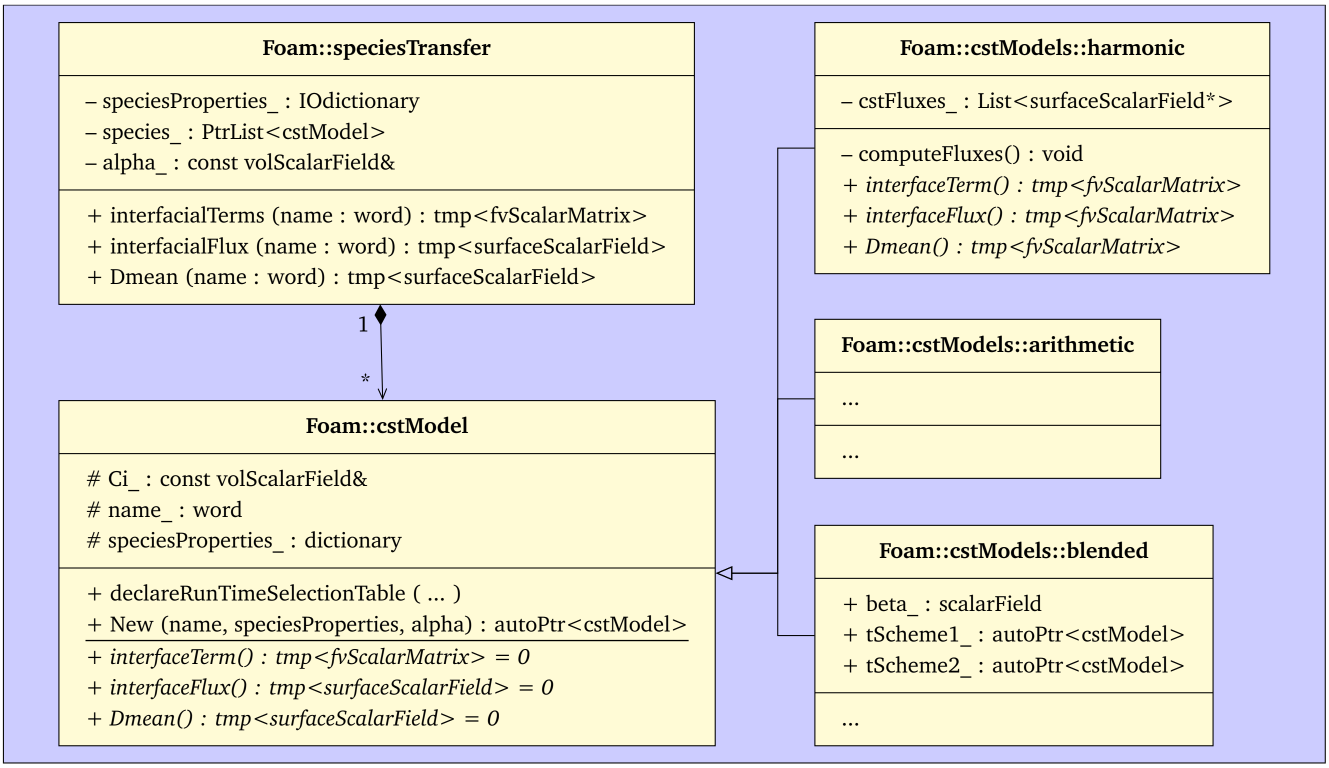

Listing 4.3.: CST model library structure – UML class diagram

pective mean diffusion coefficient, interfacial flux and interface term discretization matrix, whose implementation is found in the different specializations of the *cstModel*-class. The *cstModel* is an abstract base class for the different CST model formulations, which are specified at run time via the *run time selection table*, a standard procedure within OpenFOAM® to allow for maximum flexibility and usability while also minimizing code duplication. From the side of implementation, the *blended* CST model is a special case as it creates two separate *cstModel* objects – one *harmonic* and one *arithmetic* – and re-uses their respective discretization by simply blending them based on the cell-face/interface orientation.

4.2 Reference Frames

A Finite Volume-based algebraic VOF method is employed to study the hydrodynamics and species transfer at single rising bubbles and bubble groups. This creates several questions regarding the problem formulation: How should the simulations be performed to be computationally most efficient? The answer lies in the correct choice of reference frame for each specific problem.

To simulate single rising bubbles it is sufficient, also efficient and thus common practice to employ methods that allow to follow the bubble during the simulation. To achieve this, one can either move the computational domain with the bubble (Moving Window Technique) as, e.g., in Bothe and Fleckenstein (2013) while observing the flow system from the same inertial frame, or transform the governing equations into a frame of reference in which the bubble barycentre is stationary (Moving Reference Frame (MRF) technique). Application of the Moving

Window Technique to unstructured meshes is not straight-forward. In a Cartesian unstructured mesh, one could use the same strategy as, e.g., in Bothe and Fleckenstein (2013) on structured meshes and use layer addition and removal techniques combined with field mapping. On arbitrary polyhedral unstructured meshes, this approach is no longer viable. A suitable approach on unstructured meshes is a flux-based window technique as employed in this work, named Inertial Reference Frame (IRF) technique, where only the phase fraction advection equation is transformed into the moving reference frame.

The different techniques introduced above, namely MRF and IRF are presented in detail in the following.

4.2.1 Moving Reference Frame

Application of the Moving Reference Frame (MRF) on arbitrary unstructured grids is relatively simple and thus has been successfully used in the simulation of rising bubbles, e.g., in Rusche (2002). When changing from an inertial frame into a non-inertial frame, additional forces will appear due to the different acceleration observed in both frames. The acceleration of a fluid particle in an arbitrary non-inertial frame $(\tilde{x}, \tilde{y}, \tilde{z})$ relative to the inertial frame (x, y, z) is given by

$$\mathbf{a}_{xyz} = \mathbf{a}_{\tilde{x}\tilde{y}\tilde{z}} + \mathbf{a}_F + 2\omega \times \mathbf{u}_{\tilde{x}\tilde{y}\tilde{z}} + \omega \times (\omega \times \mathbf{r}_F) + \partial_t \omega \times \mathbf{r}_F \ . \tag{4.1}$$

The additional acceleration terms are the absolute rectilinear acceleration of the origin of the moving reference frame relative to the fixed frame ($\mathbf{a}_F$), the Coriolis acceleration ($2\omega \times \mathbf{u}_{\tilde{x}\tilde{y}\tilde{z}}$), the centripetal acceleration ($\omega \times (\omega \times \mathbf{r}_F)$) and the tangential or Euler acceleration ($\partial_t \omega \times \mathbf{r}_F$).

If the moving reference frame is not allowed to rotate, i.e. only a non-rotating non-inertial frame of reference following the bubble centre-of-mass is considered, then only one additional term appears in the momentum equation viz.

$$\partial_t \rho \mathbf{u}_F + \rho \mathbf{a}_F + \nabla\cdot (\rho \mathbf{u}_F \mathbf{u}_F) = -\nabla p + \rho \mathbf{g} + \nabla\cdot \boldsymbol{\tau} + \boldsymbol{f}_\sigma \ , \tag{4.2}$$

where $\mathbf{a}_F$ denotes the frame acceleration. Frame velocity and acceleration are given relative to the inertial frame of reference (of a stationary observer) as

$$\mathbf{u}_F = \frac{d\mathbf{x}_F}{dt} \tag{4.3}$$

$$\mathbf{a}_F = \frac{d\mathbf{u}_F}{dt} \ . \tag{4.4}$$

The applied methodology as well as its numerical implementation is based on the approach of Rusche (2002). The velocity relative to the moving reference frame is adjusted to keep the bubble fixed within the computational domain ($\mathbf{u}_F = -\mathbf{u}_b$). This is achieved by applying a correction to the inlet velocity boundary condition at each time step as described below.

Rusche (2002) proposed the usage of a PD controller to estimate the necessary velocity correction, where the controller constant of the derivative part is dependent on the current time

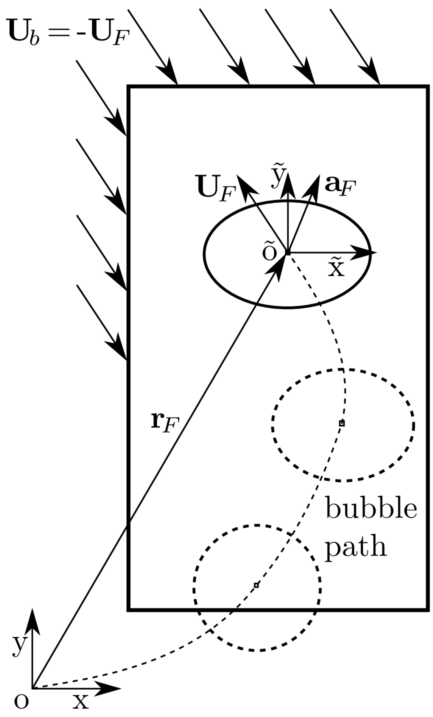

Figure 4.1.: Moving Reference Frame setting based on Rusche (2002)

step. For adaptive time steps, this will induce small periodic disturbances onto the velocity field which can influence solver convergence and might also affect the bubble hydrodynamic behaviour. In the present work, a PID controller is applied which showed to be able to significantly dampen the generated oscillations. The control variable of the PID controller is the bubble position, which is compared to a given constant target position and the applied velocity correction is calculated from

$$\Delta \mathbf{u}_F = \left(K_P \, e^n + K_I \int_0^t e^n \, dt + K_D \frac{e^n - e^o}{\Delta t} \right) \frac{1}{\Delta t} \,, \tag{4.5}$$

where the control error e is the difference of the target bubble position to the current position

$$e = \mathbf{x}_{\text{target}} - \mathbf{x}_{\text{current}} \,. \tag{4.6}$$

In every time step, the velocity field in the reference frame $\mathbf{u}_F$ is updated according to

$$\mathbf{u}_F^n = \mathbf{u}_F^o + \Delta \mathbf{u}_F \tag{4.7}$$

and the corresponding frame acceleration is calculated from

$$\boldsymbol{a}_F = \frac{\Delta \mathbf{u}_F}{\Delta t} \,. \tag{4.8}$$

For a discussion on the interpretation of the controller and useful settings of control parameters, the interested reader is referred to Weber (2016), who analytically explores the optimal parameter setting.

4.2.2 Inertial Reference Frame

A suitable alternative approach to the MRF technique introduced in this work is a flux-based window technique. The basis of this approach is the fact that it does not matter in which reference frame the equations are solved as long as the boundary conditions are corrected appropriately. Hence, the momentum equation can be solved in a stationary observer frame while the transport of the volumetric phase fraction is solved in a moving reference frame moving with the bubble barycentre. Thus, the Inertial Reference Frame (IRF) approach combines the inertial frame and moving reference frame formulations. For this, the relative velocity between both observer frames – which is the bubble velocity in the new time step – needs to be estimated. Then the phase fraction equation can be solved for, using the velocity from the momentum equation and subtracting the relative velocity:

$$\partial_t \rho \mathbf{u} + \nabla\cdot(\rho \mathbf{u}\mathbf{u}) = -\nabla p + \rho \mathbf{g} + \nabla\cdot\boldsymbol{\tau} + \boldsymbol{f}_\sigma \tag{4.9}$$

$$\partial_t \alpha_1 + \nabla\cdot(\alpha_1 \mathbf{u}_F) = 0\,, \tag{4.10}$$

where $\mathbf{u}_F = \mathbf{u} - \mathbf{u}_{\text{rel}}$. In the Finite Volume framework, the advection term is expressed as face fluxes over cell faces. So, the method can be summarized as follows:

1. estimate bubble rise velocity $\mathbf{u}_b = -\mathbf{u}_F$ in the new time step (using PID-controller)
2. subtract the flux bias which translates the bubble barycentre from the current flux:

$$F_F = \mathbf{u}_F \cdot \mathbf{S}_f = \underbrace{F}_{\approx \mathbf{u}\cdot\mathbf{S}_f} - \mathbf{u}_b \cdot \mathbf{S}_f \tag{4.11}$$

3. solve phase fraction advection using the fluxes F_F
4. solve for new velocity $\mathbf{u}$, given the corrected momentum flux ρF

This flux-based window technique, which to the authors' knowledge has not been presented in the literature, is herein termed *Inertial Reference Frame (IRF)* approach. The approach is very similar to the MRF technique but circumvents the additional acceleration term in the momentum equation. As a result, it was found to be more insensitive against non-smooth varying velocity fields in time (e.g. due to parasitic currents or in case of strongly transient velocities).

4.2.3 Comparison

The two different reference frame formulations are compared against each other for a path-instable rising bubble at Eo = 1.2 and Mo = 1.267*e*-10, resulting in $\text{Re}_{\text{max}} \approx 580$. The simulations are conducted on a relatively coarse mesh with a maximum resolution of 36 cells per diameter around the interface. Figure 4.2 shows the results of rise velocity over time and bubble trajectory. Here, the bubble trajectory was projected onto cylindrical coordinates for easier comparison. The actual resulting path of the bubbles shows a zigzag behaviour of both frames. However, the plane in which the bubble rises is different for both. While the bubble trajectory

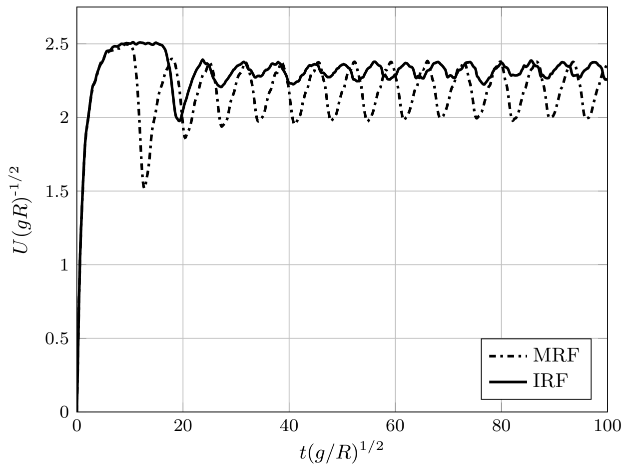

(a) Magnitude of bubble velocity.

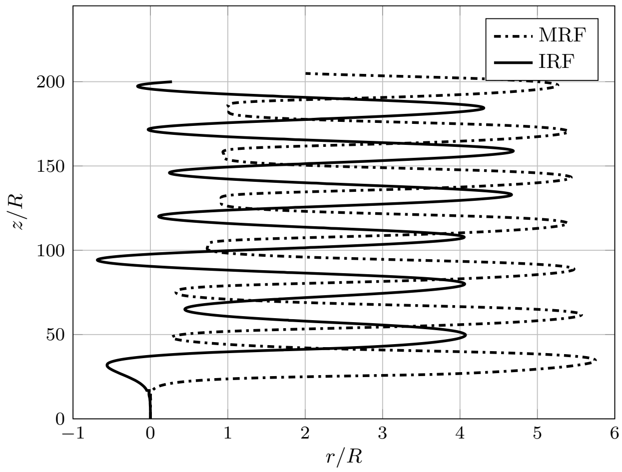

(b) Projected bubble trajectory.

Figure 4.2.: Comparison of MRF and IRF for a path-instable single rising bubble of radius R

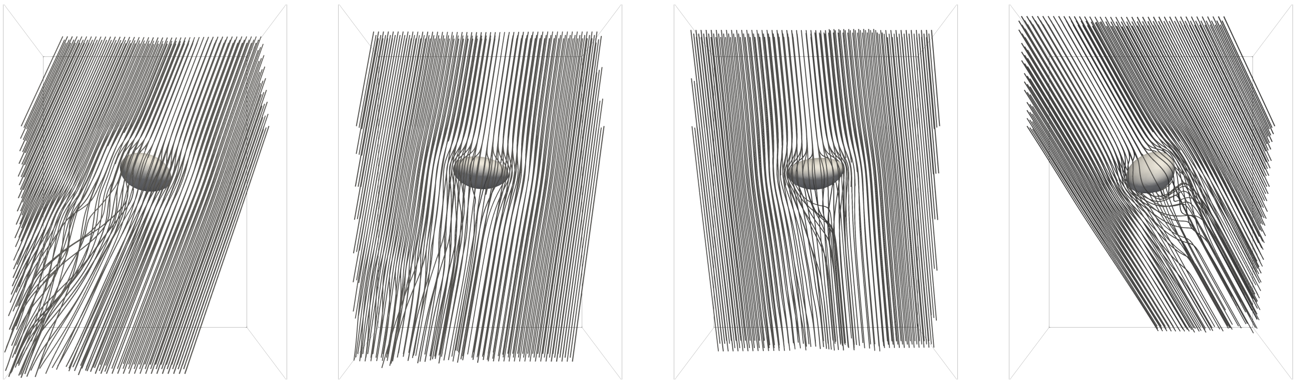

(a) $t = 1.2s$. **(b)** $t = 1.22s$. **(c)** $t = 1.24s$. **(d)** $t = 1.26s$.

Figure 4.3.: Rising bubble during one path oscillation with streamlines

is very similar for both reference frames (cf. Figure 4.2b), the rise velocity shows significant differences regarding its transient behaviour (cf Fig. 4.2a). The change in the bubble velocity over time is about 2.5 times larger for the MRF. The cause for this effect is most probably the additional acceleration term in the momentum equation for the MRF formulation. The bubble shape and velocity streamlines over time for the MRF case are shown in Figure 4.3.

Comparison with Mougin and Magnaudet (2002), who investigate path instability under very similar (although not identical) conditions, yields good agreement for both formulations. In their work, the effect of sphericity onto path instability is tested, fixing an ellipsoidal bubble form with given aspect ratio. They mainly investigate the bubble path and lateral velocities, non-dimensionalizing the simulation results based on the equivalent bubble radius R and gravitational acceleration g. The projected bubble path (Fig. 4.2b) and lateral velocity components (Fig. 4.4) yields very similar results for the MRF and IRF simulation with differences being less than 20%. However, it can be seen that the oscillation is out-of-phase as they oscillate in different planes. Comparison with (Mougin and Magnaudet, 2002, Fig.3,4) shows accept-

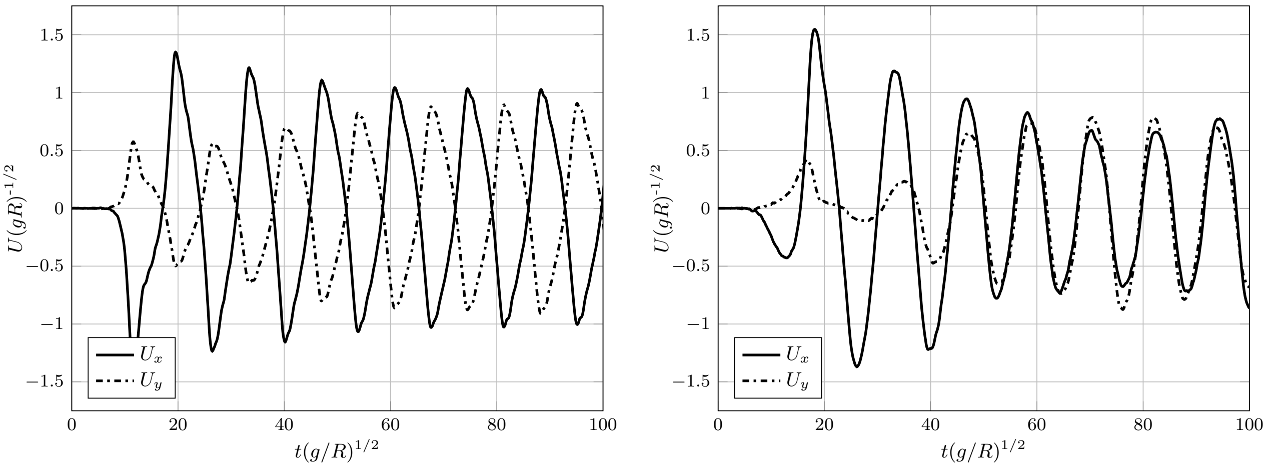

(a) MRF. **(b)** IRF.

Figure 4.4.: Comparison of lateral velocity components

able agreement with the simulation results presented here. The amplitude of the change in rise velocity can only be estimated from (Mougin and Magnaudet, 2002, Fig. 6), according to which the bubble rise velocity predicted by the IRF is in better agreement. A quantitative

Table 4.1.: Comparison to numerical results of Mougin and Magnaudet (2002)

	Galilei number	aspect ratio	max. lateral displacement	lateral velocity amplitude [-]	max angle [°]	Strouhal number
MRF	121	≈ 1.6	4.5*R*	1.35	40	0.135
IRF	121	≈ 1.6	4.4*R*	1.1	28	0.145
Mougin	138	2-2.5	9.6*R*	1.4	29	0.09

comparison of the different simulations is given in Table 4.1. It should be noted that the bubble shape in Mougin and Magnaudet (2002) is pre-determined and their prescribed aspect ratio is significantly higher, leading to a doubling of the non-dimensionalized lateral displacement compared to the results presented here. Also, the maximum angle between the bubble rise direction and the gravitational acceleration agrees well. It is found that the results obtained in the IRF frame are in better agreement. Thus, the IRF supposedly yields more accurate results. Also, it is numerically more stable as it avoids having a controller-dependent acceleration term in the momentum equation. However, a final conclusion of which approach is to be prefered over the other is not possible since this would mean further computationally expensive simulations and possibly further research. A main issue here is that the underlying algebraic VOF method is not strictly mesh convergent due to parasitic velocities stemming mostly from the numerical computation of the surface tension force (cf. D.2).

4.3 Solver Enhancement

The original interFoam solver, although developed and validated in Ubbink (1997) for general purpose two-phase flows, is still mainly meant for – and applied to – cases where surface tension is negligible, i.e. ship hydrodynamics. Therefore, it is only natural that some problems arise when utilizing the solver for the Direct Numerical Simulation of disperse gas-liquid flow systems. Two major enhancements have been added in this work to enable the accurate simulation of bubbly flows with dynamic sharp interfaces:

1. **Improved curvature estimation**
   One of the major drawbacks of the solver are problems associated with the incorporation of the surface tension force. The utilized CSF model (Brackbill et al., 1992) in its flux-based formulation formally allows for a balanced-force implementation which strongly reduces parasitic currents in the velocity field. However, this requires an accurate method for the calculation of interface curvature. The implementation in interFoam computes the curvature from the divergence of the interface normal and uses a simple Gauss integration to obtain the cell-centred interface normals which are then interpolated to the face centres. This estimation of the curvature is very inaccurate and deviations of the obtained to the exact curvature are up to several hundred percent ($\approx +/-300-500\,\%$). Smoothing algorithms for the phase fraction field before calculating the interface normal as suggested, e.g., by Ubbink (1997), Rusche (2002) are not able to circumvent this problem and offer only a small enhancement of the calculated interface normals and therefore the curvature.
2. **Advection based on Interface Capturing Schemes**
   The solver originally utilized the CICSAM discretization scheme for the advection of the volumetric phase fraction field (Ubbink, 1997), which was substituted by the MULES FCT algorithm with counter-gradient diffusion introduced by Weller (2006) (cf. Section A.6) before the first release version. Due to problems of the MULES approach regarding consistent advection (cf. Section 3.2.4), it is advisable for the study of interface physics such as heat or species transfer to switch to alternative advection algorithms. For this reason, a library of different high-resolution interface capturing schemes is implemented, including the following discretization schemes for the advection of sharp fields: CICSAM (Ubbink, 1997), HRIC (Muzaferija et al., 1999), M(odified)-CICSAM (Waclawczyk and Koronowicz, 2008), M(odified)-HIRC (Ansys Fluent 12.0 Theory Guide) and InterGamma (Jasak and Weller, 1995).

For the interested reader, the incorporated improvements to circumvent above mentioned drawbacks of the original interFoam implementation are presented in Appendix D.

4.4 High Performance Computing

To resolve the thin concentration boundary layer at the fluid interface, the High Performance Computing (HPC) techniques of dynamic local adaptive mesh refinement (AMR) and dynamic load balancing are employed. Application of AMR significantly reduces the overall mesh size, whereas dynamic load balancing ensures efficient usage of cores in parallel computations. The simultaneous application of both techniques massively reduces the overall computation time. To quantify the speed-up effect compared to utilizing a uniform mesh of same interface resolution, a comparison for the 3D dam break tutorial case with obstacle was conducted (cf. Figure 4.5).

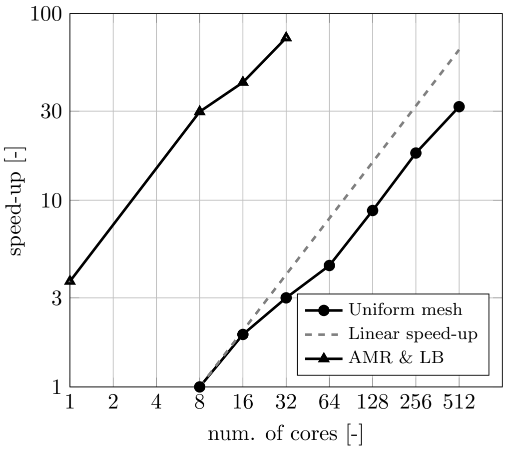

(a) Lichtenberg Cluster (AVX node).

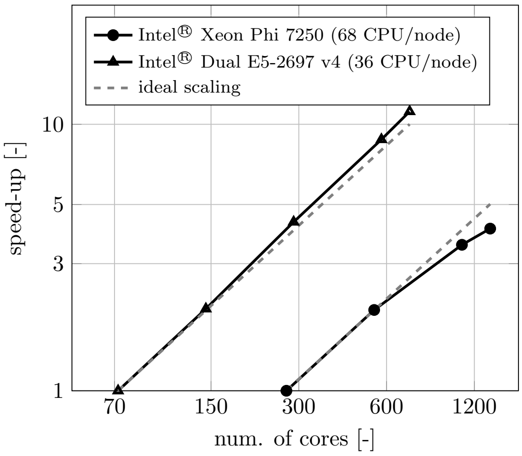

(b) Intel®UK (static refinement).

Figure 4.5.: Scale-up plot for 3D dam break with obstacle using uniform mesh and AMR with load balancing – right Figure curtesy of Intel®UK

In the employed OpenFOAM®-library both techniques are already present in principle but need modifications in order to function together. In the recent few years, two different methodologies to achieve load balancing have been developed, at TTD TU Darmstadt (Batzdorf, 2015), and at Purdue University (T.G. Voskuilen). The former is based on the use of a special decomposition method (clustered decomposition) to maintain the refinement history required for AMR, while the latter includes the load balancing directly into the mesh refinement algorithm. Both methods, however, are currently not applicable to cases where periodic boundary conditions are used. Above proposed methods are unified in scope of this work into one library framework and further improved through major enhancement of the multi-criterion refinement library originally introduced by T.G. Voskuilen and addition of a surface field mapping algorithm in cooperation with M.Sc. Daniel Rettenmaier (SLA, TU Darmstadt).

4.4.1 Adaptive Mesh Refinement

The mesh refinement in OpenFOAM®is based on the *hexRef8*-class which essentially is a mesh cutter class that splits hexahedral cells in half along each edge direction, given a label list of cells to be refined. The class can also perform the reverse, merging back cut cells into one. For this purpose, information about cut cells is stored in form of a *refinementHistory*, containing information about the cells' parent cell (original uncut cell) and the number of refinements performed on that cell. The mesh is refined in such a way as to maintain a one-irregular mesh (i.e. a mesh with a maximum of one hanging node per cell face).

```
refinementControls
{
    enableRefinementControl   true;
    interface
    (
        alpha1  (2  5)
    );
    fields
    (
        alpha1  (0.01  1.1  3)
        C1  (0.001  0.05  2)
    );
    gradients
    (
        alpha1  (0.01  2  2)
    );
    curls
    (
        U    (100  1e+05  3)
    );
    regions
    (
        cylinderToCell
        {
            p1        (0.015  0.015  0.015);
            p2        (0.015  0.033  0.015);
            radius    0.006;
        }
    );
}
```

(a) Employed multi-criterion refinement dictionary setting.

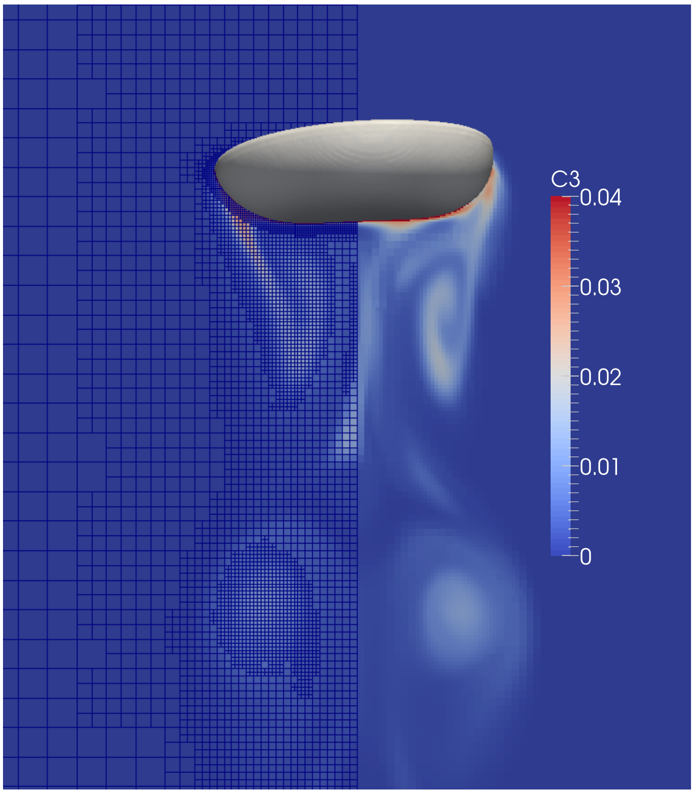

(b) Species concentration field simulated with local adaptive grid and dynamic load balancing.

Figure 4.6.: Local dynamic adaptive mesh refinement

In this work, a multi-criterion refinement is introduced, allowing the user to specify multiple refinement criteria and respective target refinement levels for this criterion in form of a text file input. For each criterion, minimum and maximum values of the respective quantity and the number of maximum refinement steps can be specified. Further, domain regions can be refined by defining geometrical shapes as boxes and spheres. An exemplary dictionary entry, leading to the refinement field shown in Figure 4.7b, is given in Figure 4.7a.

Local adaptive mesh refinement leads to new cells and faces, at which values of the respective transport quantities have to be specified. For fields stored in cell centres, a simple conservative algebraic mapping is employed, which for refined cells copies the value of the parent cell onto each child cell and for unrefined cells performs a simple averaging onto the agglomerated cell. For face-centred fields however, the employed mapping algorithm in the OpenFOAM®library simply copies the value from local face zero of the parent cell onto all newly generated faces of the child cells. As the solver relies on a divergence free volumetric flux field, the field needs to be corrected after each AMR step in order to ensure a divergence free flux. For this, a pressure correction step is introduced after each AMR step, which solves the pressure Laplace equation for the newly mapped flux field

$$\sum_f \left[\frac{1}{\mathscr{A}_f} \nabla_f^{\perp} p_{\mathrm{corr}}^n |\mathbf{S}_f| \right] = \sum_f F_f^o \,. \tag{4.12}$$

In above Equation, $\mathscr{A}_f$ denotes the central coefficient in the discretized momentum equation. The flux field is then updated according to the pressure field by

$$F_f^n = F_f^o - \frac{1}{\mathscr{A}_f} \nabla_f^{\perp} p_{\text{corr}}^n |\mathbf{S}_f| \tag{4.13}$$

to enforce a divergence free field. To also ensure an accurate flux field, the initial volumetric flux F^o, obtained from the mapping needs to be improved. For this, the flux field in the standard interFoam is re-computed from the cell-centred velocity field according to

$$F_f^o = (\mathbf{u}^o)_{f(CD)} \cdot \mathbf{S}_f \, . \tag{4.14}$$

This approach is sufficient for many applications but still faces problems in DNS simulations as the volumetric flux field may be highly oscillating in time due to frequent disturbances. Also, the approach may fail as the pressure correction equation may not be able to converge under the given flux field.

To remedy this problem, an alternative mapping algorithm specifically for the face-centred velocity field $\mathbf{u}_f$ (to be distinguished from the interpolated velocity $(\mathbf{u})_{f(CD)}$) is introduced. This field is calculated after the solution of the pressure equation as

$$\mathbf{u}_f = \left(\mathbf{I} - \mathbf{n}_f \otimes \mathbf{n}_f\right) (\mathbf{u})_{f(CD)} + \frac{F_f}{|\mathbf{S}_f|} \mathbf{n}_f \, . \tag{4.15}$$

The introduced mapping algorithm works as follows: The face velocity at faces generated from splitting an existing parent face are simply mapped (i.e. they all get the parent face value). The value at newly generated internal faces is then averaged from the surrounding mapped faces. The averaging stencil is constructed from direct face neighbours and co-planar faces of the cell.

4.4.2 Dynamic Load Balancing

For efficient parallel computing, the decomposition of the mesh onto the computation cores is modified at run time, when a user-defined imbalance threshold is reached. This mainly involves the combination of two steps which are readily available within the OpenFOAM®framework. At first, a decomposition is created, which is basically a list of integer values that specify for each cell in the domain the respective core it belongs to. In a second step, the mesh and all fields are communicated to the cores based on the aforementioned list. In terms of program code structure, the two relevant classes to achieve dynamic load balancing are *decompositionMethods* and *fvMeshDistribute*. The former creates the decomposition and the latter performs the inter-core communication, field mapping and creation of new patch fields if necessary.

However, several problems with the current load balancing method occur, that have only partially been solved in scope of this work. One main drawback of the mesh balancing approach

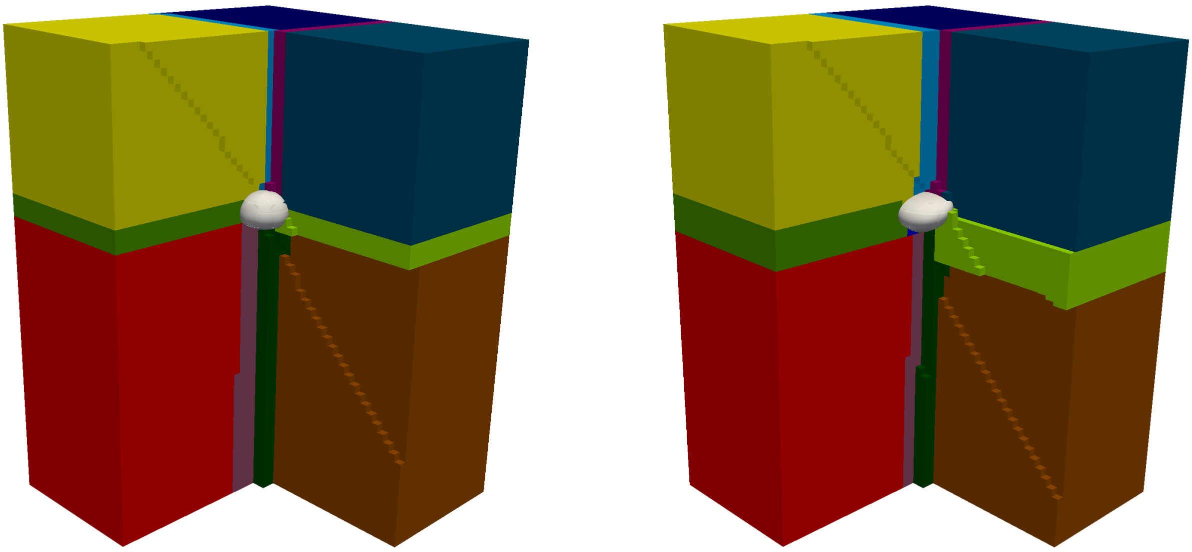

(a) Core distribution at time $t = 0.02\ s$.   **(b)** Core distribution at time $t = 0.17\ s$.

Figure 4.7.: Dynamic load balancing using clustered hierarchical decomposition

introduced by (T.G. Voskuilen) is that all simulation steps, including the pre-processing, need to be executed in parallel in order to correctly maintain the refinement history file. Also, a redistribution onto a different number of cores is not possible.

To overcome these problems, work has been done at TTD TU Darmstadt (Batzdorf, 2015) who introduced an additional *clusteredDecomposition* method. Essentially, this decomposition ensures that all refined cells stemming from the same base cell remain on one core (thus the term *clustered*), which enables decomposition and reconstruction of the refinement history. Drawback is that decompositions obtained by different available algorithms have to be corrected to achieve clustering. This correction is currently only available for *hierarchical* and *simple* decomposition. A different limitation of the usage of dynamic load balancing is currently the application of periodic boundary conditions, which is not supported, as well as boundary conditions which need to store an additional variable. The reason for this lies in the inter-core communication, which has yet to be modified accordingly.

5 Verification Test Cases

To validate the developed and utilized methods for advection and interfacial species transfer, both methods are first compared against generic test cases, where analytical solutions exist. As the strong emphasis of this thesis is on mass transfer rather than hydrodynamics, the verification test cases for the advection of sharp fields as well as for curvature computation can be found in Appendix D. The brief hydrodynamic validation given in this chapter consists only of the necessary steps to enable the simulation of species transfer from single rising bubbles. These two steps are the verification of the introduced advection algorithms regarding consistent advection and the validation of the complete hydrodynamic solver framework regarding the predictive simulation of single rising bubbles.

The greater part of this chapter is dedicated to the developed CST model for interfacial species transfer, which is validated against pure diffusion and diffusion-advection test cases. The numerical results are compared against analytical or numerical exact solutions.

5.1 Bubble Hydrodynamics

To assess the capabilities of the enhanced hydrodynamic solver framework for the accurate simulation of single rising bubbles, the presented numerical method is validated against experimental results of Duineveld (1995) for gas bubbles in ultra-pure water.

5.1.1 Single Rising Bubbles in Ultra-Pure Water

The main question regarding hydrodynamics is whether the algebraic VOF framework is capable of accurately simulating a single rising bubble in quiescent liquid at moderate Reynolds numbers. To this end, after introducing solver enhancements and their respective verification (see Appendix D), numerical simulations for the water-air system are performed and compared to experimental data of Duineveld (1995), who conducted a series of measurements in an ultra-pure water system (without surfactant influence). The investigated range of bubble diameters is $d_b \in [0.3, 1]\,\mathrm{mm}$. For the numerical simulations, the bubble diameters $d_b = \{0.35, 0.5, 0.65, 0.85, 0.95\,\mathrm{mm}\}$ are chosen. The comparison in Figures 5.1a and 5.1b show the results for bubble rise velocity and bubble aspect ratio respectively. For the simulations, the blended CICSAM advection scheme and isosurface-based curvature model are used.

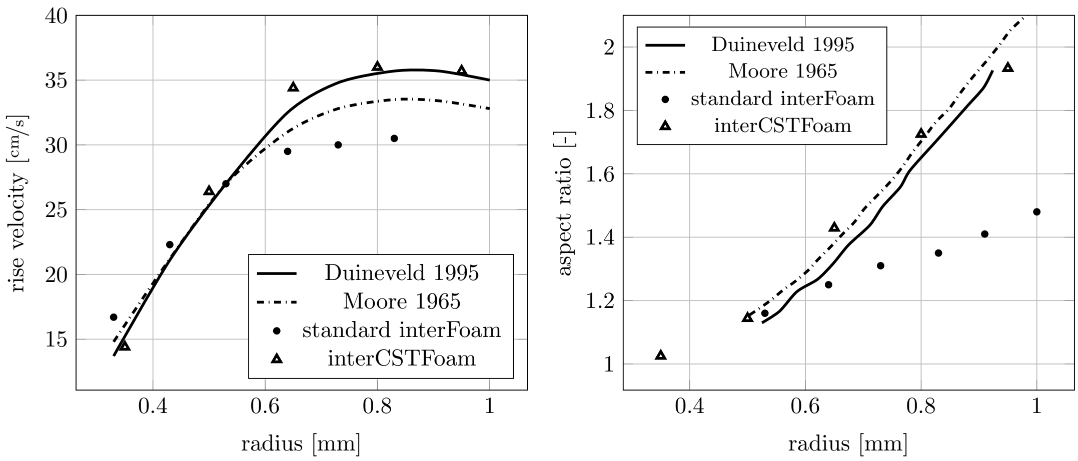

(a) Rise velocity. **(b)** Bubble shape.

Figure 5.1.: Comparison of numerical results to measurements of Duineveld (1995)

It can be seen that the numerical results deviate only slightly from the experimental results. It should be noted that this relatively good agreement is obtained employing all solver modifications explained in Chapter 4 and Appendix D. Without these modifications, the discrepancies in rise velocity and shape are far greater (cf. Figure 5.1 standard interFoam). The main reason for this is the deficient curvature calculation in the standard interFoam solver. The improved advection and viscosity calculations also help to alleviate the errors.

Hence, it is shown that the algebraic VOF method implemented in the interFoam solver framework as utilized in this work is capable of simulating rising bubble hydrodynamics with sufficient accuracy.

5.2 Interfacial Species Transfer

To check the capabilities and restrictions of the derived CST model, several tests are performed to validate first the diffusion terms and then the complete diffusion-advection equation against a series of simplified test cases. Aim of these tests is to verify the proposed CST model formulations and, further, to get a better understanding of the model-required interface resolution to obtain predictive results of interfacial species transfer in two-phase flow systems, as well as to assess the influence of mesh topology onto the numerical method.

5.2.1 Species Concentration Profile Advection (1D)

In a first step, the CICSAM scheme as well as the MULES algorithm with interface compression term are verified upon their capability for consistent advection, which is an indispensable prerequisite for preventing artificial mass transfer. Here, a typical profile of phase fraction and species concentration fields is advected simultaneously and then compared regarding accuracy as well as sharpness (interface width) of the utilized transport algorithm. The fields are herein transported by a constant velocity $|\mathbf{u}| = 6\,\mathrm{cm/s}$ in a one-dimensional case setup. The resulting profile is then compared to its initial state for a quantitative error analysis. Also, the position and width of the jump in the profiles of species concentration and volume fraction field are compared. For the application of the CST model it is very important that the position of the jump as well as the spatial width over which the jump is distributed are equal for both fields.

In this test setup, the domain size is 9 x 1 cm with a mesh resolution of 180 x 20 cells. The concentration profile is obtained by first initializing a unit box profile with range $[0.0125, 0] \times [0.0175, 0.01]$ and then calculating species transfer for 2 s at $\mathrm{H} = 30$ and diffusion coefficients $D_1 = 1e{-}03\,\mathrm{m^2/s}$ and $D_2 = 1e{-}06\,\mathrm{m^2/s}$ inside and outside the box, respectively. The test setup is sketched in Figure 5.2. The initial profile is advected to the right for one second, at which

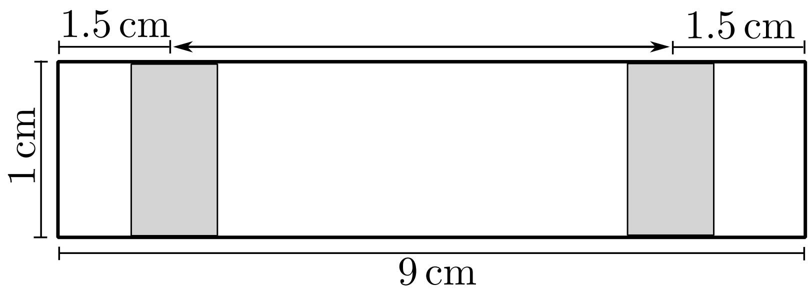

Figure 5.2.: Setup of 1D consistent advection test case

time the flow field is reversed and the profile is transported back to the original position. The resulting profiles for different advection schemes after one and two seconds of advection is shown in Figure 5.3. The profiles at $t = 1\,\mathrm{s}$ are translated 6 cm to the left to match the initial state for comparison.

From the resulting profiles in Figure 5.3 it is obvious that none of the algebraic schemes are able to transport the initial profile. All tested discretizations have two features in common: they reduce the interface concentration in the outer phase and significantly flatten the concentration gradient at the interface. The reason of this behaviour lies in the numerical diffusion or anti-diffusion exhibited by the respective schemes. Here, numerical diffusion leads to a reduced interface concentration and a smooth profile with lower gradient at the interface, while anti-diffusion leads to a step profile near the interface due to the kink in the volume-averaged concentration field.

From above tested discretizations, only the CICSAM scheme ensures that the concentration inside the box stays constant, while the discretization practices employing the interface compression term lead to either increase or decrease of concentration. Insofar, the CICSAM scheme seems indeed to be the best choice regarding consistent advection as it ensures that no mass is transferred over the interface. However, the CICSAM scheme, as basically all other tested discretizations, changes the concentration profile in the outer phase significantly and thus does influence the mass transfer process indirectly. Judging from the final profile shown in Figure 5.3a it is assumed – as indeed it shows also for cases of mass transfer from rising bubbles in the next Chapter – that application of the CICSAM scheme always leads to a reduction of the

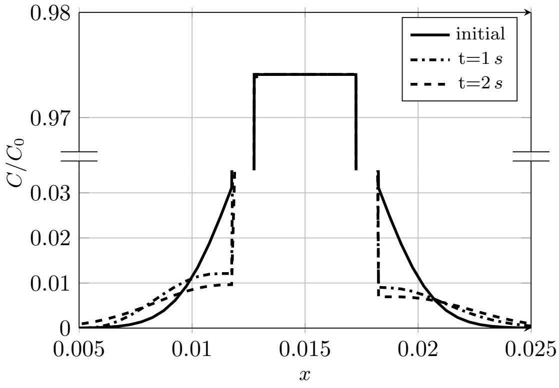

(a) CICSAM.

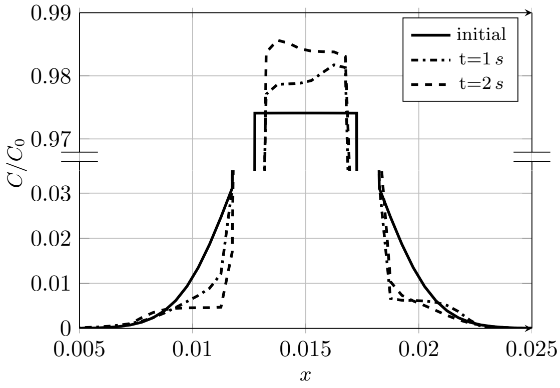

(b) vanLeer with ICS (c_α=1).

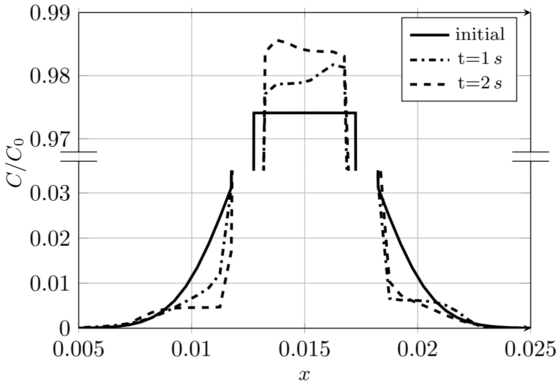

(c) vanLeer with ICS (c_α=3).

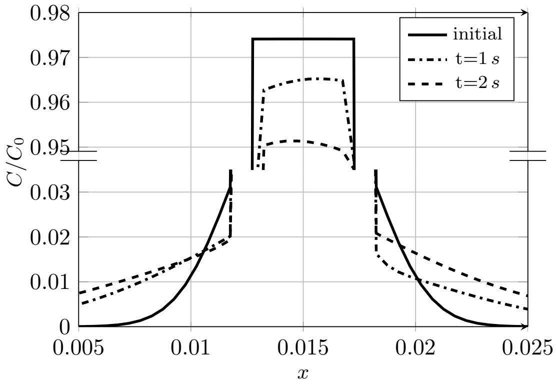

(d) vanLeer with linear.

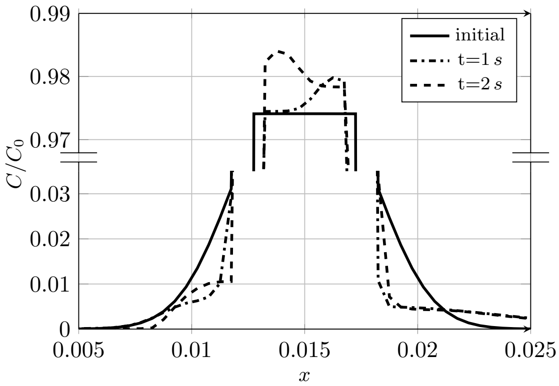

(e) MClimiter with ICS (c_α=1).

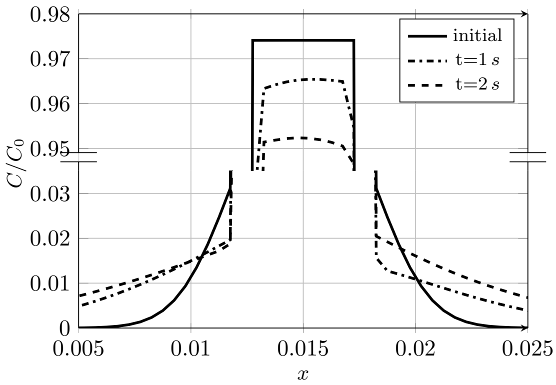

(f) MClimiter with linear.

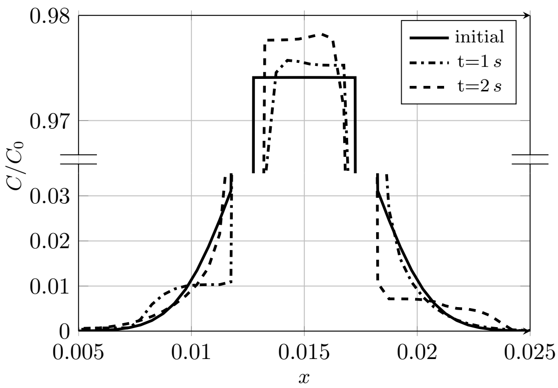

(g) Gamma with ICS (c_α=1, β=0.25).

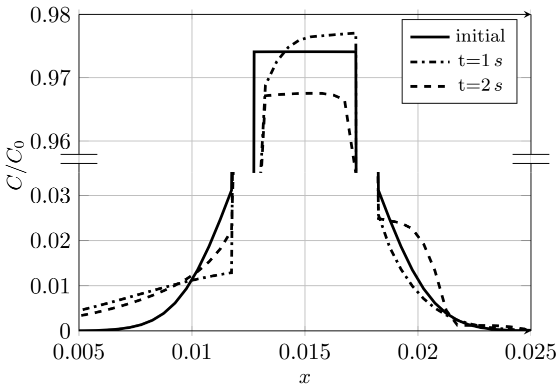

(h) Gamma with linear (β=0.25).

Figure 5.3.: Consistent advection of a 1D profile for different advection schemes

interfacial species transfer due to reduction of concentration and concentration gradient at the interface.

It can further be seen that usage of the interface compression term does not improve the advection and, on the contrary, only adds additional artificial mass transfer due to inconsistent advection.

5.2.2 Stagnant Planar Interface in Quiescent Flow

In the first diffusion test case, the 1D diffusion over a centrally positioned interface is simulated. In order to verify the validity of the derived CST model as well as its correct discretization and implementation, only the CST single-field equation is solved during the simulation and the momentum and pressure equation as well as the phase-fraction advection equation are omitted. The domain length is $x = 0.1m$, the diffusion coefficient left and right from the interface is

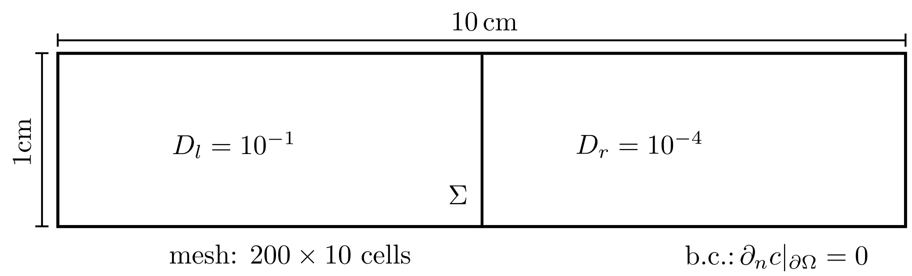

Figure 5.4.: Numerical setup for planar interface diffusion case

$D_l = 10^{-1}$ and $D_r = 10^{-4}$ respectively. The setup is shown in Figure 5.4. Henry coefficients are varied in the range $\mathrm{H} \in [0.033333, 30]$. The numerical results are compared to a numerical exact reference solution obtained with a 1D finite difference method. From Figures 5.5 it can be seen that, in principle, both derived formulations, the arithmetic and harmonic CST model are applicable, given sufficient resolution of the concentration boundary layer. To get a more detailed insight into the performance of both methods, the concentration profiles after a short time ($t = 0.02$s) are shown in Figure 5.6.

In Figure 5.6a, it can be seen that both CST model formulations yield very similar results for $\mathrm{H} > 1$ and that both models smear out the jump over about 3−4 cells, although the initialization for above case is a sharp field with $\alpha = 0.5$ in the interface cell (201 cells in x-direction). However, the important fact is that the predicted interfacial flux from both CST models matches well the one from the numerical exact solution, since the depletion of concentration in the left side of the interface is predicted correctly. The reason for this can be better seen if the concentration profiles predicted from the CST model are shifted to the left by exactly one cell width onto the numerical exact profile (cf. Figure 5.7). Then it becomes evident that the concentration profiles in the vicinity of the interface is captured correctly, albeit shifted by one cell width. The results for this simple diffusion test case lead to three conclusions about the performance of the derived CST model formulations:

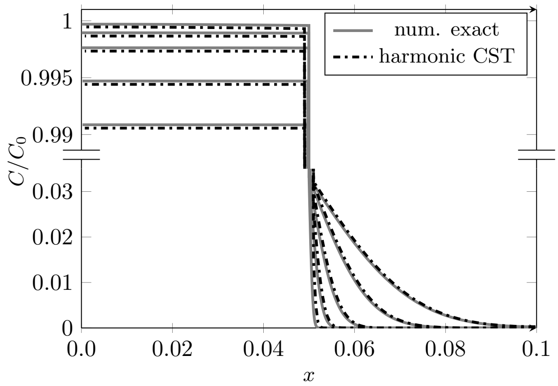

(a) H = 30, harmonic.

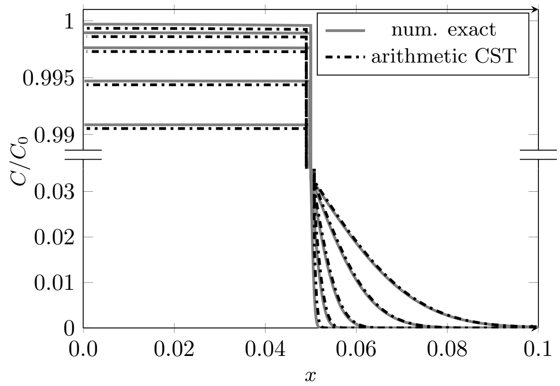

(b) H = 30, arithmetic.

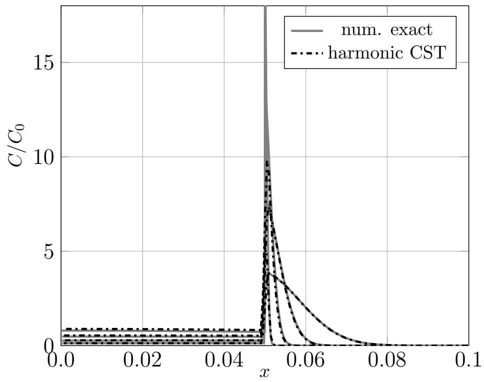

(c) H = 30^{-1}, harmonic.

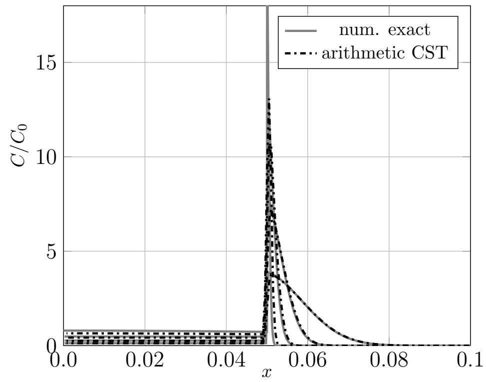

(d) H = 30^{-1}, arithmetic.

Figure 5.5.: Planar diffusion for different CST models and Henry coefficients at $t = 0.02, 0.2, 1, 5$s

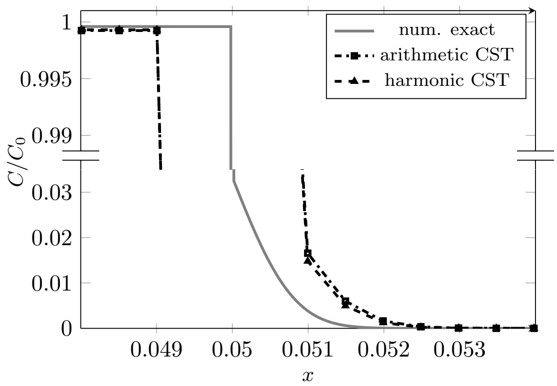

(a) H = 30.

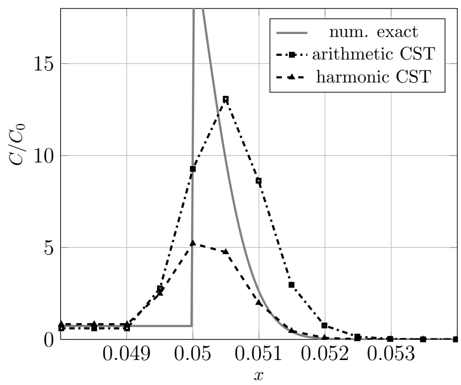

(b) H = 30^{-1}.

Figure 5.6.: Planar diffusion for different CST models and Henry coefficients at $t = 0.02$s

1. both methods produce reliable results given sufficient resolution at the interface
2. the necessary boundary layer resolution for the CST models is about 4 to 6 cells
3. the *arithmetic* CST model needs a higher resolution than the *harmonic* model.

To close the test case, the influence of interface position onto the required mesh resolution is investigated. For this, two different initializations of the alpha and species fields are considered.

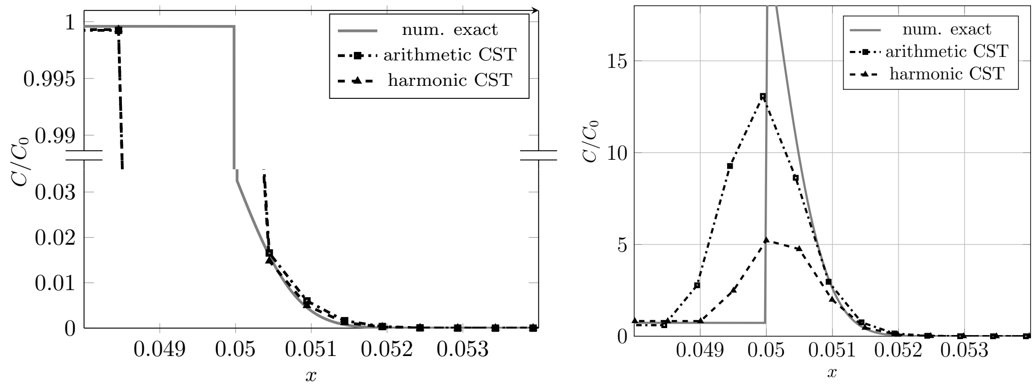

(a) H = 30. **(b)** H = 30^{-1}.

Figure 5.7.: Planar diffusion for different CST models and Henry coefficients at $t = 0.02$s – shifted (matched) profiles

In the first case, the interface is initialized to coincide with a cell face (mesh with 200x10 cells; *sharp field*) and in the second case, it is initialized to coincide with the cell centre (mesh with 201x10 cells; *mid-cell*). The resulting species concentration fields for H = 30 are shown in Figure 5.8. It can be seen that the *sharp field* initialization, where the cell face coincides

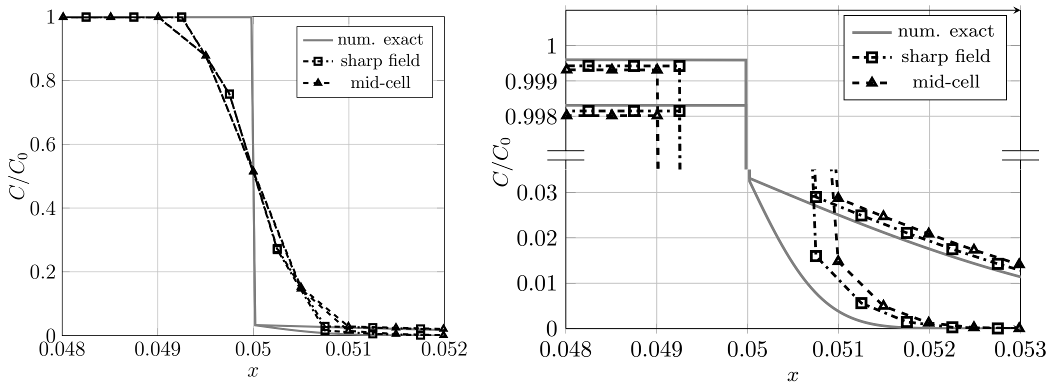

(a) H = 30. **(b)** H = 30^{-1}.

Figure 5.8.: Planar diffusion for harmonic CST model and varying initialization for H = 30 and $t = 0.02$ and 0.5s

with the interface, slightly improves the accuracy of the results for a given mesh resolution. This shows that the exact position of the interface within the cell has only a small influence, although the CST model does not contain any information about the interface position.

Additionally, a mesh convergence study was performed for the different CST model formulations to assess the method quantitatively. Error analysis is based on the L_1-error of the concentration in the left-sided subdomain Ω_l, i.e.

$$L_1 := \frac{1}{|\Omega_l|}\int\limits_{\Omega_l} |C_{\text{ref}} - C_{\text{sim}}|\, dV = |\overline{C_{\text{ref}} - C_{\text{sim}}}^{\,l}| \quad , \quad \text{norm. } L_1 := \frac{L_1}{1 - \overline{C_{\text{ref}}}^{\,l}} , \tag{5.1}$$

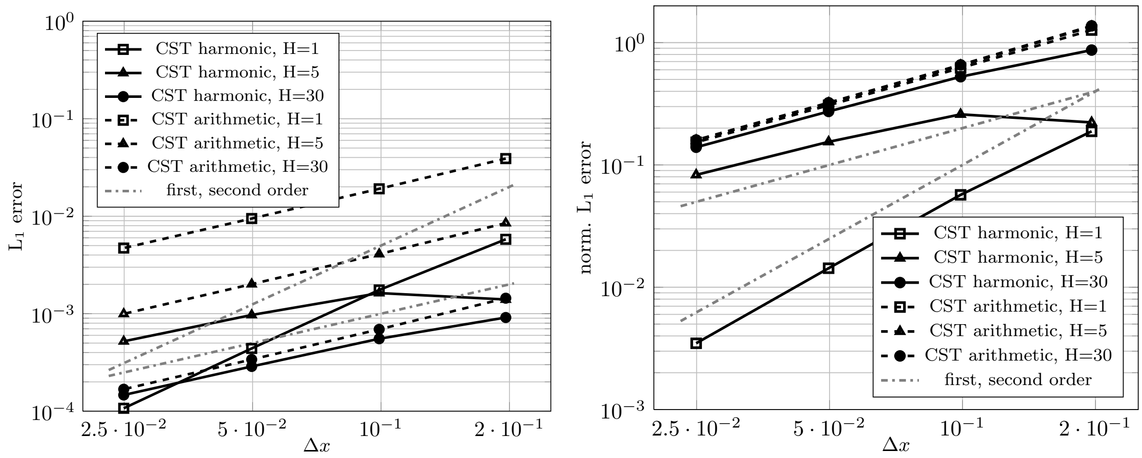

(a) L_1 error.

(b) normalized L_1 error.

Figure 5.9.: Mesh convergence study for meshes with 51, 101, 201, 401 cells in x-direction at $t = 0.2\,\mathrm{s}$ for H = 1, H = 5 and H = 30 respectively

with the numerical exact solution C_{ref}. The error is normalized by the analytical left-sided concentration depletion. The results for different Henry coefficients are shown in Figure 5.9. Only in case of harmonic mean diffusion coefficient and H = 1, i.e. no concentration jump at the interface, second order convergence is obtained. Otherwise, the CST method shows at best first order convergence. Further, the errors for the harmonic mean CST formulation are significantly lower at small Henry coefficients but tend to be equal with the errors of the arithmetic mean formulation for higher values of the Henry coefficient. In Figure 5.9b it is shown that the relative error of the arithmetic CST method is nearly independent of the Henry coefficient while the harmonic CST model shows a significant dependency and the errors approach the ones from the arithmetic model for high values of H. The blended CST formulation is not mentioned here since for this grid arrangement it is identical to the harmonic model.

5.2.3 Stagnant Disc in Quiescent Liquid

In a second test case the influence of cell face/interface orientation onto the diffusion is to be tested. For this purpose, the diffusion of a dilute species originally concentrated in a 2D stagnant gas bubble into the surrounding liquid is simulated. The simulations are carried out on a bubble-fitted O-grid mesh and a hexahedral mesh with a resolution near the interface of about 270 cells per diameter. A view of the employed meshes is given in Figure 5.10. The disc of diameter $d_b = 3\,\mathrm{mm}$ is placed in the centre of the domain with diameter $D = 10\,d_b$. The diffusion coefficients in the gas and liquid phase are $D_g = 10^{-1}\,\mathrm{m^2/s}$ and $D_l = 10^{-4}\,\mathrm{m^2/s}$ respectively. The case setup is summarized in Table 5.1.

To further investigate the influence of interface position and sharpness of the volumetric phase-fraction field onto the CST model, the species transport equation is solved given a phase-fraction field which is smeared out over 4 cells radial to the interface by elliptic relaxation (i.e. solving a Laplace equation for a given phase-fraction field (Rusche, 2002)). Aim of this test case

bubble diameter	$d_b = 3\,\mathrm{mm}$	gas side diffusion coefficient	$D_g = 10^{-1}\,\mathrm{m}^2/\mathrm{s}$
domain diameter	$d = 10\,d_b$	liquid side diffusion coefficient	$D_l = 10^{-4}\,\mathrm{m}^2/\mathrm{s}$
Henry constant	$\mathrm{He} = 25$	boundary condition	$\partial_n c\vert_{\partial\Omega} = 0$
domain discretization	O-grid with 85,000 cells (interface resolution $\approx 11\,\mu$m) hexahedral mesh with 100,000 cells (equal interface resolution)		

Table 5.1.: Simulation setup – diffusion from stagnant disc

is to prove that the CST model predicts the correct species fluxes over the interface regardless of mesh topology, interface position/orientation and sharpness of the volumetric phase-fraction field, given that a certain mesh resolution is provided. The obtained species concentration pro-

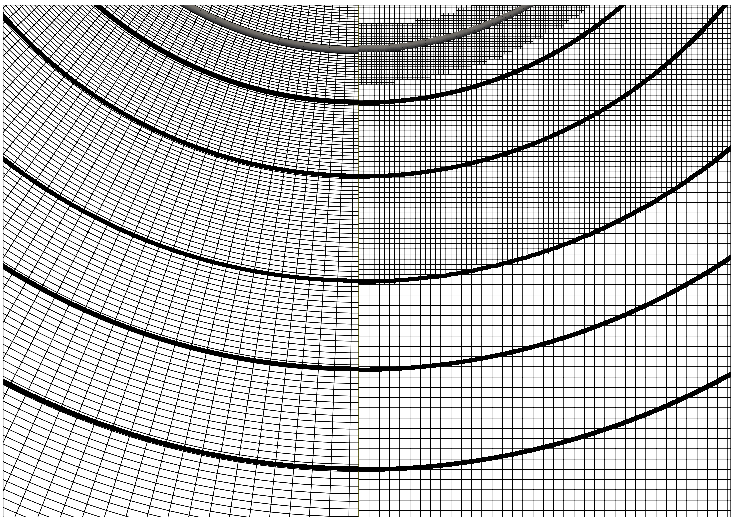

Figure 5.10.: Domain discretization – mesh types, interface position (gray) and concentration isosurfaces (C = $0.002, 0.005, 0.01, 0.02, 0.03$) at $t = 0.005\,\mathrm{s}$

files are then compared to the numerical exact solution at different times t up to $t = 0.2\,\mathrm{s}$ obtained by the method of lines employing Mathematica 8. The result is shown in Figure 5.11a. It can be observed that the species concentration profiles are in very good agreement to the numerical exact solution. Figure 5.11b shows the comparison of the arithmetic and harmonic models on the same mesh. Here, it can be seen that the arithmetic model slightly overpredicts the species transfer compared to the harmonic model for equal mesh resolution. The comparison of concentration isosurfaces in Figure 5.10 shows that the solution on body-fitted and hexahedral meshes is nearly identical, which proves that the choice of discretization practice is indeed appropriate.

5.2.4 Thin Liquid Film – Plug Flow

Typical bubbly flows – the simulation of which is the original aim of this work – are strongly advection dominated, while diffusion processes are several orders of magnitude slower. Therefore, in this test case, the presented CST model is verified in an advection dominated flow problem, additionally evaluating the employed algebraic advection regarding artificial species trans-

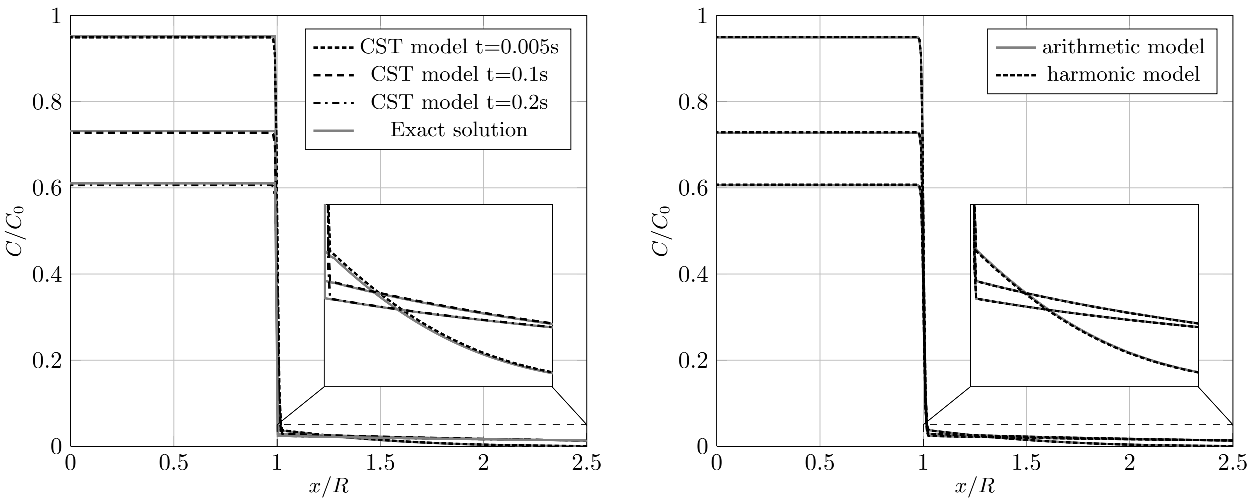

(a) CST method vs. exact numerical solution.

(b) Arithmetic vs. harmonic mean value formulation.

Figure 5.11.: Comparison of concentration profiles on hexahedral mesh – diffusion from radial disc at He$=25$ and diffusivity ratio 1000

fer. Here, the species transfer from a surrounding gas into a thin liquid film at constant velocity $\mathbf{u}$ in both phases (plug flow) is considered. If the advection is dominant, i.e. the Peclet number is sufficiently high, the flow can be described by a 1D advection-diffusion problem, where advection takes place in the x-direction and diffusion only in the perpendicular y-direction.

For this test case setting, which was also used in Haroun (2008), an analytical solution for the concentration profile in the film is given by

$$c(\eta) = c_I \left(1 - \operatorname{erf}\left(\frac{\bar{y}}{\sqrt{4\,\mathrm{Pe}^{-1}\,\bar{x}}}\right)\right), \tag{5.2}$$

where $\bar{x}$ and $\bar{y}$ are dimensionless space variables based on the film thickness d and the Peclet number is defined as $\mathrm{Pe} = \frac{|\mathbf{u}|d}{D_l}$. The Peclet number used in this test case is $\mathrm{Pe} = 1000$. The

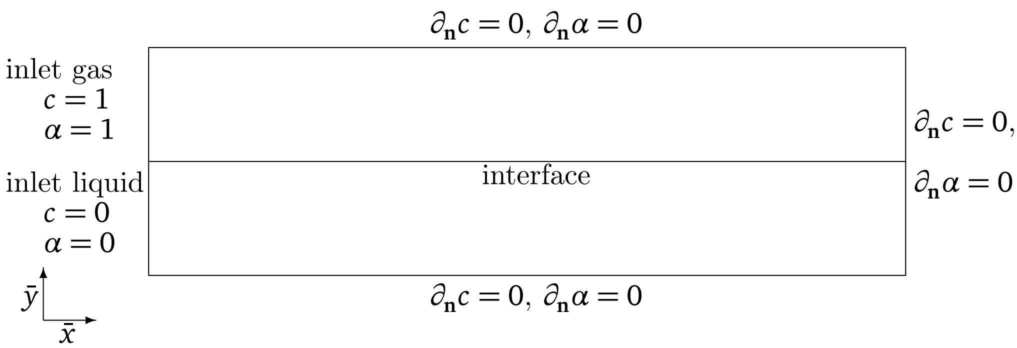

Figure 5.12.: Test-case setup – initial and boundary conditions interface

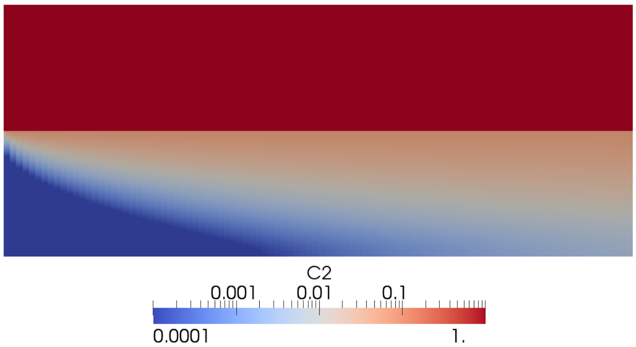

Figure 5.13.: Species concentration field in the film (x axis scaled 1 : 20)

simulations are carried out on a domain of length $L = 100\,d$ and thickness of the gas and liquid film of $d_g = d_l = d = 1\,\mathrm{mm}$. The diffusion coefficients in the gas and liquid phase are $D_g = 2\cdot10^{-4}\,\mathrm{m}^2/\mathrm{s}$ and $D_l = 2\cdot10^{-7}\,\mathrm{m}^2/\mathrm{s}$. At the beginning of the simulation, the dimensionless concentration is $c = 1$ in the gas phase and $c = 0$ in the liquid phase. The applied boundary conditions can be seen in figure 5.12. The simulations are carried out on a hexahedral mesh with 100×200 cells. The obtained concentration profiles are taken at different positions downstream the inlet and compared to the analytical solution (see figure 5.14a). Again, the results obtained

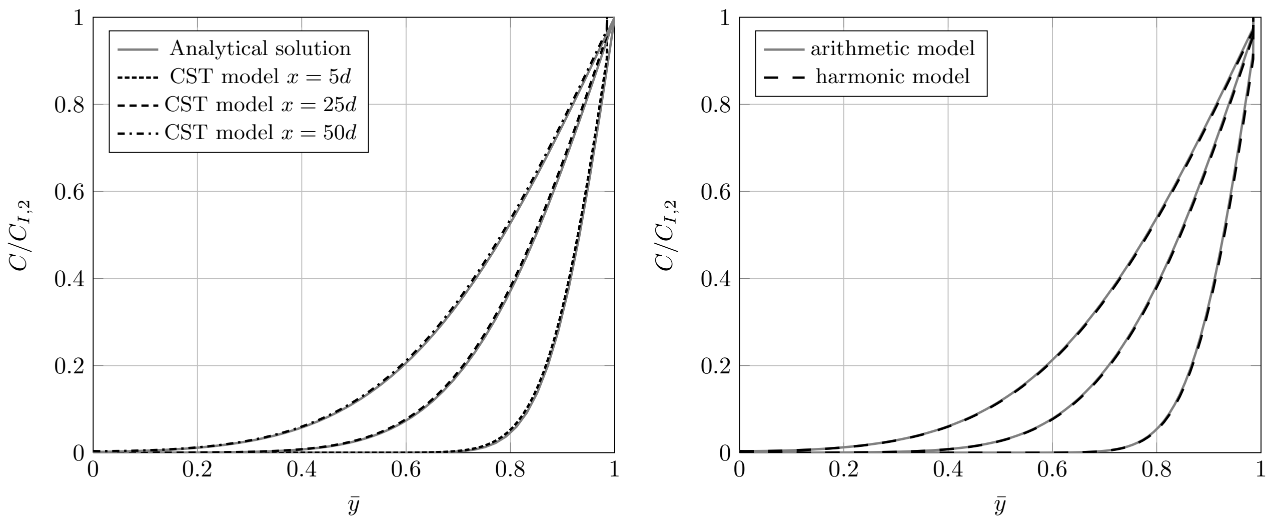

(a) CST method vs. analytical solution.

(b) Arithmetic vs. harmonic mean value formulation on the same mesh.

Figure 5.14.: Comparison of concentration profiles – species transfer in falling film of constant Velocity at Pe=1000 ($\overline{D}^1/\overline{D}^2$=1000, H=15)

by the CST model show very good agreement to the analytical solution. The comparison of the arithmetic and harmonic model in figure 5.14b shows no visible difference which proves that if the concentration boundary layer is sufficiently resolved, both models give the same result.

To further assess the CST model capabilities regarding artificial mass transfer, a single rising bubble is simulated in a 2D moving reference frame. In this case setup, the different simulated chemical species are chosen to be soluble in one phase only.

Hydrodynamics			
bubble diameter	$d_b = 3\,\mathrm{mm}$	fluid system	glycerol/water–air
liquid viscosity	$1\,\mathrm{e}{-5}\,\mathrm{m^2/s}$	gas viscosity	$1.5\,\mathrm{e}{-5}\,\mathrm{m^2/s}$
liquid density	$998\,\mathrm{kg/m^3}$	gas density	$1.2\,\mathrm{kg/m^3}$
surface tension coeff.	$0.073\,\mathrm{kg/s^2}$	domain size	$15 \times 20\,\mathrm{mm}$
domain discretization	hexahedral mesh $\approx 50k$ cells (interface resolution $\approx 15\,\mu\mathrm{m}$)		

Mass transfer					
species	initial conditions		material parameter $\left(D \text{ in } \mathrm{m^2/s}\right)$		
C0:	$\overline{c_0}^1 = 0.8717$	$\overline{c_0}^2 = 8.717$	$\overline{D_0}^1 = 0$	$\overline{D_0}^2 = 1.6\,\mathrm{e}{-06}$	$\mathrm{H}_0 = 0.1$
C1:	$\overline{c_1}^1 = 0$	$\overline{c_1}^2 = 8.717$	$\overline{D_1}^1 = 0$	$\overline{D_1}^2 = 1.6\,\mathrm{e}{-06}$	$\mathrm{H}_1 = 0$
C2:	$\overline{c_2}^1 = 0$	$\overline{c_2}^2 = 8.717$	$\overline{D_2}^1 = 1.6\,\mathrm{e}{-06}$	$\overline{D_2}^2 = 1.6\,\mathrm{e}{-06}$	$\mathrm{H}_2 = 0$
C3:	$\overline{c_3}^1 = 8.717$	$\overline{c_3}^2 = 0.8717$	$\overline{D_3}^1 = 1.6\,\mathrm{e}{-06}$	$\overline{D_3}^2 = 0$	$\mathrm{H}_3 = 10$
C4:	$\overline{c_4}^1 = 8.717$	$\overline{c_4}^2 = 0$	$\overline{D_4}^1 = 1.6\,\mathrm{e}{-06}$	$\overline{D_4}^2 = 0$	$\mathrm{H}_4 = 1\,\mathrm{e}08$
C5:	$\overline{c_5}^1 = 8.717$	$\overline{c_5}^2 = 0$	$\overline{D_5}^1 = 1.6\,\mathrm{e}{-06}$	$\overline{D_5}^2 = 1.6\,\mathrm{e}{-06}$	$\mathrm{H}_5 = 1\,\mathrm{e}08$

Table 5.2.: Simulation setup – modelling zero solubility

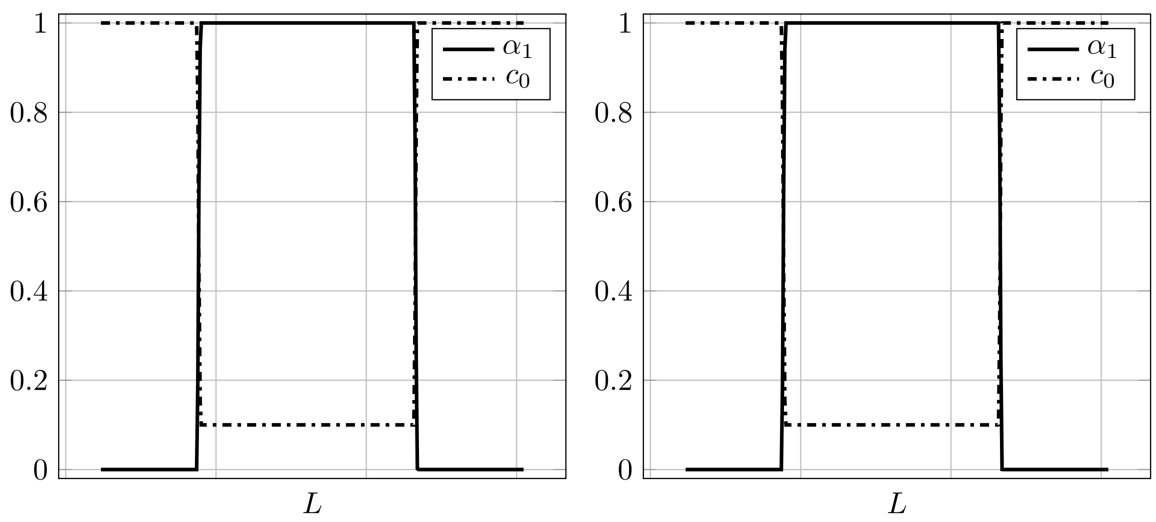

(a) harmonic. **(b)** arithmetic.

Figure 5.15.: Profiles along vertical line through the bubble centre (c_0 normalized) at $t = 0.014\,\mathrm{s}$

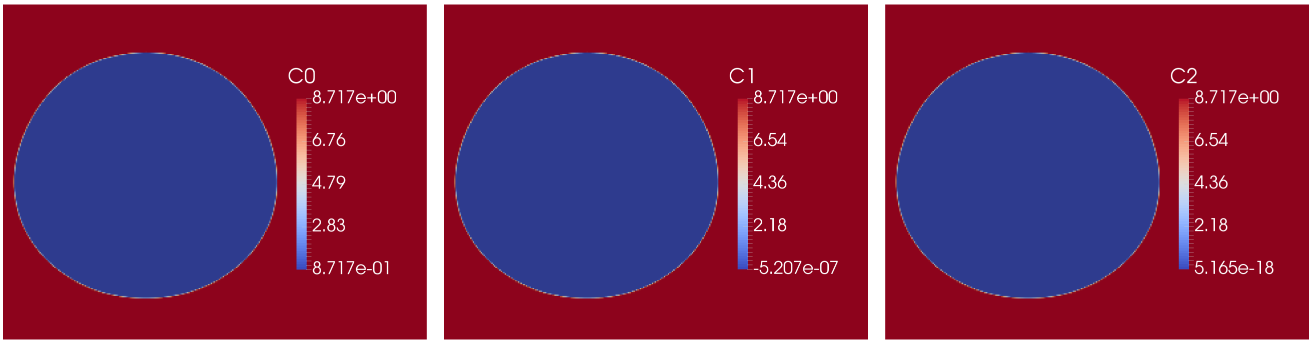

(a) C0. **(b)** C1. **(c)** C2.

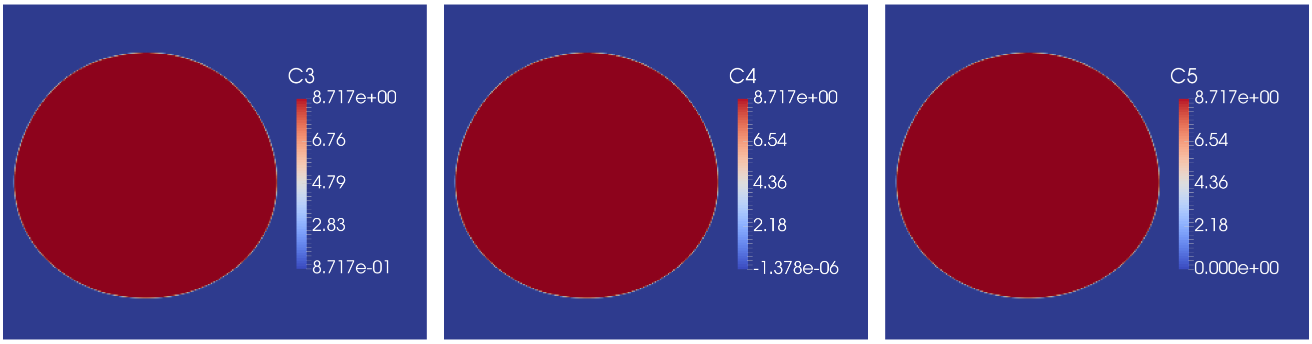

(d) C3. **(e)** C4. **(f)** C5.

Figure 5.16.: Results for harmonic CST model after $t = 0.014\,\mathrm{s}$ of bubble rise

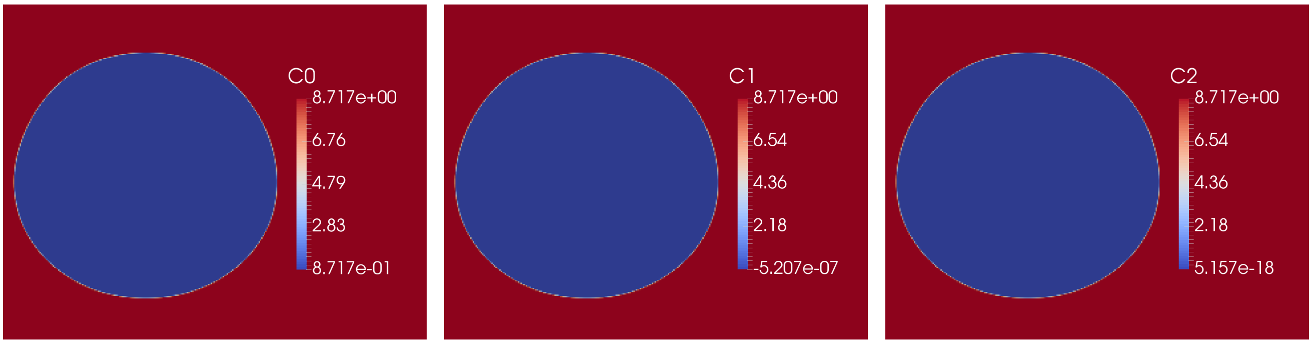

(a) C0. **(b)** C1. **(c)** C2.

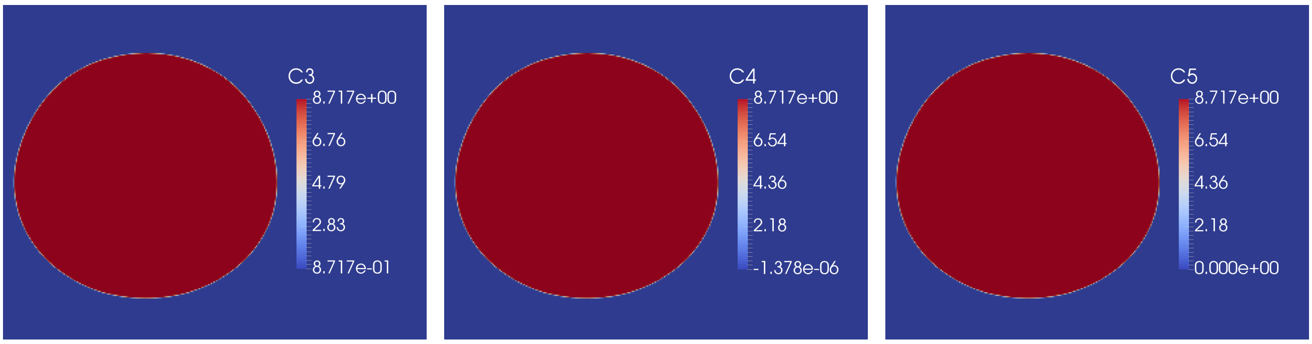

(d) C3. **(e)** C4. **(f)** C5.

Figure 5.17.: Results for arithmetic CST model after $t = 0.014\,\mathrm{s}$ of bubble rise

Any species transfer generated by the numerical model would thus be directly correlated to artificial mass transfer, stemming either from an inconsistency of the algebraic advection of phase fraction and species concentration field or from interfacial transfer terms of the CST model. To model zero solubility, either the diffusion coefficient in one phase is set to zero or the Henry coefficient is set to the respective limits ($\mathrm{H} \rightarrow 0$, $\mathrm{H} \rightarrow \infty$). The test case setup is given in Table 5.2. The simulation is carried out using a dynamic mesh with adaptive mesh refinement. Simulations are performed for both basic CST models, the harmonic (Equation 2.86) and arithmetic (Equation 2.74) model formulation.

The results depicted in Figures 5.16 and 5.17 show that artificial mass transfer does not occur for either CST model. Normalized species concentration profiles for c_0 are given in Figure 5.15 along a vertical line through the bubble centre, showing exactly matching interface positions. The presented results of the different verification cases have proven the CST model's validity and capabilities regarding accuracy of the diffusive interfacial transfer as well as artificial mass transfer. Thus, the different introduced CST model formulations are both suited for the direct numerical simulation of interfacial species transfer from single rising bubbles. However, the harmonic formulation has less strict resolution requirements and, hence, is preferred.

6 Simulation Results

Having thoroughly verified the introduced species transfer model for algebraic VOF methods against multiple test cases, the model is finally applied to the simulation of species transfer of dilute species from rising bubbles (see also Deising et al. (2016, 2018)). As main scientific contribution of this work, an extensive parameter study is conducted to deduce improved mass transfer correlations for single rising bubbles. One particular focus in this study is the influence of bubble shape onto the mass transfer.

6.1 Species Transfer from Single Rising Bubbles

This Section presents the validation of the CST single-field model for mass transfer from single rising bubbles in an infinite medium for low Schmidt numbers and small to medium Peclet numbers based on comparison with numerical results and mass transfer correlations reported in the literature. Here, the term *infinite medium* refers to a sufficiently large computational domain (e.g. $8d \times 11d \times 8d$ for case 1, Table 6.1), so that the bubble rise velocity is not affected significantly by the domain boundaries. With increasing bubble Reynolds number, the hydrodynamic boundary layer becomes smaller and thus a smaller computational domain can be used without affecting the rise velocity.

6.1.1 Validation for Small and Medium Peclet Numbers

The case setup for this series of test cases is described in Roghair (2012) who conducted simulations of species transfer at rising bubbles using a front-tracking method. The obtained results employing the CST model are compared to their numerical results and to existing Sherwood correlations in the literature (Clift et al., 1978, Takemura and Yabe, 1998). The case setup in form of the characteristic numbers of the flow is repeated in Table 6.1. All simulations in this section are carried out with a diffusion coefficient ratio of $D_g/D_l = 1000$ and Henry coefficient of $\mathrm{H} = 30$ in a reference frame as outlined in Chapter 4.2, employing local dynamic adaptive mesh refinement (cf. Chapter 4.4) to significantly reduce the overall number of computational cells. Local mesh resolution at the interface is 42 cells per diameter for cases 1-3 and 64 cells per diameter for case 4. In comparison, Roghair (2012) used a significantly finer mesh resolution of about 100 cells per diameter for all their simulations.

In the literature, many different Sherwood correlations for single rising bubbles can be found which usually are valid for a specific flow regime. Typically, these Sherwood numbers can be written as a function of the Reynolds and Schmidt numbers in the following form:

$$\mathrm{Sh} = c_1 + c_2 \, \mathrm{Re}^a \, \mathrm{Sc}^b \, . \tag{6.1}$$

Table 6.1.: Case setup and results of 3D bubbles in different bubble regimes

Case	Mo	Eo	Reynolds number			Sherwood number			
			Clift et al. (1978)	Roghair (2012)	interFoam	spherical (Clift et al., 1978)	Takemura and Yabe (1998)	Roghair (2012)	CST model
1	1e-04	1.0	5	5.53	6.4	2.5	3.6	3.2	3.6
2	5e-04	3.125	10	11.31	10.5	3.6	4.7	4.4	4.2
3	9.2e-04	40.0	33	32.35	32.5	6.5	7.1	6.3	6.4
4	5e-07	3.125	103	102.78	97.7	11.5	12.0	12.03	11.5

In the limit of potential flow around a spherical bubble, an analytical solution for the velocity at the bubble interface exists. Using a thin concentration boundary layer approximation, Clift et al. (1978) showed that, given the potential flow velocity profile, the following equation for the average particle Sherwood number can be obtained

$$\mathrm{Sh} = \frac{2}{\sqrt{\pi}} \mathrm{Pe}^{1/2} \,. \tag{6.2}$$

Takemura and Yabe (1998) present a Sherwood correlation based on experimental studies on spherical gas bubbles valid in the range $\mathrm{Re} < 100$ and $\mathrm{Pe} > 1$ which reads

$$\mathrm{Sh} = \frac{2}{\sqrt{\pi}} \left(1 - \frac{2}{3} \frac{1}{\left(1 + 0.09\,\mathrm{Re}^{2/3}\right)^{3/4}} \right)^{1/2} \left(2.5 + \sqrt{\mathrm{Pe}}\right) . \tag{6.3}$$

The comparison of global Sherwood numbers is given in Table 6.1 and Fig. 6.1a and shows that the simulations employing the presented Continuous Species Transfer model are in good agreement to the numerical simulations of Roghair (2012) and the Sherwood correlations of Clift et al. (1978) and Takemura and Yabe (1998). Additionally, the performance of the derived arithmetic and harmonic CST models is compared for case setup 1. Fig. 6.1b shows the development of the global Sherwood number over time for case 1 using the three different CST model formulations Eq. (2.74), (2.86) and (2.89). Again, the results show a very good agreement for the presented models. From this, it can be concluded that the different CST model formulations presented in this work are very similar in terms of accuracy (and performance) and are able to predict interfacial species transfer in a wide range of diffusivity ratios and Henry coefficients. The concentration profile around the rising bubbles for all cases are shown in Fig. 6.2. Fig. 6.1c shows the relative conservation errors over time, where the relative conservation errors Δ_α and Δ_C are defined as

$$\Delta_\phi := \frac{\int_\Omega \phi\,(t)\; dV - \int_\Omega \phi\,(t=0)\; dV}{\int_\Omega \phi\,(t=0)\; dV} \times 100 \quad \text{for } \phi = \alpha, C. \tag{6.4}$$

This proves that – as claimed before – the CST method shows indeed good conservation properties in terms of the conservation of phase volume (Δ_α) and species concentration (Δ_C).

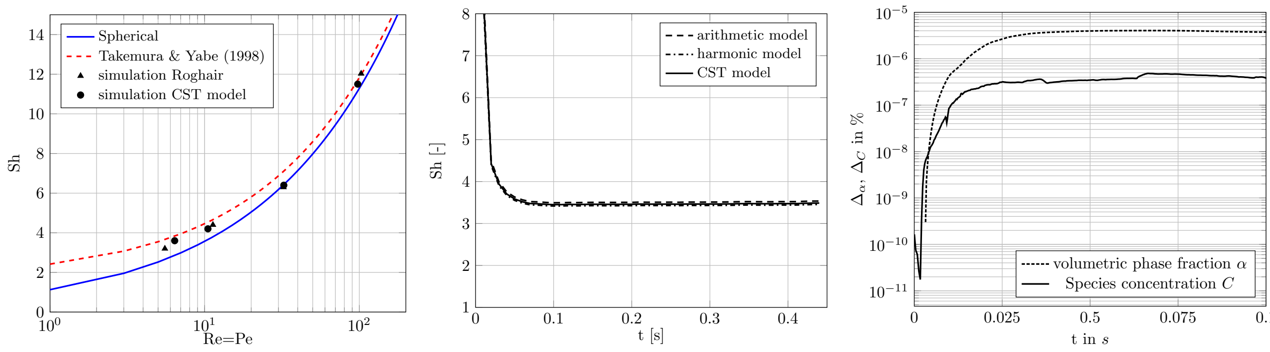

(a) Sherwood over Reynolds number.

(b) Sherwood number over time for case 1.

(c) Mass conservation errors over time for case 3.

Figure 6.1.: Global Sherwood number and comparison with literature data

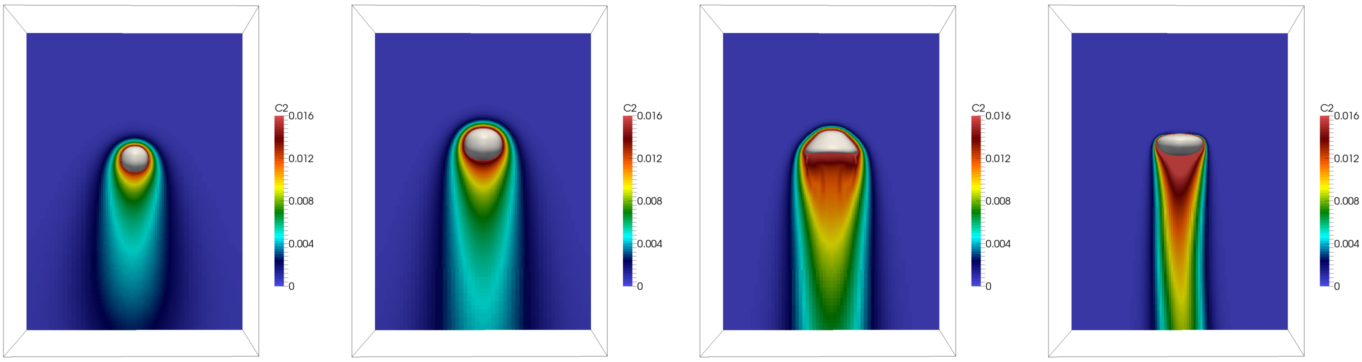

(a) Case 1.

(b) Case 2.

(c) Case 3.

(d) Case 4.

Figure 6.2.: Concentration field around rising bubbles for different bubble regimes

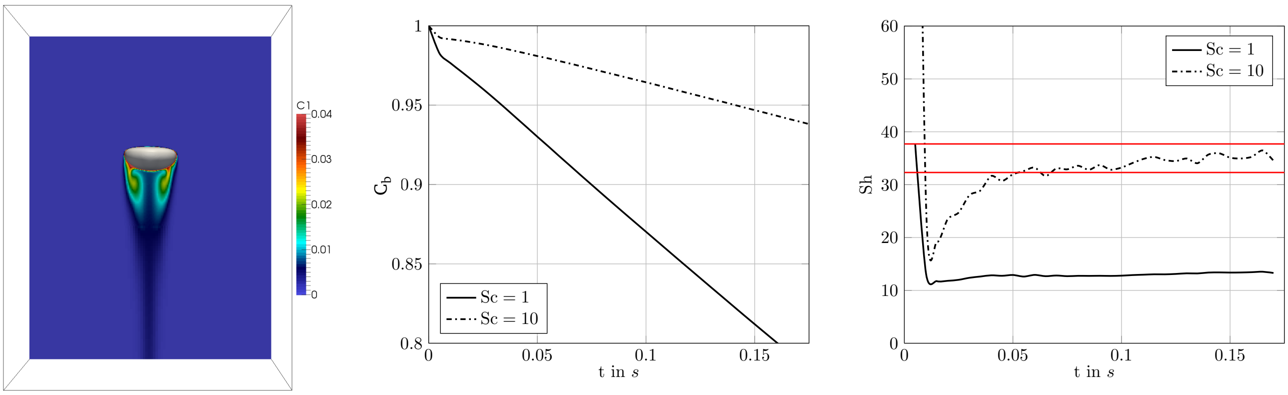

(a) Concentration profile for $\mathrm{Sc} = 10$.

(b) Average bubble concentration over time.

(c) Average Sherwood number over time.

Figure 6.3.: Simulation results for case 4 and $\mathrm{Sc} = 1, 10$

To further analyse the range of applicability of the derived CST model, Direct Numerical Simulations of rising bubbles for medium Schmidt numbers are performed. Here, the setting of case 4 is re-used with increased Schmidt number (Sc = 10). Diffusion coefficient ratio and Henry coefficient remain unchanged. In this setting, the concentration boundary layer thickness is significantly reduced which leads to strong changes in the concentration profile in the bubble wake (cf. Fig. 6.3a and 6.2d). The obtained global Sherwood number is compared to correlations of Takemura and Yabe (1998) and Oellrich et al. (1973) (cf. Figure 6.3c). The global Sherwood number estimated by both models are Sh = 37.7 (Oellrich et al., 1973) and Sh = 32.3 (Takemura and Yabe, 1998) and are shown as red lines in Figure 6.3c. It can be seen that the numerical results are in good agreement to above correlations. The species concentration within the bubble over time for Sc = 1 and Sc = 10 is given in Figure 6.3b.

6.1.2 Application to Unstructured Polyhedral Meshes

The CST method, due to the local discretization utilizing only face neighbour information, can readily be applied to unstructured meshes of general cell shape such as tetrahedral and polyhedral meshes as well as meshes of mixed type. To demonstrate the capabilities of the method, the presented CST model is employed for the simulation of species transfer from a rising bubble at a very low Reynolds number (Re $\ll$ 1). The results are compared to the numerical exact solution obtained by employing the analytical velocity field given by Hadamard-Rybczinski (Hadamard, 1911), utilizing a hexahedral and a polyhedral computational mesh of comparable resolution (see Figure 6.4).

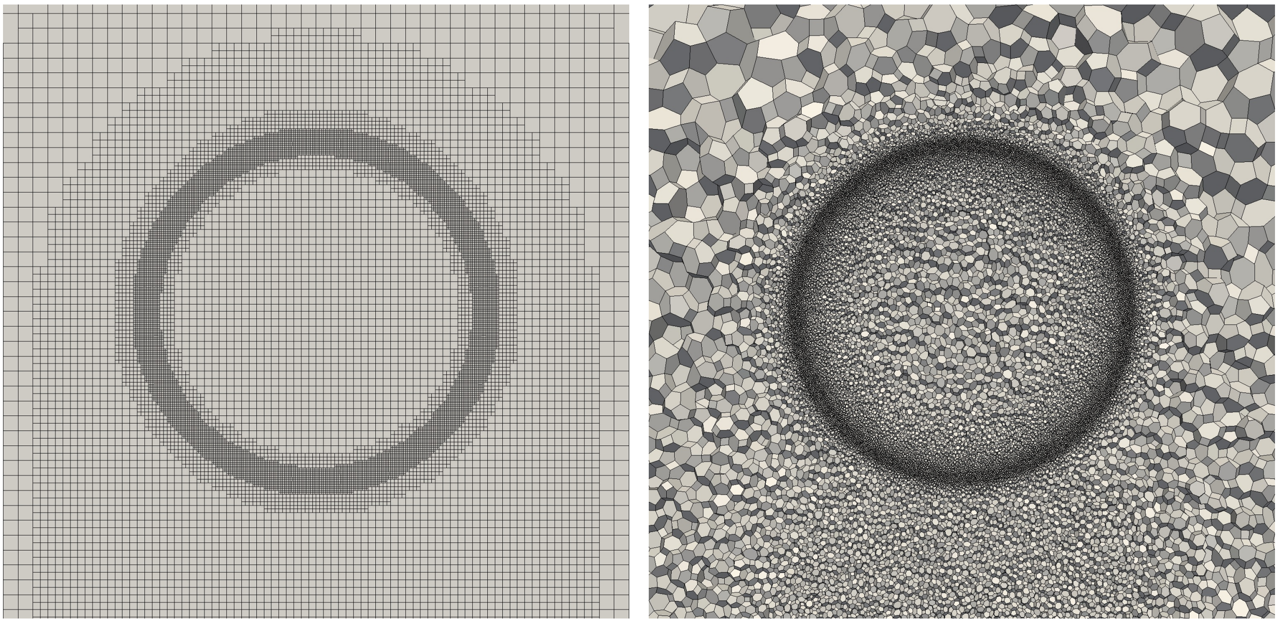

(a) Hexahedral mesh.   **(b)** Polyhedral mesh.

Figure 6.4.: Computational meshes

As mentioned above, two main discretization errors may occur on general meshes, non-orthogonality errors and skewness errors. A successful application of the presented model on general meshes, where skewness errors appear demands the usage of a skew-correction to the

bubble diameter	$d_b = 4\,\mathrm{mm}$
domain length	$d = 32\,d_b$
liquid density	$\rho_l = 1000\,\mathrm{kg/m^3}$
liquid viscosity	$\mu_l = 2\cdot 10^{-3}\,\mathrm{m^2/s}$
surface tension coefficient	$\sigma = 0.0523\,\mathrm{kg/s^2}$
species 1: (Sc $= 2,000$, Pe ≈ 26)	
liquid side diffusion coefficient	$D_l = 10^{-6}\,\mathrm{m^2/s}$
Henry constant	He $= 35$
species 2: (Sc $= 20,000$, Pe ≈ 260)	
liquid side diffusion coefficient	$D_l = 10^{-7}\,\mathrm{m^2/s}$
Henry constant	He $= 35$
viscosity ratio (μ_l/μ_g)	1000
density ratio (ρ_l/ρ_g)	1000
diffusivity ratio (D_l/D_g)	0.001

Table 6.2.: Simulation setup – Hadamard-Rybczinski

		global Sherwood number	
	terminal rise velocity [m/s]	species 1	species 2
hexahedral mesh	0.00645	4.83	12.2
polyhedral mesh	0.00641	4.94	12.3
numerical exact	0.00653	5.05	12.4

Table 6.3.: Simulation results – Hadamard-Rybczinski

applied algebraic advection scheme (here CICSAM) as e.g. proposed by Denner and van Wachem (2014) to counter-act numerical diffusion and maintain a (relatively) sharp interface representation. Also, non-orthogonality errors introduced by the diffusive terms are to be corrected, applying non-orthogonal correction techniques as e.g. proposed by Jasak (1996). In the present work, however, no skew-correction is added to the employed advection scheme CICSAM as the numerical diffusion generated by the scheme in the moving reference frame is negligible due to the very low velocities in the vicinity of the interface, especially at the bubble rear. The numerical exact solution is obtained using the analytical solution for the velocity field and solving the advection-diffusion equation in the liquid domain, prescribing a fixed uniform concentration at the bubble surface. The numerical setup is given in Table 6.2. For the simulations, the harmonic CST model (Equation 2.86) was used. Figures 6.5a and 6.5b show the comparison of concentration iso-contours to the numerical exact solution for both employed meshes. The simulation results are summarized in Table 6.3 and agree well with the analytical solution of the terminal rise velocity and the numerical exact solution of the concentration profile. As to be expected, the results on the polyhedral mesh are slightly better due to more neighbouring cells in more directions which corresponds to more accurate gradient calculations and approximation of the

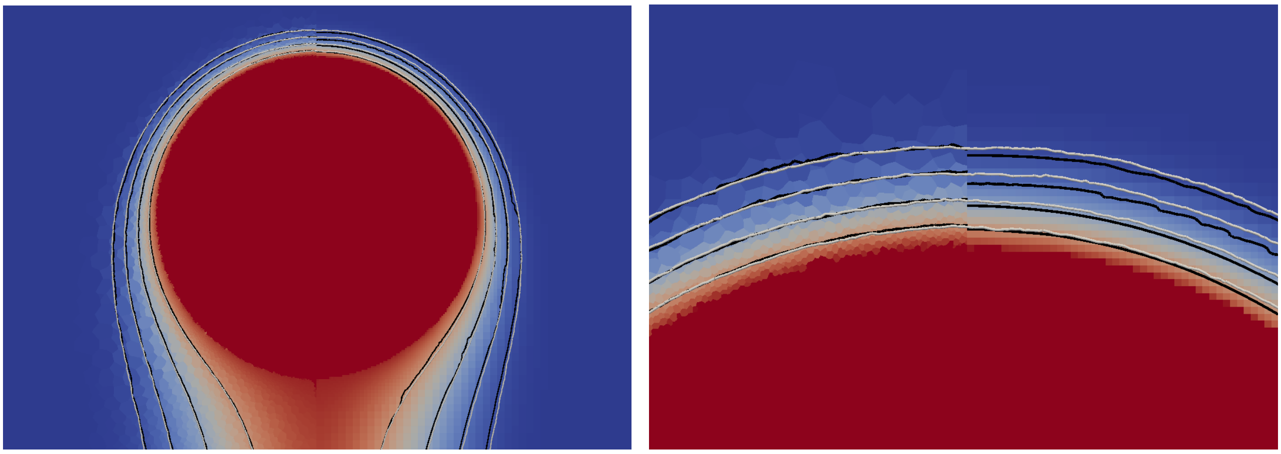

(a) Concentration iso-contours around bubble.

(b) Concentration iso-contours bubble front.

Figure 6.5.: Concentration field with iso-contours ($\bar{c}_2 = 0.02, 0.01, 0.005, 0.002$); left: polyhedral mesh; right: hexahedral mesh; grey iso-contour: numerical exact solution (small kinks in iso-contour due to interpolation)

flux-based transport. In conclusion, it is shown that the presented model is suitable to be used on general meshes. Further, the results show that for a face-based solver such as interFoam, it is beneficial to use polyhedral meshes rather than hexahedral. However, the present work mainly focusses on the latter, as currently dynamic local adaptive mesh refinement capabilities in OpenFOAM are only available with hexahedral mesh types. An extension of the CST model to unstructured meshes of poor quality, where skewness correction becomes a necessity, has recently been published in Hill et al. (2018).

6.1.3 High Peclet Numbers

Most gas-liquid systems encountered in nature and those utilized in industrial processes exhibit very high Peclet numbers, which means that the advective transport is many orders of magnitude faster than the diffusive transport, leading to extremely thin concentration boundary layers compared to the hydrodynamic length scales involved. Thus, it is of major interest for many applications to be able to predict the mass transfer for medium and high Reynolds and high Schmidt numbers and to understand the influence of both dimensionless numbers onto the mass transfer process.

Making use of local adaptive mesh refinement and dynamic load balancing strategies, in this work the concentration boundary layer is sufficiently resolved for Peclet numbers up to $\mathrm{Pe} = 10^4$ (cf. Figure 6.11b), while still maintaining a somewhat reasonable overall simulation time of about 8000 to 10000 CPU hours per case (3 to 4 weeks on 16 CPU's). The maximum resolution at the interface for all cases in the parameter study is about 224 cells per bubble diameter. The total mesh cell count is about $4 \cdot 10^6$ cells, although it depends for each case – due to the dynamic adaptive mesh refinement – on the current bubble shape.

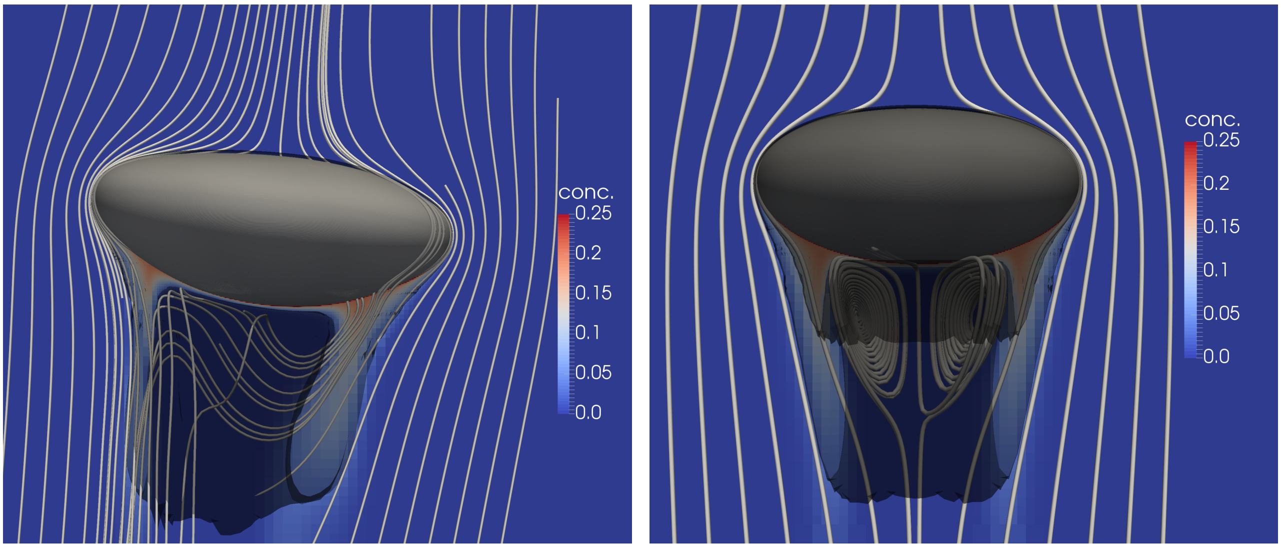

(a) $\mathrm{Eo} = 0.3$, $\mathrm{Mo} = 10^{-11}$. **(b)** $\mathrm{Eo} = 5$, $\mathrm{Mo} = 10^{-05}$.

Figure 6.6.: Species concentration field with iso-contours and streamlines ($\mathrm{H} = 5$, $\mathrm{Pe} \approx 8000$)

Figure 6.6 shows the concentration profiles around rising single bubbles for two different material parameter settings. In addition to the species concentration profiles, concentration isosurfaces and velocity streamlines are plotted in order to give a better insight into the flow structure around both bubbles. It can be seen that the overall concentration profile looks similar, while the flow around both bubbles is entirely different. The velocity and pressure fields for case $\mathrm{Eo} = 0.3$, $\mathrm{Mo} = 1e\text{-}11$ are given in Figure 6.7. Figure 6.8 shows the cell values (original data, non-smoothed) of the species concentration at $\mathrm{Pe} \approx 6300$. In Figure 6.8b, additionally, the employed computational mesh is shown, using three level of refinement in the vicinity of the

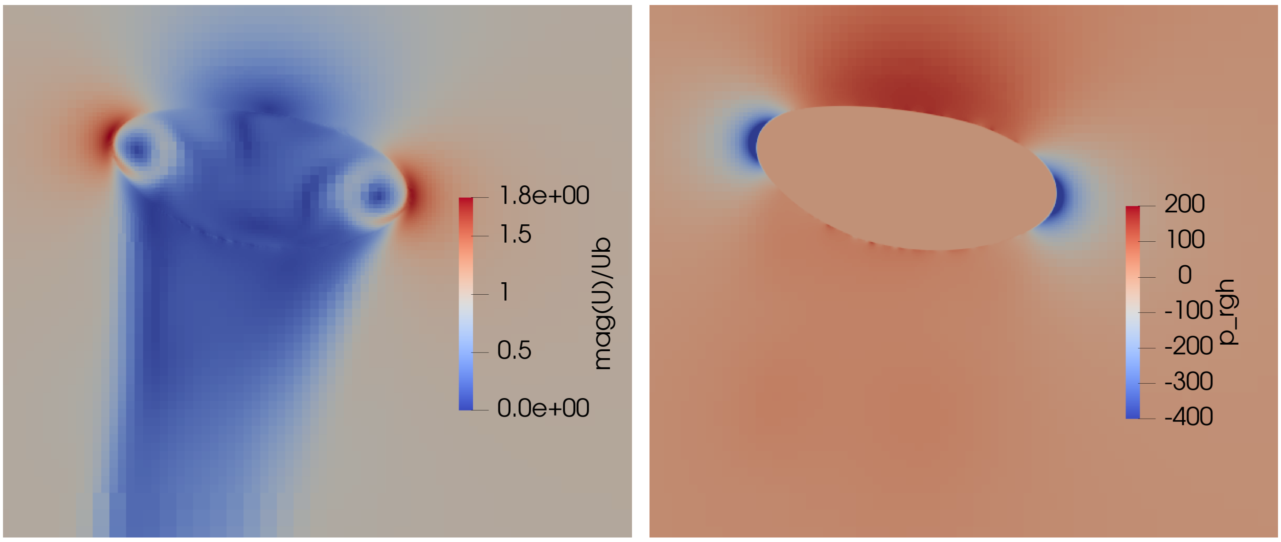

(a) Velocity field. **(b)** Pressure field.

Figure 6.7.: Velocity and pressure field for case $\mathrm{Eo} = 0.3$, $\mathrm{Mo} = 1e\text{-}11$ at $t = 0.1379\,\mathrm{s}$

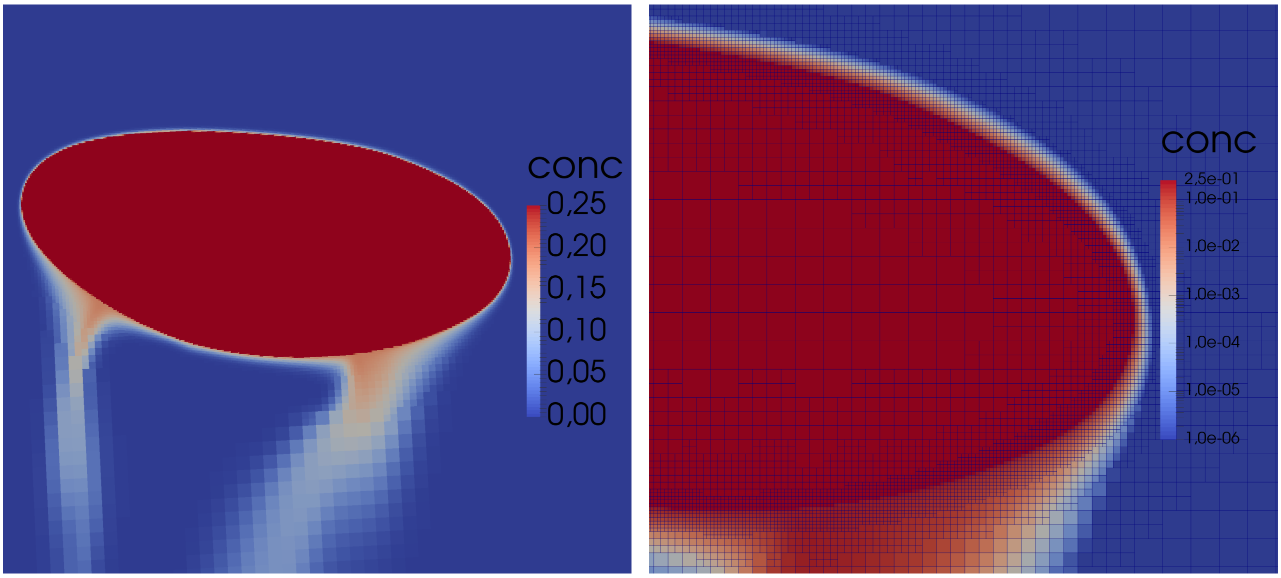

(a) Concentration field.   **(b)** Logarithmic concentration field.

Figure 6.8.: Concentration field for case $\mathrm{Eo} = 0.3$, $\mathrm{Mo} = 1e\text{-}11$, $\mathrm{Sc} = 10$ at $t = 0.1379\,\mathrm{s}$

interface and seven refinement levels in total. The cases for the conducted parameter study are given in the Grace diagram in Figure 6.9 With exception of the spherical bubbles, the simulated Reynolds numbers (red dots) are in good agreement to the Grace diagram. For spherical bubbles, the rise velocity is over-predicted. The hydrodynamic results of the parameter study are

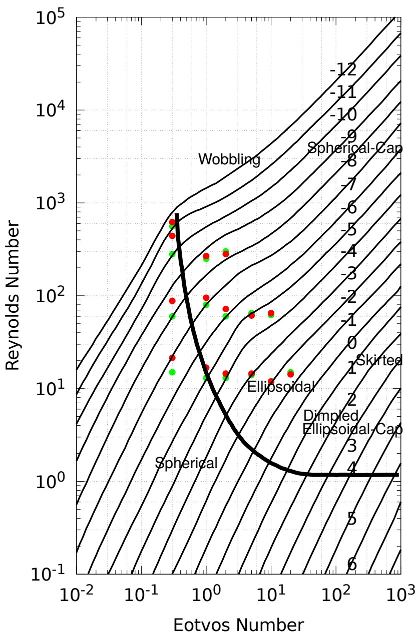

Figure 6.9.: Grace diagram with simulated settings: (green) setup, (red) simulation results

shown in Figure 6.10.The left Figure shows a comparison of the computed Reynolds numbers to the correlation in Legendre et al. (2012) which reads

$$\mathrm{Re} = 2.05\,\mathrm{We}^{\frac{2}{3}}\,\mathrm{Mo}^{-\frac{1}{5}}\,, \tag{6.5}$$

while the right Figure shows a comparison of the compute aspect ratios to the correlations obtained by Legendre et al. (2012) based on a fitting of collected data over a large parameter space for pure and contaminated systems. It can be seen that there are two limiting curves for the aspect ratio, given as

$$\chi = 1 + \frac{9}{64}\,\mathrm{We} \quad \text{(Moore, 1965)} \tag{6.6}$$

$$\chi = \frac{1}{1 - \frac{9}{64}\,\mathrm{We}} \quad \text{(Legendre et al., 2012, Eq. 6)}\,. \tag{6.7}$$

The computed aspect ratios agree well with the proposed correlation

$$\chi = \frac{1}{1 - \frac{9}{64}\,\mathrm{We}\left(1 + 0.2\,\mathrm{Mo}^{\frac{1}{10}}\,\mathrm{We}\right)^{-1}} \quad \text{(Legendre et al., 2012, Eq. 7)} \tag{6.8}$$

over the entire parameter range investigated in this study. There is still scope for various im-

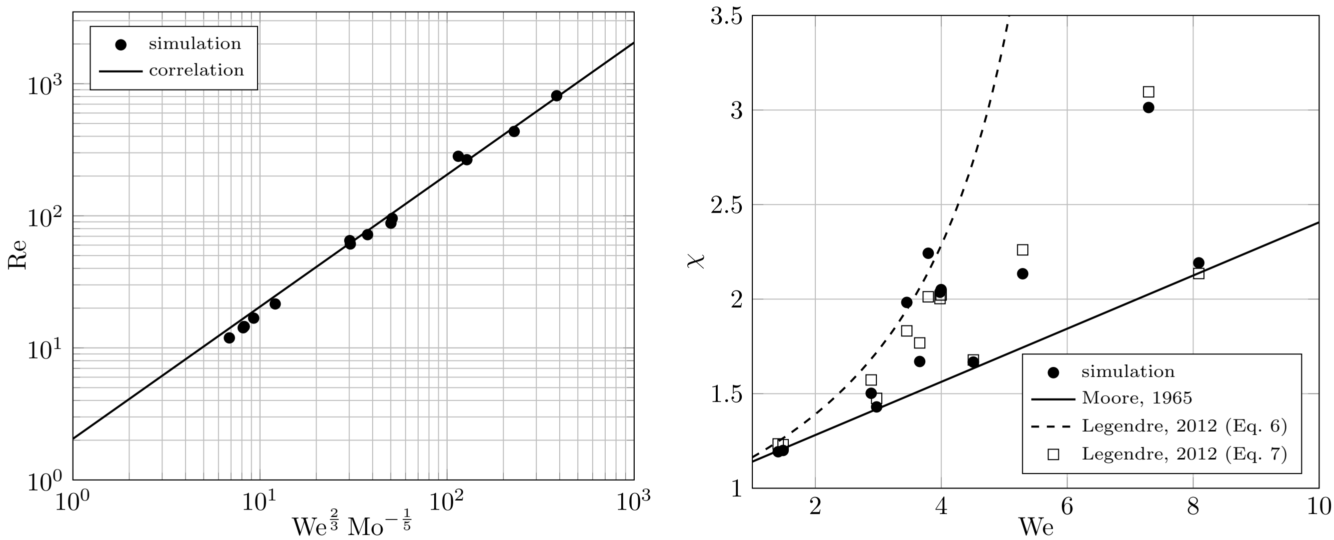

(a) Correlation between Re, We and Mo based on Legendre et al. (2012).

(b) Aspect ratio comparison to correlations presented in Legendre et al. (2012).

Figure 6.10.: Comparison of parameter study hydrodynamic results to literature data

provements of the interFoam solver family (see Appendix D) and a large number of different parameters have been varied in the presented simulation campaign. For these two reasons, despite this would be desirable, extending the parameter space and/or a mesh sensitivity study has been found out of scope (and potentially out of reach due to limited computational resources).

6.2 Towards an Improved Sherwood Correlation

The final main aim of this work is the derivation of a closure model for interfacial species transfer with a large range of validity, taking into account all influencing parameter. Standard closure approaches take a form as given in Eq. (6.1), modelling the mass transfer in dependence of the Schmidt and Reynolds numbers only, disregarding the effects of bubble shape. To obtain a full description of the mass transfer, additional influence parameters are to be considered. In order to obtain all relevant influence parameter for a mass transfer correlation, a dimension analysis is performed. Considering the simplified species transport equation (2.61), here repeated for convenience of the reader,

$$\partial_t c + \nabla\cdot(c\mathbf{u}) = \nabla\cdot(D\nabla c)\ ,$$

the non-dimensional form then reads

$$\partial_{t^*} c^* + \nabla^*\cdot(c^*\mathbf{u}^*)\,\frac{\mathbf{u}_{\text{rel}} t_{\text{rel}}}{\mathbf{x}_{\text{rel}}} = \nabla^*\cdot(D^*\nabla^* c^*)\,\frac{D_{\text{rel}} t_{\text{rel}}}{\mathbf{x}_{\text{rel}}^2}\ . \tag{6.9}$$

Defining $\mathbf{u}_{\text{rel}} t_{\text{rel}} = \mathbf{x}_{\text{rel}}$ then leads to the non-dimensional species transport equation with one non-dimensional parameter

$$\begin{aligned}\partial_{t^*} c^* + \nabla^*\cdot(c^*\mathbf{u}^*) &= \nabla^*\cdot(D^*\nabla^* c^*)\,\frac{D_{\text{rel}}}{\nu_{\text{rel}}}\,\frac{\nu_{\text{rel}}}{\mathbf{x}_{\text{rel}}\mathbf{u}_{\text{rel}}} \\ &= \nabla^*\cdot(D^*\nabla^* c^*)\,\frac{1}{\text{Re Sc}}\ .\end{aligned} \tag{6.10}$$

Thus, the non-dimensional species concentration transport is only dependent on the Peclet number (Pe = Re Sc). From this result, the Sherwood correlation (which is a non-dimensionalized form of the concentration gradient at the interface, cf. Eq. (2.96)) is assumed to be a function of the Peclet number only. However, the dimensionless velocity profile and the bubble shape is a function of the Eötvös and Reynolds numbers. Thus, the Sherwood correlation is assumed to take the following form:

$$\text{Sh} = f(\text{Re}, \text{Eo}) \cdot g(\text{Pe})\ ,$$

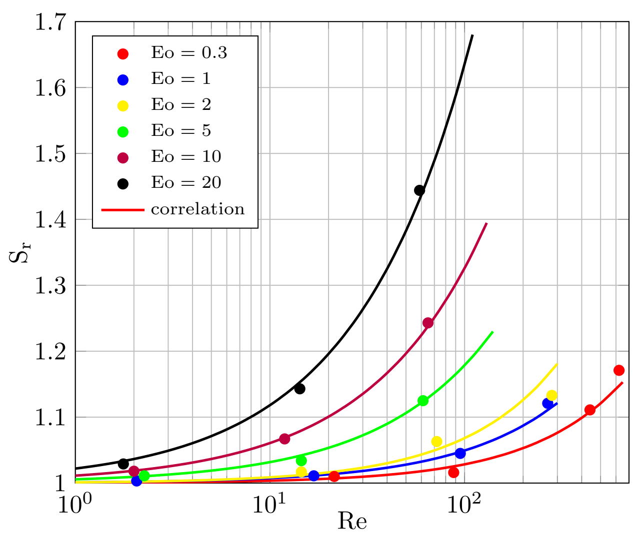

(a) Bubble area closure.

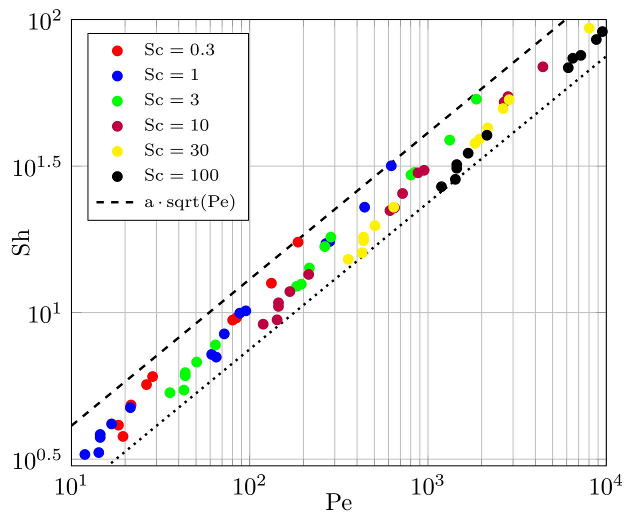

(b) Sherwood number closure.

Figure 6.11.: Towards an improved closure model for interfacial mass transfer

where $f(\mathrm{Re}, \mathrm{Eo})$ denotes a correction factor describing the influence of changes in the local velocity field due to bubble deformation. This form of correlation can also be found in the literature, for example in Lochiel and Calderbank (1964), who introduce an aspect ratio to include the bubble shape influence onto the velocity field. From the above reasoning, it can be deduced that the influence of the Schmidt number for a given set of material parameter (and thus fixed velocity field) is approximately constant. From the solution of a potential flow field around a sphere, the Sherwood number is expected to be a function of Sc^a with a close to 0.5.

In order to improve existing mass transfer correlations, the results of the conducted parameter study are utilised to obtain insights into the surface area dynamically changing with the bubble shape and its dependency on the global Sherwood number. The main results are visualised in Figures 6.11a and 6.11b.

Figure 6.11a shows that the interfacial area increases significantly with increasing Reynolds and Eötvös numbers. Here, the influence of the Eötvös number is dominant, which is not surprising. The well-known Grace diagram (Clift et al., 1978) for instance visualises – although not quantifies – this effect. Figures 6.11b and 6.13a on the other hand show that the global Sherwood number decreases with increasing bubble deformation (i.e. increasing Eötvös number). However, Figure 6.11b also shows that the decrease in global Sherwood number due to

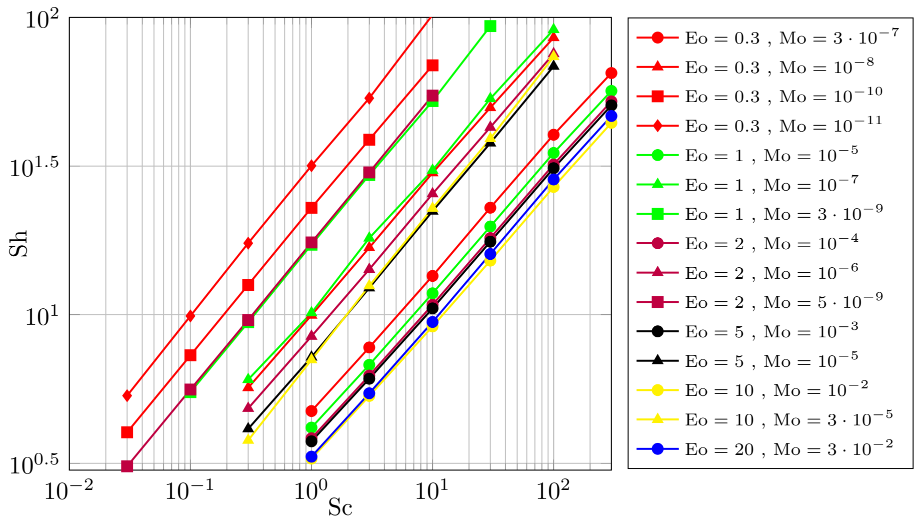

Figure 6.12.: Dependency of global Sherwood number from Schmidt number

bubble deformation is strictly limited by a lower bound, while the upper bound is approximately given by $\mathrm{Sh}_{\mathrm{max}} = \frac{2}{\sqrt{\pi}} \sqrt{\mathrm{Pe}}$. The simulation results show that the upper limit is only surpassed for (nearly) spherical path-instable bubbles (cf. Figure 6.13a). The dependency of the global Sherwood number on the Schmidt number is further investigated. It was found from the simulation results that this functional relation follows in good approximation a power law with a constant exponent and a material system-dependent pre-factor. This means that the global Sherwood number for any given material system is seen to solely depend on the Schmidt number via

$$\mathrm{Sh} = a \cdot \mathrm{Sc}^b \,, \tag{6.11}$$

where $a = g(\mathrm{Eo}, \mathrm{Re})$ and b have been found to be almost constant. Fitting b for different cases

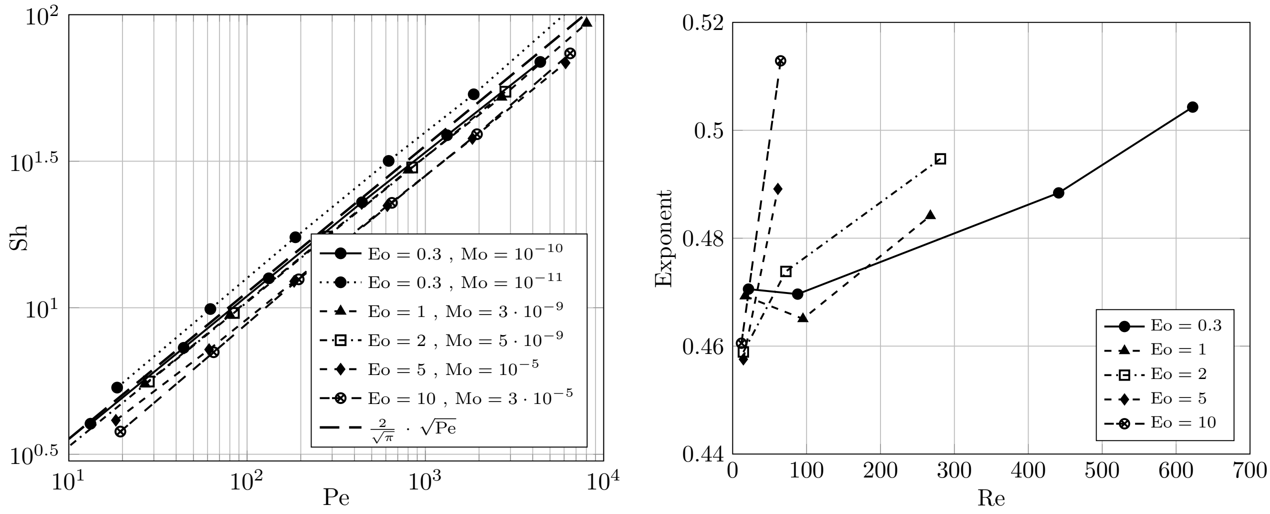

(a) Bubble shape dependency. **(b)** Schmidt number exponent.

Figure 6.13.: Influence of bubble shape onto global Sherwood number

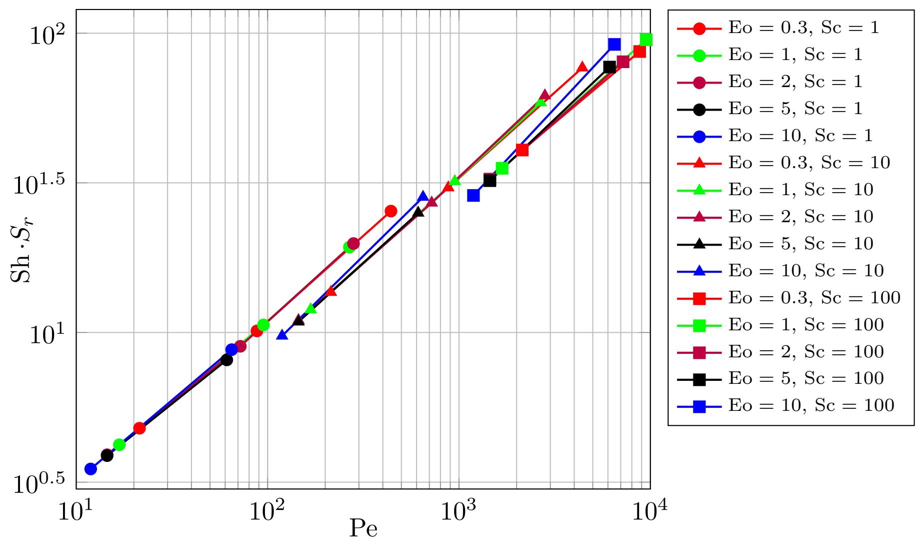

Figure 6.14.: Non-dimensionalized $k_l A$ as a function of the Peclet number

yields values of approximately 0.5 (cf. Figure 6.13b). This then results with a set of curves, where all simulation data points lie on straight lines of slope ≈ 0.5 in the double-logarithmic plot as shown in Figure 6.12. It can be seen that the exponent, as expected, varies only slightly from the theoretical value of 0.5, obtained, e.g., in the analytical solution of potential flow around a sphere. However, Figure 6.13b shows that the exponent does indeed slightly increase with increasing Reynolds and Eötvös number (i.e. increasing bubble deformation). The functional relation of the pre-factor a can be described in good agreement by

$$a = \gamma(S_r)\,\mathrm{Re}^{0.5}\,, \tag{6.12}$$

hence depending on the surface ratio and Reynolds number. This form is also suggested by Lochiel and Calderbank (1964) based on analytical investigations of mass transfer from ellipsoidal bubbles. Since nearly all Sherwood correlations reported in the literature are based on the

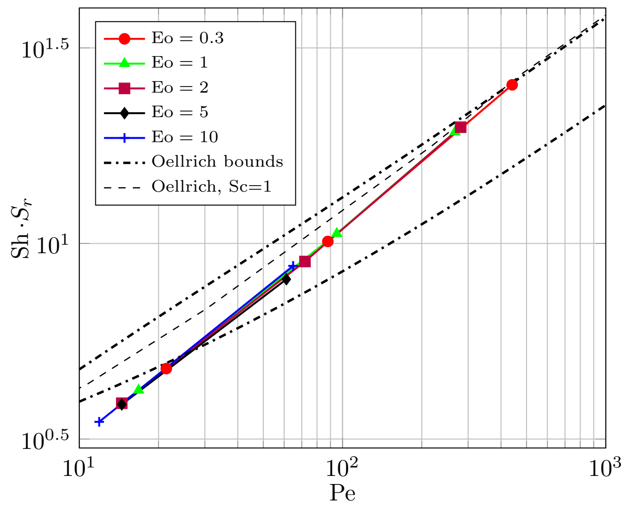

(a) Sc = 1.

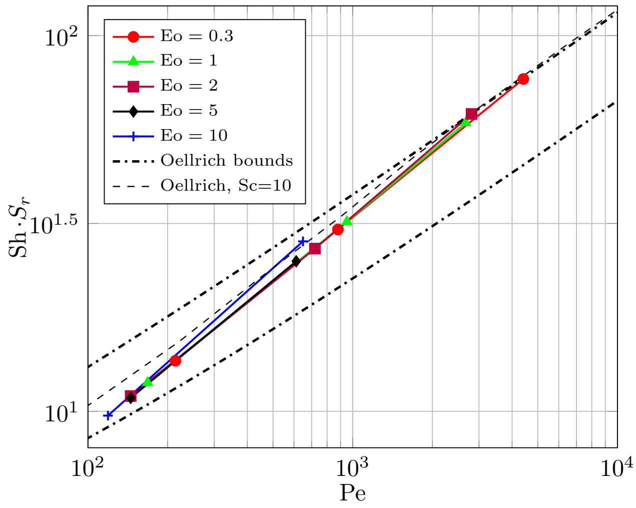

(b) Sc = 10.

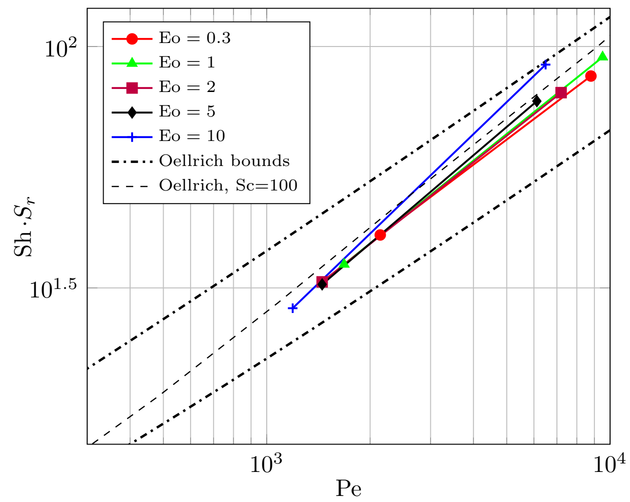

(c) Sc = 100.

Figure 6.15.: Comparison of simulation results with correlation of Oellrich et al. (1973)

area of volume-equivalent spheres, they are a non-dimensional form of $k_l A$ and thus comparison with numerical results presented here have to account for this fact. The non-dimensionalized $k_l A$ coefficient ($= \mathrm{Sh} \cdot S_r$) as a function of the Peclet number is given in Figure 6.14. It can be seen that for Schmidt equal to unity, the total mass transfer from volume-equivalent bubbles is virtually independent of the material system over the investigated range of Eötvös and Reynolds numbers. A comparison of the numerical results to the correlations of Oellrich et al. (1973) is given in Figures 6.15. It can be seen that the numerical results agree well with the correlations proposed in Oellrich et al. (1973), in both upper and lower bound, as well as the dependency of the Sherwood number on the Schmidt number. A further comparison to the correlation proposed in Takemura and Yabe (1998) is given in Figure 6.16. Here, to better distinguish between the different curves, the numerical results are plotted separately for each Eötvös number against the correlation of Takemura and Yabe (1998). As the correlation is only valid for large Schmidt numbers, deviation from the numerical results at small Schmidt numbers can be ignored. How-

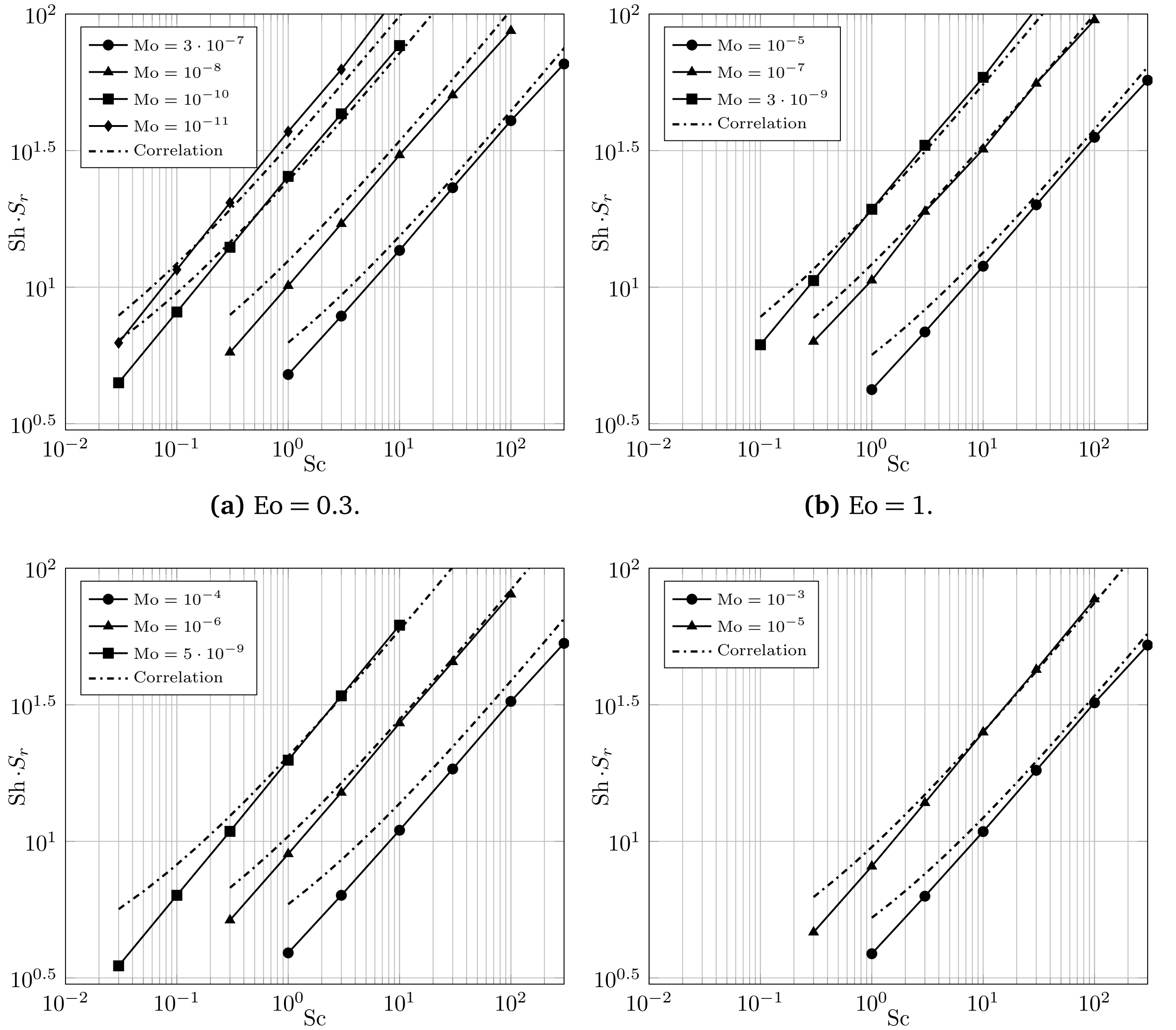

(a) Eo = 0.3.

(b) Eo = 1.

(c) Eo = 2.

(d) Eo = 5.

Figure 6.16.: Comparison of simulation results with correlation of Takemura and Yabe (1998)

ever, especially for very small and very large Reynolds numbers, a deviation from the proposed correlation can be seen. The deviation at large Reynolds numbers (cf. Figure 6.16a, $\mathrm{Mo} = 10^{-11}$) is to be expected as the correlation of Takemura and Yabe (1998) is derived from experimental data for $\mathrm{Re} < 100$. The source of deviation for small Reynolds numbers (cf. Figure 6.16c, $\mathrm{Mo} = 10^{-4}$) remains unclear. Overall, it can be seen that the numerical results agree well with the correlation.

At larger Schmidt numbers, the increase of the slope as shown in Figure 6.13b results in a separation, leading to enhanced mass transfer for bubbles with stronger deformation. From Figure 6.13b, the increase in mass transfer with stronger bubble deformation is expected to increase further with increasing Schmidt number.

In industrial processes though, especially the material system but also the total gas volume is usually fixed, allowing only for changes in bubble diameter. Since the dependence of the mass transfer from the Reynolds number can be described as a power law with exponent smaller than unity, for such processes smaller bubble size is expected to lead to an increase in total mass transfer. In cases, though, where the total gas holdup in the process depends on the bubble size, an optimal finite bubble size may exist.

7 Summary & Outlook

7.1 Conclusion of This Work

This Thesis investigates the transfer process of a dilute species in two-phase gas-liquid flows, employing Direct Numerical Simulations based on an algebraic Volume-of-Fluid method. A novel single-field model, named *Continuous Species Transfer (CST)* model is introduced which enables the accurate simulation of species transfer in context of above class of methods (Deising et al., 2016, 2018).

A major challenge in the simulation of species transfer processes is to capture the very thin concentration boundary layer adjacent to the interface, typical for gas-liquid flows. In this work, local dynamic adaptive mesh refinement and dynamic load balancing techniques are employed to sufficiently resolve the concentration boundary layer in a computationally very efficient way. The presented framework supports unstructured meshes of general topology, enabling also the simulation of species transfer in complex geometries. This contribution contains the method development, verification and validation as well as the application to single rising bubbles with the aim of deducing an improved closure relation for interfacial species transfer. Critical influence parameter onto the mass transfer are identified and studied based on a dimensional analysis of the species transport equation. Besides the Peclet number, the velocity profile in the boundary layer also affects mass transfer and can be formulated as a function of the Reynolds and Eötvös numbers. Further, unlike in literature the effects of changes in the concentration gradient at the interface as well as the changes of bubble shape onto the mass transfer are also studied separately, showing a significant reduction of the Sherwood number with increasing Eo and decreasing Mo. At the same time the interfacial area increases, eventually leading to enhanced mass transfer at strongly deformed bubbles. Thus it is argued that splitting of the mass transfer coefficient into a closure relation for the interfacial area and the Sherwood number is beneficial and leads to a more detailed description of the mass transfer process. Additionally, the influence of the Schmidt number is found to be (nearly) constant in context of physisorption for a given bubble diameter and fixed material properties (= fixed flow field). Thus in order to predict the species transfer (physisorption only) for realistic gas-liquid systems, it is sufficient to investigate the Schmidt number influence at increased diffusivities and then apply a scaling based on the actual Schmidt number. It was found that the change in Schmidt number dependence onto the Sherwood correlation with varying material parameter is very limited and was found to being close to its square root ($\mathrm{Sh} = a\ \mathrm{Sc}^{0.5}$) for the investigated parameter range.

One major aspect of this work is the identification of the necessity to separately investigate the two different causes for changes in global mass/species transfer: changes in local concentration gradients and changes in interfacial area. The numerical results presented in this thesis highlight the importance of accounting for bubble shape in mass transfer correlations. As reported in Lochiel and Calderbank (1964), bubble deformation is shown to lead to a substantial reduction in the Sherwood number but at the same time leads to an increase of interfacial area. Further, select mass transfer ($k_l A$) correlations in literature (Takemura and Yabe, 1998, Oellrich et al., 1973) are found to be in good agreement with the numerical results of the parameter study conducted in the scope of this research and thus applicable over a large parameter range. The numerical findings of this work can be utilized to improve the accuracy of detail-reduced simulation methods. An example is the two-fluid model, which requires an accurate species transfer correlation over a wide range of bubble shapes and local Reynolds numbers and also an accurate description of the local interfacial area which should also account for changes due to interface deformation.

7.2 Open Questions & Further Work

To obtain species transfer closures with a larger range of applicability, the utilized hydrodynamic solver framework needs further improvements, mainly –but not solely– regarding the treatment of the surface tension force. This would enable the study of the Reynolds and Eötvös numbers onto the mass transfer over a large parameter range. Also, further studies regarding the influence of the Schmidt number onto the mass transfer should be undertaken to gain final insight into the exponent dependency from the Reynolds and Eötvös numbers (cf. Figure 6.13b) over a wide parameter range. In terms of method development, additional studies have to be performed to understand the influence of mesh resolution onto model closure in scope of conditional volume-averaged single-field equation methods.

Future work is foremost concerned with the study of species transfer in bubble groups. A main aim is the understanding and quantification of swarm influence onto species transfer processes. Additionally, the method is to be systematically applied to the study of chemisorption processes at single rising bubbles and bubble swarms. A major advantage of the presented framework is its applicability to unstructured meshes of general topology. Thus, the study of species transport processes in complex geometries like structured packings should be feasible within the presented framework. In terms of method development, an interesting step forward would be the investigation of (non-dilute) mass transfer processes which however requires considerable modifications to the presented method.

A High Resolution Schemes for the Advection of Sharp Fields

For reasons of applicability on unstructured meshes, only interpolation schemes utilizing a two- or three-node stencil as in Figures 3.2a and 3.2b are considered here. Focussing on the advective transport of an arbitrary quantity, as mentioned in Section 3.1.1, boundedness of the discretization is not inherently given and needs to be enforced through boundedness criteria. To better understand the effects of truncation errors, a stability analysis based on the modified partial differential equation (Warming and Hyett, 1974) can be performed. The modified equation is obtained by first deriving the discretized PDE utilizing any specific discretization schemes, then expanding each term by a Taylor series expansion and finally eliminating time derivatives higher than first-order (Warming and Hyett, 1974). Based on the study of a one-dimensional advection equation

$$\partial_t \phi + u \frac{\partial \phi}{\partial x} = 0\,, \tag{A.1}$$

different modified equations are obtained, depending on the utilized discretization schemes. An exemplary analysis for four different Finite Difference discretizations yields the modified equations listed in Table A.1. For first-order schemes, the modified equation always takes the

scheme	modified equation
upwind	$\partial_t \phi + u \frac{\partial \phi}{\partial x} = \frac{u \Delta x}{2} \left(1 - \mathrm{C}\right) \frac{\partial^2 \phi}{\partial x^2}$
Lax-Friedrichs	$\partial_t \phi + u \frac{\partial \phi}{\partial x} = \frac{u \Delta x}{2} \left(\frac{1}{\mathrm{C}} - \mathrm{C}\right) \frac{\partial^2 \phi}{\partial x^2}$
Lax-Wendroff	$\partial_t \phi + u \frac{\partial \phi}{\partial x} = -\frac{u \Delta x^2}{2} \left(1 - \mathrm{C}^2\right) \frac{\partial^3 \phi}{\partial x^3}$
Beam-Warming	$\partial_t \phi + u \frac{\partial \phi}{\partial x} = \frac{u \Delta x^2}{6} \left(1 - \mathrm{C}\right)\left(2 - \mathrm{C}\right) \frac{\partial^3 \phi}{\partial x^3}$

Table A.1.: Modified equations for first- and second-order schemes

form

$$\partial_t \phi + u \frac{\partial \phi}{\partial x} = D_n \frac{\partial^2 \phi}{\partial x^2}\,. \tag{A.2}$$

The system actually solved for is an advection-diffusion equation with the numerical diffusion coefficient D_n. Second-order schemes result in a modified equation of the form

$$\partial_t \phi + u \frac{\partial \phi}{\partial x} = \mu_n \frac{\partial^3 \phi}{\partial x^3} \tag{A.3}$$

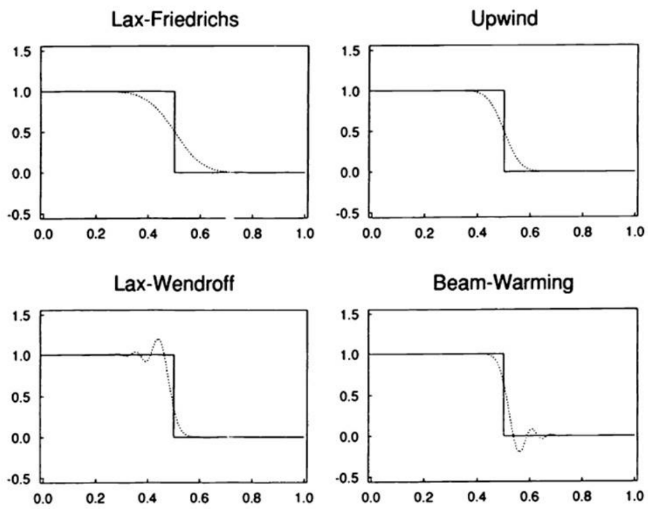

Figure A.1.: Numerical and exact solution of the Riemann problem for $u = 1$, $\Delta x = 0.01$, $\Delta t = 0.005$ at time $t = 0.5$

with the numerical dispersion coefficient μ_n. While it is obvious from Eq. A.2 that first-order schemes add numerical diffusion, the effect of numerical dispersion is not directly evident. Based on a Fourier series analysis, it can be shown that numerical dispersion leads to oscillations in the transport of a sharp field (LeVeque, 2002, Hirsch, 2007), which occur upwind of the discontinuity for negative and downwind of the discontinuity for positive dispersion coefficients (see Figure A.1).

The difficulty for a suitable discretization of the advection term is to obtain a scheme which minimizes numerical diffusion without introducing oscillations. One natural choice would be to take a dispersive (second-order) scheme and add an artificial diffusion term with constant diffusivity $\Gamma = Q\Delta x^2$, hoping that for large diffusion coefficients, the numerically induced oscillations would vanish. However, as proven by Godunov's theorem: "A linear, monotonicity-preserving scheme is at most first-order accurate."

The term **monotonicity-preserving** is the central point in the development of suitable schemes for the discretization of advection schemes. Monotonicity is a property of the numerical scheme, preserving boundedness by ensuring that

(i) no new extrema are generated

(ii) the value at local minima is non-decreasing and value at local maxima is non-increasing.

This can be formulated as an inequality, leading to

$$\min_k \left(\phi_k^o\right) \leq \phi_P^n \leq \max_k \left(\phi_k^o\right) \ \forall \ P \,, \tag{A.4}$$

where k addresses all nodes utilized in the interpolation scheme. Another way to define monotonicity is through **positivity** of all coefficients constituting the numerical discretization. Any time-explicit linear discretization to the advection equation (A.1) can be written as

$$\phi_P^n = \phi_P^o + \sum_k b_k \left(\phi_k^o - \phi_P^o\right) \quad \text{, with } \sum_k b_k = 1 \tag{A.5}$$

and is monotone if the constituting coefficients b_k are positive ($b_k \geq 0\ \forall k$), which is similar to the *positivity condition* by Spekreijse (1987). From A.5 it can directly be seen that the values at local extrema cannot increase. in the literature, many different methods to derive bounded advection schemes exist which essentially result in the same conditions, especially for linear schemes (Hirsch, 2007). These different methods are the *Total Variation Diminishing (TVD)* (Harten, 1982, 1983), the aforementioned *positivity condition* (Spekreijse, 1987), the *Convection Boundedness Criterion* (Gaskell and Lau, 1988, Leonard, 1988) based on the *Normalized Variable Formulation* (Leonard, 1988) and the *Local Extremum Diminishing* (Jameson, 1995). It should be noted that all these criteria were derived to ensure boundedness of explicit discretization schemes. Boundedness criteria for implicit schemes are not as restrictive (due to the induced numerical diffusion) and are discussed in Section A.3. The analysis of bounded advection schemes presented here is adapted to the implementation of high-order advection schemes in the OpenFOAM®library.

A.1 Total Variation Diminishing (TVD) Schemes

One possible practical way to derive bounded higher-order advection schemes was introduced by Harten (1983) based on the concept of *Total Variation Diminishing (TVD)*. This concept follows directly from the monotonicity criterion in Equation A.4 and reads (for the discrete case)

$$\mathrm{TV}(\phi^n) \overset{!}{\leq} \mathrm{TV}(\phi^o)\ ,\ \text{with}\ \mathrm{TV}(\phi) \equiv \sum_{\Omega} |\phi_P - \phi_N|\,. \tag{A.6}$$

Based on a Finite Volume discretization using only face-neighbouring cell information, a numerical scheme for the advection equation yields

$$\begin{aligned} &\partial_t \phi + \mathbf{u}\frac{\partial \phi}{\partial x} = 0 \quad \overset{\text{FVM}}{\Rightarrow} \quad \frac{\phi^n_C - \phi^o_C}{\Delta t} + \frac{1}{V_P}\sum_f F^o_f \phi^o_f = 0 \\ &\Leftrightarrow \phi^n_C = \phi^o_C + \mathrm{U}^o_C\left(\phi^o_U - \phi^o_C\right) + \mathrm{D}^o_C\left(\phi^o_D - \phi^o_C\right)\,, \end{aligned} \tag{A.7}$$

with arbitrary coefficients U^o_C and D^o_C depending on the chosen face interpolation scheme. It was shown by Harten (1983) that above discretization ensures the TVD criterion if the coefficients fulfil the following conditions

$$\begin{aligned} &\mathrm{U}^o_C \geq 0 \quad \forall C \\ &\mathrm{D}^o_C \geq 0 \quad \forall C \\ &\mathrm{U}^o_C + \mathrm{D}^o_C \leq 1 \quad \forall C\,. \end{aligned} \tag{A.8}$$

An extension of the TVD analysis to implicit and semi-implicit schemes can be found in Jameson and Lax (1986). The TVD criterion shown in Equation A.8 can be utilized to derive a class of homonymous advection schemes based on a **flux limiter** formulation.

The *flux limiter* approach is based on writing a Finite Volume discretization as a sum of a bounded lower-order 'lo' scheme and an unbounded higher-order 'ho' correction to be limited:

$$\phi_C^n = \phi_C^o + \frac{\Delta t}{\Delta x}\left(F_{\phi,D}^o - F_{\phi,U}^o\right) = \phi_C^o + \frac{\mathbf{u}\Delta t}{\Delta x}\left(\phi_{f+}^o - \phi_{f-}^o\right)\text{ , with} \tag{A.9}$$

$$\phi_{f+} = \left(\phi_{f+}^o\right)^{\text{lo}} + \psi(r_C)\left[\left(\phi_{f+}^o\right)^{\text{ho}} - \left(\phi_{f+}^o\right)^{\text{lo}}\right], \tag{A.10}$$

$$\phi_{f-} = \left(\phi_{f-}^o\right)^{\text{lo}} + \psi(r_U)\left[\left(\phi_{f-}^o\right)^{\text{ho}} - \left(\phi_{f-}^o\right)^{\text{lo}}\right], \tag{A.11}$$

$$\text{where } r_C \equiv \left.\frac{\partial\phi}{\partial x}\right|_{f-} \Big/ \left.\frac{\partial\phi}{\partial x}\right|_{f+} \overset{\text{uniform mesh}}{=} \frac{\phi_C - \phi_U}{\phi_D - \phi_C} \tag{A.12}$$

denotes the solution gradient ratio. The definition for the limiter function $\psi(r_C)$ and the solution gradient ratio r_C given here is not unique and other definitions can also be found in the literature. In above equation, a constant velocity $\mathbf{u}$ is assumed. The case of multidimensional advection with a varying velocity field is discussed in Section A.4. When used in the form as shown in Eq. A.9, the flux limiter is also called *slope limiter*, as it actually limits the face interpolated value depending on the gradients over the current and upwind faces. In Sweby (1984), conditions for a flux limiter based on the first-order Lax-Wendroff scheme are derived, which are widely cited in the literature. However, a common implementation of TVD schemes, e.g., in the C++library OpenFOAM®, is based on blending of upwind and central differences scheme:

$$\phi_{f+} = \phi_C^o + \psi(r_C)\left[\left(\phi_D^o\delta_{f+} + \phi_C^o\left(1-\delta_{f+}\right)\right) - \phi_C^o\right] = \phi_C^o + \delta_{f+}\psi(r_C)\left(\phi_D^o - \phi_C^o\right), \tag{A.13}$$

$$\phi_{f-} = \phi_U^o + \delta_{f-}\psi(r_U)\left(\phi_C^o - \phi_U^o\right). \tag{A.14}$$

Here, δ_{f+} and δ_{f+} denote the mesh weights on non-uniform meshes, defined as

$$\delta_{f+} := \frac{\left(\mathbf{x}_{f+} - \mathbf{x}_C\right)\cdot\mathbf{S}_{f+}}{\left(\mathbf{x}_D - \mathbf{x}_C\right)\cdot\mathbf{S}_{f+}}\;,\quad \delta_{f-} := \frac{\left(\mathbf{x}_{f-} - \mathbf{x}_U\right)\cdot\mathbf{S}_{f-}}{\left(\mathbf{x}_C - \mathbf{x}_U\right)\cdot\mathbf{S}_{f-}}\,. \tag{A.15}$$

This, however, leads to **different** conditions for the flux limiter compared to Sweby (1984) as is shown in the following (interested readers are also referred to Hou et al. (2012)). Substituting Equation A.13 and A.14 into A.9 yields

$$\begin{aligned}\phi_C^n &= \phi_C^o - \frac{\mathbf{u}\Delta t}{\Delta x}\left(\phi_C^o + \delta_{f+}\psi(r_C)\left(\phi_D^o - \phi_C^o\right) - \phi_U^o - \delta_{f-}\psi(r_U)\left(\phi_C^o - \phi_U^o\right)\right)\\ &= \phi_C^o - \mathrm{C}\left[1 + \delta_{f+}\frac{\psi(r_C)}{r_C} - \delta_{f-}\psi(r_U)\right]\left(\phi_C^o - \phi_U^o\right).\end{aligned} \tag{A.16}$$

In order for above discretization to be monotonicity preserving, one can enforce the positivity or TVD criterion (or others). For above equation to fulfil the TVD criterion, Equation A.8, the following condition must hold

$$\begin{aligned} & 0 \le \mathrm{C}\left[1 + \delta_{f+}\frac{\psi(r_C)}{r_C} - \delta_{f-}\psi(r_U)\right] \le 1\\ \Leftrightarrow\quad & -\frac{1}{\delta_{f+}} \le \frac{\psi(r_C)}{r_C} - \frac{\delta_{f-}}{\delta_{f+}}\psi(r_U) \le \frac{1}{\delta_{f+}}\left(\frac{1}{\mathrm{C}} - 1\right)\end{aligned} \tag{A.17}$$

for the two independent limiter functions $\psi(r_C)$ and $\psi(r_U)$ which are assumed to be positive ($\psi(r) \geq 0\,,\ \forall r$). The reader should note that application of the positivity criterion to Eqn. A.16 leads to exactly the same condition. It is evident that the limiter functions must be zero for negative r, i.e. when an extremum exists in cell C or U. Considering the worst-case scenarios

$$(i)\ \text{ from } \ \tfrac{\psi(r_C)}{r_C} \to \max\,,\ \psi(r_U) = 0 \quad \text{follows that} \quad 0 \leq \frac{\psi(r_C)}{r_C} \leq \frac{1}{\delta_{f+}} \frac{1-\mathrm{C}}{\mathrm{C}}\,, \tag{A.18}$$

$$(ii)\ \text{ from } \ \tfrac{\psi(r_C)}{r_C} = 0\,,\ \psi(r_U) \to \max \quad \text{follows that} \quad 0 \leq \psi(r_U) \leq \frac{1}{\delta_{f-}}\,, \tag{A.19}$$

the following conditions for the limiter function ψ can be derived which enforces the TVD criterion on the numerical discretization for time-explicit schemes and thus ensures boundedness of the advective transport:

$$\boxed{0 \leq \psi(r) \leq \min\left(\frac{1}{\delta_f} r \frac{1-\mathrm{C}}{\mathrm{C}}, \frac{1}{\delta_f}\right)}\,. \tag{A.20}$$

In comparison, based on an analysis of the flux limiter for the first-order Lax-Wendroff scheme, Sweby (1984) obtained the following conditions

$$0 \leq \psi(r) \leq \min(2r, 2)\,. \tag{A.21}$$

This leads to three conclusions about TVD criteria: The flux limiter condition

1. is dependent on the lower and higher-order schemes to be blended
2. of Sweby (1984) for the Lax-Wendroff scheme gives only a restrictive criterion and does not make full use of the TVD region
3. of Sweby (1984), in case of blending between upwind and central differences, only holds true for $\mathrm{C} \leq 0.5$ and uniform meshes.

The flux limiter function ψ limits the higher-order part of the transported flux. As shown in the derivation process, the same limiter can also be used to obtain a bounded face interpolation. It was shown by Sweby (1984) that in order for the face interpolation to be TVD and of second-order accuracy, the flux limiter function needs to be further restricted. The limiter function is required to fulfil $\psi(1) = 1$ and should be constructed by a convex combination of the Lax-Wendroff and Beam-Warming schemes, leading to the following criterion

$$\begin{aligned} r \leq \psi(r) \leq \min(2r, 1) \quad & \text{for } r < 1 \\ 1 \leq \psi(r) \leq \min(2r, 2) \quad & \text{else}\,. \end{aligned} \tag{A.22}$$

Another important property of limiter functions is the symmetry. When aiming to transport a variable initially symmetric in space, one usually would want the discrete (sometimes also called *reconstructed* (LeVeque, 2002)) data to have the same property. It is shown in LeVeque

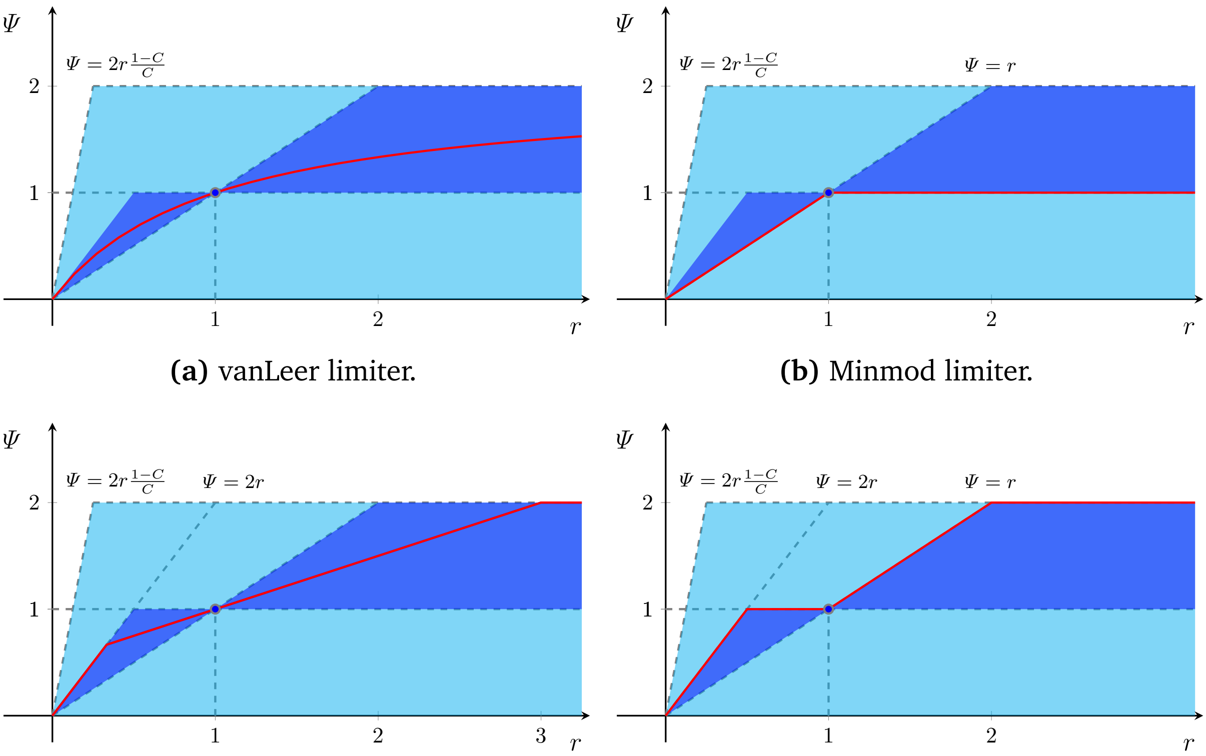

(a) vanLeer limiter.

(b) Minmod limiter.

(c) MC limiter.

(d) Superbee limiter.

Figure A.2.: Important limiter functions and TVD regions in the Sweby diagram

(2002) and Hirsch (2007) that this leads to a further requirement on the limiter function ψ, which must also satisfy

$$\psi\left(\frac{1}{r}\right) = \frac{\psi(r)}{r}\,. \tag{A.23}$$

Important limiter functions and the different above introduced TVD regions are shown in Figures A.2a to A.2d in form of the Sweby diagram (Sweby, 1984). It can be seen that the Minmod and Superbee limiters describe the outer borders of the second-order TVD region depending on Sweby's restriction on the flux limiter according to Equations A.21 and A.22. The maximum region to fulfil TVD (Equation A.20) is shown in figure A.2d. The vanLeer and MC limiters are symmetric limiters, the latter being linear in the region around $r = 1$, indicating that the MC limiter is second-order accurate over a relatively large region, whereas the vanLeer limiter is of second-order only at $\psi(r = 1) = 1$.

Based on the flux limiter formulation, the interpolation weights for the face interpolation can be calculated as

$$\phi_f = \phi_C + \delta_f \psi(r)\,(\phi_D - \phi_C) = \phi_C \underbrace{\left(1 - \delta_f \psi(r)\right)}_{\omega_C} + \phi_D \underbrace{\delta_f \psi(r)}_{1-\omega_C}\,. \tag{A.24}$$

On unstructured meshes, the centre cell of the interpolation stencil is either the parent or the neighbour cell of a face, based on the flux direction. Assuming a face flux $F_f > 0$, then $\phi_C = \phi_P$ and $\phi_D = \phi_N$ and defining the mesh weights $\omega_{\mathrm{CD}} \equiv \frac{(\mathbf{x}_N - \mathbf{x}_f)\cdot\mathbf{S}_f}{(\mathbf{x}_N - \mathbf{x}_P)\cdot\mathbf{S}_f}$ leads to

$$\phi_f = \phi_P \left[1 - \psi(r)\left(1 - \omega_{\mathrm{CD}}\right)\right] + \phi_N \psi(r)\left(1 - \omega_{\mathrm{CD}}\right) \quad \text{with } \delta_f = 1 - \omega_{\mathrm{CD}} \,. \tag{A.25}$$

Assuming a face flux $F_f < 0$, then $\phi_C = \phi_N$ and $\phi_D = \phi_P$ which leads to

$$\phi_f = \phi_N \left[1 - \psi(r)\,\omega_{\mathrm{CD}}\right] + \phi_P \psi(r)\,\omega_{\mathrm{CD}} \quad \text{with } \delta_f = \omega_{\mathrm{CD}} \,. \tag{A.26}$$

Assuming that – as is the case in OpenFOAM®– a face interpolation is formulated as

$$\phi_f = \omega_P \phi_P + \left(1 - \omega_P\right) \phi_N \,, \tag{A.27}$$

then the interpolation weights ω_P can be calculated from

$$\omega_P = \omega_{\mathrm{CD}} \psi(r) + \mathrm{pos}\left(F_f\right)\left[1 - \psi(r)\right] . \tag{A.28}$$

Above equation is utilized in the OpenFOAM®-library to calculate the interpolation weights from a given limiter function.

A.2 Normalized Variable Formulation (NVF) Schemes

Another approach to derive bounded non-linear higher-order discretization schemes for advection was introduced in Leonard (1988). Leonard herein utilizes the so-called Normalized Variable Formulation in correspondence with the Convection Boundedness Criterion (CBC) of Gaskell and Lau (1988) to derive another class of discretization schemes, known as Normalized Variable Diagram (or short: NVD) schemes. This procedure is analogous to the derivation of TVD schemes but instead of adding a limiter and ensuring boundedness by enforcing TVD conditions upon this limiter, in NVD schemes the boundedness criterion is directly enforced upon the face interpolated value. The introduced normalization of variables reads

$$\widetilde{\phi} := \frac{\phi - \phi_U}{\phi_D - \phi_U} \,. \tag{A.29}$$

To ensure monotonicity and not create new extrema, the normalized variable needs to be in the interval $\widetilde{\phi} \in [0, 1]$. This essentially is the Convection Boundedness Criterion introduced by Gaskell and Lau (1988) which reads

$$\begin{cases} \widetilde{\phi}_C \leq \widetilde{\phi}_f \leq 1 & \text{for } 0 \leq \widetilde{\phi}_C \leq 1 \\ \widetilde{\phi}_f = \widetilde{\phi}_C & \text{else} \,. \end{cases} \tag{A.30}$$

Here, the benefit of the normalized variables becomes eminent – the straight-forward way to define boundedness. The CBC criterion simply states that the face-interpolated value should be between the values in the two neighbouring cells C and D. In comparison, the application of the TVD criterion leads to a more complex condition on the discretization weights (see Equation A.8). However, above criterion only ensures boundedness for implicit solutions and in steady-state cases as it only considers information from one time level. It does not ensure that the solution in the next time step remains bounded. Therefore, Leonard (1991) introduces a time-dependent criterion for explicit solutions, the transient CBC criterion depending on the Courant number, which reads

$$\begin{cases} \widetilde{\phi}_C \leq \widetilde{\phi}_f \leq \frac{\widetilde{\phi}_C}{\mathrm{C}_f} & \text{for } 0 \leq \widetilde{\phi}_C \leq \mathrm{C}_f \text{ , with } \mathrm{C}_f < 1\,, \\ \widetilde{\phi}_C \leq \widetilde{\phi}_f \leq 1 & \text{for } \mathrm{C}_f < \widetilde{\phi}_C \leq 1\,, \\ \widetilde{\phi}_f = \widetilde{\phi}_C & \text{else}\,. \end{cases} \tag{A.31}$$

The interpolation schemes following the bounds of the transient CBC region are the upwind scheme (lower bound) and the Hyper-C scheme (upper bound). In the following it is shown that the condition for the flux limiter function (Eq. A.20) derived by application of the TVD criterion (Eq. A.8), poses the exact same conditions on the face-interpolated variable as does above transient Convection Boundedness Criterion, which, to the author's best knowledge, has not been shown before. To see this, the Hyper-C scheme is transferred into a limiter formulation based on the assumption of a uniform mesh:

$$\begin{aligned}
&\widetilde{\phi}_{f,\text{Hyper-C}} = \min\left(\frac{\widetilde{\phi}_C}{\mathrm{C}_f}, 1\right) \\
&\phi_{f,\text{Hyper-C}} \stackrel{!}{=} \phi_C + \delta_f \psi(r)\left(\phi_D - \phi_C\right) \\
\overset{\phi_C \leq \frac{1}{\mathrm{C}_f}}{\Longleftrightarrow}\ &\widetilde{\phi}_{f,\text{Hyper-C}} = \widetilde{\phi}_C + \delta_f \psi(\widetilde{r})\left(\widetilde{\phi}_D - \widetilde{\phi}_C\right) = \widetilde{\phi}_C + \delta_f \psi(\widetilde{r})\left(1 - \widetilde{\phi}_C\right) \stackrel{!}{=} \frac{\widetilde{\phi}_C}{\mathrm{C}_f} \\
\Rightarrow\ &\psi(\widetilde{r}) = \frac{1}{\delta_f}\widetilde{r}\,\frac{1-\mathrm{C}_f}{\mathrm{C}_f} \quad \text{, with } \widetilde{r} \equiv r\left(\widetilde{\phi}_C\right) = \frac{\widetilde{\phi}_C}{1-\widetilde{\phi}_C} && \text{(A.32)} \\
\Longleftrightarrow\ &\psi(r) = \min\left(\frac{1}{\delta_f} r\,\frac{1-\mathrm{C}_f}{\mathrm{C}_f}, \frac{1}{\delta_f}\right). && \text{(A.33)}
\end{aligned}$$

From above derivation, five important facts about NVD and TVD schemes can be obtained:

(a) Every NVD scheme can be written as $\widetilde{\phi}_f = f\left(\widetilde{\phi}_C\right)$

(b) TVD and transient CBC criterion result in the exact same restrictions on the face-interpolation (Equation A.20 with the definition of the face-interpolated variable Eq. A.13, is identical to Eq. A.31)

(c) TVD schemes can conveniently be transferred into NVD schemes and vice versa

(d) The interpolation scheme which follows the upper limit of the transient CBC and TVD criteria is the Hyper-C scheme by Leonard (1988)

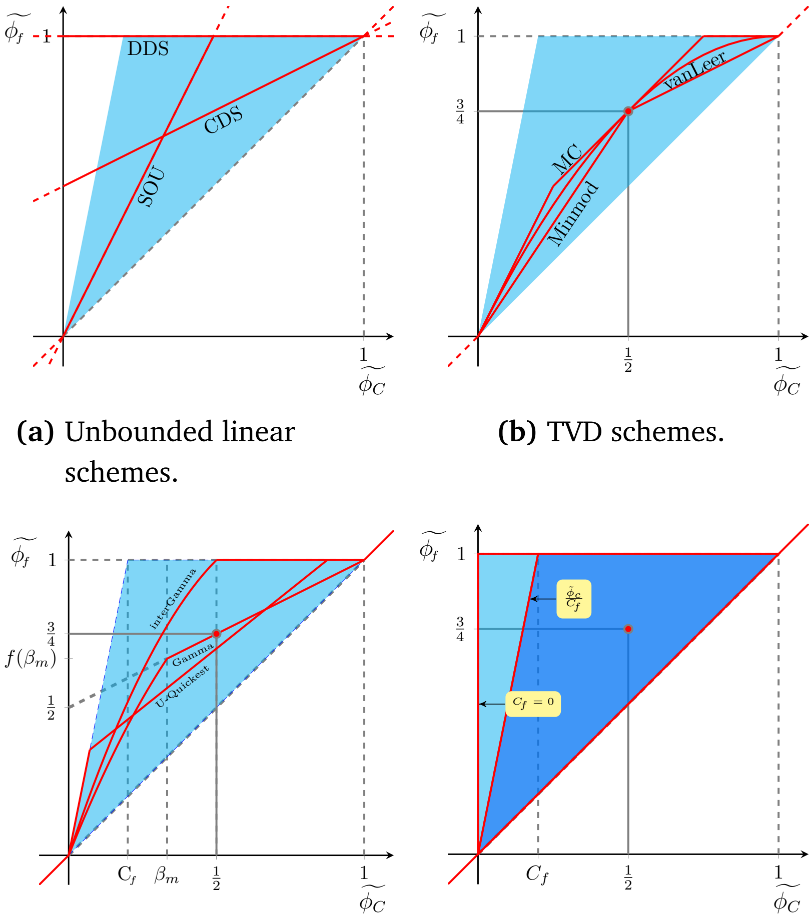

(a) Unbounded linear schemes.

(b) TVD schemes.

(c) NVD schemes.

(d) CBC and transient CBC.

Figure A.3.: Important interpolation schemes in the Normalized Variable Diagram

(e) While the TVD criterion is dependent on the mesh grading (δ), the transient CBC criterion on uniform and non-uniform meshes is the same.

The construction point of higher-order schemes can also be transferred into normalized variables. In the flux limiter formulation, the TVD scheme is second-order accurate if $\psi = 1$, in which case the central difference scheme is recovered. Second-order is usually enforced in the smooth region ($r \equiv (\phi_C - \phi_U)/(\phi_D - \phi_C) = d_{UC}/d_{CD}$), so that second-order TVD schemes are characterized by $\psi(r = d_{UC}/d_{CD}) = 1$. In normalized variables, the construction point translates to

$$\psi(r = d_{UC}/d_{CD}) = 1 \quad \Leftrightarrow \quad \psi(\tilde{r} = d_{UC}/d_{CD}) = 1$$

$$\tilde{r} = d_{UC}/d_{CD} = \frac{1-\widetilde{\phi}_C}{\widetilde{\phi}_C} \quad \Rightarrow \quad \widetilde{\phi}_C = \frac{1}{1+d_{UC}/d_{CD}} \tag{A.34}$$

$$\psi(d_{UC}/d_{CD}) = 1 \quad \Rightarrow \quad \widetilde{\phi}_f = \widetilde{\phi}_C + \delta_f\left(1-\widetilde{\phi}_C\right) = \frac{1}{1+d_{UC}/d_{CD}}\left(1-\delta_f\right) + \delta_f\,. \tag{A.35}$$

Hence, every scheme of at least second-order accuracy passes through $\left[\frac{1}{1+d_{UC}/d_{CD}}, \frac{1}{1+d_{UC}/d_{CD}}\left(1-\delta_f\right)+\delta_f\right]$ (or $\left[\frac{1}{2}, \frac{3}{4}\right]$ on uniform meshes) in the Normalized Variable

Diagram which shows the face-interpolated value as function of the cell-centred value in the face-upwind cell ($\widetilde{\phi}_f = f\left(\widetilde{\phi}_C\right)$). Figure A.3 shows some important interpolation schemes in the Normalized Variable Diagram, including unbounded linear schemes, TVD and NVD schemes.

A.3 Boundedness Criteria for Time-Implicit Schemes

This section contains a short discussion on time-implicit TVD schemes, based on the work of Harten (1982) with the aim of deriving a boundedness criterion for first-order time implicit discretization of an advection equation. As in Equation A.7, any discretization of the advection equation using information only from neighbouring cells (3-point stencil for face interpolations) can be written in the following form

$$\begin{aligned}
&\phi_C^n + \eta \frac{\Delta t}{\Delta x}\left[F^n_{\phi,f+} - F^n_{\phi,f-}\right] = \phi_C^o - (1-\eta)\frac{\Delta t}{\Delta x}\left[F^o_{\phi,f+} - F^o_{\phi,f-}\right] \quad \text{with} \\
&F_{f+} = \phi_C - \frac{\Delta x}{\Delta t} U_{f+}(\phi_D - \phi_C) = \phi_D - \frac{\Delta x}{\Delta t} D_{f+}(\phi_D - \phi_C) \quad \text{and} \\
&F_{f-} = \phi_U - \frac{\Delta x}{\Delta t} U_{f-}(\phi_C - \phi_U) = \phi_C - \frac{\Delta x}{\Delta t} D_{f-}(\phi_C - \phi_U) \\
\Leftrightarrow\; &\phi_C^n - \eta\left[U^n_{f+}\left(\phi_D^n - \phi_C^n\right) - D^n_{f-}\left(\phi_C^n - \phi_U^n\right)\right] \\
&= \phi_C^o + (1-\eta)\left[U^o_{f+}\left(\phi_D^o - \phi_C^o\right) - D^o_{f-}\left(\phi_C^o - \phi_U^o\right)\right],
\end{aligned} \tag{A.36}$$

with the implicitness factor $\eta \in [0, 1]$. It can be shown that above discretization is TVD if the l.h.s. ($L \cdot \phi^n$) is TVI (total variation increasing) and the r.h.s. ($R \cdot \phi^o$) is TVD:

$$\mathrm{TV}(\phi^n) \le \mathrm{TV}(L \cdot \phi^n) = \mathrm{TV}(R \cdot \phi^n) \le \mathrm{TV}(\phi^o)\,. \quad \square \tag{A.37}$$

Applying now the definition of TVD and TVI, conditions for the pre-factors U and D can be derived. Here, the discretization is performed for two neighbouring cells to formulate the Total Variation. The resulting conditions for the r.h.s. to be TVD are

$$\boxed{\begin{aligned}
&(1-\eta)\,U_f \ge 0 \\
&(1-\eta)\,D_f \ge 0 \\
&(1-\eta)\left(U_f + D_f\right) \le 1\,.
\end{aligned}} \tag{A.38}$$

These conditions are equivalent to Equation A.8 with the exception of the pre-factor $(1-\eta)$, which is not surprising since the derivation of both conditions is equivalent. For the semi-implicit discretization (A.36) to be TVD, the conditions for the l.h.s. pre-factors are still to be derived, leading to

$$U_f \ge 0 \;\text{ and }\; D_f \ge 0\,. \tag{A.39}$$

To understand what these criteria mean in terms of a flux (or slope) limiter formulation, the definition of the flux limited face-interpolant can be substituted into Eq. A.36, leading to the following restrictions for the limiter function:

$$0 \leq 1 + \delta_{f+} \frac{\psi(r_C)}{r_C^o} - \delta_{f-} \psi(r_U) \leq \frac{1}{1-\eta} \tag{A.40}$$

for the time-explicit limiters on the right-hand side and

$$1 + \delta_{f+} \frac{\psi(r_C)}{r_C^n} - \delta_{f-} \psi(r_U) \geq 0 \tag{A.41}$$

for the time-implicit limiters on the left-hand side of Eq. A.36. Exploiting the worst-case scenarios and keeping in mind that the limiter function ψ must always be greater or equal to zero, this leads to the following conditions on the limiter for semi-implicit discretization:

$$\boxed{\begin{array}{ll} 0 \leq \psi(r) \leq \min\left(\dfrac{1}{\delta_f} r \dfrac{1-\mathrm{C}}{\mathrm{C}} \dfrac{1}{1-\eta}, \dfrac{1}{\delta_f}\right) & \text{for explicit limiter} \\ 0 \leq \psi(r) \leq \dfrac{1}{\delta_f} & \text{for implicit limiter.} \end{array}} \tag{A.42}$$

The problem that appears for the implicit part is that the conditions on the slope limiter depend on the solution in the new time step. Hence, it requires iterating to a steady-state in each time step for transient calculations. On the other side, it can be seen that the implicit limiter is no longer dependent on the Courant number, allowing for a compressive face interpolation regardless of the time step length, whereas the conditions on the limiter for explicit time discretization are becoming more restrictive with increasing C, degenerating to first-order upwind scheme for $\mathrm{C} = 1$. It should be noted that the limiter conditions in Equation A.42 hold true for all values of the implicitness factor $\eta \in [0, 1]$. In case $\eta \equiv 1$, a pure implicit first-order time discretization is employed and the first condition is dropped.

However, the implicit criterion does not hold true on unstructured meshes, where the upwind node value is calculated explicitly and its information merged into the face-interpolation weights. Application of the implicit boundedness criterion on such meshes would require an accurate calculation of the solution gradient ratio r and outer iterations (e.g. SIMPLE loop) even in a steady-state case. Unfortunately, in tests performed in scope of this thesis, the outer iterations did not converge but rather the equation residuals were alternating and no bounded solution to the transport equation could be achieved.

A stability analysis for the implicit discretization using central differences shows that the discretization is semi-stable as all eigenvalues of the matrix are equal to unity. Hence, a numerical solution of the system is bound to create oscillations in the solution.

The transfer from discretization schemes on structured uniform meshes to unstructured meshes of arbitrary cell shape requires a series of modifications of the so-far presented theory. All conditions for boundedness presented in Sections A.1 and A.2 were derived for a one-dimensional advection equation with constant velocity. Thus, the derived criteria should first be enhanced by the inclusion of a non-constant velocity field. Unfortunately, literature about boundedness criteria in multiple dimensions is very scarce and fragmentary and moreover largely limited to Cartesian meshes. However, it can be proven that the transient CBC criterion is still applicable in multiple dimensions when defining the face Courant number as

$$\mathrm{C}_f := \left(\frac{\Delta t}{V_C} \sum_f \max\left(0, F_f\right) \right)_{f(\mathrm{upw}, F_f)} \qquad \text{, where } F_f = \mathbf{u}_f \cdot \mathbf{S}_f \,. \tag{A.43}$$

Here, a cell-based Courant number is computed, taking into account all outgoing fluxes of cell C and then interpolated on the face centres using the upwind scheme. This definition of the local Courant number ensures boundedness of the transient CBC and TVD regions also in multiple dimensions in case that no mesh-induced skewness errors appear. However, if this criterion makes use of the maximum boundedness region is not known to the author at present.

Another problem on unstructured meshes is the definition of the normalized variable $\tilde{\phi}$ and gradient ratio r which hold the influence of the upwind node onto the face interpolation in terms of NVD and TVD schemes, respectively. As on unstructured meshes of arbitrary polyhedral cell shape the definition of the upwind node is unclear, a different approach must be taken compared to the formulation of interpolation schemes on structured meshes. This leads to the introduction of a *virtual* upwind node U^* which is assumed to be positioned thus that cell C is centred between U^* and the downwind node D (Jasak et al., 1999)

$$\mathbf{x}_{U^*} = \mathbf{x}_C - \mathbf{d}_{CD} = \mathbf{x}_C - (\mathbf{x}_D - \mathbf{x}_C) \,. \tag{A.44}$$

The value of the transported quantity at the virtual upwind position is then approximated by

$$\begin{aligned} \nabla\phi_C \cdot \mathbf{d}_{UD} = 2\nabla\phi_C \cdot \mathbf{d}_{CD} \quad &\overset{\text{sec. order}}{\approx} \quad (\phi_D - \phi_{U^*}) \\ \Rightarrow \quad \phi_{U^*} \quad &\overset{\text{sec. order}}{\approx} \quad \phi_D - 2\nabla\phi_C \cdot \mathbf{d}_{CD} \,. \end{aligned} \tag{A.45}$$

Given Eqns. A.44 and A.45, the normalized values and gradient ratio can be computed as follows. The gradient ratio r under above assumptions reads

$$r = \left(\nabla\phi|_{f-} \,/\, \nabla\phi|_{f+} \right) \cdot \mathbf{n}_{f+} = \frac{\phi_C - \phi_{U^*}}{\phi_D - \phi_C} \approx \frac{\phi_C - \phi_D + 2\nabla\phi_C \cdot \mathbf{d}_{CD}}{\phi_D - \phi_C} = \frac{2\nabla\phi_C \cdot \mathbf{d}_{CD}}{\phi_D - \phi_C} - 1 \,. \tag{A.46}$$

According to Eq. A.46, normalized variables on unstructured meshes can be computed as

$$\tilde{\phi}_C = \frac{\phi_C - \phi_{U^*}}{\phi_D - \phi_{U^*}} = 1 - \frac{\phi_D - \phi_C}{2\nabla\phi_C \cdot \mathbf{d}_{CD}} \,. \tag{A.47}$$

Above formulae, however, are only accurate on uniform Cartesian meshes which can easily be shown. On unstructured meshes of arbitrary polyhedral cell shape and even on non-uniform Cartesian meshes, Equations A.46 and A.47 may lead to unbounded solutions as the derived boundedness criteria depend on the correct value of the upwind node rather than an estimated value. As a result, the boundedness criteria derived in the previous sections can strictly only be applied to equidistant meshes. Interpolation schemes which do not follow the borders of the boundedness criterion may still exhibit boundedness, depending on the mesh grading. The effect of reduced TVD region with increasing mesh grading shown in Equation A.20 is thus even stronger when utilizing a virtual upwind estimation. However, the reader should note that, if the mesh grading is large enough, any numerical scheme implemented on unstructured meshes using the virtual upwind approximation (Eqns. A.46 and A.47) will introduce unboundedness. This is a major drawback of NVD and TVD methods, which can be circumvented by using flux-corrected transport (FCT) algorithms (Zalesak, 1979). The FCT algorithm applied in the OpenFOAM®interFoam solver – multidimensional universal limiter with explicit solution (MULES) – introduced by Weller (2006) is discussed in Section A.6. A detailed derivation of the algorithm, as implemented prior to version 2.4.x, can be found in Deising (2015).

To dampen the negative effects of the virtual upwind introduction on arbitrary meshes, a limiting of the estimated virtual upwind value based on the neighbouring cells can be performed, as suggested e.g. by Przulj and Basara (2001). Here, based on the position of the virtual upwind node (Eq. A.44), a local search is performed to find a cell with centre position $\mathbf{x}_X$, so that the distance $|\mathbf{x}_{U*} - \mathbf{x}_X|$ becomes minimal. The utilized local search algorithm is described in Löhner (1995) and Maric et al. (2015). Then, the minimum and maximum values of ϕ in the vicinity of node X are computed and the virtual upwind value, estimated by Eq. A.45, is limited as

$$\phi_{U*} = \min\left[\max\left(\phi_{\min}, \phi_{U*}\right), \phi_{\max}\right] . \tag{A.48}$$

At last, the gradient ratio or normalized variables can be calculated using the definitions

$$r = \frac{\phi_C - \phi_{U*}}{\phi_D - \phi_C} , \tag{A.49}$$

$$\widetilde{\phi}_C = \frac{\phi_C - \phi_{U*}}{\phi_D - \phi_{U*}} . \tag{A.50}$$

Different limiting strategies of the virtual upwind node are, e.g., to limit ϕ_{U*} by the global minimum and maximum values or to calculate the normalized variable $\widetilde{\phi}_C$ from Eq. A.47 and then limit the result as $\widetilde{\phi}_C = \min\left[\max\left(0, \widetilde{\phi}_C\right), 1\right]$. A short overview of different approaches for virtual upwind limiting is given in Hill et al. (2018).

An alternative approach introduced in this work is a *weighted gradient interpolation*. Assuming a 1D mesh with arbitrary grading

$$\delta_{f+} = \frac{\mathbf{x}_{f+} - \mathbf{x}_C}{\mathbf{x}_D - \mathbf{x}_C} \quad \text{and} \quad \delta_{f-} = \frac{\mathbf{x}_{f-} - \mathbf{x}_U}{\mathbf{x}_C - \mathbf{x}_U} , \tag{A.51}$$

the gradient in cell C using Gauss' gradient computation reads

$$\begin{aligned}
\nabla\phi_C &= \frac{1}{\Delta x}\left(\phi_{f+(CDS)} - \phi_{f+(CDS)}\right) = \frac{1}{\Delta x}\left[\delta_{f+}\phi_D + \left(1-\delta_{f+}\right)\phi_C - \delta_{f-}\phi_C - \left(1-\delta_{f-}\right)\phi_U\right] \\
\Leftrightarrow\ \phi_U &= \frac{\mathbf{d}_{UC}}{\mathbf{d}_{CD}}\left[\phi_D - 2\nabla\phi_C \cdot \mathbf{d}_{CD} - \phi_C\right] + \phi_C\,,
\end{aligned} \tag{A.52}$$

where the identities $\Delta x = 2\delta_{f+}\mathbf{d}_{CD}$ and $\frac{\mathbf{d}_{UC}}{\mathbf{d}_{CD}} = \frac{\delta_{f+}}{1-\delta_{f-}}$ have been used. This means an improved algorithm could be obtained simply by estimating the ratio $\frac{\mathbf{d}_{UC}}{\mathbf{d}_{CD}}$. However, although reported here, the method has thus far not been tested thoroughly.

The interpolation schemes on unstructured meshes are implemented using the *down-wind weighting factor* as proposed by Leonard and Mokhtari (1990) and further discussed in Moukalled et al. (2015). Here, the influence of the virtual upwind node is explicitly used in the interpolation weights and the face-interpolated value is obtained according to

$$\phi_f = \gamma_{\mathrm{DWF}}\phi_C + \left(1-\gamma_{\mathrm{DWF}}\right)\phi_D\,, \tag{A.53}$$

where the downwind weighting factor γ_{DWF} is calculated from the TVD limiter or Normalized Variable Formulation as

$$\begin{aligned}
\gamma_{\mathrm{DWF}} &:= 1 - \frac{1}{2}\psi(r_C) \quad \text{or} \\
\gamma_{\mathrm{DWF}} &:= \frac{\widetilde{\phi}_f - \widetilde{\phi}_C}{1-\widetilde{\phi}_C}\,,
\end{aligned} \tag{A.54}$$

respectively. This interpolation technique in combination with the definition of the virtual upwind value and the TVD or CBC boundedness criteria only guarantees a bounded face interpolation on uniform hexahedral meshes. On other meshes, the virtual upwind value does not correspond exactly to the upwind cell value which leads to a higher interpolation error and can lead to unboundedness. However, the approach described in this section seems to preserve boundedness also on unstructured meshes of general topology, which is confirmed in Hill et al. (2018).

Furthermore, the usage of a downwind weighting factor will lead to stability problems in the implicit solution, if the explicit boundedness criterion is not fulfilled. It leads to off-diagonal entries in the matrix with opposite signs as shown, e.g., in Moukalled et al. (2015). Hence, one has to comply the transient CBC criterion even for fully time-implicit discretizations due to the usage of downwind weighting factors. A way to circumvent this problem was introduced in Moukalled et al. (2015) but could not be confirmed to maintain boundedness in scope of this thesis.

One other major problem with the discretization of the advection term on unstructured meshes are mesh-induced errors due to non-conjunctionality, commonly also referred to as *mesh skewness* (which actually includes both types of mesh-induced errors, non-conjunctionality and non-orthogonality). This error, in effect, reduces the overall accuracy and more importantly for the transport of sharp fields, adds numerical diffusion. Standard in the literature is a simple explicit correction which, however, cannot be used for the transport of fields with discontinuities or sharp gradients, as this approach leads to severe unboundedness. In this work, (semi-)implicit correction approaches for the advective and diffusive transport on unstructured meshes, as first introduced in Denner and van Wachem (2014, 2015) and enhanced in Hill et al. (2018), are employed.

A.5 Compressive Interface Capturing Schemes

The aim of the whole discussion on the Finite Volume discretization of advection terms is to obtain an interpolation scheme which allows for the bounded transport of a discontinuity in both the volumetric phase fraction field and the concentration field(s) in a consistent way and at the same time maintain a maximum sharp field. Consistent here means that the numerical diffusion in the transport of α_1 and $\bar{c}_i$ leads to exactly the same interface thickness for both quantities and thus minimizes or completely nullifies artificial mass transfer. The problem of artificial mass transfer is discussed in Chapter 3.2.4.

Considering the numerical transport of a discontinuity, the main issue is not the order of convergence or overall accuracy. In interpolation schemes based on TVD or the transient CBC criterion, the higher-order of accuracy is only obtained in the smooth region which does not play a role for the transport of a discontinuous marker field like the volume fraction. In the presence of steep gradients, all schemes based on above criteria reduce to first-order accuracy. The main task for the algebraic transport of sharp fields is to introduce maximum numerical anti-diffusion into the discretization of the advection term while maintaining a bounded solution. The key to this is the downwind discretization scheme.

Usage of the downwind scheme steepens any profile, even initially smooth profiles, into a discontinuous step profile. The problem is that the downwind scheme is unbounded. Enforcing the TVD or transient CBC criterion on the downwind scheme leads to the Hyper-C scheme introduced in the previous section. Indeed, it can be shown that for a time-explicit discretization of the one-dimensional advection equation with initial step profile, only the Hyper-C scheme can reproduce the numerical exact solution while all other discretization schemes lead to a smearing of the initially sharp step. Hence, the analysis of discretization schemes and boundedness criteria presented in Sections A.1 and A.2 lead to the conclusion that the most suitable scheme for the transport of a sharp field based on a three-node stencil is the Hyper-C scheme. The drawback of maximum downwinding becomes eminent in two- and three-dimensional advection problems, sharpening any profile into a step parallel to the face normal directions. For example, the two-dimensional transport of an initially circle-shaped step on a uniform Cartesian mesh would result in a square. This behaviour of compressive discretization schemes is known in the literature also as *wrinkling* and obviously not acceptable for any numerical method aiming at the Direct Numerical Simulation of two-phase flow systems.

To circumvent this problem or at least minimize its effects, blending strategies have been proposed by many authors, blending compressive schemes (meaning schemes with high amount

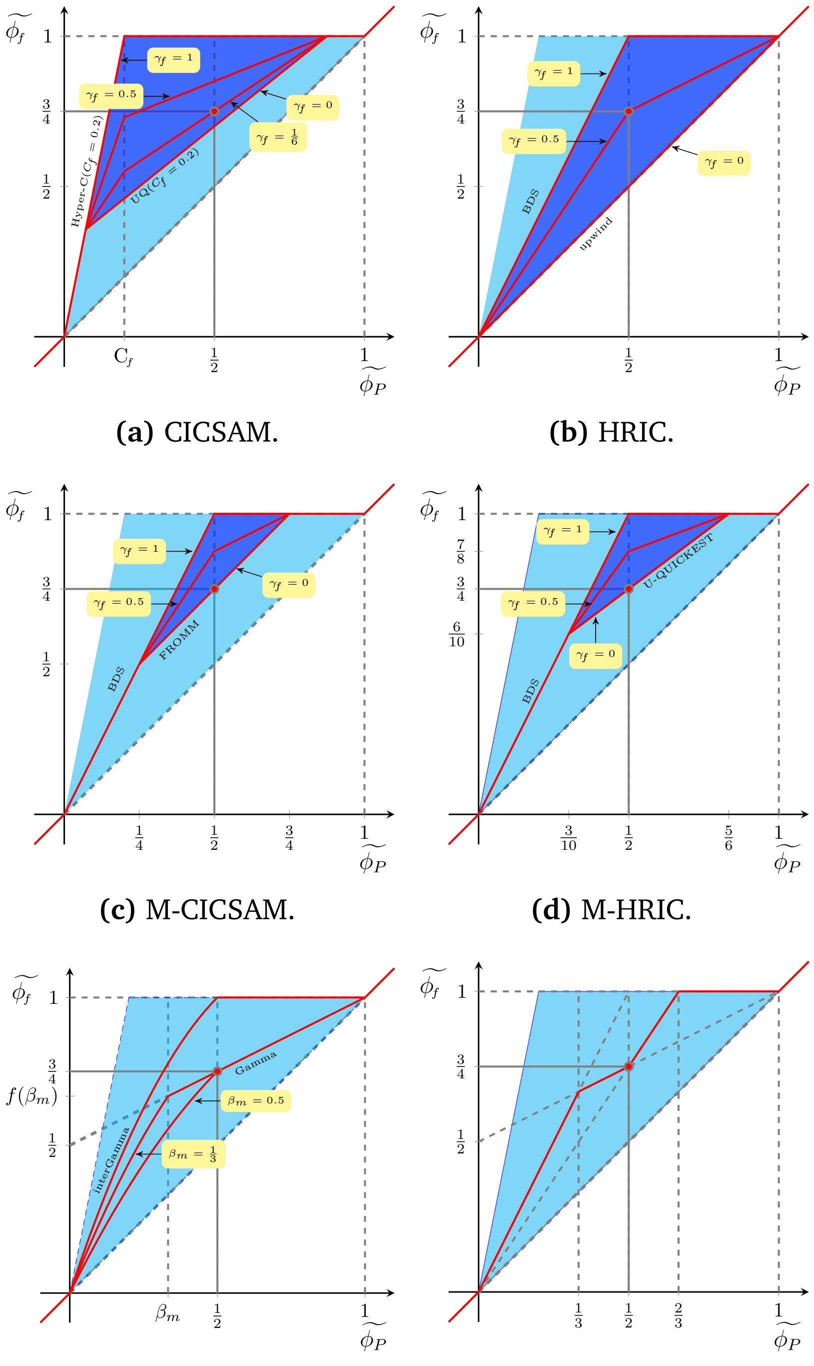

(a) CICSAM. **(b)** HRIC.

(c) M-CICSAM. **(d)** M-HRIC.

(e) interGamma. **(f)** SuperBee.

Figure A.4.: Important compressive Interface Capturing Schemes in the Normalized Variable Diagram

of downwinding) with diffusive schemes (meaning schemes which introduce a certain amount of numerical diffusion). Examples of such interpolation schemes are the *HRIC* scheme of Muzaferija et al. (1999), the *CICSAM* scheme by Ubbink (1997) and modified versions of both (*M-CICSAM* (Waclawczyk and Koronowicz, 2008) and *M-HRIC* (ANSYS Inc.)). Further important representatives of the class of Compressive Interface Capturing Schemes which do not utilize a blending are the Superbee scheme (Roe, 1986) and the interGamma scheme (Jasak and Weller, 1995). The compressive discretization schemes are listed below in their Normalized Variable Formulation:

HRIC

$$\widetilde{\phi}_{f,\mathrm{HRIC}} = \begin{cases} \widetilde{\phi}_f^* = \widetilde{\phi}_{f,\mathrm{BDS}}\sqrt{\cos\Theta} + \widetilde{\phi}_C\left(1-\sqrt{\cos\Theta}\right) & \text{for } \mathrm{C}_f < 0.3\,, \\ \widetilde{\phi}_C + \left(\widetilde{\phi}_f^* - \widetilde{\phi}_C\right)\frac{0.7-\mathrm{C}_f}{0.7-0.3} & \text{for } 0.3 \le \mathrm{C}_f \le 0.7\,, \\ \widetilde{\phi}_C & \text{else}\,. \end{cases}$$

$$\widetilde{\phi}_{f,\mathrm{BDS}} = \begin{cases} \min\left(2\widetilde{\phi}_C,\, 1\right) & \text{for } 0 \le \widetilde{\phi}_C \le 1\,, \\ \widetilde{\phi}_C & \text{else}\,. \end{cases}$$

M-HRIC

$$\widetilde{\phi}_{f,\text{M-HRIC}} = \widetilde{\phi}_{f,\mathrm{BDS}}\sqrt{\cos\Theta} + \widetilde{\phi}_{f,\mathrm{UQ}}\left(1-\sqrt{\cos\Theta}\right)$$

$$\widetilde{\phi}_{f,\mathrm{UQ}} = \begin{cases} \min\left(\widetilde{\phi}_{f,\mathrm{BDS}},\, \frac{6\widetilde{\phi}_C+3}{8}\right) & \text{for } 0 \le \widetilde{\phi}_C \le 1\,, \\ \widetilde{\phi}_C & \text{else}\,. \end{cases}$$

interGamma

$$\widetilde{\phi}_{f,\mathrm{interGamma}} = \begin{cases} \min\left(-2\widetilde{\phi}_C{}^2 + 3\widetilde{\phi}_C,\, 1\right) & \text{for } 0 \le \widetilde{\phi}_C \le 1\,, \\ \widetilde{\phi}_C & \text{else}\,. \end{cases}$$

CICSAM

$$\widetilde{\phi}_{f,\mathrm{CICSAM}} = \gamma_f\widetilde{\phi}_{f,\text{Hyper-C}} + \left(1-\gamma_f\right)\widetilde{\phi}_{f,\mathrm{UQuickest}} \quad , \; \gamma_f := \min\left(k_\gamma\frac{\cos\left(2\Theta\right)+1}{2},\, 1\right)$$

$$\widetilde{\phi}_{f,\mathrm{UQuickest}} = \begin{cases} \min\left(\widetilde{\phi}_{f,\text{Hyper-C}},\, \frac{8\,\mathrm{C}_f\,\widetilde{\phi}_C + \left(1-\mathrm{C}_f\right)\left(6\widetilde{\phi}_C+3\right)}{8}\right) & \text{for } 0 \le \widetilde{\phi}_C \le 1\,, \\ \widetilde{\phi}_C & \text{else}\,. \end{cases}$$

$$\widetilde{\phi}_{f,\text{Hyper-C}} = \begin{cases} \min\left(\frac{\widetilde{\phi}_C}{\mathrm{C}_f},\, 1\right) & \text{for } 0 \le \widetilde{\phi}_C \le 1\,, \\ \widetilde{\phi}_C & \text{else}\,. \end{cases}$$

M-CICSAM

$$\widetilde{\phi}_{f,\text{M-CICSAM}} = \gamma_f\widetilde{\phi}_{f,\mathrm{BDS}} + \left(1-\gamma_f\right)\widetilde{\phi}_{f,\mathrm{Fromm}} \quad , \; \gamma_f := \left|\cos\Theta\right|^{\frac{1}{4}}$$

$$\widetilde{\phi}_{f,\mathrm{Fromm}} = \begin{cases} \min\left(\frac{1}{4} + \widetilde{\phi}_C,\, \widetilde{\phi}_{f,\mathrm{BDS}}\right) & \text{for } 0 \le \widetilde{\phi}_C \le 1\,, \\ \widetilde{\phi}_C & \text{else}\,. \end{cases}$$

However, out of the class of Compressive Interface Capturing Schemes, only the CICSAM scheme is really suitable for the transport of a sharp field as needed in algebraic VOF methods, as it uses the Hyper-C scheme as its base to achieve compression. The only two options to create a discretization scheme based on a three-node stencil that could be more suitable for advection of fields exhibiting discontinuities than the CICSAM scheme, would be to change the higher-order scheme used for blending with Hyper-C or to change the blending function or both.

An alternative to the aforementioned High Resolution Schemes based on TVD or NVD analysis, is to use local boundedness criteria based on the actual computed fluxes. The resulting flux corrected transport (FCT) methods are based, as the TVD schemes, on the idea of a flux limiter formulation, meaning that the advective fluxes are split into a lower-order bounded flux (obtained by upwind interpolation) and a higher-order anti-diffusive correction. Within the FCT algorithm, a face-based limiter for the higher-order correction of the face interpolation is calculated. Starting point of the MULES algorithm (multidimensional universal limiter with explicit solution) – an FCT algorithm introduced in Weller (2006) – is an advection equation inclusive linearized source term and relative flux term

$$\partial_t \phi + \nabla\cdot(\phi \mathbf{u}) = \nabla\cdot(\phi\,(1-\phi)\,\mathbf{u}_r) + S_p \phi + S_u\,. \tag{A.55}$$

The divergence term on the r.h.s. (containing $\mathbf{u}_r$) is formally zero due to the DNS assumptions (see Chapter 2.3.2) but its form is used as a justification to create a bi-normal counter gradient diffusion to the interface and thus keep the interface sharp. A Finite Volume discretization of above equation using first-order explicit time discretization and implicit discretization of the source term S_p reads

$$\begin{aligned}\frac{\phi_C^n - \phi_C^o}{\Delta t} + \frac{1}{V_C}\sum_f \Bigg[& \underbrace{F_f^o \phi^o_{f\left(\mathrm{upw},F_f^o\right)}}_{=F^o_{f,\mathrm{BD}}} + \underbrace{F_f^o \left(\phi^o_{f\left(\mathrm{ho},F_f^o\right)} - \phi^o_{f\left(\mathrm{upw},F_f^o\right)}\right) + F_c^o \left(1-\phi^o_{f\left(\mathrm{IC},F_c^o\right)}\right)\phi^o_{f\left(\mathrm{IC},F_c^o\right)}}_{=F^o_{f,\mathrm{corr}}}\Bigg] \\ & = S_p \phi_C^n + S_u\,,\end{aligned} \tag{A.56}$$

where the bounded first-order flux is denoted $F^o_{f,\mathrm{BD}}$, the anti-diffusive correction flux is denoted $F^o_{f,\mathrm{corr}}$ and the counter gradient flux F_c is defined as

$$F_c := \min\left[\frac{|F_f|}{|\mathbf{S}_f|}c_\alpha,\ \max\left(\frac{|F_f|}{|\mathbf{S}_f|}\right)\right]\left(\frac{(\nabla\alpha)_f}{|\nabla\alpha|_f}\cdot\mathbf{S}_f\right) \tag{A.57}$$

with the constant c_α which is introduced to adjust the compression of the interface and is standardly set to unity. In Equation A.56, the velocity flux F_f is assumed to be known on the faces and to be divergence free. This is the setup in OpenFOAM which utilizes flux-based algorithms and therefore solves for the fluxes F_f, rather than the cell-centred velocity $\mathbf{u}$. In the present work, fluxes leaving a cell are assumed to be positive and fluxes entering a cell are assumed to be negative, i.e., $\mathbf{S}_f$ is the outward-pointing normal vector at face f times the face area. One main difficulty in discretizing Eq. (A.56) is to maintain a bounded solution, meaning that the utilized face interpolation schemes must be chosen in a way that the value in the new time step (ϕ_C^n) is bounded between the values of the discretization stencil in the old time step:

$$\boxed{\phi_{\min} := \min\left(\phi_N^o,\, \phi_C^o\right) \le \phi_C^n \le \max\left(\phi_N^o,\, \phi_C^o\right) =: \phi_{\max}}\,, \tag{A.58}$$

where "N" denotes all face neighbours of cell "C". This statement, Eq. (A.58), is the basis for the development of TVD, NVD, FCT and other discretization methods and follows directly from enforcing monotonicity and/or positivity onto a numerical discretization scheme. In discretization schemes based on the TVD criterion or based on the transient CBC criterion and NVF, a global mathematical criterion is derived which gives quantitative a-priori limitations on the interpolation weights based on the local Courant number to preserve boundedness. A derivation of such a mathematical constraint onto the discretization weights was so far only presented for one-dimensional schemes and can be also applied to multi-dimensional problems if a direction split algorithm is used. However, this is only feasible for structured Cartesian meshes.

Therefore, a different method for use in multidimensional problems and arbitrary cell shapes was developed (Zalesak, 1979), which does not rely on a given global formula for the boundedness constraint but rather is based on a stencil-based local limiting of anti-diffusive fluxes to preserve boundedness. This leads to the FCT methods which introduce local limiting of fluxes (therefore the naming: flux corrected) to maintain a bounded solution. Introducing the limiter in Eq. (A.56) yields

$$\frac{\phi_C^n - \phi_C^o}{\Delta t} + \frac{1}{V_C}\sum_f \left[F_{f,\mathrm{BD}}^o + \lambda_f F_{f,\mathrm{corr}}^o\right] = S_p \phi_C^n + S_u\,, \tag{A.59}$$

with the limiter $\lambda_f \in [0, 1]$. The original FCT algorithm developed by Boris and Book (1973) is only applicable to one-dimensional problems as the local limiting only takes into account the anti-diffusive flux at face f and not the sum of all fluxes in the face neighbouring cells. The first FCT algorithm applicable to multiple dimensions was introduced by Zalesak (1979) which takes into account anti-diffusive fluxes acting in concert. The MULES algorithm is slightly different from the FCT method introduced in Zalesak (1979) and works as follows:

Let us assume a time-explicit discretization of an advection equation as in Eq. (A.59). Knowing that the resulting numerical scheme needs to fulfil Eq. (A.58), the maximum and minimum allowed correction fluxes can be obtained. Since positive anti-diffusive fluxes (out of cell C) are leading to a reduction of ϕ_C^n and negative anti-diffusive fluxes (into cell C) to an increase of ϕ_C^n, both effects can be examined separately.

$$\frac{\phi_C^n - \phi_C^o}{\Delta t} + \frac{1}{V_C}\sum_f \left[F_{f,\mathrm{BD}}^o + \lambda_f F_{f,\mathrm{corr}}^o\right] = S_p \phi_C^n + S_u$$

$$\overset{\text{Eq. A.58}}{\Longleftrightarrow} \quad \phi_{\min} \le \left[\frac{\phi_C^o}{\Delta t} + S_u - \frac{1}{V_C}\sum_f \left(F_{f,\mathrm{BD}}^o + \lambda_f F_{f,\mathrm{corr}}^o\right)\right] \Big/ \left(\frac{1}{\Delta t} - S_p\right) \le \phi_{\max}$$

$$\Rightarrow \quad 1.\ \underbrace{V_C\left[\phi_{\min}\left(\frac{1}{\Delta t} - S_p\right) - \left(\frac{\phi_C^o}{\Delta t} + S_u - \frac{1}{V_C}\sum_f F_{f,\mathrm{BD}}^o\right)\right]}_{=:-Q^-} \le -\sum_f \lambda_f F_{f,\mathrm{corr}}^o \tag{A.60}$$

$$2.\ -\sum_f \lambda_f F_{f,\mathrm{corr}}^o \le \underbrace{V_C\left[\phi_{\max}\left(\frac{1}{\Delta t} - S_p\right) - \left(\frac{\phi_C^o}{\Delta t} + S_u - \frac{1}{V_C}\sum_f F_{f,\mathrm{BD}}^o\right)\right]}_{=:Q^+} \tag{A.61}$$

In summary, the limited anti-diffusive fluxes need to fulfil the following condition:

$$\boxed{-Q^+ \leq \sum \lambda_f F^o_{f,\mathrm{corr}} \leq Q^-} \tag{A.62}$$

to maintain a bounded solution of the transported variable ϕ. The FCT algorithm proposed by Zalesak (1979) and the MULES FCT algorithm calculate the limiters λ_f by making use of the above-mentioned fact that increases in ϕ^n_C are produced by ingoing fluxes into cell C and decreases in ϕ^n_C by fluxes leaving cell C. The sum of all limited ingoing fluxes in cell C is defined as

$$P^+ = -\sum_f \min\left(0,\, F^o_{f,\mathrm{corr}}\right) \tag{A.63}$$

$$S^+ := -\sum_f \min\left(0,\, \lambda_f F^o_{f,\mathrm{corr}}\right) \tag{A.64}$$

and, analogously, the sum of all fluxes leaving the cell C as

$$P^- = \sum_f \max\left(0,\, F^o_{f,\mathrm{corr}}\right) \tag{A.65}$$

$$S^- := \sum_f \max\left(0,\, \lambda_f F^o_{f,\mathrm{corr}}\right)\ . \tag{A.66}$$

In order to prevent the creation of a new maximum, the limited sum of the magnitude of all incoming fluxes is required to be lower or equal than the allowed flux Q^+ plus the sum of all (un-limited) outgoing fluxes:

$$\begin{aligned} & -Q^+ \leq S^- - S^+ \leq Q^- \\ \Rightarrow\ & S^- - S^+ \geq S^- - R^+ P^+ \geq -Q^+ \\ \Rightarrow\ & \boxed{R^+ = \max\left[0,\, \min\left(1,\, \frac{Q^+ + S^-}{P^+}\right)\right]}\ , \end{aligned} \tag{A.67}$$

which yields a condition for the cell-based limiter R^+. For the case of local minima, the equivalent criterion to above can be derived:

$$\begin{aligned} & -Q^+ \leq S^- - S^+ \leq Q^- \\ \Rightarrow\ & S^- - S^+ \geq R^- P^- - S^+ \leq Q^- \\ \Rightarrow\ & \boxed{R^- = \max\left[0,\, \min\left(1,\, \frac{Q^- + S^+}{P^-}\right)\right]}\ , \end{aligned} \tag{A.68}$$

resulting in a condition for the cell-based limiter R^-.

The cell-centred limiters cannot be applied to Finite Volume methods as their values are different for each cell which results in different limiting of anti-diffusive fluxes in the face-neighbouring cells and thus flux conservation cannot be achieved. Hence, based on the cell-centred limiters R^- and R^+ defined in Eqns. A.67 and A.68, face-based limiters λ_f are still to be derived which allow for a conservative flux formulation. If the anti-diffusive flux over face f is positive, meaning going out of cell C, then the value of cell C decreases, whereas the value in the face-neighbour cell N increases. Therefore, the face limiter λ_f needs to prevent cell C from falling under the minimum value and cell N from rising above the maximum value, which results in

$$\boxed{\lambda_f = \min\left(R_C^-, R_N^+\right)} \quad \text{for } F^o_{f,\text{corr}} > 0 \ \ (\text{leaving cell } C)\,. \tag{A.69}$$

If the anti-diffusive flux at face f is entering cell C, then the value in C increases and the value in N decreases. Hence, the limiter ensuring boundedness needs to be chosen as

$$\boxed{\lambda_f = \min\left(R_C^+, R_N^-\right)} \quad \text{for } F^o_{f,\text{corr}} < 0 \ \ (\text{entering cell } C)\,. \tag{A.70}$$

The MULES algorithm is iterative, starting with $\lambda_f = 1$. The iterations are performed over Equations A.64, A.66 to A.70. In the implementation of the algorithm, three iteration steps are performed.

B CST Model Discretization Using FCT Advection Algorithm

An alternative to the CICSAM scheme to discretize the advection of volumetric phase fraction and species concentration is to utilize the MULES FCT algorithm with artificial interface compression, the standard advection employed in the interFoam solver. Although – as discussed before – this advection does not guarantee a consistent advection, one might still raise the question if it is not possible to utilize the algorithm in some way. This is indeed possible as outlined below. However, the numerical results shown in Chapter 5.2.1 prove that this advection algorithm introduces artificial mass transfer unlike the CICSAM scheme. To see how the MULES FCT advection algorithm with artificial compression term can be utilized for a species concentration, it is essential to look at the conditional volume averaged equation system. From the definition of the mixture velocity

$$\overline{\mathbf{u}} := \alpha_1 \overline{\mathbf{u}}^1 + \alpha_2 \overline{\mathbf{u}}^2$$

and the relative velocity

$$\mathbf{u}_r := \overline{\mathbf{u}}^2 - \overline{\mathbf{u}}^1 ,$$

the following relations can be derived:

$$\alpha_1 \overline{\mathbf{u}}^1 = \alpha_1 \overline{\mathbf{u}} - \alpha_1 \alpha_2 \mathbf{u}_r \tag{B.1}$$

$$\alpha_2 \overline{\mathbf{u}}^2 = \alpha_2 \overline{\mathbf{u}} + \alpha_1 \alpha_2 \mathbf{u}_r . \tag{B.2}$$

From the conditional volume averaged species concentration equation it thus follows

$$\begin{aligned}
&\partial_t \left(\alpha_1 \overline{c}^1 + \alpha_2 \overline{c}^2\right) + \nabla\cdot \left(\alpha_1 \overline{c}^1 \overline{\mathbf{u}}^1 + \alpha_2 \overline{c}^2 \overline{\mathbf{u}}^2\right) \\
&= \partial_t \left(\alpha_1 \overline{c}^1 + \alpha_2 \overline{c}^2\right) + \nabla\cdot \left(\alpha_1 \overline{c}^1 \overline{\mathbf{u}} + \alpha_2 \overline{c}^2 \overline{\mathbf{u}}\right) - \nabla\cdot \left(\alpha_1 \alpha_2 \mathbf{u}_r \left(\overline{c}^1 - \overline{c}^2\right)\right) \\
&= \partial_t \overline{c} + \nabla\cdot \left(\overline{c}\, \overline{\mathbf{u}}\right) - \nabla\cdot \left(\alpha_1 (1-\alpha_1) \mathbf{u}_r \left(\overline{c}^1 - \overline{c}^2\right)\right) .
\end{aligned} \tag{B.3}$$

Above form suggests that the interface compression term could be included into the species concentration transfer equation to obtain a consistent advection with the volumetric phase fraction. However, there are two problems one should be aware of: First, the term containing the relative velocity was used by Weller (2006) for introducing a numerical motivated compression with no physical basis. Second, Equation (B.3) suggests that for a consistent transport of a temperature (same equation form but no interfacial jump), the compression term would vanish. However, the remaining advection term is standardly discretized with a diffusive TVD scheme, e.g. using the vanLeer limiter (van Leer, 1974). In this case, the introduced numerical diffusion onto the transport of the temperature field is inconsistent to the volume fraction advection, as the latter contains a bi-normal counter gradient diffusion.

Additionally, to employ the MULES algorithm to above Equation (B.3), it is important to understand how it works. The algorithm returns a local face-based limiter in order to maximize the usage of a given discretization scheme under the sole aspect of boundedness preservation. Thus, there are two ways the MULES algorithm can be used: Either the limiters to discretize the species advection are taken from the phase fraction advection, thus retaining some advection consistency, or new limiters based on the local species concentration field are computed. Furthermore, the phasic averaged concentrations on both sides of the interface are needed in order to arrive at a closed formulation. These can either be taken from the introduced closure relation Eq. (2.68) or estimated under the assumption of a homogeneous concentration field within the gas bubble

$$\overline{c}^1 - \overline{c}^2 \approx \left(1 - \frac{1}{\mathrm{H}}\right) \overline{c}^b \tag{B.4}$$

by utilizing Henry's law. The average species concentration inside the bubble is defined as

$$\overline{c}^b := \frac{1}{|V_b|} \int\limits_{V_b} c \, dV \,. \tag{B.5}$$

All above described variants for the advection of the species concentration have been thoroughly tested within this work, the reason being the large influence of the advection onto the mass transfer process in context of single-field formulations. As shown in Chapter 5.2.1, the advection based on the blended CICSAM scheme (see Chapter 3.2.3) is to be preferred.

C Bubble Group Simulation

To conduct Direct Numerical Simulations of bubble swarms, an approach commonly used in the literature, e.g., in Bunner and Tryggvason (2002a,b), Koynov et al. (2005), Roghair (2012), is to follow a group of bubbles in a fully periodic domain, meaning a box with periodic boundary conditions for all transported quantities. A fully periodic domain introduces one numerical problem: When solving the Navier-Stokes equations in their common form (fixed observer) nothing prevents the phases from accelerating infinitely downwards, because the gravitational force acting on the domain cannot be balanced due to the lack of “walls” in the domain, no Dirichlet boundary condition which fixes the velocity field at some point. A re-formulation of the set of governing equations into the Centre-of-Moment (COM) frame of reference remedies this problem and also gives a definition of a periodic pressure, which is needed if periodic boundary conditions are to be prescribed for each transported quantity.

C.1 Centre-of-Moment Reference Frame (COM)

As previously stated in the introduction to this Chapter, the Centre-of-Moment Reference Frame (COM) is suited for mimicking a bubble swarm by numerically modelling a group of bubbles in a fully periodic domain. If gravitational forces act on a domain with no specified Dirichlet boundary conditions, measures have to be taken to prevent the phases from accelerating infinitely in the direction of the gravitational force. To overcome this numerical problem, a

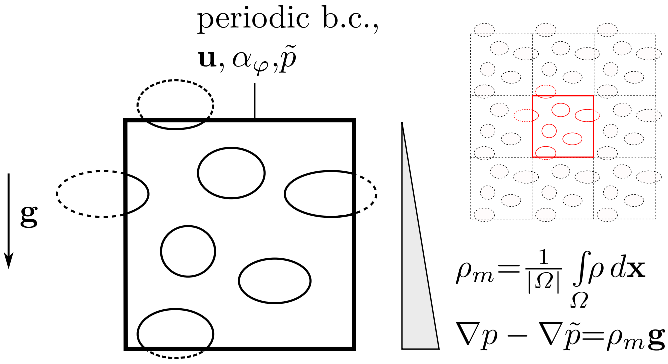

Figure C.1.: Bubble group in a periodic box

re-formulation of the set of governing equations into the Centre-of-Moment frame of reference can be made, which eliminates the acceleration term by introducing a periodic pressure, which allows to prescribe periodic pressure boundary conditions.

In this unique inertial frame, the centre of mass of the system is at rest and the total momentum over the computational domain Ω vanishes (thus the naming COM) which leads to

$$\int_{\Omega} \left[\partial_t (\rho \mathbf{u}) + \nabla\cdot (\rho \mathbf{u}\mathbf{u})\right] dx = \int_{\Omega} \left[-\nabla p + \rho \mathbf{g} + \nabla\cdot \boldsymbol{\tau} + \mathbf{f}_\sigma\right] dx \stackrel{!}{=} 0 \,. \tag{C.1}$$

As the domain is periodic, the mixture velocity and thus the stress at opposite boundaries is the same. Therefore, the divergence of the stress is zero,

$$\int_{\Omega} \nabla\cdot \boldsymbol{\tau} \, dx = \sum_{\partial\Omega} \boldsymbol{\tau} \cdot \mathbf{n}_f = 0 \,. \tag{C.2}$$

The net surface tension force in the system is zero as well:

$$\int_{\Omega} \mathbf{f}_\sigma \, dx = 0 \,. \tag{C.3}$$

The remaining terms on the right-hand side of the momentum equation are the pressure gradient and the body force due to gravity, which thus are required to fulfil

$$\int_{\Omega} \left[-\nabla p + \rho \mathbf{g}\right] dx \stackrel{!}{=} 0 \,. \tag{C.4}$$

The pressure gradient can then be split in a periodic part and a constant pressure gradient according to

$$\nabla p = \nabla \tilde{p} + \rho_m \mathbf{g} \,, \tag{C.5}$$

where ρ_m is the average density of the whole computational domain,

$$\rho_m = \frac{1}{|\Omega|} \int_{\Omega} \rho \, dx \,. \tag{C.6}$$

This newly defined periodic pressure $\tilde{p} = p - \rho_m \mathbf{g} \cdot \mathbf{x}$ fulfils Eq. (C.4) and thus transforms the fully periodic computational system into the centre-of-momentum frame. The resulting momentum equation in the centre-of-momentum frame reads

$$\partial_t \rho \mathbf{u} + \nabla\cdot (\rho \mathbf{u}\mathbf{u}) = -\nabla \tilde{p} + (\rho - \rho_m)\, \mathbf{g} + \nabla\cdot \boldsymbol{\tau} + \mathbf{f}_\sigma \,. \tag{C.7}$$

In order to verify that this definition of a periodic pressure is consistent to the mathematical model introduced in Chapter 2.1.2, it needs to be shown that the momentum jump conditions are not altered by introduction of this pressure definition. That the definition of a periodic pressure has no effect on the jump conditions can be proven as follows: Substituting the pressure in the local instantaneous momentum equation and jump condition (see Chapter 2.1.2) by $p = \tilde{p} + \rho_m \mathbf{g} \cdot \mathbf{x}$ yields

$$\partial_t(\rho\mathbf{u}) + \nabla\cdot(\rho\mathbf{u}\mathbf{u}) = -\nabla(\tilde{p} + \rho_m\mathbf{g}\cdot\mathbf{x}) + \nabla\cdot\boldsymbol{\tau} + \rho\mathbf{g} \tag{C.8}$$

$$[\![\rho\mathbf{u}\left(\mathbf{u} - \mathbf{u}^{\Sigma}\right) - \boldsymbol{\tau}]\!] \cdot\mathbf{n}_{\Sigma} = \sigma\kappa\mathbf{n}_{\Sigma} + \nabla_{\Sigma}\sigma - [\![(\tilde{p} + \rho_m\mathbf{g}\cdot\mathbf{x})\mathbf{I}]\!] \cdot\mathbf{n}_{\Sigma}\,. \tag{C.9}$$

Application of the conditional volume averaging framework to Eq. (C.8) leads to

$$\begin{aligned}\partial_t\left(\alpha_1\,\overline{\rho\mathbf{u}}^1\right) + \nabla\cdot\left(\alpha_1\,\overline{\rho\mathbf{u}\mathbf{u}}^1\right) + \overbrace{\rho\mathbf{u}\left(\mathbf{u} - \mathbf{u}^{\Sigma}\right)\cdot\mathbf{n}_{\Sigma}}^{1} a_{\Sigma} = -\nabla\left(\alpha_1\,\overline{\tilde{p}}^1\right)\\ - \nabla\left(\alpha_1\,\overline{\rho_m\mathbf{g}\cdot\mathbf{x}}^1\right) + \nabla\cdot\left(\alpha_1\,\overline{\boldsymbol{\tau}}^1\right) + \alpha_1\,\overline{\rho}^1\mathbf{g} + \overbrace{\left[\boldsymbol{\tau} - (\tilde{p} + \rho_m\mathbf{g}\cdot\mathbf{x})\mathbf{I}\right]\cdot\mathbf{n}_{\Sigma}}^{1} a_{\Sigma}\,.\end{aligned} \tag{C.10}$$

Summation over both phases and utilizing the surface-averaged jump condition then yields

$$\partial_t\left(\overline{\rho}\,\overline{\mathbf{u}}\right) + \nabla\cdot\left(\overline{\rho}\,\overline{\mathbf{u}}\,\overline{\mathbf{u}}\right) = -\nabla\overline{\tilde{p}} + \left(\overline{\rho} - \rho_m\right)\mathbf{g} + \nabla\cdot\langle\tau\rangle + \widehat{f_{\sigma}}a_{\Sigma}\,. \tag{C.11}$$

Thus, it is proven that the transformation of the momentum equation into the COM reference frame is consistent with the momentum jump condition and leads to the definition of a periodic pressure. This formulation is suitable for the numerical computation of fully periodic systems in context of multiphase flows.

C.2 Multi-Phase Solver Development

In order to simulate bubble swarms, a multi-phase solver framework is developed. This allows for the simulation of groups of bubbles in a fully periodic domain (pseudo-swarm; cf. Appendix C.1) and additional modelling of coalescence inhibition. The aim of this development is to quantify swarm effects onto the species transfer and include it into correlations of species transfer from single rising bubbles.

C.2.1 Modelling of Coalescence Inhibition

In the Volume-of-Fluid framework, which employs a single indicator field to distinguish both phases present in the system, model-inherent coalescence occurs when two bubbles or droplets come closer to each other than one mesh cell. In this case, a single indicator is not sufficient to distinguish between both fluid particles anymore and important quantities as, e.g., the curvature can no longer be computed. This effect of numerical coalescence is even more pronounced in algebraic VOF methods, where the interface is not exactly sharp, meaning in one cell layer. Unfortunately, to resolve the hydrodynamics in the thin films when two fluid particles approach each other requires locally very fine mesh resolutions which are nowadays still unfeasible for Direct Numerical Simulations.

Another possible approach to numerically model coalescence inhibition is to introduce multiple indicator fields – one for each fluid particle – and then adding twice the surface tension locally, wherever interfaces of two fluid particles (bubble-bubble or droplet-droplet) are in direct contact. Thus, the effect of the thin film between both particles is partially taken into account by incorporation of the resulting surface tension force. This model corresponds to 100% coalescence inhibition.

Other models to numerically prevent coalescence can also be found in the literature. They mainly introduce a repulsive force between approaching fluid particles which increases in magnitude inverse to the local distance. It should be noted that front tracking methods do not suffer from this problem as they method-inherently prevent coalescence. This, however, requires the interface marker points to be corrected in a manner to prevent bubble intersections and thus is a purely numerical intervention into the interface dynamics. There, the opposite problem arises: numerical modelling of coalescence needs to be introduced.

C.2.2 Bubble Groups and Pseudo-Swarm

In order to simulate a swarm of bubbles rising under buoyancy, a suitable model for the swarm needs to be found as only a small fraction of the application domain size can be simulated. The numerical modelling of bubble swarms in DNS methods is commonly done by simulating bubbles rising in a fully periodic box. Thus, a pseudo-swarm is formed which is assumed to show the same interactions and hydrodynamic behaviour as the real swarm. Indeed, it is shown, e.g., in Bunner and Tryggvason (2002a) and Dijkhuizen et al. (2008) that a small number of fluid particles (about 8 bubbles) is sufficient to numerically characterize the swarm behaviour. Important characteristics such as the turbulent kinetic energy spectrum in these pseudo-swarms agree with measurement results in bubble swarms (Bunner and Tryggvason, 2002b, Lance and Bataille, 1991). Also, a significant change in rise velocity compared to single rising bubbles of same fluid properties is observed in the pseudo-swarm (Krishna et al., 1999, Roghair et al., 2013). Hence, it can be assumed that simulating a few bubbles in a fully periodic domain allows for accurate conclusions regarding bubble swarms, in view of hydrodynamic and mass transfer properties of the fluid system.

The numerical modelling needed to simulate a fully periodic domain is outlined in the previous section. Here, the Centre-of-Moment reference frame is introduced as well as the necessary changes required in the numerical model.

C.2.3 Coupling Strategies for Phase Fraction Fields

The block-coupling of an arbitrary number of multiple phase fraction fields α_i can be done by a zero addition to the transport equation of each α_i, making use of the algebraic constraint and the incompressibility constraint, i.e.

$$\sum_i \alpha_i \overset{!}{=} 1 \quad \text{and} \quad \nabla\cdot\mathbf{u} \overset{!}{=} 0\,, \tag{C.12}$$

which yields

$$\partial_t \alpha_i + \nabla\cdot(\alpha_i \mathbf{u}) + \nabla\cdot(\alpha_i \mathbf{u}) + \underbrace{\sum_{j\neq i} \nabla\cdot\left(\alpha_j \mathbf{u}\right)}_{\text{implicit coupling terms}} = \underbrace{\nabla\cdot\mathbf{u}}_{\text{explicit source term}} . \tag{C.13}$$

This leads to the following discretization:

$$[\![\partial_t([\alpha_i])]\!] + \left[\!\!\left[\nabla\cdot\left(\mathbf{u}[\alpha_i^{\text{ho}}]\right)\right]\!\!\right] + \left[\!\!\left[\nabla\cdot\left(\mathbf{u}[\alpha_i^{\text{cd}}]\right)\right]\!\!\right] + \sum_{j\neq i}\left[\!\!\left[\nabla\cdot\left(\mathbf{u}[\alpha_j^{\text{cd}}]\right)\right]\!\!\right] = \nabla\cdot\mathbf{u}\,. \tag{C.14}$$

It was found that the coupling terms have to be discretized with central differences as only then, boundedness could be achieved. This seems strange as any linear interpolation scheme should ensure this:

$$\sum_i (\alpha_i)_f = \sum_i \omega_i\,(\alpha_i)_P + (1-\omega_i)(\alpha_i)_N \overset{\text{lin. scheme}}{=} \omega\sum_i(\alpha_i)_P + (1-\omega)\sum_i(\alpha_i)_N \equiv 1\,. \tag{C.15}$$

The flux is then reconstructed from all phase fraction fields in the new time step as

$$\rho F = \sum_{j=1}^{k-1}\left[F\left(\alpha_j\right)_{f,\text{ho}}\left(\rho_j - \rho_k\right) + F\frac{\rho_k}{k-1}\right]. \tag{C.16}$$

Note that this treatment of the fluxes is not strictly accurate as new interpolation weights are calculated from the solution of α_j in the new time step and thus are different than the ones in the matrix. Also, the coupling terms are neglected although they do not cancel out exactly and might have a small influence. The current method to obtain the flux field ρF is thus not fully consistent.

It was found in numerical experiments that above discretization fails when more than two phases come into direct contact. An alternative to the coupling strategy above is to utilize a flux limiter formulation

$$[\![\partial_t([\alpha_i])]\!] + \left[\!\!\left[\nabla\cdot\left(\mathbf{u}\left([\alpha_i]_{f,\text{lo}} + \lambda_i\,[\alpha_i]_{f,\text{corr}}\right)\right)\right]\!\!\right] = 0 \tag{C.17}$$

and adjust the λ_i to ensure that the algebraic constraint remains fulfilled exactly. This is done by summing up correction fluxes in and out of a face for all phases, i.e.

$$S^+ = \sum_i \max\left(F_{i,\text{corr}}, 0\right), \tag{C.18}$$

$$S^- = \sum_i \min\left(F_{i,\text{corr}}, 0\right), \tag{C.19}$$

$$S = S^+ + S^-\,. \tag{C.20}$$

When $S > 0$ this leads to

$$\lambda_i = -\frac{S^-}{S^+} \quad , F_{i,\text{corr}}* = \text{pos}\,(S)\,\lambda_i\,, \tag{C.21}$$

and, for $S < 0$,

$$\lambda_i = -\frac{S^+}{S^-} \quad , F_{i,\text{corr}}* = \text{pos}\,(-S)\,\lambda_i\,. \tag{C.22}$$

This ensures that in sum the anti-diffusive corrections vanish and thus the sum over all α_i remains one. This is a similar rationale as in the χ-schemes by Darwish and Moukalled (2003).

D Hydrodynamic Solver Enhancement

D.1 Interface Capturing Schemes - Library

For reasons of advection accuracy and consistent advection of volumetric phase fraction and species concentration, a library of Interface Capturing Schemes was implemented, including the following schemes known in the literature (cf. Chapter A.5):

- CICSAM (Ubbink, 1997)
- HRIC (Muzaferija et al., 1999)
- M(odified)-CICSAM (Waclawczyk and Koronowicz, 2008)
- M(odified)-HIRC (Ansys Fluent 12.0 Theory Guide)
- InterGamma (Jasak and Weller, 1995) .

Out of above schemes, the CICSAM scheme leads to the sharpest interface representation and is thus preferable for VOF simulations of rising bubbles and virtually prevents shrinking of the bubble due to numerical diffusion, which is introduced by all other above-mentioned schemes.

The schemes are implemented in a blended version (cf. Chapter 3.2.4, Eq. (3.55)), meaning that the original scheme is utilized in the vicinity of the interface and is reduced to the respective higher-order scheme in the rest of the domain. In case of the CICSAM scheme, this means that full CICSAM is only applied in the interface cells, whereas the Ultimate-Quickest scheme is applied elsewhere. The InterGamma scheme is blended with the Gamma scheme. This strategy is introduced to allow for an accurate transport not only of a sharp field but also for other quantities as, e.g., species concentrations, which also exhibit a jump across the interface. Technically, this procedure is similar to the standardly employed advection algorithm in interFoam, which also employs a compression in the vicinity of the interface and reduces to a locally bounded higher-order differencing scheme (due to MULES FCT) elsewhere.

To enhance the accuracy of the interpolation on unstructured meshes, the virtual upwind value is limited by the neighbouring cell values as suggested in Przulj and Basara (2001). To find the computational cell containing the virtual upwind point, a local vicinity search algorithm is employed (Löhner, 1995, Maric et al., 2015).

Implementation of the library is based on the *limitedSurfaceInterpolationScheme*-class in OpenFOAM®. The structure of the Interface Capturing Schemes library – in form of an UML class diagram – is given in Listing D.1 below. Herein, the base class *interfaceCapturingScheme* contains the implementation of the virtual member function *weights* dependent on the private scalar-valued member function *weights*, whose actual implementation is found in the derived classes. The newly implemented discretization schemes are then added to the runtime selection table of *limitedSurfaceInterpolationScheme*, making them globally available within OpenFOAM®without further changes by simply loading the library in the local *controlDict*.

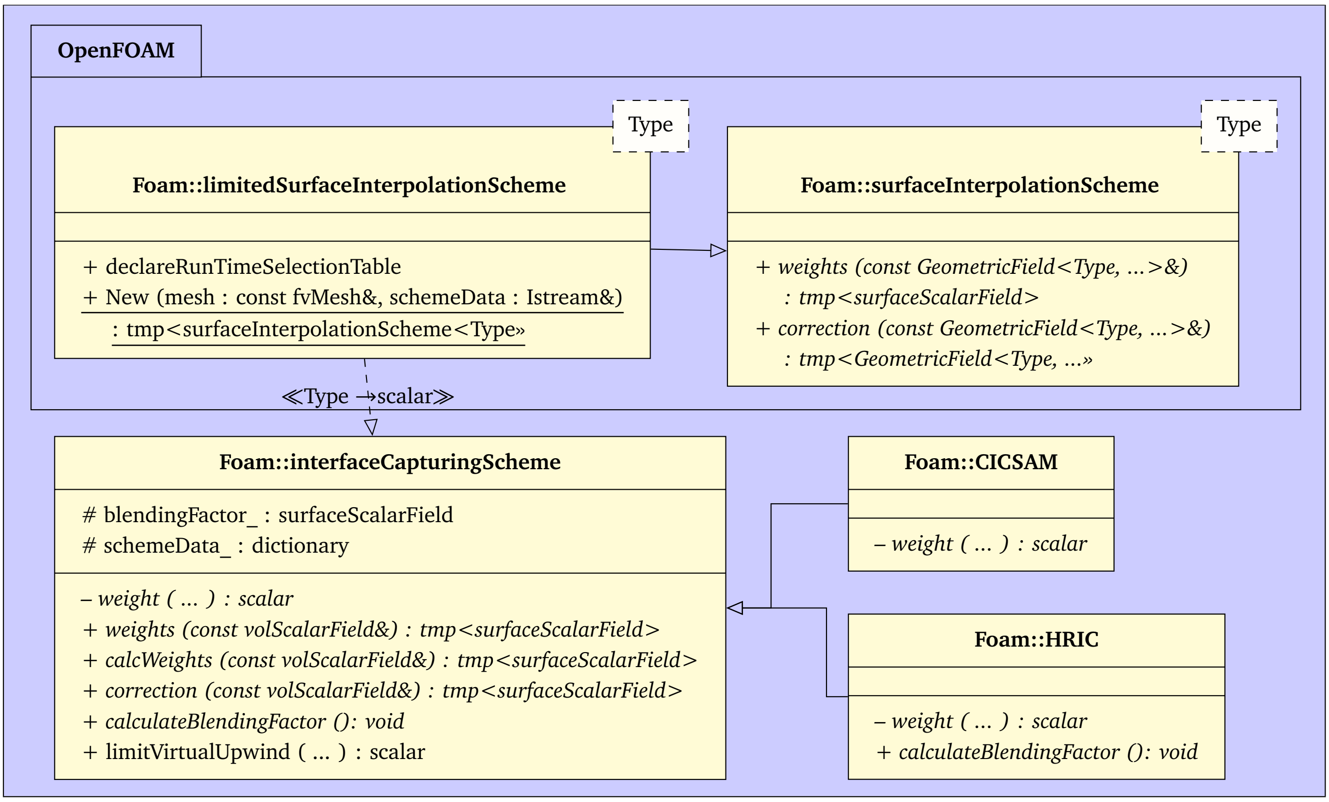

Listing D.1.: Interface Capturing Schemes library structure – UML class diagram

D.2 Surface Tension Force Computation

D.2.1 Curvature Estimation

One of the main issues of Direct Numerical Simulation methods for two-phase flow systems is the consistent and accurate incorporation of the surface tension force. In this work, a flux-based Continuous Surface Force (CSF) model (Brackbill et al., 1992) is used, but other models can be found in the literature as well, e.g., the Continuum Surface Stress (CSS) model (Lafaurie et al., 1994). Ideally, the included surface tension force should be balanced by the pressure gradient on a discrete level in case of constant velocity field in time and space. A surface tension model which fulfils this condition is known in the literature as a balanced-force algorithm (Popinet, 2009, Francois et al., 2006). In the local instantaneous two-phase Navier-Stokes equation, the CSF model corresponds to the term

$$\mathbf{f}_\sigma = \sigma \kappa \mathbf{n}_\Sigma \,. \tag{D.1}$$

In the context of conditional volume averaging, the above equation translates into

$$\begin{aligned} &\frac{1}{|V|}\int\limits_V \mathbf{f}_\sigma \, dV = \widetilde{\mathbf{f}_\sigma} a_\Sigma \approx \widetilde{\sigma}\,\widetilde{\kappa}\,\widetilde{\mathbf{n}_\Sigma} \|\nabla \alpha_1\| \\ &\approx -\widetilde{\sigma}\left(\nabla \cdot \frac{\nabla \alpha_1}{\|\nabla \alpha_1\|}\right) \frac{\nabla \alpha_1}{\|\nabla \alpha_1\|} \|\nabla \alpha_1\| = -\widetilde{\sigma}\left(\nabla \cdot \frac{\nabla \alpha_1}{\|\nabla \alpha_1\|}\right) \nabla \alpha_1 \,. \end{aligned} \tag{D.2}$$

In the flux-based approach, the surface tension force is calculated at the face centres in order to balance the pressure (balanced-force). Thus, the force is translated into a face flux by pointing with the face normal vector times face area:

$$\left(\widetilde{\mathbf{f}_\sigma}\right)_f \cdot \mathbf{S}_f a_\Sigma \approx -\left(\widetilde{\sigma}\right)_f \left(\nabla\cdot \frac{(\nabla\alpha_1)_f}{\|(\nabla\alpha_1)_f\|}\right) \nabla_f^\perp \alpha_1 \|\mathbf{S}_f\| , \tag{D.3}$$

where the term $\nabla\alpha_1 \cdot \mathbf{S}_f$ is calculated using the surface normal gradient. This is done to ensure the same discretization stencil for the pressure and surface tension force and thus balance surface tension force and pressure on the faces. It should be noted that if the pressure gradient is in some way corrected for mesh-induced errors (on meshes of general topology), the exact same correction would have to be employed to the phase fraction gradient in order to retain a balanced-force algorithm.

Calculation of the interface curvature from the divergence of the normalized gradient of the volumetric phase fraction field, i.e.

$$\kappa = -\nabla\cdot (\mathbf{n}_\Sigma)_f = -\nabla\cdot \left(\frac{\nabla\alpha_1}{\|\nabla\alpha_1\|}\right)_f \approx -\sum_f \left(\frac{\nabla\alpha_1}{\|\nabla\alpha_1\|}\right)_f \cdot \mathbf{S}_f , \tag{D.4}$$

leads to poor results. A second native approach for curvature estimation often employed in the literature is to use smoothing algorithms of the phase fraction field, as introduced, e.g., by Ubbink (1997), Rusche (2002), Francois et al. (2006) in order to improve the interface normal vectors and thus the curvature estimation. Here, smoothing of the volumetric phase fraction field is commonly achieved either by means of convolution with different kernel functions or by elliptical relaxation (Rusche, 2002). The curvature calculation is then again performed applying Gauss' theorem

$$\kappa \approx -\sum_f \left(\frac{\nabla(\alpha_1)_s}{\|\nabla(\alpha_1)_s\|}\right)_f \cdot \mathbf{S}_f , \tag{D.5}$$

using the smoothed phase fraction field $(\alpha_1)_s$. Independent of the smoothing algorithm, this approach only slightly improves the interface normals and thus the curvature. On structured grids, the curvature can be estimated sufficiently accurate by using height functions (Popinet, 2009) which, however, is not trivial to translate to unstructured grid arrangements. Therefore, an isosurface reconstruction of the phase fraction field based on Batzdorf (2015) is employed, which reconstructs the interface as a volume fraction iso-contour at $\alpha_1 = 0.5$. The isosurface is utilized to calculate the interface normal vectors, which are then distributed in the interface area by interpolation. Finally, the curvature is calculated as before from

$$\kappa = \sum_f (\mathbf{n}_\Sigma)_{f,\mathrm{iso}} \cdot \mathbf{S}_f . \tag{D.6}$$

Actual cell-cutting to obtain an interface surface is not performed, the algorithm is only used for calculating the interface normal vectors and the interface curvature in cells containing the interface. The reconstruction algorithm of Batzdorf (2015) is incorporated in the solver framework developed in this work and used for the sole purpose of increasing the accuracy of the interface normal vector and thus the curvature calculation.

Further changes on the surface tension model are not included, as the employed approach ensures balance of pressure and surface tension forces by using the same discretization stencils for surface tension and pressure equation. The impact of the different curvature estimation algorithms described above on parasitic currents is discussed in Chapter D.2.2.

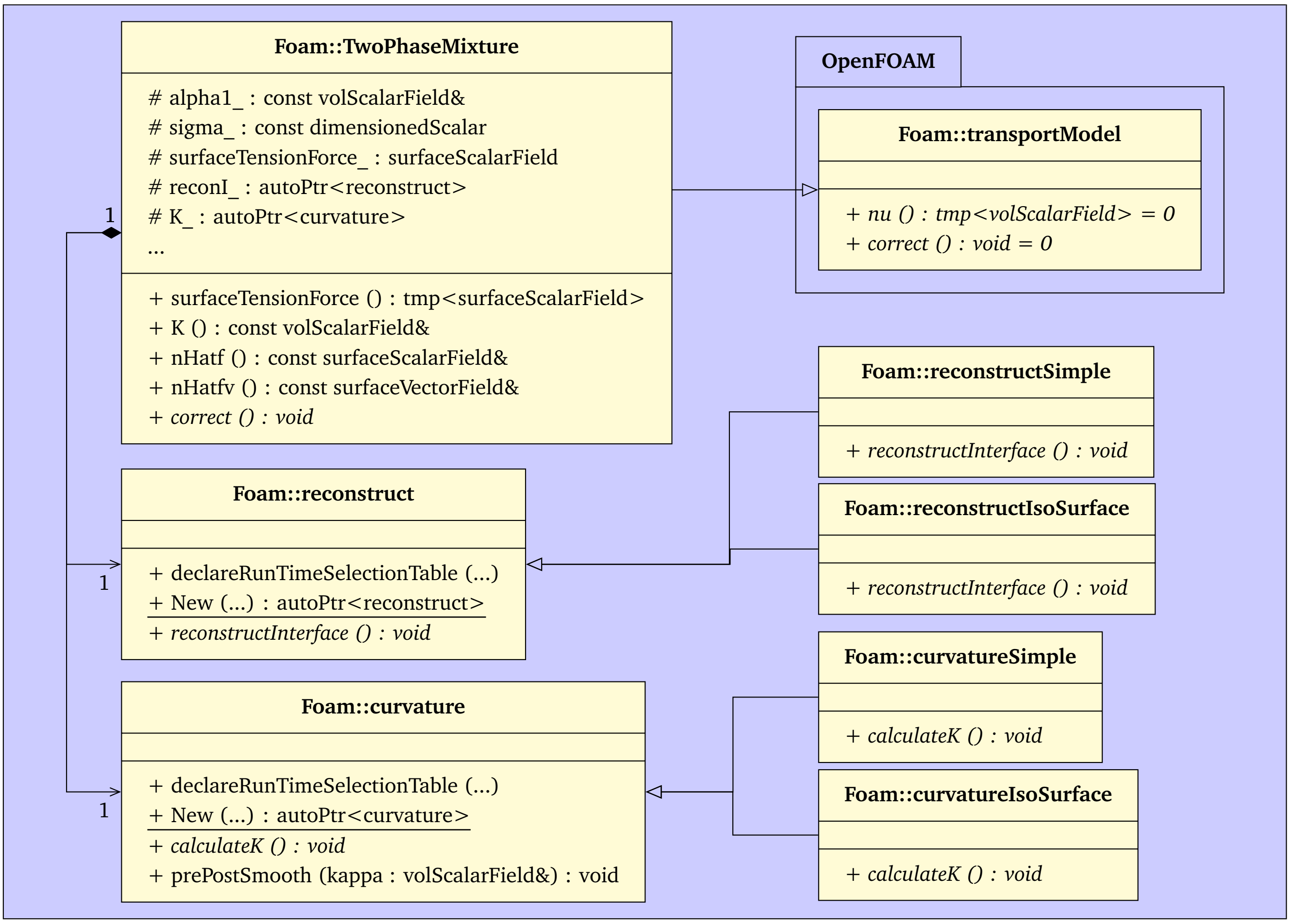

Listing D.2.: Two-phase transport model structure – UML class diagram

The implementation structure is given in Listing D.2. Relevant implementation for the improved curvature modeling is found in the classes *reconstruct* and *curvature*, which are held by the *TwoPhaseMixture*. The class *reconstruct* provides the interface normal vector, computed either from the phase fraction gradient field (*reconstructSimple*) or based on an isosurface reconstruction (*reconstructIsoSurface*) of the phase fraction field 0.5 level. The class *reconstructIsoSurface* additionally executes a distribution algorithm which interpolates the normal vectors from the interface cells to neighbouring cells. In the *curvature* class, the curvature is then computed from the divergence of the provided normal field of the *reconstruct* class. The class *curvaturetIsoSurface* additionally provides smoothing algorithms. First, the computed curvature is deleted from all cells not containing a reconstructed interface and a pre-smoothing is executed in the interface cells only. Then, the curvature is re-distributed over the interfacial region (all cells containing $\alpha_1 \in (0,1)$) and a post-smoothing of the curvature field is executed.

D.2.2 Stagnant Drop in Quiescent Liquid

The consistent and accurate incorporation of the surface tension force is of major importance for the Direct Numerical Simulation of rising bubbles, especially at higher Reynolds numbers. As previously discussed in Appendix D.2, the flux-based CSF model allows – in principle – for balancing of surface tension and pressure forces at the bubble interface. The main issue for parasitic currents is therefore the insufficient accuracy at curvature estimation. Here, different suitable techniques for curvature calculation on unstructured grids introduced in Appendix D.2 are compared to literature results for structured Cartesian meshes.

Based on Francois et al. (2006), the employed surface tension model is validated against a stagnant drop in a quiescent liquid in two dimensions. The drop of radius 2 m is placed in the centre of an 8x8 m domain with grid size 40x40 cells and slip boundary condition for velocity and zero gradient condition for the pressure. The volume fraction field is initialized numerically exact by cutting the mesh with a cylinder and computing the volume fraction of the cut cells, using the library of (Maric et al., 2013). The maximum velocity magnitude in the domain is then compared to the results of Francois et al. (2006).

Table D.1.: Error in maximum velocity $|\mathbf{u}|_{\max}$ after one time step for the inviscid static drop in equilibrium when the exact curvature is specified

ρ_1/ρ_2	interCSTFoam	CSF cell-centred (Francois et al., 2006)	SSF face-centred (Francois et al., 2006)
1	$9.81e-19$	$5.19e-5$	$5.43e-19$
10^3	$9.11e-17$	$6.15e-3$	$4.44e-18$
10^5	$7.17e-15$	$6.91e-3$	$2.71e-19$

In the first case setup, the flux-based CSF formulation is tested for force balancing by specifying the exact curvature value. The comparison in Table D.1 shows that the parasitic currents are of the same order as reported in Francois et al. (2006). However, the interFoam algorithm shows a significant influence of the density ratio onto parasitic currents, unlike the results reported in the literature.

Table D.2.: Effect of the time step on the error in maximum velocity $|\mathbf{u}|_{\max}$ at $t = 0.001$ for the inviscid static drop in equilibrium

Δt	# of time steps	interFoam	interCSTFoam isoSurface	interCSTFoam exact curvature	CSF, height function (Francois et al., 2006)	SSF, convolution (Francois et al., 2006)
$1e-3$	1	$1.98e-1$	$1.93e-2$	$8.11e-12$	$4.35e-4$	$2.58e-3$
$1e-4$	10	$1.72e-1$	$1.57e-2$	$7.58e-13$	$3.92e-4$	$2.53e-3$
$1e-5$	100	$1.47e-1$	$1.33e-2$	$3.14e-13$	$3.64e-4$	$2.56e-3$
$1e-6$	1000	$1.31e-1$	$1.22e-2$	$2.97e-13$	$3.53e-4$	$2.50e-3$

In a second test case (cf. Table D.2), the influence of time step length onto the creation of parasitic currents is investigated for an inviscid static drop. Here, the curvature in the interFoam algorithm is calculated first by standard Gauss theorem without smoothing the volume fraction field and second by the isosurface approach. It can be seen that $|\mathbf{u}|_{\max}$ slightly reduces with smaller time steps but that the absolute errors in the interFoam solver are about two orders of magnitude higher compared to the height function approach.

Table D.3.: Effect of the fluid density ratio on the error in maximum velocity $|\mathbf{u}|_{\max}$ after one time step for the viscous static drop in equilibrium

ρ_1/ρ_2	interFoam	interCSTFoam isoSurface	interCSTFoam exact curvature	CSF, height function (Francois et al., 2006)	SSF, convolution (Francois et al., 2006)
10	$1.99e-4$	$1.93e-5$	$1.17e-18$	$4.40e-7$	$2.30e-6$
10^3	$2.47e-3$	$5.03e-4$	$7.14e-17$	$6.22e-7$	$2.59e-6$
10^5	$2.01e-1$	$5.30e-2$	$5.24e-13$	$6.25e-7$	$2.59e-6$

Investigation of the density ratio influence in Table D.3 shows the severe increase of parasitic currents in the interFoam solver with increasing density ratio. The viscosities for the cases shown in Tables D.3 and D.4 are set to $\mu_1 = 10^{-2}$ and $\mu_2 = 10^{-3}$. Again, for small density ratios, $|\mathbf{u}|_{\max}$ is approximately two orders of magnitude higher for interFoam compared to the height function method utilized in Francois et al. (2006). On the positive side, curvature calculation by using the isosurface reduces the parasitic currents by one order of magnitude compared to the standard approach.

Table D.4.: Effect of the time step magnitude on the error in maximum velocity $|\mathbf{u}|_{\max}$ after one time step for the viscous static drop in equilibrium

Δt	interFoam	interCSTFoam isoSurface	interCSTFoam exact curvature	CSF, height function (Francois et al., 2006)	SSF, convolution (Francois et al., 2006)
$1e-3$	$2.21e+0$	$4.33e-1$	$7.45e-11$	$6.22e-4$	$2.59e-3$
$1e-4$	$2.44e-1$	$4.95e-2$	$1.10e-13$	$6.22e-5$	$2.59e-4$
$1e-5$	$2.47e-2$	$5.03e-3$	$1.20e-14$	$6.22e-6$	$2.59e-5$
$1e-6$	$2.47e-3$	$5.03e-4$	$7.14e-17$	$6.22e-7$	$2.59e-6$

In Table D.4, the maximum velocity is compared after one time step for different time step lengths. The results indicate that the parasitic currents increase approximately linearly over simulation time. The same behaviour is also reported in the literature. In this case setup, the parasitic velocities resulting from the interFoam algorithm are about three to four orders of magnitude higher. As the errors for specifying the exact curvature value are also given in Table D.4, the main source for the comparatively large errors is surely the insufficient curvature estimation, while the other is the scaling of parasitic currents with the density ratio.

In the last test case (cf. Table D.5), the influence of viscosity magnitude onto the algorithm under a constant viscosity ratio is tested. The results show a slight dependency of the error in respect to the viscosity magnitude in case of the interFoam method. Again, the error for the height function approach is approximately three orders of magnitude smaller than for the standard interFoam algorithm, while the isosurface reconstruction algorithm reduces this difference by about one order of magnitude.

To sum up, the presented verification tests show that the flux-based CSF approach in interFoam allows for force balancing if the curvature calculation is exact. In that case, the algorithm produces comparable results to Francois et al. (2006). Two main differences are observed: First, the interFoam solver shows – unlike reported in Francois et al. (2006) – a strong dependency

Table D.5.: Effect of fluid viscosity on the error in maximum velocity $|\mathbf{u}|_{\max}$ after (a) 100 and (b) 1000 time steps for the viscous static drop in equilibrium

μ_1	μ_2	interFoam	interCSTFoam isoSurface	interCSTFoam exact curvature	CSF, height function (Francois et al., 2006)	SSF, convolution (Francois et al., 2006)
(a) after 100 time steps						
1	$1e-1$	$1.01e-1$	$2.17e-2$	$2.81e-16$	$4.73e-5$	$2.73e-4$
$1e-2$	$1e-3$	$1.55e-1$	$4.05e-2$	$4.65e-16$	$4.83e-5$	$2.73e-4$
$1e-4$	$1e-5$	$1.57e-1$	$4.21e-2$	$5.24e-16$	$4.83e-5$	$2.73e-4$
(b) after 1000 time steps						
1	$1e-1$	$6.09e-1$	$4.09e-2$	$2.96e-16$	$4.28e-4$	$2.82e-3$
$1e-2$	$1e-3$	$1.26e+0$	$3.52e-1$	$3.80e-16$	$4.56e-4$	$2.87e-3$
$1e-4$	$1e-5$	$1.35e+0$	$3.78e-1$	$4.55e-15$	$4.58e-4$	$2.83e-3$

on the density ratio which clearly indicates problems with the numerical handling of the surface tension force. Second, the employed curvature estimation via isosurface, while reducing parasitic currents compared to the standard implementation, still produces spurious velocities which are about two orders of magnitude higher than for height functions.

D.3 Advection of Sharp Fields

The test cases presented here have the aim to quantify the errors of different utilized advection algorithms. For this, an initial field is transported by a given velocity field which can be a function of space and time. All test cases are set up so that the end position and form of the transported field revert to the initial state ideally. Comparing the initial to the end state of the transported sharp field, an error analysis is performed and the results are compared against those reported in the literature. The advection test cases cover the basic movements of a sharp field, translation, rotation, shear and deformation. The analyzed errors are the geometrical (L1), boundedness and conservation errors, which are defined as (Aulisa et al., 2007)

$$\begin{aligned}
E_g(t) &:= \sum_V |\alpha(t_0) - \alpha(t)| V \quad \text{(geometrical) L1 error ,}\\
\operatorname{norm}(E_g(t)) &:= \frac{\sum_V |\alpha(t_0) - \alpha(t)| V}{\sum_V \alpha(t_0) V} \quad \text{normalized L1 error ,}\\
E_v(t) &:= \frac{|\sum_V \alpha(t_0) V - \sum_V \alpha(t) V|}{\sum_V \alpha(t_0) V} \quad \text{volumetric error ,}\\
E_b(t) &:= \max(\alpha(t) - 1, -\alpha(t), 0) \quad \text{boundedness error .}
\end{aligned} \tag{D.7}$$

Boundedness and conservation errors presented in this thesis are obtained by taking the maximum error over all time steps of the simulation. Additionally to above errors, different sharpness estimators of the transported field are introduced and evaluated. The utilized sharpness estimators are defined as

$$\begin{aligned} E_{s,1}(t) &:= 1 - \frac{\sum_V |\alpha(t) - 0.5| V}{\sum_V 0.5 V} , \\ E_{s,2}(t)) &:= \frac{\sum_V V \left[\alpha(t_0) I(t_0) - \alpha(t) I(t) \right]}{\sum_V V \alpha(t_0) I(t_0)} , \\ E_{s,3}(t) &:= \frac{\sum_V V \left[I(t_0) - I(t) \right]}{\sum_V V I(t_0)} \quad \text{with } I(t) := \operatorname{pos}(\alpha(t) - 0.001) \operatorname{pos}(0.999 - \alpha(t)) . \end{aligned} \tag{D.8}$$

The sharpness indicators are introduced in this thesis to evaluate the ability of a given algebraic advection scheme to preserve a sharp field. An increasing value of $E_{s,i}$ as defined above, states that additional interface cells are produced.

The first introduced indicator is $E_{s,1}$, which inherently contains also information about the number of cells and reduces with a sharper interface as well as a smaller ratio of interfacial to global cell number. As such, it is expected to decrease approximately linearly with the mesh size. Therefore, additional sharpness indicators are introduced, which are independent of the number of cells. A value of $E_{s,2} = N$ or $E_{s,3} = N$ ideally correlates to N-times more interface cells as in the initial condition and thus quantifies the number of interface cells and a value of $E_{s,2/3} \approx 1$ would indicate a very sharp field. However, these two error indicators inherently contain the geometrical error, as they compare between initial and final states. For above reasons, a low $E_{s,i}$ value does not necessarily translate to a sharp field and phase loss can still occur, where part of the α-field detaches. Although they do not allow for a strict quantification, the introduced error indicators still allow for qualitative measurement of sharp fields.

In this work, the explicit and second-order semi-implicit MULES algorithms available in OpenFOAM-2.4.x are compared against the blended CICSAM scheme with implicit and second-order Crank-Nicolson time discretization for different Courant numbers and different mesh resolutions. The employed Courant numbers are 0.01, 0.1 and 0.5 and the mesh resolutions are case-dependently from 16 to 256 cells per dimension.

Unlike in the cited reference papers, the 3D cases are conducted using local adaptive mesh refinement and dynamic load balancing techniques as well as adaptive time steps. This is the realistic setting in which algebraic methods are supposed to be utilized, although it was also found to increase the numerical errors. To be able to use adaptive meshes while maintaining a divergence-free flux field, the analytical velocity fields described in the reference papers had to be integrated over the cell faces, rather than simply evaluating the analytical function in the face centre and pointing it with the face normal. The latter would introduce a flux divergence and thus destroy boundedness.

In this basic test case, a sphere of diameter 0.3 m, initially positioned in the centre of a unit box, is transported with a constant velocity field in diagonal direction (cf. Aulisa et al. (2007)). As the employed load balancing strategy does not yet support periodic boundary conditions, the test case setup is slightly modified so that AMR and load balancing could be applied. The centre of the sphere is initially positioned at $\mathbf{x}_C = (0.25, 0.25, 0.25)$ and moves in diagonal direction to $\mathbf{x}_F = (0.75, 0.75, 0.75)$, where the flow field is reversed and the sphere translated back to the initial position. This procedure is repeated to obtain a total translation distance of twice the box diagonal length as in Aulisa et al. (2007). Due to the employed flux-based advection approach, the diagonal translation leads to shape deformations which are quantified.

Studying the geometrical advection errors for different Courant numbers and mesh resolutions (Figures D.6a to D.6c) it can be seen that all employed algebraic advection methods are less than first-order convergent and at smaller Courant numbers almost grid independent. This behaviour is a direct result of the flux-based algorithm which utilizes only information of face-neighbouring cells in the discretization of the advection term. Hence, information traveling in diagonal direction needs to be communicated over two faces before reaching the diagonal point-neighbouring cell. As a result, the initial sphere is deformed independent of the mesh size

(a) CICSAM + Crank-Nicolson ($C = 0.01$).

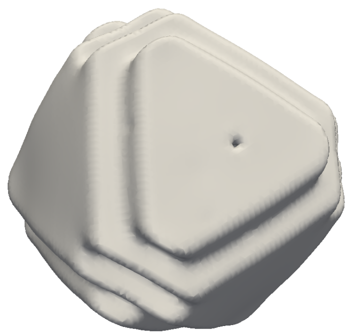

(b) MULES + Crank-Nicolson ($C = 0.01$).

Figure D.1.: Final shape of translated body (initially spherical)

and, hence, a constant geometrical error is obtained which describes the difference between the deformed and initial shape.

The final shape ($\alpha = 0.5$ isosurface) of the field for the different advection methods at Courant 0.01 and mesh resolution 256 is shown in Figure D.1. It can be seen that the CICSAM scheme transforms the initial sphere into a rhombicuboctahedron, whereas the MULES advection algorithm with interface compression term produces a deformed double pyramid with wavy surfaces replacing all corners. It can also be seen that both advection algorithms tend to produce surface oscillations depending on the cell-face/interface orientation and flux direction. The deformations, as stated above, are nearly mesh independent and thus is the geometrical error. It

Table D.6.: Diagonal translation of 3D sphere – normalised L_1 error

	n=32	n=64	n=128	n=256
$C_f = 1.5$				
norm(E_g (MYC))	$4.436e-02$	$1.388e-02$	$2.862e-03$	-
norm(E_g (LSF))	$1.216e-02$	$5.247e-03$	$1.734e-03$	-
$C_f = 0.5$				
norm(E_g (CICSAM-CN))	0.6010	0.4043	0.2671	0.1578
norm(E_g (CICSAM-Euler))	0.8401	0.5994	0.3795	0.2469
norm(E_g (MULES-CN))	0.6681	0.3760	0.3040	0.3009
norm(E_g (MULES-Euler))	1.366	1.165	0.8484	0.5661
$C_f = 0.1$				
norm(E_g (CICSAM-CN))	0.1526	0.08494	0.06924	0.06239
norm(E_g (CICSAM-Euler))	0.3136	0.1562	0.1051	0.07449
norm(E_g (MULES-CN))	0.3541	0.2760	0.2499	0.1995
norm(E_g (MULES-Euler))	0.3769	0.2784	0.2088	0.1303
$C_f = 0.01$				
norm(E_g (CICSAM-CN))	0.1039	0.07794	0.07663	0.05991
norm(E_g (CICSAM-Euler))	0.1071	0.07637	0.07675	0.05853
norm(E_g (MULES-CN))	0.1600	0.2243	0.2115	0.1381
norm(E_g (MULES-Euler))	0.1601	0.2218	0.2001	0.1221

should be noted that the deformation is also independent of the Courant number. The only influence being that a higher Courant number adds a larger numerical diffusion and, hence, the resulting shape is smeared out.

Figures D.6d to D.6l show that boundedness and sharpness of the transported field are sufficiently preserved for the CICSAM schemes and explicit MULES algorithm, whereas the second-order MULES algorithm (with standard settings) introduces a large unboundedness. Mass conservation is not shown in the Figures as the maximum conservation error over all runs is well below 0.1% for $C = 0.5$ and below 0.001% for $C = 0.01$. The largest volume conservation errors appear for the second-order MULES algorithm in cases with large unboundedness.

Given all relevant criteria, sharpness, conservation, boundedness and accuracy, the CICSAM scheme with second-order Crank-Nicolson time-discretization shows the best behaviour in this test case between the four algebraic schemes. However, compared to geometrical methods, the errors are orders of magnitude higher. This is to be expected, since the case of diagonal translation maximizes the errors of algebraic advection methods. It should further be noted that the geometrical errors are bound to reduce on polyhedral grids, due to the increased number of neighbouring cells and thus considerably better gradient approximations. The large influence of mesh topology onto the accuracy is shown, e.g., in Hill et al. (2018).

D.3.2 Rotation of a Sphere

A sphere of diameter 0.3 m, initially positioned in a unit box at [0.5 m, 0.75 m, 0.5 m], is rotated by a constant angular velocity around the z-axis (cf. Jofre et al. (2010)). The errors are calculated after one rotation and compared to literature results from Jofre et al. (2010).

It can be observed in Figure D.7 that the second-order MULES algorithm with standard setting induces a large unboundedness in case of rotation. In general, the algorithm was found

Table D.7.: Rotation of 3D sphere – L_1 error

	n=32	n=64	n=128	n=256
$C_f = 0.5$				
E_g (Youngs)	$6.34e-04$	$5.47e-04$	$3.20e-04$	–
E_g (CICSAM-CN)	$1.815e-03$	$1.459e-03$	$9.771e-04$	$6.538e-04$
E_g (CICSAM-Euler)	$3.677e-03$	$3.450e-03$	$2.671e-03$	$1.971e-03$
E_g (MULES-CN)	$3.800e-03$	$1.872e-03$	$2.384e-03$	$2.013e-03$
E_g (MULES-Euler)	$3.733e-03$	$2.845e-03$	$2.346e-03$	$1.781e-03$
$C_f = 0.1$				
E_g (CICSAM-CN)	$1.593e-03$	$6.613e-04$	$3.614e-04$	$2.158e-04$
E_g (CICSAM-Euler)	$1.800e-03$	$8.743e-04$	$4.799e-04$	$2.790e-04$
E_g (MULES-CN)	$1.864e-03$	$1.073e-03$	$1.153e-03$	$1.310e-03$
E_g (MULES-Euler)	$1.737e-03$	$9.930e-04$	$5.279e-03$	$2.946e-04$
$C_f = 0.01$				
E_g (CICSAM-CN)	$1.599e-03$	$7.932e-04$	$4.623e-04$	$2.802e-04$
E_g (CICSAM-Euler)	$1.619e-03$	$8.024e-04$	$4.689e-04$	$2.827e-04$
E_g (MULES-CN)	$1.477e-03$	$7.733e-04$	$4.726e-04$	$3.712e-04$
E_g (MULES-Euler)	$1.465e-03$	$7.553e-04$	$4.029e-04$	$2.276e-04$

to be non-robust. As to be expected for Finite Volume methods, the tested algebraic advection algorithms all show a good volume conservation property with a volumetric error well below 0.01%, which is why the corresponding graphs are not shown here. Comparing the obtained geometrical errors to the reference solution, an approximate first-order convergence can be seen for all methods, which is to be expected. However, it should be noted that the absolute error in the reference paper, which was obtained with a Courant number of 0.5, is nearly one order of magnitude lower than for the algebraic methods at $C_f = 0.5$. For lower Courant numbers, however, the errors are comparable to the geometrical method's reference solution.

In Figure D.7, the ability of the respective schemes to preserve a sharp interface is investigated. Here, all schemes, except the second-order MULES algorithm, result in a relatively sharp field of about two cell layers for the interface region when small Courant numbers are used. At larger Courant numbers, the MULES algorithm results in a considerably sharper field, due to the time step-independent counter gradient diffusion term, whereas the anti-diffusive term in the CICSAM scheme inversely proportional depends on the Courant number. It should also be noted that the second-order MULES algorithm leads to unbounded solutions in some cases due to non-convergence of the algorithm.

D.3.3 Rotation of Zalesak-Disc

This test case is based on the case setup of Zalesak (1979), but in a three-dimensional setup. For this case, no error tables for comparison to literature are available. The setup is the same as in the 3D rotational case above, only with a small central cut in the sphere of width 0.05 and depth 0.175. Figure D.2 shows the final shape of the (initially sharp) slotted sphere after one rotation. Unlike in the quantitative analysis (cf. Table D.8 and Figure D.8), which shows no significant differences between CICSAM and MULES, here it can be seen that the employed interface compression in the MULES advection algorithm introduces strong wrinkling of the interface. This is due to the fact that the compression needs the interface normal vector, whose computation is not accurate enough. In this case, the *leastSquares* gradient was used. Employing the standard *Gauss gradient* will lead to worse results.

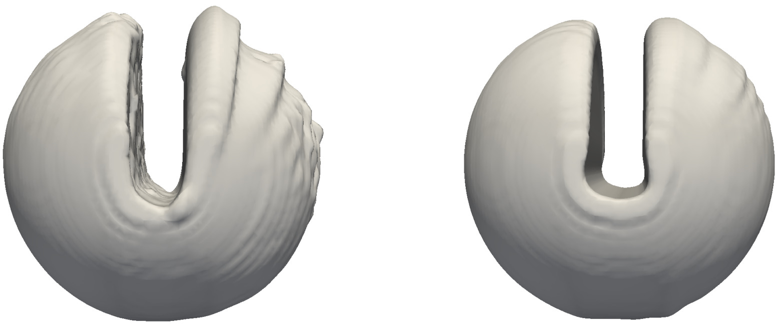

(a) MULES (2nd order). **(b)** CICSAM + CrankNicolson.

Figure D.2.: Final shape of the interface after one rotation of the Zalesak sphere

Table D.8.: Rotation of 3D Zalesak sphere – normalized L_1 error

	n=32	n=64	n=128	n=256
$C_f = 0.5$				
norm(E_g (CICSAM-CN))	0.3481	0.1930	0.09407	0.06093
norm(E_g (CICSAM-Euler))	0.4495	0.4576	0.3343	0.2556
norm(E_g (MULES-CN))	0.5271	0.6016	0.2784	0.1839
norm(E_g (MULES-Euler))	0.6535	0.7693	0.2049	0.1440
$C_f = 0.1$				
norm(E_g (CICSAM-CN))	0.3140	0.1241	0.05698	0.03250
norm(E_g (CICSAM-Euler))	0.3258	0.1755	0.07282	0.03943
norm(E_g (MULES-CN))	0.4767	0.2621	0.1202	0.1103
norm(E_g (MULES-Euler))	0.4713	0.1904	0.08994	0.05205
$C_f = 0.01$				
norm(E_g (CICSAM-CN))	0.3124	0.1256	0.06093	0.03509
norm(E_g (CICSAM-Euler))	0.3138	0.1282	0.06198	0.03545
norm(E_g (MULES-CN))	0.4139	0.1796	0.08114	0.05874
norm(E_g (MULES-Euler))	0.4178	0.1717	0.07303	0.04060

D.3.4 Shear Advection 2D

This case setup is taken from Liovic et al. (2006), where the reference solutions are obtained with C = 1.0. To not introduce flux divergence on dynamically refined meshes, the analytical velocity field is integrated over the cell faces, yielding the following expression of the flux field, which is utilized in this work:

$$F_f = \frac{\sin(4\pi\Delta x)}{4\pi\Delta x}\mathbf{u}\left(\mathbf{x}_f\right)\cdot\mathbf{S}_f \,. \tag{D.9}$$

The comparison of geometrical errors (cf. Table D.9 and Figure D.9) clearly shows that geometrical reconstruction methods are far superior in terms of accuracy. However, given small

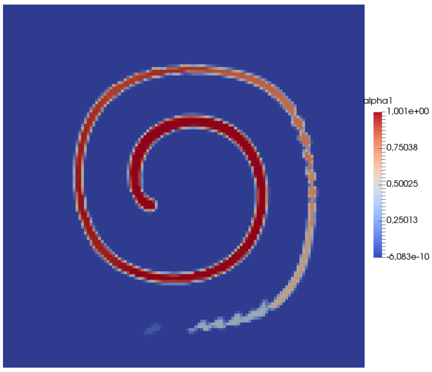

(a) MULES (2nd order).

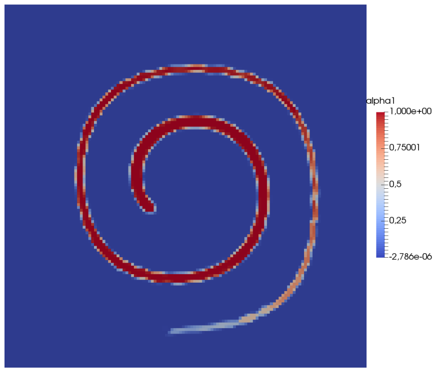

(b) CICSAM + CrankNicolson.

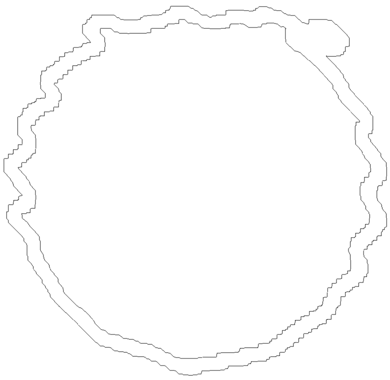

(c) MULES (2nd order).

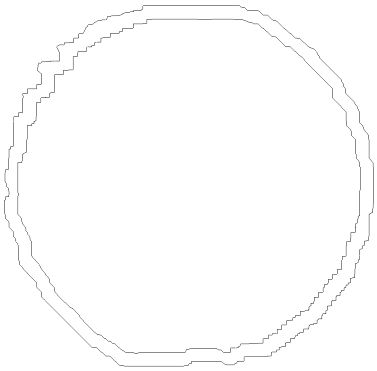

(d) CICSAM + CrankNicolson.

Figure D.3.: Shape of the interface at maximal deformation (128^2 grid, C=0.1) and final stage (256^2 grid, C=0.01) (iso-contours for α=0.01 and 0.99)

time steps, sufficiently accurate results can also be produced by algebraic advection methods, although the absolute error remains larger than for methods with geometrical reconstruction.

Table D.9.: 2D shear flow – L_1 error

	n=32	n=64	n=128	n=256
$C_f = 1$ (Liovic et al., 2006)				
E_g (linear fit + EI-LE)	$1.75-03$	$4.66-04$	$1.02e-04$	–
$C_f = 0.5$				
norm(E_g (CICSAM-CN))	$9.79e-02$	$7.34e-02$	$3.77e-02$	$7.59e-03$
norm(E_g (CICSAM-Euler))	$1.01e-01$	$7.71e-02$	$4.18e-02$	$9.98e-03$
norm(E_g (MULES-CN))	$6.52e-02$	$1.88e-02$	$1.43e-02$	$1.07e-02$
norm(E_g (MULES-Euler))	$1.03e-01$	$7.60e-02$	$7.58e-02$	$7.48e-02$
$C_f = 0.1$				
norm(E_g (CICSAM-CN))	$7.06e-02$	$3.04e-02$	$4.39e-03$	$1.25e-03$
norm(E_g (CICSAM-Euler))	$6.99e-02$	$3.14e-02$	$4.81e-03$	$1.63e-03$
norm(E_g (MULES-CN))	$7.62e-02$	$2.34e-02$	$6.40e-03$	$4.40e-03$
norm(E_g (MULES-Euler))	$1.07e-01$	$3.55e-02$	$7.36e-03$	$7.71e-03$
$C_f = 0.01$				
norm(E_g (CICSAM-CN))	$6.04e-02$	$2.29e-02$	$3.93e-03$	$1.53e-03$
norm(E_g (CICSAM-Euler))	$6.04e-02$	$2.29e-02$	$3.98e-03$	$1.54e-03$
norm(E_g (MULES-CN))	$9.15e-02$	$2.64e-02$	$6.54e-03$	$3.43e-03$
norm(E_g (MULES-Euler))	$1.11e-01$	$3.66e-02$	$6.35e-03$	$3.32e-03$

Interesting is that all algebraic methods (for small Courant numbers) show a nearly second-order convergence in the geometrical error, whereas only a first-order convergence would be expected due to the derivation of these schemes. From Figure D.9, it can be deduced that the utilized algebraic methods retain boundedness, sharpness and accuracy at small Courant numbers and that the MULES schemes produce a sharper field. However, the figures do not contain information about accuracy and sharpness over time, only about the final state. If the field shape given with the MULES and CICSAM schemes are compared at different time instances (cf. Fig D.3), the differences between both advection methods becomes eminent. The MULES algorithm produces surface oscillations with high amplitudes, whereas the CICSAM schemes retain a (relatively) smooth surface.

Also, from the intermediate state (Figures D.3a and D.3b) it becomes clear why the CICSAM schemes lead to a smearing of the interface: At the point of maximal deformation, the minimal thickness of the alpha field is only 2 to 3 cells at a resolution of 256^3, leading to smearing in algebraic schemes which utilize a three-cell stencil and hence cannot capture the field shape in this case. This also leads to a larger L1 error. However, for the simulation of rising bubbles, such structures are only encountered in the skirted bubble regime and, hence, it can be concluded that such bubble shapes may not be captured correctly with algebraic methods.

D.3.5 Field Deformation

The final advection test cases are taken from Rider and Kothe (1995) and Liovic et al. (2006) respectively and evaluate the influence of strong deformation onto the algebraic transport.

Deformation 2D

This advection case is taken from Rider and Kothe (1995) and geometrical errors are compared to their results on a 64x64 mesh with first-order upwind scheme (worst case) and the marker particle method (best case) for different particle distributions, which in effect correlates to higher mesh resolution. The integrated flux field over cell faces leads to the following correction to the face-centred velocity, which is utilized here for the advection to obtain a divergence-free flux field on adaptive meshes:

$$F_f = \frac{\sin(4\pi\Delta x)}{4\pi\Delta x}\mathbf{u}\left(\mathbf{x}_f\right)\cdot\mathbf{S}_f\,. \tag{D.10}$$

It can be seen that the geometrical error of the tested algebraic schemes at high Courant numbers are not much lower than for the upwind scheme (cf. Table D.10). This is expected for several reasons: firstly, the CICSAM scheme tends to the upwind scheme for higher Courant numbers and is identical to the upwind scheme for $C_f = 1$. Secondly, the interface in this test case is stretched to become extremely thin and thus the shape of the field cannot be preserved (see Figures D.4a and D.4b) which leads to excessive smearing of the interface (see Figures

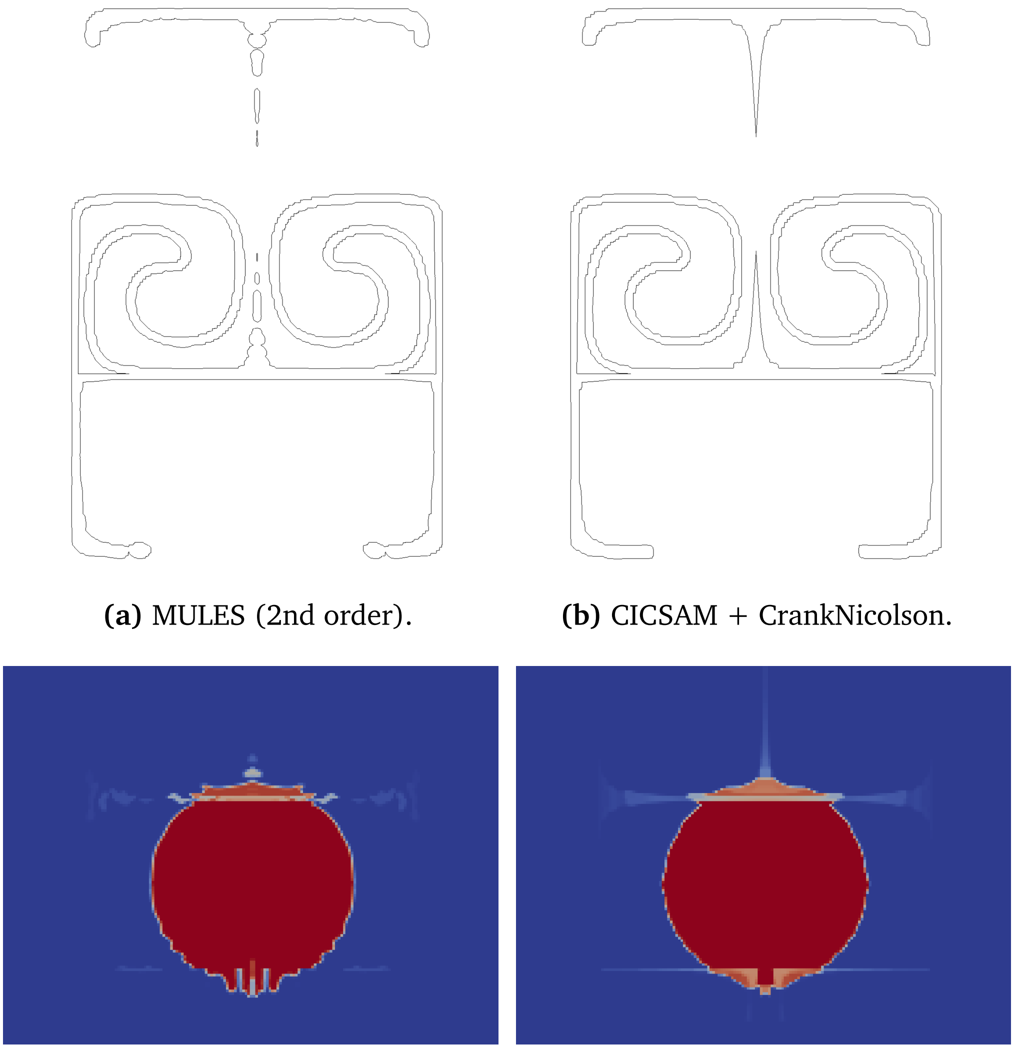

(a) MULES (2nd order). **(b)** CICSAM + CrankNicolson.

(c) MULES (2nd order). **(d)** CICSAM + CrankNicolson.

Figure D.4.: Shape of the interface at maximal deformation (iso-contours for α=0.01 and 0.99) and final stage for 256^2 grid and C=0.01

D.4c and D.4d). As for nearly all previous cases, the error shows a first-order convergence with respect to mesh resolution and also reduces with smaller Courant numbers. Field sharpness, however, is nearly mesh independent in this case (cf. Figure D.10), owing to the extreme thinning of the phase below 3 cells thickness (cf. Fig. D.4). As in the previous cases, the MULES advection algorithm introduces significantly more severe interface wrinkling than CICSAM.

Deformation 3D

This advection test case is taken again from Liovic et al. (2006). Here, again, the flux integration is performed in order to maintain a divergence-free face flux field and, hence, a

Table D.10.: 2D deformation flow – L_1 error

	n=32	n=64	n=128	n=256
$C_f = 1$ (Rider and Kothe, 1995)				
E_g (1st order upwind)	–	$5.60e-02$	–	–
E_g (marker particles)	–	$4.08-03$	$1.62e-03$	$1.28e-03$
$C_f = 0.5$				
norm(E_g (CICSAM-CN))	$3.25e-02$	$1.88e-02$	$1.15e-02$	$6.24e-03$
norm(E_g (CICSAM-Euler))	$3.96e-02$	$2.45e-02$	$1.53e-02$	$8.69e-03$
norm(E_g (MULES-CN))	$2.88e-02$	$2.09e-02$	$1.36e-02$	$7.50e-03$
norm(E_g (MULES-Euler))	$2.46e-02$	$1.78e-02$	$1.26e-02$	$9.92e-03$
$C_f = 0.1$				
norm(E_g (CICSAM-CN))	$2.31e-02$	$1.30e-02$	$8.03e-03$	$3.91e-03$
norm(E_g (CICSAM-Euler))	$2.39e-02$	$1.35e-02$	$8.35e-03$	$4.05e-03$
norm(E_g (MULES-CN))	$2.37e-02$	$1.38e-02$	$8.90e-03$	$4.59e-03$
norm(E_g (MULES-Euler))	$2.18e-02$	$1.34e-02$	$8.04e-03$	$4.20e-03$
$C_f = 0.01$				
norm(E_g (CICSAM-CN))	$2.26e-02$	$1.30e-02$	$7.71e-03$	$3.67e-03$
norm(E_g (CICSAM-Euler))	$2.26e-02$	$1.30e-02$	$7.71e-03$	$3.69e-03$
norm(E_g (MULES-CN))	$2.18e-02$	$1.22e-02$	$7.80e-03$	$3.82e-03$
norm(E_g (MULES-Euler))	$2.12e-02$	$1.24e-02$	$7.21e-03$	$3.77e-03$

bounded solution. The integrated flux field over cell faces leads to the following correction to the face-centred velocity, which is utilized here for computation of the advection flux:

$$F_f = \frac{\sin(2\pi\Delta x)}{2\pi\Delta x}\mathbf{u}\left(\mathbf{x}_f\right)\cdot\mathbf{S}_f\,. \tag{D.11}$$

The comparison with literature data from the geometrical methods in Liovic et al. (2006) (see Table D.11 and Figure D.11) shows that algebraic methods are sufficiently accurate and lead to comparable errors. Initially, on coarse grids, the geometrical errors are of similar size. Due to the first-order convergence of the employed algebraic methods, however, the errors on finer meshes are comparatively larger than in Liovic et al. (2006), who employ second-order convergent geometrical methods for the advection. The results in Figure D.11 show that boundedness and sharpness of the transported field are approximately maintained for all algebraic advection methods, with the exception being the second-order MULES algorithm.

As for the previous cases, all algebraic methods tested here result in very similar geometrical errors, whereas the explicit MULES algorithm has the advantage of retaining a sharp field also for larger Courant numbers (cf. Fig. D.11). However, when viewing the intermediate profiles, differences between CICSAM and MULES advection can be seen (cf. Fig. D.5). Similar to the previous advection test cases, the *interface compression* employed in the MULES advection algorithm introduces significantly stronger wrinkling of the interface compared to the CICSAM scheme.

D.3.6 Conclusion of Advection Cases

General outcome of the advection cases is that the employed algebraic methods are only first-order accurate and exhibit larger errors in comparison to geometrical advection methods

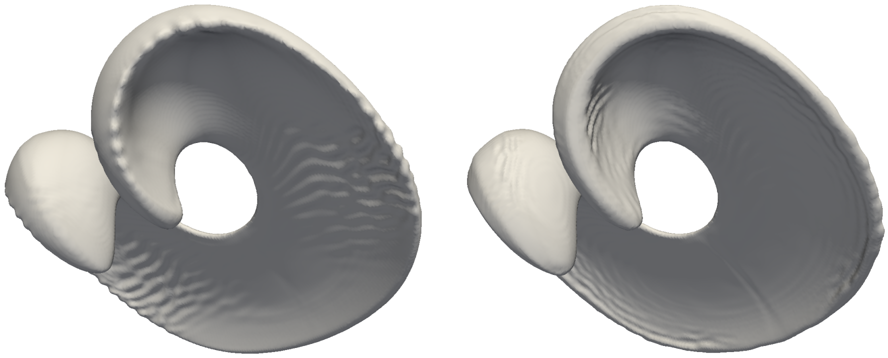

(a) MULES (2nd order). **(b)** CICSAM + CrankNicolson.

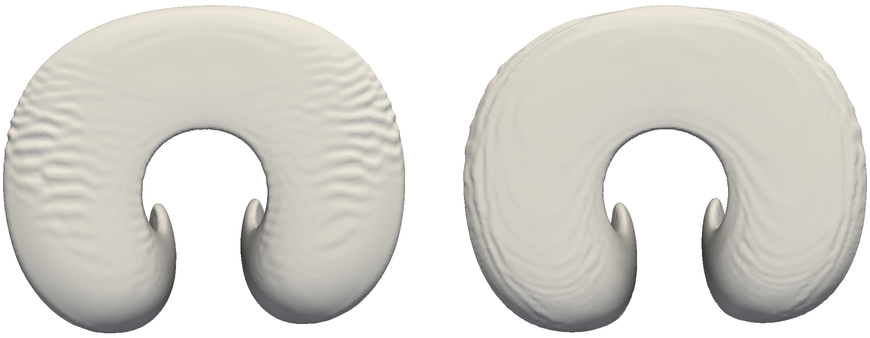

(c) MULES (2nd order). **(d)** CICSAM + CrankNicolson.

Figure D.5.: Shape of the interface (α=0.5 iso-contour) at maximal deformation from different views for 256^3 grid and C=0.01

Table D.11.: 3D deformation flow – L_1 error

	n=32	n=64	n=128	n=256
$C_f = 0.5$ (Liovic et al., 2006)				
E_g (Youngs + PCFSC unsplit)	$7.86e-03$	$2.91e-03$	$7.36e-04$	$2.26e-04$
E_g (CVTNA + PCFSC unsplit)	$7.41e-03$	$1.99e-03$	$3.09e-04$	$7.03e-05$
$C_f = 0.5$				
norm(E_g (CICSAM-CN))	$1.41e-02$	$8.40e-03$	$4.35e-03$	$1.66e-03$
norm(E_g (CICSAM-Euler))	$1.52e-02$	$9.66e-03$	$5.20e-03$	$2.36e-03$
norm(E_g (MULES-CN))	$8.06e-03$	$3.62e-03$	$2.04e-03$	$2.15e-03$
norm(E_g (MULES-Euler))	$8.15e-03$	$5.14e-03$	$3.83e-03$	$4.67e-03$
$C_f = 0.1$				
norm(E_g (CICSAM-CN))	$9.38e-03$	$4.41e-03$	$1.86e-03$	$6.13e-04$
norm(E_g (CICSAM-Euler))	$9.62e-03$	$4.68e-03$	$2.00e-03$	$6.90e-04$
norm(E_g (MULES-CN))	$8.33e-03$	$2.71e-03$	$1.44e-03$	$1.38e-03$
norm(E_g (MULES-Euler))	$7.68e-03$	$3.56e-03$	$1.39e-03$	$7.86e-03$
$C_f = 0.01$				
norm(E_g (CICSAM-CN))	$8.94e-03$	$4.19e-03$	$1.64e-03$	$6.65e-04$
norm(E_g (CICSAM-Euler))	$8.98e-03$	$4.21e-03$	$1.66e-03$	$6.67e-04$
norm(E_g (MULES-CN))	$8.08e-03$	$2.90e-03$	$1.30e-03$	$8.09e-04$
norm(E_g (MULES-Euler))	$7.92e-03$	$3.57e-03$	$1.31e-03$	$7.53e-03$

for all mesh sizes and Courant numbers. On the positive side, however, it can be seen that algebraic methods are capable to transport sharp fields with sufficient accuracy while maintaining a bounded solution, given small enough time steps and fine mesh resolutions.

In terms of the geometrical error evaluated at the final time step, all employed algebraic advection methods yield very similar results, although the CICSAM scheme has a small advantage especially at lower Courant numbers. On the other side, the explicit MULES algorithm performs significantly better in terms of boundedness and sharpness of the transported field. A closer look at the transported profiles reveals that the MULES algorithm introduces – in all cases – strong oscillations of the interface. As the flow field is reversed, also these oscillations diminish again and thus this error is not visible in the evaluated geometrical error.

In conclusion, the CICSAM scheme exhibits higher accuracy, while the explicit MULES algorithm maintains a sharper field and exhibits – inherent to the model – better boundedness of the transported field. Thus, the CICSAM scheme is to be preferred at small Courant numbers and fine meshes for its increase in accuracy, whereas the explicit MULES algorithm should be applied when larger time steps are necessary. As the MULES algorithm additionally causes inconsistencies in the advection of volumetric phase fraction and other transported fields as, e.g., species concentration, it should be avoided in such cases.

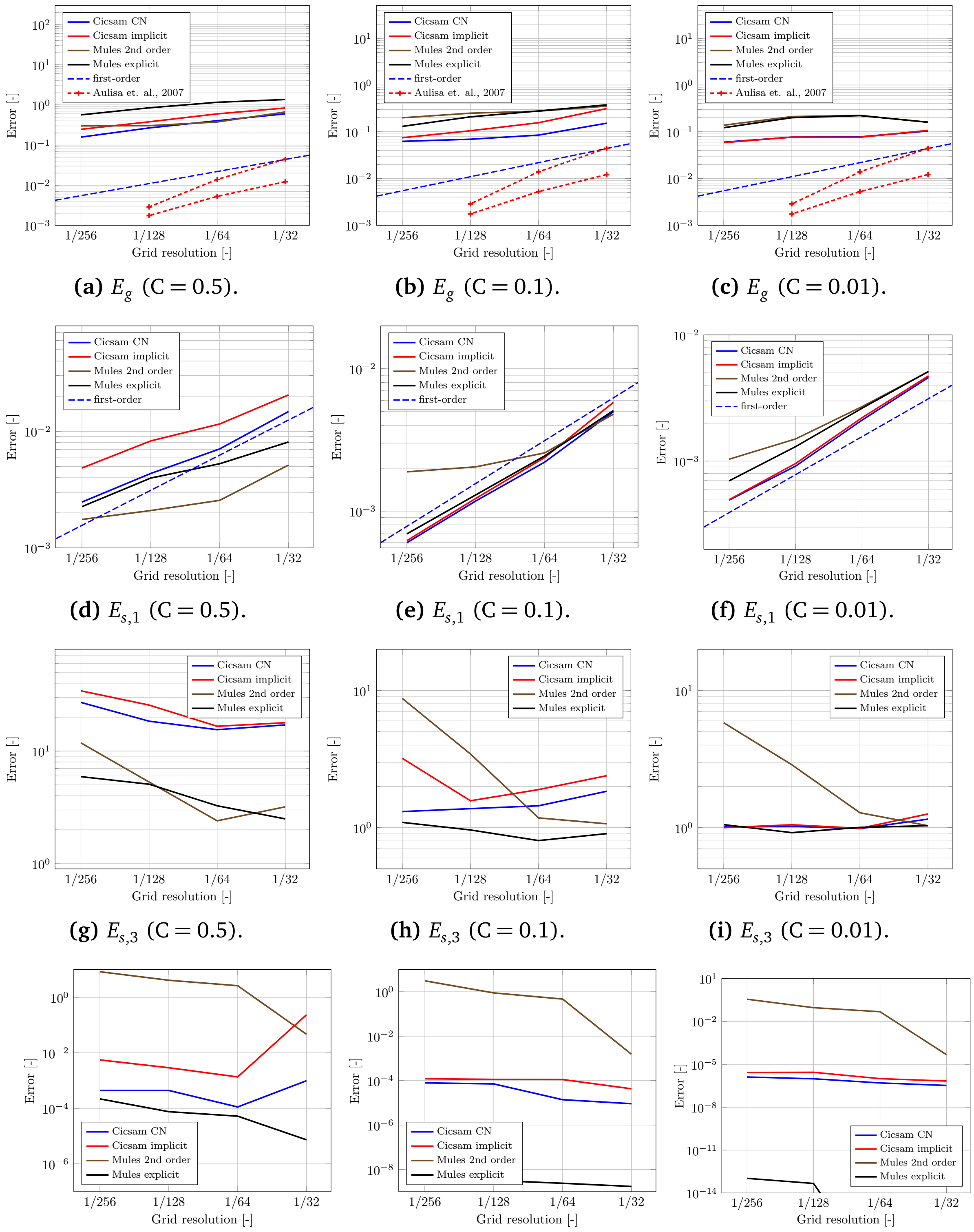

(a) E_g (C = 0.5). **(b)** E_g (C = 0.1). **(c)** E_g (C = 0.01).

(d) $E_{s,1}$ (C = 0.5). **(e)** $E_{s,1}$ (C = 0.1). **(f)** $E_{s,1}$ (C = 0.01).

(g) $E_{s,3}$ (C = 0.5). **(h)** $E_{s,3}$ (C = 0.1). **(i)** $E_{s,3}$ (C = 0.01).

(j) E_b (C = 0.5). **(k)** E_b (C = 0.1). **(l)** E_b (C = 0.01).

Figure D.6.: Diagonal translation of 3D sphere – Error plots

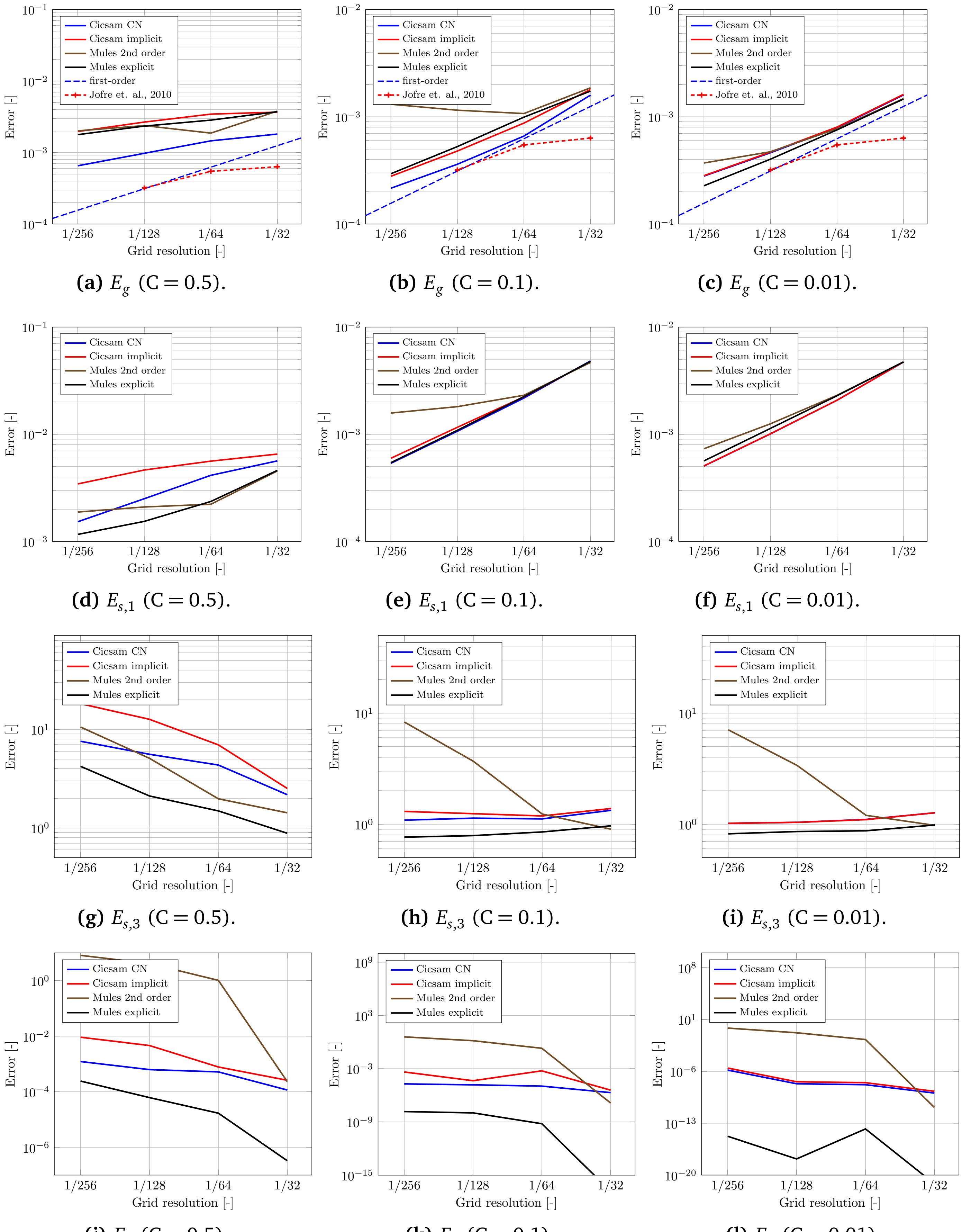

(a) E_g (C = 0.5). **(b)** E_g (C = 0.1). **(c)** E_g (C = 0.01).

(d) $E_{s,1}$ (C = 0.5). **(e)** $E_{s,1}$ (C = 0.1). **(f)** $E_{s,1}$ (C = 0.01).

(g) $E_{s,3}$ (C = 0.5). **(h)** $E_{s,3}$ (C = 0.1). **(i)** $E_{s,3}$ (C = 0.01).

(j) E_b (C = 0.5). **(k)** E_b (C = 0.1). **(l)** E_b (C = 0.01).

Figure D.7.: Rotation of 3D sphere – Error plots

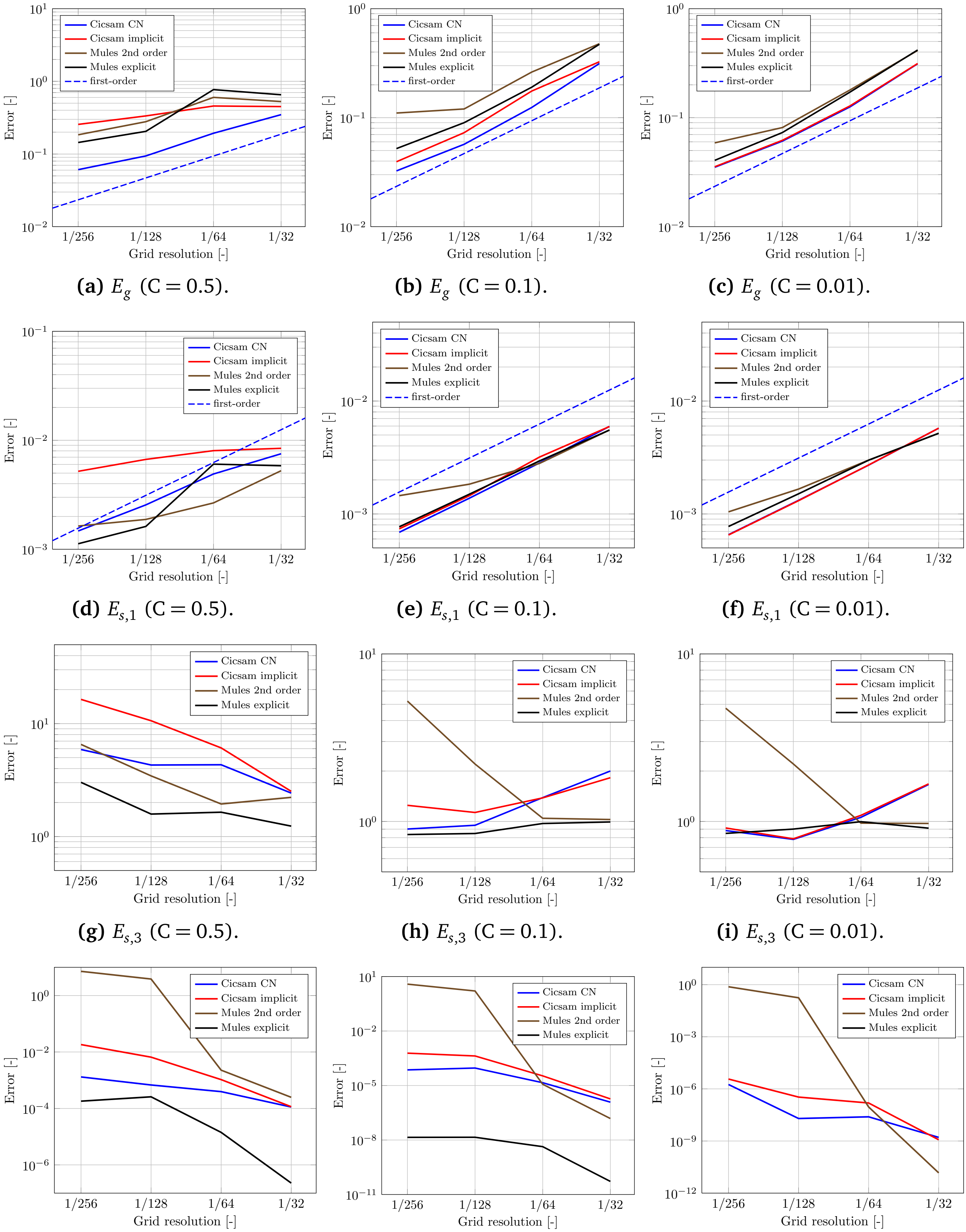

(a) E_g (C = 0.5). (b) E_g (C = 0.1). (c) E_g (C = 0.01).

(d) $E_{s,1}$ (C = 0.5). (e) $E_{s,1}$ (C = 0.1). (f) $E_{s,1}$ (C = 0.01).

(g) $E_{s,3}$ (C = 0.5). (h) $E_{s,3}$ (C = 0.1). (i) $E_{s,3}$ (C = 0.01).

(j) E_b (C = 0.5). (k) E_b (C = 0.1). (l) E_b (C = 0.01).

Figure D.8.: Rotation of 3D Zalesak disc – Error plots

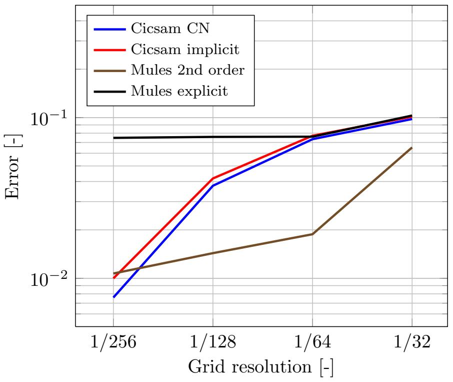

(a) E_g (C = 0.5).

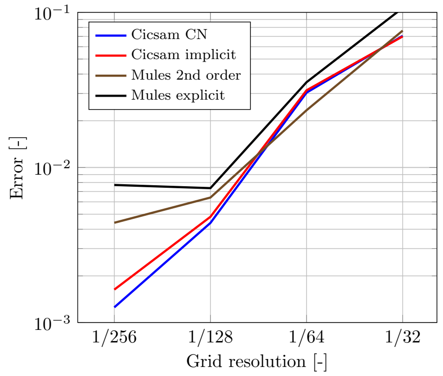

(b) E_g (C = 0.1).

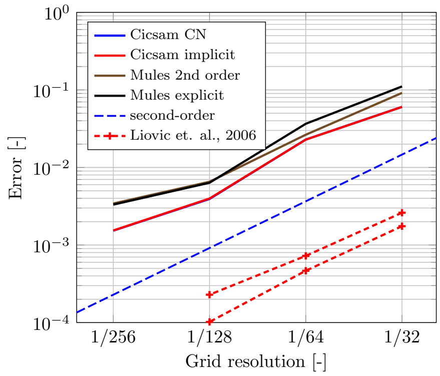

(c) E_g (C = 0.01).

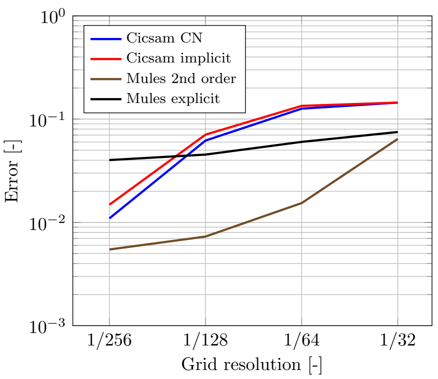

(d) $E_{s,1}$ (C = 0.5).

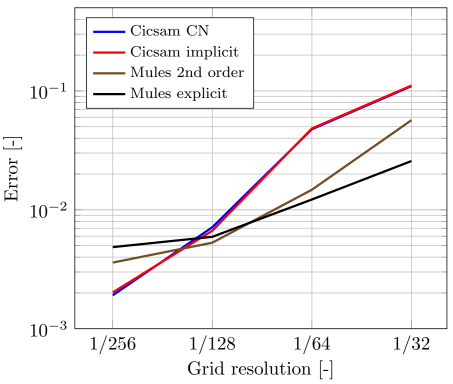

(e) $E_{s,1}$ (C = 0.1).

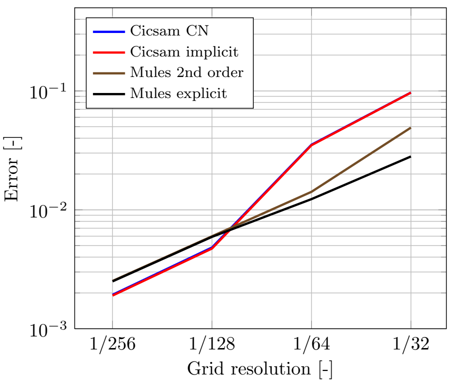

(f) $E_{s,1}$ (C = 0.01).

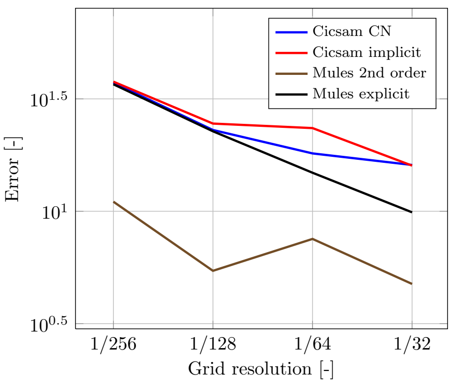

(g) $E_{s,3}$ (C = 0.5).

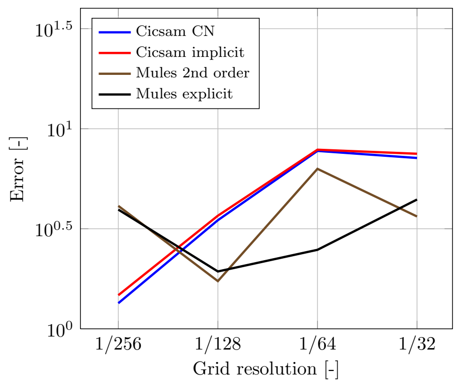

(h) $E_{s,3}$ (C = 0.1).

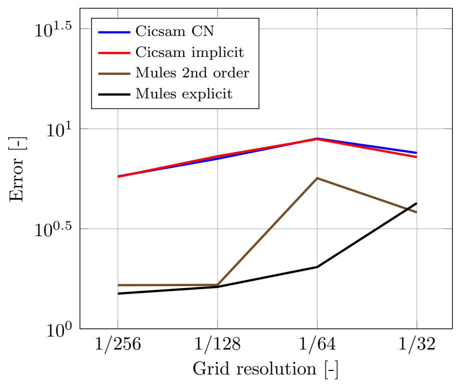

(i) $E_{s,3}$ (C = 0.01).

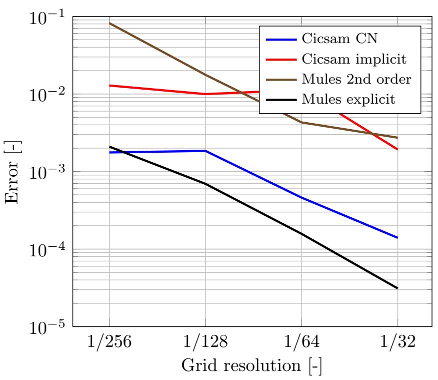

(j) E_b (C = 0.5).

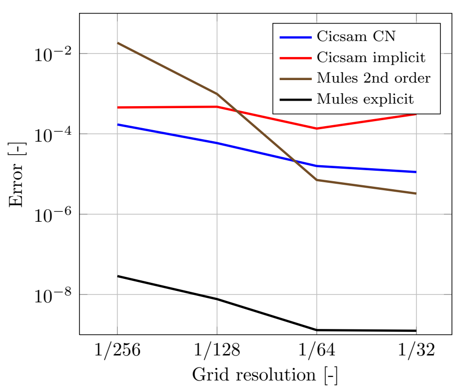

(k) E_b (C = 0.1).

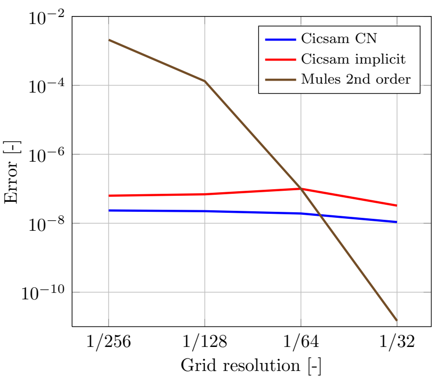

(l) E_b (C = 0.01).

Figure D.9.: 2D shear test – Error plots

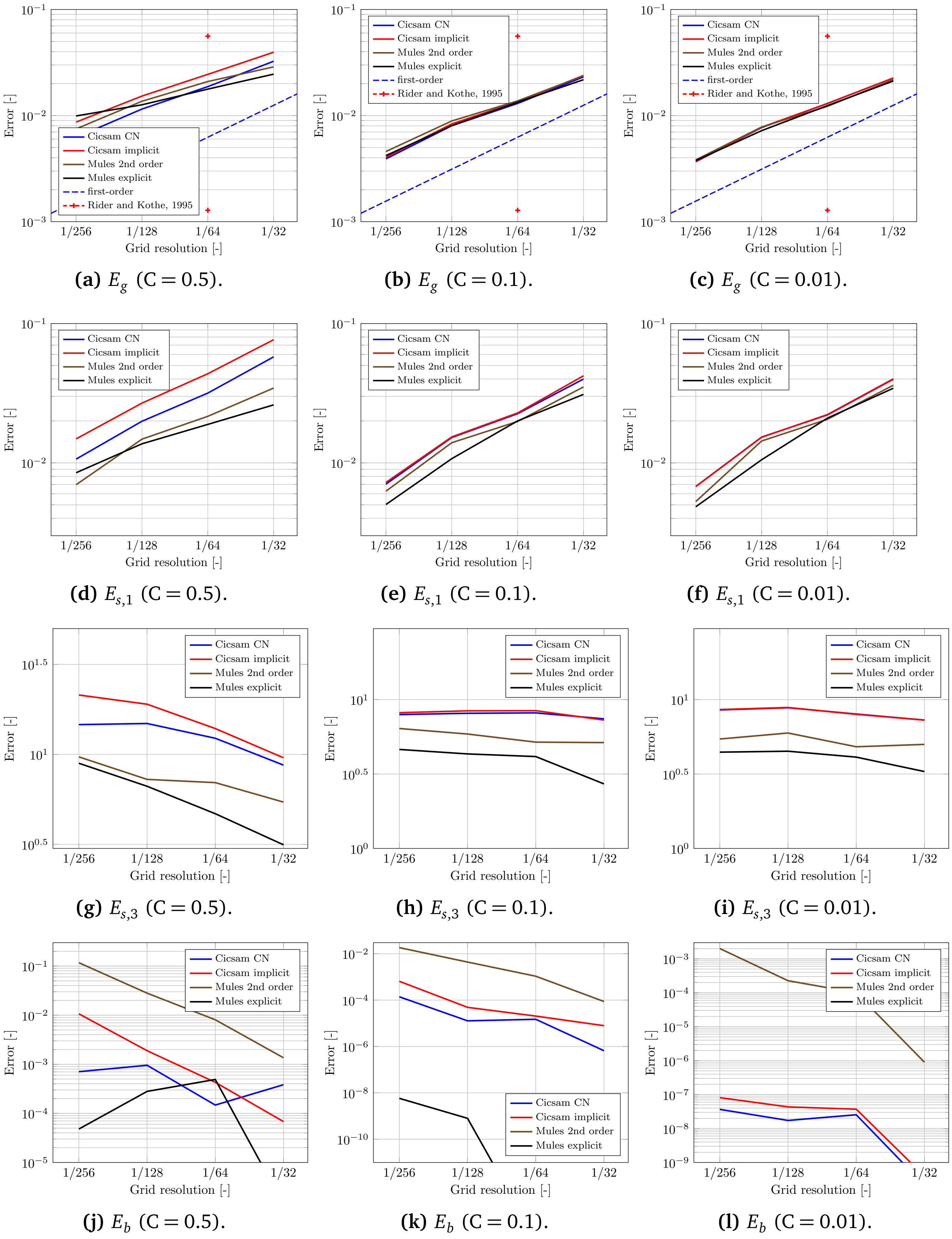

(a) E_g (C = 0.5). **(b)** E_g (C = 0.1). **(c)** E_g (C = 0.01).

(d) $E_{s,1}$ (C = 0.5). **(e)** $E_{s,1}$ (C = 0.1). **(f)** $E_{s,1}$ (C = 0.01).

(g) $E_{s,3}$ (C = 0.5). **(h)** $E_{s,3}$ (C = 0.1). **(i)** $E_{s,3}$ (C = 0.01).

(j) E_b (C = 0.5). **(k)** E_b (C = 0.1). **(l)** E_b (C = 0.01).

Figure D.10.: 2D deformation test – Error plots

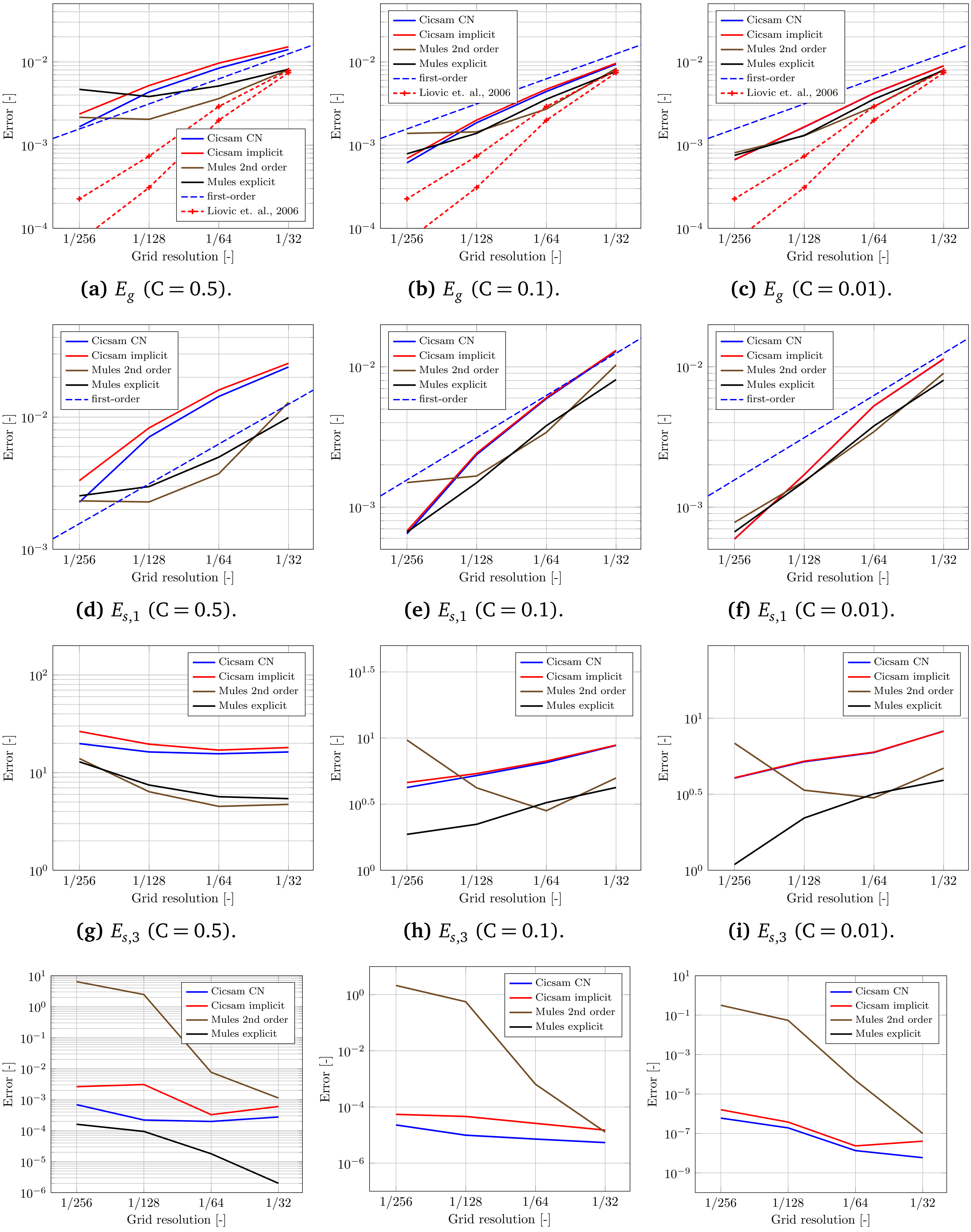

(a) E_g (C = 0.5). **(b)** E_g (C = 0.1). **(c)** E_g (C = 0.01).

(d) $E_{s,1}$ (C = 0.5). **(e)** $E_{s,1}$ (C = 0.1). **(f)** $E_{s,1}$ (C = 0.01).

(g) $E_{s,3}$ (C = 0.5). **(h)** $E_{s,3}$ (C = 0.1). **(i)** $E_{s,3}$ (C = 0.01).

(j) E_b (C = 0.5). **(k)** E_b (C = 0.1). **(l)** E_b (C = 0.01).

Figure D.11.: 3D deformation test – Error plots

Bibliography

B. Aboulhasanzadeh, S. Thomas, M. Taeibi-Rahni, and G. Tryggvason. Multiscale computations of mass transfer from buoyant bubbles. *Chem. Eng. Sci.*, 75:456–467, 2012.

A. Alke and D. Bothe. Direct numerical simulation of bubble dynamics and transfer processes in pure and contaminated systems. In *Proceedings of 6th International Conference on CFD in Oil & Gas, Metallurgical and Process Industries*, SINTEF/NTNU, Trondheim, Norway, June 2008.

S.M. Allen and J.W. Cahn. Ground state structures in ordered binary alloys with second neighbor interactions. *Acta Metallurgica*, 20(3):423–433, 1972.

ANSYS Inc. Ansys fluent theory guide.

E. Aulisa, S. Manservisi, R. Scardovelli, and S. Zaleski. Interface reconstruction with least-squares fit and split advection in three-dimensional Cartesian geometry. *J. Comput. Phys.*, 225:2301–2319, 2007.

S. Batzdorf. *Heat transfer and evaporation during single drop impingement onto a superheated wall*. PhD thesis, TTD, TU Darmstadt, 2015.

K. Bäumler. *Simulation of single drops with variable interfacial tension*. PhD thesis, Applied Mathematics III, Friedrich-Alexander Universität Erlangen-Nürnberg, 2014.

M.J. Berger, C. Helzel, and R.J. LeVeque. H-box methods for the approximation of hyperbolic conservation laws on irregular grids. *SIAM J. Numer. Anal.*, 41(3):893–918, 2003.

J.P. Boris and D.L. Book. Flux-corrected transport. I. SHASTA, a fluid transport algorithm that works. *J. Comput. Phys.*, 11(1):38 – 69, 1973.

D. Bothe and S. Fleckenstein. A Volume-of-Fluid-based method for mass transfer processes at fluid particles. *Chem. Eng. Sci.*, 101:283–302, 2013.

D. Bothe, M. Koebe, K. Wielage, and H.J. Warnecke. VOF-simulations of mass transfer from single bubbles and bubble chains rising in aqueous solutions. In *4th ASME-JSME Joint Fluids Engineering Conference*, number FEDSM2003-45155, July 6-11 2003.

D. Bothe, M. Koebe, K. Wielage, J. Prüss, and H.-J. Warnecke. Direct numerical simulation of mass transfer between rising gas bubbles and water. In Martin Sommerfeld, editor, *Bubbly Flows: Analysis, Modelling and Calculation*, pages 159–174, Berlin, Heidelberg, 2004. Springer Berlin Heidelberg.

D. Bothe, M. Kröger, A. Alke, and H.J. Warnecke. A VOF-based conservative method for the simulation of reactive mass transfer. In *7th International Conference on Multiphase Flow, ICMF*, 2010.

J.U. Brackbill, D.B. Kothe, and C. Zemach. A continuum method for modeling surface tension. *J. Comput. Phys.*, 100:335–354, 1992.

B. Bunner and G. Tryggvason. Dynamics of homogeneous bubbly flows Part 1. Rise velocity and microstructure of the bubbles. *J. Fluid Mech.*, 466:17–52, 2002a.

B. Bunner and G. Tryggvason. Dynamics of homogeneous bubbly flows Part 2. Velocity fluctuations. *J. Fluid Mech.*, 466:53–84, 2002b.

J.W. Cahn and J.E. Hilliard. Free energy of a nonuniform system. I. Interfacial free energy. *J. Chem. Phys.*, 28(2):258–267, 1958.

P.H. Calderbank and M.B. Moo-Young. The continuous phase heat and mass transfer properties of dispersions. *Chem. Eng. Sci.*, 16:39–54, 1961.

J. Casey. On the derivation of jump conditions in continuum mechanics. *Int. J. Struct. Changes Sol.*, 3(2):61–84, 2011.

R. Clift, J.R. Grace, and M.E. Weber. *Bubbles, Drops, and Particles*. New York ; London : Academic Press, 1978.

D. Colombet, D. Legendre, F. Risso, A. Cockx, and P. Guiraud. Dynamics and mass transfer of rising bubbles in a homogenous swarm at large gas volume fraction. *J. Fluid Mech.*, 763: 254–285, 2014.

T.N. Croft. *Unstructured mesh – Finite volume algorithm for swirling, turbulent, reacting flows*. PhD thesis, School of Computing and Mathematical Scienes – University of Greenwich, 1998.

E.L. Cussler. *Diffusion – Mass Transfer in Fluid Systems*. Cambridge University Press, 3rd edition, 2009.

D. Darmana, N.G. Deen, and J.A.M. Kuipers. Detailed 3D modeling of mass transfer processes in two-phase flows with dynamic interfaces. *Chem. Eng. Technol.*, 29(9):1027–1033, 2006.

D. Darmana, W. Dijlhuizen, N.G. Deen, M. van Sint Annaland, and J.A.M. Kuipers. Detailed 3D modelling of mass transfer processes in two-phase flows with dynamic interfaces. In *6th International Conference on Multiphase Flow, ICMF 2007*, 2007.

M. Darwish and F. Moukalled. The χ-schemes: a new consistent high-resolution formulation based on the normalized variable methodology. *Comput. Method. Appl. M.*, 192(13-14):1711–1730, 2003.

M.R. Davidson and M. Rudman. Volume-of-Fluid calculation of heat or mass transfer across deforming interfaces in two-fluid flow. *Numer. Heat Tr. B-Fund.*, 41(3-4):291–308, 2002.

W.D. Deckwer. *Reaktionstechnik in Blasensäulen*. Otto Salle Verlag GmbH & Co, 1985.

D. Deising. Flux-Corrected Transport Algorithm in OpenFOAM – MULES. techreport, Center of Smart Interfaces, Mathematical Modeling and Analysis, Technische Universität Darmstadt, August 5th 2015.

D. Deising, H. Marschall, and D. Bothe. A unified single-field model framework for Volume-Of-Fluid simulations of interfacial species transfer applied to bubbly flows. *Chem. Eng. Sci.*, 139: 173 – 195, 2016.

D. Deising, H. Marschall, and D. Bothe. Direct numerical simulation of mass transfer in bubbly flows. *Computers & Fluids*, 2018.

I. Demirdzic and S. Muzaferija. Numerical method for coupled fluid flow, heat transfer and stress analysis using unstructured moving meshes with cells of arbitrary topology. *Comput. Method. Appl. M.*, 125:235–255, 1995.

F. Denner and B. van Wachem. Compressive VOF method with skewness correction to capture sharp interfaces on arbitrary meshes. *J. Comput. Phys.*, 279:127–144, 2014.

F. Denner and B. van Wachem. TVD differencing on three-dimensional unstructured meshes with monotonicity-preserving correction of mesh skewness. *J. Comput. Phys.*, 298:466–479, 2015.

K.B. Deshpande and W.B. Zimmerman. Simulations of mass transfer limited reaction in a moving droplet to study transport limited characteristics. *Chem. Eng. Sci.*, 61:6424–6441, 2006.

S.S. Deshpande, L. Anumolu, and M.F. Trujillo. Evaluating the performance of the two-phase flow solver interFoam. *Comput. Sci. Discov.*, 5(1):014016, 2012.

W. Dijkhuizen, I. Roghair, M. van Sint Annaland, and J.A.M. Kuipers. Numerical derivation of the drag force coefficient in bubble swarms using a front tracking model. In *6th International Conference in Computational Fluid Dynamics in the Oil & Gas, Metallurgical and Process Industries*, Trondheim, Norway, June 10–12 2008.

C. Dopazo. On conditioned averages for intermittent turbulent flows. *J. Fluid Mech.*, 81:433–438, 7 1977.

D.A. Drew. Mathematical modeling of two-phase flow. *Ann. Rev. Fluid Mech.*, 15:261–291, 1983.

D.A. Drew and S.L. Passman. *Theory of Multicomponent Fluids*. Springer-Verlag New York, 1999.

M. Dudukovic. Relevance of multiphase reaction engineering to modern technological challenges. *Ind. and Eng. Chem. Res.*, 46:8574–8686, 2007.

P.C. Duineveld. The rise velocity and shape of bubbles in pure water at high Reynolds number. *J. Fluid Mech.*, 292:325–332, 1995.

L.C. Evans and R.F. Gariepy. Measure Theory and Fine Properties of Functions. In S.G. Krantz, editor, *Studies in Advanced Mathematics*. CRC Press, 1992.

R. Eymard, T. Gallouët, and R. Herbin. *Handbook of Numerical Analysis*, volume 7, chapter Finite Volume Methods, pages 713–1020. North Holland, Amsterdam, 2000.

J.H. Ferziger and M. Peric. *Computational Methods for Fluid Dynamics*. Springer Berlin Heidelberg, 2002.

B. Figueroa-Espinoza and D. Legendre. Mass or heat transfer from spheriodal gas bubbles rising through a stationary liquid. *Chem. Eng. Sci.*, 65:6296–6309, 2010.

S. Fleckenstein and D. Bothe. A Volume-of-Fluid-based numerical method for multi-component mass transfer with local volume changes. *J. Comput. Phys.*, 301:35–58, 2015.

M.M. Francois and N.N. Carlson. The balanced-force volume tracking algorithm and global embedded interface formulation for droplet dynamics with mass transfer. In *ASME 2010 3rd Joint US-European Fluids Engineering Summer Meeting collocated with 8th International Conference on Nanochannels, Microchannels, and Minichannels*, pages 81–88. American Society of Mechanical Engineers, 2010.

M.M. Francois, S.J. Cummins, E.D. Dendy, D.B. Kothe, J.M. Sicilian, and M.W. Williams. A balanced-force algorithm for continuous and sharp interfacial surface tension models within a volume tracking framework. *J. Comput. Phys.*, 213:141–173, 2006.

D. Fuster, A. Bagué, T. Boeck, L. Le Moyne, A. Leboissetier, S. Popinet, P. Ray, R. Scardovelli, and S. Zaleski. Simulation of primary atomization with an octree adaptive mesh refinement and VOF method. *Int. J. Multiphase Flow*, 35(6):550–565, 2009.

P.H. Gaskell and A.K.C. Lau. Curvature-compensated convective transport: SMART, A new boundedness- preserving transport algorithm. *Int. J. Numer. Methods Fluids*, 8(6):617–641, 1988.

C.J. Geankoplis. *Transport processes and unit operations*. Prentice Hall, 3rd edition, 1993.

D.W. Green and R.H. Perry. *Chemical Engineers' Handbook*. McGraw-Hill, 8th edition, 2007.

D. Gründing, S. Fleckenstein, and D. Bothe. A subgrid-scale model for reactive concentration boundary layers for 3D mass transfer simulations with deformable fluid interfaces. *Int. J. Heat Mass Transfer*, 101:476–487, 2016.

J. Hadamard. Mouvement permanent lent d'une sphere liquide et visqueuse dans un liquid visqueux. *C.R. Acad. Sci.*, 152:1735–1817, 1911.

Y. Haroun. *Etude du transfert de masse réactif gaz-liquide le long de plans corrugés par simulation numérique avec suivi d'interface*. PhD thesis, Institut National Polytechnique de Toulouse, Université de Toulouse, November 2008.

Y. Haroun, D. Legendre, and L. Raynal. Volume of Fluid method for interfacial reactive mass transfer: Application to stable liquid film. *Chem. Eng. Sci.*, 65(10):2896 – 2909, 2010.

A. Harten. On a class of high resolution total-variation-stable Finite-Difference schemes. Technical report, New York University, 1982.

A. Harten. High resolution schemes for hyperbolic conservation laws. *J. Comput. Phys.*, 49(3): 357–393, 1983.

D. Hartmann, M. Meinke, and W. Schröder. A Cartesian cut-cell solver for compressible flows. In E. Krause, Y. Shokin, M. Resch, D. KrÃ¯ner, and N. Shokina, editors, *Computational Science and High Performance Computing IV*, volume 115 of *Notes on Numerical Fluid Mechanics and Multidisciplinary Design*, pages 363–376. Springer Berlin Heidelberg, 2011.

M. Hassanizadeh and W.G. Gray. General conservation equations for multi-phase systems: 1. Averaging procedure. *Adv. Water Resour.*, 2:131–144, 1979.

K. Hayashi and A. Tomiyama. Interface tracking simulation of mass transfer from a dissolving bubble. *J. Comput. Multiphas. Flow*, 3(4):247–262, 2011.

K. Hayashi, S. Hosoda, G. Tryggvason, and A. Tomiyama. Effects of shape oscillation on mass transfer from a Taylor bubble. *Int. J. Multiphase Flow*, 58(0):236 – 245, 2014.

D.P. Hill. *The computer simulation of dispersed two-phase flows*. PhD thesis, Department of Engineering - Imperial College of Science, Technology and Medicine, 1998.

S. Hill, D. Deising, T. Acher, H. Klein, D. Bothe, and H. Marschall. Boundedness-preserving implicit correction of mesh-induced errors for VoF based heat and mass transfer. *J. Comput. Phys.*, 352:285–300, 2018.

C. Hirsch. *Numerical computation of internal and external flows – The fundamentals of Computational Fluid Dynamics*, volume 1. John Wiley & Sons, Ltd., second edition edition, 2007.

J. Hou, F. Simons, and R. Hinkelmann. Improved total variation diminishing schemes for advection simulation on arbitrary grids. *Int. J. Numer. Methods Fluids*, 70(3):359–382, 2012.

G.A. Hughmark. Holdup and mass transfer in bubble columns. *Ind. Eng. Chem. Process Des. Dev.*, 6:218–220, 1967.

M. Ishii and T. Hibiki. *Thermo-Fluid Dynamics of Two-Phase Flow*. Springer-Verlag New York, 2 edition, 2011.

H.A. Jakobsen. *Chemical Reactor Modeling: Multiphase Reactive Flows*. Springer-Verlag Berlin Heidelberg, 2008.

A. Jameson. Positive schemes and shock modelling for compressible flows. *Int. J. Numer. Methods Fluids*, 20:743–776, 1995.

A Jameson and P.D. Lax. Conditions for the construction of multi-point total variation diminishing difference schemes. *Appl. Numer. Math.*, 2(3-5):335–346, November 1986.

H. Jasak. *Error analysis and estimation for the finite volume method with applications to fluid flows*. PhD thesis, Department of Mechanical Engineering, Imperial College of Science, Technology & Medicine, January 1996.

H. Jasak and H.G. Weller. Interface tracking capabilities of the interGamma differencing scheme. Technical report, Department of Mechanical Engineering, Imperial College of Science, Technology and Medicine, London, 1995.

H. Jasak, H.G. Weller, and A.D. Gossman. High resolution NVD differencing scheme for arbitrarily unstructured meshes. *Int. J. Numer. Methods Fluids*, 31:431–449, 1999.

L. Jofre, O. Lehmkuhl, J. Castro, and A. Oliva. A PLIC-VOF implementation on parallel 3D unstructured meshes. In *European Conference on Comuptational Fluid Dynamics, ECCOMAS CFD*, 2010.

A.I. Johnson, F. Besik, and A.E. Hamielec. Mass transfer from a single rising bubble. *Can. J. Chem. Eng.*, 47:559–564, 1969.

F. Juretic. *Error analysis in finite volume CFD*. PhD thesis, Department of Mechanical Engineering, Imperial College London, December 2004.

F. Juretic and A.D. Gosman. Error analysis of the finite-volume method with respect to mesh type. *Numer. Heat Tr. B-Fund.*, 57:414–439, 2010.

J.G. Khinast. Impact of 2-D bubble dynamics on the selectivity of fast gas-liquid reactions. *AIChE J.*, 47:2304–2319, 2001.

J.G. Khinast, A. Koynov, and T.M. Leib. Reactive mass transfer at gas-liquid interfaces: impact of micro-scale fluid dynamics on yield and selectivity of liquid-phase cyclohexane oxidation. *Chem. Eng. Sci.*, 58:3961–3971, 2003.

D.J. Kirwan. *Handbook of separation process technology*, chapter Mass transfer principles, pages 60–128. John Wiley & Sons, 1987.

D.B. Kothe. Perspective on Eulerian finite volume methods for incompressible interfacial flows. In *Kuhlmann and H Rath*, pages 267–331. Springer, 1999.

A. Koynov, J.G. Khinast, and G. Tryggvason. Mass transfer and chemical reactions in bubble swarms with dynamic interfaces. *AIChE J.*, 51(10):2786–2800, 2005.

R. Krishna, M.I. Urseanu, J.M. van Baten, and J. Ellenberger. Rise velocity of a swarm of large gas bubbles in liquids. *Chem. Eng. Sci.*, 54:171–183, 1999.

B. Lafaurie, C. Nardone, R. Scardovelli, S. Zaleski, and G. Zanetti. Modelling merging and fragmentation in multiphase flows with SURFER. *J. Comput. Phys.*, 113(1):134 – 147, 1994.

M. Lance and J. Bataille. Turbulence in the liquid phase of a uniform bubbly air-water flow. *J. Fluid Mech.*, 222:95–118, 1991.

J.M. Lee. *Biochemical engineering*. Prentice Hall, 1992.

D. Legendre, R. Zenit, and Velez-Cordero. R. On the deformation of gas bubbles in liquids. *Phys. Fluids*, 24(4):043303, 2012.

C. Lehrenfeld. *On a space-time extended finite element method for the solution of a class of two-phase mass transport problems*. PhD thesis, IGPM, RWTH Aachen, 2015.

B.P. Leonard. Universal limiter for transient interpolation modeling of the advective transport equations: The ULTIMATE conservative differencing scheme, 1988.

B.P. Leonard. The ULTIMATE conservative difference scheme applied to unsteady one-dimensional advection. *Comput. Methods Appl. Mech. Eng.*, 88(1):17–74, 1991.

B.P. Leonard and S. Mokhtari. ULTRA-SHARP nonoscillatory convection schemes for high-speed steady multidimensional flow. Technical report, NASA Technical Memorandum 102568, 1990.

R.J. LeVeque. *Finite Volume Methods for Hyperbolic Problems*. Cambridge Texts in Applied Mathematics, 2002.

P. Liovic, M. Rudman, J.L. Liow, D. Lakehal, and D. Kothe. A 3D unsplit-advection volume tracking algorithm with planar-preserving interface reconstruction. *Computers & Fluids*, 35: 1011–1032, 2006.

A.C. Lochiel and P.H. Calderbank. Mass transfer in the continuous phase around axisymmetric bodies of revolution. *Chem. Eng. Sci.*, 19(7):471 – 484, 1964.

R. Löhner. Robust, vectorized search algorithms for interpolation on unstructured grids. *J. Comput. Phys.*, 118:380–387, 1995.

T. Maric, H. Marschall, and D. Bothe. voFoam - A geometrical volume of fluid algorithm on arbitrary unstructured meshes with local dynamic adaptive mesh refinement using OpenFOAM. *ArXiv e-prints*, 2013.

T. Maric, H. Marschall, and D. Bothe. lentFoam - A hybrid level set/front tracking method on unstructured meshes . *Computers & Fluids*, 113:20 – 31, 2015.

H. Marschall. *Towards the numerical simulation of multi-scale two-phase flows*. PhD thesis, Technische Universität München, Lehrstuhl I für Technische Chemie, July 2011.

H. Marschall, K. Hinterberger, C. Schüler, F. Habla, and O. Hinrichsen. Numerical simulation of species transfer across fluid interfaces in free-surface flows using OpenFOAM. *Chem. Eng. Sci.*, 78(0):111 – 127, 2012.

W.L. McCabe, J.C. Smith, and P. Harriott. *Unit operations of chemical engineering*. McGraw-Hill, 7th edition, 2005.

D.W. Moore. The velocity of rise of distorted gas bubbles in a liquid of small viscosity. *J. Fluid Mech.*, 23(4):749–766, 1965.

G. Mougin and J. Magnaudet. Path Instability of a Rising Bubble. *Phys. Rev. Lett.*, 2002.

F. Moukalled and M. Darwish. Transient schemes for capturing interfaces of free-surface flows. *Numer. Heat Tr. B-Fund.*, 61:171–203, 2012.

F. Moukalled, L. Mangani, and M. Darwish. *The Finite Volume Method in Computational Fluid Dynamics – An advanced introduction with OpenFOAM and Matlab*. Springer International Publishing Switzerland, 2015.

S. Muzaferija, M. Peric, P. Sames, and T. Schellin. A two-fluid Navier-Stokes solver to simulate water entry. In *Twenty-Second Symposium on Naval Hydrodynamics*, pages 638–664, 1999.

E.B. Nauman. *Chemical Reactor Design, Optimization, and Scaleup*. McGraw-Hill Education, 2002.

H. Oellrich, H. Schmidt-Traub, and H. Brauer. Theoretische Berechnung des Stofftransports in der Umgebung einer Einzelblase. *Chem. Eng. Sci.*, 28:711–721, 1973.

OFuserGuide. OpenFOAM User Guide 2.1.1. http://www.openfoam.org/docs/, 2013.

E. Olsson and G. Kreiss. A conservative level set method for two phase flow. *J. Comput. Phys.*, 210:225–246, 2005.

A. Onea, M. Wörner, and D.G. Cacuci. A qualitative computational study of mass transfer in upward bubble train flow through square and rectangular mini-channels. *Chem. Eng. Sci.*, 64: 1416–1435, 2009.

S.V. Patankar. *Numerical Heat Transfer and Fluid Flow*. Series in computational methods in mechanics and thermal sciences. Taylor & Francis, 1980.

S.V. Patankar and D.B. Spalding. A calculation procedure for heat, mass and momentum transfer in three-dimensional parabolic flows. *Int. J. Heat Mass Transfer*, 15(10):1787 – 1806, 1972.

C.S. Peskin. Numerical analysis of blood flow in the heart. *J. Comput. Phys.*, 25:220–252, 1977.

Stephane Popinet. An accurate adaptive solver for surface-tension-driven interfacial flows. *J. Comput. Phys.*, 228:5838–5866, 2009.

A. Prosperetti. Ensemble Averaging Techniques for Disperse Flows. In Donald A. Drew, Daniel D. Joseph, and Stephen L. Passman, editors, *Particulate Flows*, volume 98 of *The IMA Volumes in Mathematics and its Applications*, pages 99–136. Springer New York, 1998.

V. Przulj and B. Basara. Bounded convection schemes for unstructured grids. In *15th AIAA Computational Fluid Dynamics Conference*, Anaheim, CA, June 2001.

S. Radl, A. Koynov, G. Tryggvason., and J.G. Khinast. DNS-based prediction of the selectivity of fast multiphase reactions: Hydrogenation of nitroarenes. *Chem. Eng. Sci.*, 63:3279–3291, 2008.

O. Reynolds. *The sub-mechanics of the universe*, volume 3. Cambridge University Press, 1903.

C.M. Rhie and W.L. Chow. Numerical study of the turbulent flow past an airfoil with trailing edge separation. *AIAA Journal*, 21:1525–1532, 1983.

W.J. Rider and D.B. Kothe. Stretching and tearing interface tracking methods. In *Proceeding of the 12th AIAA Computational Fluid Dynamics Conference*, 1995.

P.L. Roe. Characteristic-based schemes for the Euler equations. *Ann. Rev. Fluid Mech.*, 18:337–365, 1986.

P.L. Roe. Error estimates for cell-vertex solutions of the compressible Euler equations. Technical Report ICASE Report No. 87-6, NASA Langley Research Center, 1987.

I. Roghair. *Direct mumerical simulations of hydrodynamics and mass transfer in dense bubbly flows*. PhD thesis, Technische Universiteit Eindhoven, 2012.

I. Roghair, M. van Sint Annaland, and H.J.A.M. Kuipers. Drag force and clustering in bubble swarms. *AIChE J.*, 59(5):1791–1800, May 2013.

I. Roghair, M. Van Sint Annaland, and H.J.A.M. Kuipers. An improved Front-Tracking technique for the simulation of mass transfer in dense bubbly flows. *Chem. Eng. Sci.*, 152:351–369, 2016.

H. Rusche. *Computational fluid dynamics of dispersed two-phase flows at high phase fractions*. PhD thesis, Department of Mechanical Engineering, Imperial College of Science, Technology & Medicine, Exhibition Road, London SW7 2BX, December 2002.

Y.T. Shah, B.G. Kelkar, S.P. Goobole, and W.-D. Deckwer. Design parameters estimations for bubble column reactors. *AIChE J.*, 28:353–379, 1982.

T.K. Sherwood, R.L. Pigford, and C.R. Wilke. *Mass transfer*. McGraw-Hill, 1975.

J.C. Slattery. *Advanced Transport Phenomena*. Cambridge University Press, 1999.

K.K. So, X.Y. Hu, and N.A. Adams. Anti-diffusion method for interface steepening in two-phase incompressible flow. *J. Comput. Phys.*, 230(13):5155–5177, June 2011.

S.P. Spekreijse. *Multigrid Solution of the Steady Euler Equations*. PhD thesis, Technische Universiteit Delft, 1987.

G. Stokes. On a difficulty in the theory of sound. *Lond. Edinb. Phil. Mag.*, 33:349–356, 1848.

P. Sweby. High resolution schemes using flux limiters for hyperbolic conservation laws. *SIAM J. Numer. Anal.*, 21(5):995–1011, 1984.

F. Takemura and A. Yabe. Gas dissolution process of spherical rising gas bubbles. *Chem. Eng. Sci.*, 53(15):2691 – 2699, 1998.

R.E. Treybal. *Mass-transfer operations*. McGraw-Hill, 3rd edition, 1980.

Z. Tukovic and H. Jasak. Simulation of Free-Rising Bubble with Soluble Surfactant Using Moving Mesh Finite Volume/Area Method. In *Proceedings of 6th International Conference on CFD in Oil & Gas, Metallurgical and Process Industries, no. CFD08-072*, 2008.

Z. Tukovic and H. Jasak. A moving mesh finite volume interface tracking method for surface tension dominated interfacial fluid flow. *Computers & Fluids*, 55(0):70–84, 2012.

E. Turkel. Accuracy of schemes with non-uniform meshes for compressible fluid flows. Technical Report ICASE Report N1/4 85-59, NASA Langley Research Center, 1985.

O. Ubbink. *Numerical Prediction of Two Fluid Systems with Sharp Interfaces*. PhD thesis, Department of Mechanical Engineering, Imperial College of Science, Technology & Medicine, January 1997.

B. van Leer. Towards the ultimate conservative difference scheme. II. Monotonicity and conservation combined in a second-order scheme. *J. Comput. Phys.*, 14(4):361 – 370, 1974.

T. Waclawczyk and T. Koronowicz. Remarks on prediction of wave drag using VOF method with interface capturing approach. *Archives of Civil and Mechanical Engineering*, 8:6–14, 2008.

R.F. Warming and B.J. Hyett. The modified equation to the stability and accuracy analysis of finite-difference methods. *J. Comput. Phys.*, 14(2), 1974.

P. Weber, H. Marschall, and D. Bothe. Highly accurate two-phase species transfer based on ALE Interface Tracking. *Int. J. Heat Mass Transfer*, 104:759–773, 2017.

P.S. Weber. *Modeling and Numerical Simulation of Multi-Component Two-Phase Fluid Systems with Ionic Species*. PhD thesis, TU Darmstadt, 2016. PhD thesis.

A. Weiner and D. Bothe. Advanced subgrid-scale modeling for convection-dominated species transport at fluid interfaces with application to mass transfer from rising bubbles. *J. Comput. Phys.*, 347:261–289, 2017.

H.G. Weller. A code independent notation for finite volume algorithms. Technical report, OpenCFD Limited, 2005a.

H.G. Weller. Derivation, modelling and solution of the conditionally averaged two-Phase flow equations. Technical report, OpenCFD Limited, 2005b.

H.G. Weller. A new approach to VOF-based interface capturing methods for incompressible and compressible flow. Technical report, OpenCFD Limited, 2006.

G.D. Weymouth and D.K. Yue. Conservative Volume-of-Fluid method for free-surface simulations on Cartesian grids. *Journal of Computational Physics*, 229(8):2853–2865, 2010.

S. Whitaker. *The Method of Volume Averaging*, volume 13. Springer, 1999.

M. Wörner. *A Compact Introduction to the Numerical Modeling of Multiphase Flows*. FZKA, 2003.

M. Wörner, W. Sabisch, G. Grötzenbach, and D. Cacuci. Volume-averaged conservation equations for Volume-of-Fluid interface tracking. In *Fourth International Conference on Multiphase Flow, ICMF-2001*, New Orleans, Luisiana, USA, May 27 – 1 2001.

C. Yang and Z.-S. Mao. Numerical simulation of interphase mass transfer with the level set approach. *Chem. Eng. Sci.*, 60(10):2643–2660, 2005.

S.T. Zalesak. Fully multidimensional flux-corrected transport algorithms for fluids. *J. Comput. Phys.*, 31(3):335 – 362, 1979.

S. Zhang and K. Jain. Least square data reconstruction approach for unstructured grid. In *Proceedings of 5th Joint ASME/JSME Fluids Engineering Conference*, 2007.

S.J. Zhang and X. Zhao. Higher order data reconstruction schemes for unstructured grid. In *36th AIAA Fluid Dynamics Conference and Exhibit*, San Francisco, California, June 5-8 2006.